



## Copyright Statement

The digital copy of this thesis is protected by the Copyright Act 1994 (New Zealand). This thesis may be consulted by you, provided you comply with the provisions of the Act and the following conditions of use:

- Any use you make of these documents or images must be for research or private study purposes only, and you may not make them available to any other person.
- Authors control the copyright of their thesis. You will recognise the author's right to be identified as the author of this thesis, and due acknowledgement will be made to the author where appropriate.
- You will obtain the author's permission before publishing any material from their thesis.

To request permissions please use the Feedback form on our webpage.  
<http://researchspace.auckland.ac.nz/feedback>

## General copyright and disclaimer

In addition to the above conditions, authors give their consent for the digital copy of their work to be used subject to the conditions specified on the Library [Thesis Consent Form](#)

# Passive Myocardial Mechanics

---

## Constitutive Laws

### and

## Material Parameter Estimation

by Holger Schmid

Supervised by Prof Peter J. Hunter & Dr Martyn P. Nash

A thesis submitted in partial fulfilment of the requirements for  
the degree of PhD at the University of Auckland



Bioengineering Institute,  
University of Auckland,  
New Zealand

August 16, 2006



# Abstract

This study investigated the performance of orthotropic constitutive laws describing the passive mechanical behaviour of the myocardium. The performance was validated against simple shear experiments of pig hearts which were available from earlier studies.

First, a homogeneous deformation model was developed which captured the main features of the deformation process. This served as the basis for a comparative study between three phenomenological material laws that had been published in the literature. Two of these laws exhibited certain limitations and two further constitutive laws were therefore developed that removed these limitations. Thus, five material laws were investigated in terms of their performance to fit the given experimental data by reducing a least-square objective function between the experimental and model data. Furthermore the consistency of the material parameters amongst experiments was investigated. As part of this study, a modified least-squares objective function was developed that decreased the computational time involved by about two orders of magnitude with comparable error.

Second, the assumption of a homogeneous deformation of simple shear was removed and the parameters were estimated using a finite element environment using an inverse estimation technique and therefore fulfilling the equations of motion that underpin continuum mechanics. It was found that

the material parameters of all laws were in the same range compared to those obtained from the homogeneous study. Relaxing the homogeneous assumptions slightly reduced the objective function error although the computational time increased by three orders of magnitude.

Third, the experimental protocol of six simple shear modes was supplemented with three uniaxial deformations modes. The material parameters for the same constitutive relations were estimated. It was possible to show that the material parameters that were associated with shear strain were very similar to those obtained from the simple shear study. The axial material parameters, however, were considerably different.

Finally, since it is recognised that phenomenological material laws do not provide insight into the underlying micro-structural mechanisms, the framework for a multi-scale constitutive relation was developed. This is based on multi-scale images of rat myocardium.

# Acknowledgements

I am grateful to the organisations that have provided financial support for my graduate studies. In particular, the University of Auckland awarded me an International Doctoral Scholarship. Additional support for conference attendance was provided by the National Heart foundation, the Maurice Phyllis and Paykel Trust, Education New Zealand and the Research office of the University of Auckland.

I would like to thank my supervisors, Prof Peter Hunter and Dr Martyn Nash for their generous support, time and excellent guidance during my time at the Bioengineering Institute.

In addition to my supervisors, many others provided valuable input to the work covered in this thesis; Dr Alistair Young for his valuable feedback throughout my studies. Dr Ian LeGrice, Assoc Prof Bruce Smaill, Dr Paul O’Callaghan and Dr Rob Kirton for their support in organising the experiments. Vijay Rajagopal for coding the CellML background for setting up mechanical constitutive equations. Dr Greg Sands for the help in the image optimisation. Dr Oliver Röhrle for his invaluable feedback in regard to the modified objective function. Dr Cameron Walker for his advice during the setup of the algorithm for the myocyte topology. Dr Piaras Kelly for the support during my first teaching experiences.

I certainly owe a great deal to my two summer students Andy Wei Lin and

Matthew McCormick. Working with you guys was fantastic and an enriching experience.

Thanks to all in the tramping club, Lloyd, Anthea, Shane, Chantelle, Jane, Lara and all the others.

My friends Konrad, Flo, Bodo, Katrin, Marina, Linda, Alex, Wolfram, Dirk, Frithjof, Hans, Stephan, Corinna, Robert Lee Fife III, Jochen, Kohlemohr, Haubi, Raschid, Felix, Olaf, Mascha, Anke, Christian, Ann-Kathrin, Su, Jon, Vittoria, Mike, Rita, Hayley, Anita, Kilian, Daniel, Jonna, Will, Ankur, Gail, Ruth and Alice as well as Mrs Bräunig have constantly reminded me that there is a life outside the experience of a doctorate.

Nothing of this of course would have been possible without the constant support of my parents, Gisela and Thomas Schmid, my aunt and uncle Katharina and Jürgen Steuck as well as my sister Andrea Holzinger, my brother-in-law Lukas Holzinger and my little niece Svenja Holzinger with the cutest smile. They were a source of consistent refreshment and laughter.

Furthermore I am highly indebted to Dr Richard Bolstad and Fr Bernard Kiely. Their utter patience and unquestioning acceptance of myself gave me the strength I needed so often during the “thesis-blues”.

Last and by no means least I would like to thank Ardass Singh Khalsa. Words cannot describe the gratitude I feel towards him. If I may try so, however, then they would be:

**Ang Sang Wahe Guru!**

# Contents

|   |            |
|---|------------|
| <b>Abstract</b>   | <b>ii</b>  |
| <b>Acknowledgements</b>                                 | <b>iii</b> |
| <b>Table of Contents</b>                                | <b>v</b>   |
| <b>List of Figures</b>                                  | <b>x</b>   |
| <b>List of Tables</b>                                   | <b>xiv</b> |
| <b>1 Introduction</b>                                   | <b>1</b>   |
| 1.1 Objective . . . . .                                 | 3          |
| 1.2 Thesis Summary . . . . .                            | 3          |
| 1.3 Publications Resulting from this Thesis . . . . .   | 4          |
| <b>I Background</b>                                     | <b>7</b>   |
| <b>2 The Heart</b>                                      | <b>11</b>  |
| 2.1 Gross Structure . . . . .                           | 12         |
| 2.1.1 Ventricles . . . . .                              | 12         |
| 2.1.2 Connective Tissue Network . . . . .               | 13         |
| 2.2 Microstructural architecture of the heart . . . . . | 14         |



|          |   |           |
|----------|---|-----------|
| 2.3      | Tissue Experiments . . . . .                            | 17        |
| 2.3.1    | Pressure–Volume Measurements . . . . .                  | 17        |
| 2.3.2    | Uniaxial Tests . . . . .                                | 18        |
| 2.3.3    | Biaxial Tests . . . . .                                 | 18        |
| 2.3.4    | Triaxial Tests . . . . .                                | 19        |
| 2.3.5    | Multiaxial Simple Shear Experiments . . . . .           | 19        |
| 2.3.6    | Simple Shear & Uniaxial Extension . . . . .             | 20        |
| 2.4      | Summary . . . . .                                       | 22        |
| <b>3</b> | <b>Continuum Mechanics</b>                              | <b>23</b> |
| 3.1      | Kinematics . . . . .                                    | 23        |
| 3.1.1    | Body & Motion . . . . .                                 | 24        |
| 3.1.2    | Configurations . . . . .                                | 24        |
| 3.1.3    | Representation of Functions . . . . .                   | 24        |
| 3.1.4    | Deformation Gradient Tensor . . . . .                   | 26        |
| 3.1.5    | Deformation Measures . . . . .                          | 30        |
| 3.2      | Stress & Balance Equations . . . . .                    | 32        |
| 3.2.1    | Forces . . . . .  | 32        |
| 3.2.2    | Cauchy’s Hypothesis . . . . .                           | 33        |
| 3.2.3    | Balance of Linear & Angular Momentum . . . . .          | 34        |
| 3.2.4    | Cauchy Stress Tensor . . . . .                          | 35        |
| 3.2.5    | 1 <sup>st</sup> Piola–Kirchhoff Stress Tensor . . . . . | 35        |
| 3.2.6    | 2 <sup>nd</sup> Piola–Kirchhoff Stress Tensor . . . . . | 36        |
| 3.3      | Constitutive Theory . . . . .                           | 36        |
| 3.3.1    | Hyperelasticity . . . . .                               | 37        |
| 3.3.2    | Objectivity . . . . .                                   | 37        |
| 3.3.3    | Stress–Strain Relationship . . . . .                    | 38        |
| 3.3.4    | Isotropy & Anisotropy . . . . .                         | 39        |

|           |  |           |
|-----------|--|-----------|
| 3.3.5     | Incompressibility . . . . .                                  | 40        |
| <b>4</b>  | <b>Numerical Tools</b>                                       | <b>43</b> |
| 4.1       | Finite Element Method . . . . .                              | 43        |
| 4.1.1     | Galerkin Finite Element Equations . . . . .                  | 44        |
| 4.2       | Optimisation Techniques for Parameter Estimation . . . . .   | 46        |
| 4.2.1     | Least-Squares Objective Function . . . . .                   | 47        |
| 4.2.2     | Newton Method . . . . .                                      | 47        |
| 4.2.3     | Levenberg-Marquardt Method . . . . .                         | 48        |
| 4.3       | A Novel Optimisation Technique . . . . .                     | 48        |
| 4.4       | Statistical Tools . . . . .                                  | 50        |
| 4.4.1     | Normalised Standard Deviation . . . . .                      | 50        |
| 4.4.2     | Goodness of Fit . . . . .                                    | 51        |
| 4.4.3     | Akaike Information Criterion (AIC) . . . . .                 | 51        |
| 4.4.4     | M- & D-Optimality . . . . .                                  | 52        |
| 4.4.5     | Material Parameter Variability amongst Experiments . . . . . | 53        |
| 4.4.6     | Material Parameter Variability amongst Models . . . . .      | 54        |
| <b>II</b> | <b>Application</b>   | <b>55</b> |
| <b>5</b>  | <b>Myocardial Material Laws</b>                              | <b>59</b> |
| 5.1       | Historical Introduction . . . . .                            | 59        |
| 5.2       | Published Laws . . . . .                                     | 61        |
| 5.2.1     | Costa Law . . . . .  | 61        |
| 5.2.2     | Pole-Zero Law . . . . .                                      | 63        |
| 5.2.3     | Langevin Eight-Chain Law . . . . .                           | 63        |
| 5.3       | Modified Laws . . . . .                                      | 65        |
| 5.3.1     | Separated Fung Law . . . . .                                 | 66        |

|          |  |            |
|----------|--|------------|
| 5.3.2    | Tangent Law . . . . .                                    | 66         |
| 5.3.3    | Theoretical Considerations . . . . .                     | 67         |
| 5.3.4    | Practical Considerations . . . . .                       | 68         |
| 5.4      | Summary . . . . .  | 69         |
| <b>6</b> | <b>Shear Homogeneous Model</b>                           | <b>71</b>  |
| 6.1      | Development of Homogeneous Model . . . . .               | 72         |
| 6.1.1    | Derivation of Analytical Model . . . . .                 | 72         |
| 6.1.2    | Derivation of Objective Function . . . . .               | 74         |
| 6.1.3    | Convergence Analysis of Optimisation Technique . . . . . | 75         |
| 6.1.4    | Applicability of Optimisation Technique . . . . .        | 77         |
| 6.1.5    | Initial Guesses . . . . .                                | 78         |
| 6.2      | Homogeneous Results . . . . .                            | 79         |
| 6.3      | Discussion . . . . .                                     | 87         |
| 6.4      | Summary . . . . .  | 87         |
| <b>7</b> | <b>Shear FE Model</b>                                    | <b>89</b>  |
| 7.1      | Development of FE Model . . . . .                        | 89         |
| 7.1.1    | Validation of constitutive laws . . . . .                | 91         |
| 7.1.2    | Optimisation Kernel . . . . .                            | 91         |
| 7.1.3    | Convergence Analysis . . . . .                           | 92         |
| 7.2      | Results FE Shear Model . . . . .                         | 92         |
| 7.3      | Discussion . . . . .                                     | 99         |
| 7.4      | Comparison FE & Homogeneous Model . . . . .              | 100        |
| 7.5      | Summary . . . . .  | 101        |
| <b>8</b> | <b>Full FE Model</b>                                     | <b>103</b> |
| 8.1      | Development of FE Model . . . . .                        | 104        |
| 8.2      | Estimation Strategy . . . . .                            | 104        |

|            |  |            |
|------------|--|------------|
| 8.2.1      | All Parameters to Shear Modes . . . . .                | 106        |
| 8.2.2      | Axial Parameters to Uniaxial Extension Modes . . . . . | 107        |
| 8.2.3      | All Parameters to All Modes . . . . .                  | 109        |
| 8.3        | Results Full FE Model . . . . .                        | 113        |
| 8.4        | Discussion . . . . .                                   | 116        |
| 8.5        | Summary . . . . .                                      | 117        |
| <b>9</b>   | <b>Conclusion</b>                                      | <b>119</b> |
| <b>III</b> | <b>Outlook: Microstructural Models</b>                 | <b>123</b> |
| <b>10</b>  | <b>Multi-Scale Modeling Framework</b>                  | <b>127</b> |
| 10.1       | Topology . . . . .                                     | 129        |
| 10.2       | System Identification Model . . . . .                  | 131        |
| 10.3       | Digitisation of Myocardial Topology . . . . .          | 132        |
| 10.3.1     | Digitisation of Myocyte Topology . . . . .             | 133        |
| 10.3.2     | Voronoi Cells . . . . .                                | 136        |
| 10.4       | Algorithm of Myocyte Topology . . . . .                | 137        |
| 10.4.1     | Regression Analysis . . . . .                          | 139        |
| 10.4.2     | Algorithm for Segment Topology . . . . .               | 140        |
| 10.4.3     | Preliminary Results . . . . .                          | 141        |
| 10.5       | Discussion . . . . .                                   | 143        |
| 10.6       | Summary . . . . .                                      | 144        |
| <b>IV</b>  | <b>Appendices</b>                                      | <b>145</b> |
| <b>A</b>   | <b>Ambiguities</b>                                     | <b>149</b> |
| A.1        | Introduction . . . . .                                 | 149        |

|          |  |            |
|----------|--|------------|
| A.2      | Derivation of Stress–Strain Relations . . . . .    | 151        |
| A.3      | Conclusion . . . . .                               | 156        |
| A.4      | Nomenclature for this Section . . . . .            | 156        |
| <b>B</b> | <b>Additional Data, Homogeneous Model</b>          | <b>159</b> |
| B.1      | Example File for Homogeneous Model . . . . .       | 159        |
| B.2      | All Graphs, Homogeneous Model . . . . .            | 167        |
| <b>C</b> | <b>Additional Data for FE Model</b>                | <b>199</b> |
| C.1      | Example File, FE Model . . . . .                   | 199        |
| C.2      | Mesh Convergence . . . . .                         | 202        |
| C.3      | All Graphs for all Experiments, FE Model . . . . . | 207        |
|          | <b>References</b>                                  | <b>233</b> |

# List of Figures

|     |   |     |
|-----|---|-----|
| 2.1 | Longitudinal cross-section of the heart . . . . .             | 13  |
| 2.2 | Schematic of cardiac micro-structure . . . . .                | 16  |
| 2.3 | Schematic of cardiac micro-structure . . . . .                | 17  |
| 2.4 | Six simple shear modes . . . . .                              | 20  |
| 2.5 | NS-shear deformation graph . . . . .                          | 21  |
| 2.6 | Uniaxial Extension & Compression . . . . .                    | 22  |
| 5.1 | Orthotropic Unit Cell of LECL . . . . .                       | 64  |
| 6.1 | Convergence analysis of modified objective function . . . . . | 76  |
| 6.2 | Graph of homogeneous model, experiment 3, CL . . . . .        | 85  |
| 6.3 | Graph of homogeneous model, experiment 3, LECL . . . . .      | 86  |
| 7.1 | Finite element mesh, shear . . . . .                          | 90  |
| 7.2 | Graph of FE model, experiment 3, SFL . . . . .                | 97  |
| 7.3 | Graph of FE model, experiment 3, CL . . . . .                 | 98  |
| 7.4 | Comparison parameters, CL . . . . .                           | 102 |
| 8.1 | Finite element mesh, extension . . . . .                      | 105 |
| 8.2 | Shear Graphs First Step . . . . .                             | 107 |
| 8.3 | Axial Graphs All Steps . . . . .                              | 110 |
| 8.4 | Shear Graphs Second Step . . . . .                            | 111 |

|      |  |     |
|------|--|-----|
| 8.5  | Shear Graphs Last Step . . . . .                         | 112 |
| 10.1 | Transmural block of myocardium . . . . .                 | 128 |
| 10.2 | Cross Sectional Area of Myocardium . . . . .             | 129 |
| 10.3 | Transmural collagen distribution . . . . .               | 130 |
| 10.4 | Small block of myocardium . . . . .                      | 133 |
| 10.5 | Digitisation Process . . . . .                           | 134 |
| 10.6 | Length Distribution Segments . . . . .                   | 136 |
| 10.7 | Digitisation Process . . . . .                           | 137 |
| 10.8 | Model Sample Images . . . . .                            | 142 |
| 10.9 | Comparison of Sample and Model . . . . .                 | 143 |
| B.1  | Graph of homogeneous model, experiment 1, CL . . . . .   | 168 |
| B.2  | Graph of homogeneous model, experiment 1, SFL . . . . .  | 169 |
| B.3  | Graph of homogeneous model, experiment 1, PZL . . . . .  | 170 |
| B.4  | Graph of homogeneous model, experiment 1, TL . . . . .   | 171 |
| B.5  | Graph of homogeneous model, experiment 1, LECL . . . . . | 172 |
| B.6  | Graph of homogeneous model, experiment 2, CL . . . . .   | 173 |
| B.7  | Graph of homogeneous model, experiment 2, SFL . . . . .  | 174 |
| B.8  | Graph of homogeneous model, experiment 2, PZL . . . . .  | 175 |
| B.9  | Graph of homogeneous model, experiment 2, TL . . . . .   | 176 |
| B.10 | Graph of homogeneous model, experiment 2, LECL . . . . . | 177 |
| B.11 | Graph of homogeneous model, experiment 3, CL . . . . .   | 178 |
| B.12 | Graph of homogeneous model, experiment 3, SFL . . . . .  | 179 |
| B.13 | Graph of homogeneous model, experiment 3, PZL . . . . .  | 180 |
| B.14 | Graph of homogeneous model, experiment 3, TL . . . . .   | 181 |
| B.15 | Graph of homogeneous model, experiment 3, LECL . . . . . | 182 |
| B.16 | Graph of homogeneous model, experiment 4, CL . . . . .   | 183 |

|   |     |
|---|-----|
| B.17 Graph of homogeneous model, experiment 4, SFL . . . . .  | 184 |
| B.18 Graph of homogeneous model, experiment 4, PZL . . . . .  | 185 |
| B.19 Graph of homogeneous model, experiment 4, TL . . . . .   | 186 |
| B.20 Graph of homogeneous model, experiment 4, LECL . . . . . | 187 |
| B.21 Graph of homogeneous model, experiment 5, CL . . . . .   | 188 |
| B.22 Graph of homogeneous model, experiment 5, SFL . . . . .  | 189 |
| B.23 Graph of homogeneous model, experiment 5, PZL . . . . .  | 190 |
| B.24 Graph of homogeneous model, experiment 5, TL . . . . .   | 191 |
| B.25 Graph of homogeneous model, experiment 5, LECL . . . . . | 192 |
| B.26 Graph of homogeneous model, experiment 6, CL . . . . .   | 193 |
| B.27 Graph of homogeneous model, experiment 6, SFL . . . . .  | 194 |
| B.28 Graph of homogeneous model, experiment 6, PZL . . . . .  | 195 |
| B.29 Graph of homogeneous model, experiment 6, TL . . . . .   | 196 |
| B.30 Graph of homogeneous model, experiment 6, LECL . . . . . | 197 |
|   |     |
| C.1 Graph of FE model, experiment 1, CL . . . . .             | 208 |
| C.2 Graph of FE model, experiment 1, SFL . . . . .            | 209 |
| C.3 Graph of FE model, experiment 1, PZL . . . . .            | 210 |
| C.4 Graph of FE model, experiment 1, TL . . . . .             | 211 |
| C.5 Graph of FE model, experiment 2, CL . . . . .             | 212 |
| C.6 Graph of FE model, experiment 2, SFL . . . . .            | 213 |
| C.7 Graph of FE model, experiment 2, PZL . . . . .            | 214 |
| C.8 Graph of FE model, experiment 2, TL . . . . .             | 215 |
| C.9 Graph of FE model, experiment 3, CL . . . . .             | 216 |
| C.10 Graph of FE model, experiment 3, SFL . . . . .           | 217 |
| C.11 Graph of FE model, experiment 3, PZL . . . . .           | 218 |
| C.12 Graph of FE model, experiment 3, TL . . . . .            | 219 |
| C.13 Graph of FE model, experiment 4, CL . . . . .            | 220 |



|   |     |
|---|-----|
| C.14 Graph of FE model, experiment 4, SFL . . . . . | 221 |
| C.15 Graph of FE model, experiment 4, PZL . . . . . | 222 |
| C.16 Graph of FE model, experiment 4, TL . . . . .  | 223 |
| C.17 Graph of FE model, experiment 5, CL . . . . .  | 224 |
| C.18 Graph of FE model, experiment 5, SFL . . . . . | 225 |
| C.19 Graph of FE model, experiment 5, PZL . . . . . | 226 |
| C.20 Graph of FE model, experiment 5, TL . . . . .  | 227 |
| C.21 Graph of FE model, experiment 6, CL . . . . .  | 228 |
| C.22 Graph of FE model, experiment 6, SFL . . . . . | 229 |
| C.23 Graph of FE model, experiment 6, PZL . . . . . | 230 |
| C.24 Graph of FE model, experiment 6, TL . . . . .  | 231 |

# List of Tables

|     |   |     |
|-----|---|-----|
| 6.1 | Comparison MP's, homogeneous model, CL . . . . .  | 82  |
| 6.2 | Comparison MP's, homogeneous model, SFL . . . . .   | 82  |
| 6.3 | Comparison MP's, homogeneous model, PZL . . . . .   | 83  |
| 6.4 | Comparison MP's, homogeneous model, TL . . . . .  | 83  |
| 6.5 | Comparison MP's, homogeneous model, LECL . . . . .  | 84  |
| 6.6 | Comparison of all material laws . . . . .   | 84  |
| 7.1 | Comparison MP's, FE model, CL . . . . .   | 93  |
| 7.2 | Comparison MP's, FE model, SFL . . . . .  | 93  |
| 7.3 | Comparison MP's, FE model, PZL . . . . .  | 94  |
| 7.4 | Comparison MP's, FE model, TL . . . . .   | 94  |
| 8.1 | Residuals First Step, CL . . . . .  | 106 |
| 8.2 | Residuals Second Step, CL . . . . .   | 108 |
| 8.3 | Residuals Last Step, CL . . . . .   | 109 |
| 8.4 | Residuals All Steps, CL . . . . .   | 114 |
| 8.5 | Residuals All Steps, SFL . . . . .  | 114 |
| 8.6 | Residuals All Steps, PZL . . . . .  | 115 |
| 8.7 | Residuals All Steps, TL . . . . .   | 115 |
| A.1 | A non-exhaustive summary of consistent, inconsistent and po-<br>tentially ambiguous formulæ . . . . . | 157 |

|     |                                     |     |
|-----|-------------------------------------|-----|
| C.1 | Convergence analysis, CL . . . . .  | 203 |
| C.2 | Convergence analysis, SFL . . . . . | 204 |
| C.3 | Convergence analysis, PZL . . . . . | 205 |
| C.4 | Convergence analysis, TL . . . . .  | 206 |

## Dedication

O, never say that I was false of heart,  
Though absence seem'd my flame to qualify.

As easy might I from myself depart  
As from my soul, which in thy breast doth lie:

That is my home of love: if I have ranged,  
Like him that travels I return again,  
Just to the time, not with the time exchanged,

So that myself bring water for my stain.

Never believe, though in my nature reign'd

All frailties that besiege all kinds of blood,

That it could so preposterously be stain'd,

To leave for nothing all thy sum of good;

For nothing this wide universe I call,

Save thou, my rose; in it thou art my all.

**William Shakespeare:** Sonnet 109



# Chapter 1

## Introduction

Although it is well understood that taking preventative measures to maintain a healthy lifestyle are amongst the major means to decrease the risk of heart failure, a better understanding of the heart's mechanical and electrical properties is crucial in supporting treatment of occurring cardiovascular diseases.

At a simplified level the heart can be described as a source of blood flow or pressure and its mechanical behaviour can be understood in terms of the time-varying relationship between ventricular blood pressure and cavity volume. For many years this relationship has been used by clinicians as a measure of cardiac function [115, 59]. More recently, it has become apparent that an understanding of the regional variation of myocardial material properties is important to understand the fundamental mechanisms underlying ventricular mechanics. Moreover, in order to estimate the energy consumption of various portions of the myocardium, the distribution of mechanical stress throughout the cardiac muscle is important [101, 57]. More recent evidence has shown that changes in wall stress due to altered haemodynamic load contribute to the remodelling of myocardial tissue with respect to its

cellular and connective tissue composition [34]. In addition, it may also influence tissue changes due to ischaemia and hypertrophy [77].

Myocardial stress can be distinguished into active and passive stress. Active stress is developed through calcium activated contraction of the muscle filaments and passive stress arises from the collagenous network that maintains the structural integrity of the muscle.

Among the first calculations of myocardial stress were formulated by Woods [122] based on a simple thin walled sphere with uniform internal pressure. A similar idea was employed by Sandler and Dodge [98] to model the left ventricle using an axisymmetric ellipsoid.

The last decades have shown tremendous improvement in the description of myocardial stress via the use of computational techniques such as the Finite Element Method (FEM) and improved experimental observations. For example, Guccione et al. [39] modelled the equatorial region of the canine left ventricle as a thick-walled cylinder consisting of an incompressible Fung-type hyperelastic material with homogeneous properties. The tissue was assumed to be locally transversely isotropic with respect to the fiber axis. Nielsen et al. [88] developed a anatomically realistic tri-cubic Hermite finite element model that captured the detailed transmural fibre distribution.

Based on histological studies from LeGrice and coworkers [66] and experimental investigation from Dokos and coworkers [30] it is now accepted that the most suitable way of describing the myocardial material symmetry is via an orthotropic constitutive relation. Menzel and Steinmann [80] have recently compared two strategies to formulate orthotropic hyperelasticity, i.e. the classical approach based on the incorporation of an enriched sets of invariants in the free energy function and on fictitious isotropic configurations via an appropriate tangent map. This study, however, was mainly of theoret-

ical character and did not apply the findings to available experimental data for the myocardium. It therefore remains to compare existing orthotropic constitutive relations and determine their suitability to model myocardial mechanics.

## 1.1 Objective

*The aim of this research was to determine the most suitable constitutive relation for describing passive mechanical behaviour of the myocardium.*

## 1.2 Thesis Summary

**Chapter 1** provides a motivation for the study of myocardial constitutive relations and outlines the objective of this study.

**Chapter 2** provides background on the myocardial anatomy on several scales.

It introduces the gross structure, the laminar arrangement of the muscle, the micro-structural constituents and their respective arrangement.

Furthermore it describes simple shear experiments, upon which the major part of this study is based, as well as uniaxial extension experiments, which served to further the investigations.

**Chapter 3** introduces the necessary background of continuum mechanics.

In particular, it derives the kinematic relationships, the balance equations and the constitutive theory.

**Chapter 4** presents a short overview of the finite element method, a brief introduction to standard optimisation techniques as well as some fundamental statistical measures. Furthermore it introduces a newly devel-



oped optimisation technique for inverse material parameter estimation based on Gaussian quadrature.

**Chapter 5** provides a background of literature of myocardial constitutive relations and the details of those investigated in this study.

**Chapter 6** introduces a homogeneous simple shear deformation model and the results of the estimation process.

**Chapter 7** introduces a finite element simple shear deformation model and the results of the estimation process.

**Chapter 8** introduces a finite element simple shear deformation model as well as uniaxial extension and the results of the estimation process.

**Chapter 9** gives a summary and presents the conclusion of the study.

**Chapter 10** shows initial results for investigating the connection between the macro-structural material parameters and the micro-structural constituents and its topology.

### 1.3 Publications Resulting from this Thesis

Some of the work described in this thesis was published in the following papers and can be found in the related chapters.:

**Chapter 6:** H. Schmid, M.P. Nash, A.A. Young and P.J. Hunter, Myocardial Material Parameter Estimation – A comparative Study for Simple Shear, *Journal of Biomechanical Engineering*, 2006, accepted.

**Chapter 6:** H. Schmid, M.P. Nash, A.A. Young, O. Röhrle and P.J. Hunter, A computationally efficient optimization kernel for material parameter

estimation procedures, *Journal of Biomechanical Engineering*, 2006, at review.

**Chapter 7** H. Schmid, M.P. Nash and A.A. Young and P.J. Hunter, Myocardial Material Parameter Estimation from Simple Shear Tests — A Non-homogeneous Finite Element Study, *Journal of Biomechanical Engineering*, 2006, at review.

**Chapter 10** H. Schmid, M.P. Nash, C. Walker, G.B. Sands, A. Pope, I.J. LeGrice, A.A. Young, P. Nielsen and P.J. Hunter, A framework for multi-scale modeling of the heart, *IFMBE Proceedings, Prague: IFMBE, ISSN 1727-1983. Eds: Jiri Hozman, Peter Kneppo (Proceedings of the 3rd European Medical & Biological Engineering Conference - EMBEC 05. Prague, Czech Republic, 20-25.11.2005), Id. 2535, 11, 2005, 4201–4205.*



# Part I

## Background



# Synopsis

This part presents the required background for the models built in this research.

Chapter 2 presents the anatomy of the heart as well as the experimental protocol of simple shear and uniaxial tests. Chapter 3 introduces the basics of continuum mechanics and Chapter 4 gives a summary of the required numerical tools.



# Chapter 2

## The Heart

The human heart can be considered a pump, which sustains the whole body with required nutrients through a network of blood vessels of varying size. The heart consists of four chambers, the left ventricle (LV), the right ventricle (RV), the left atria (LA) and the right atria (RA). For a detailed description of the individual functionality of these chambers please refer to [61]. The left ventricle plays a key role, as it has the largest volume of all four chambers and is responsible for distributing blood throughout the body.

Myocardial tissue consists of discrete layers of muscle cells whose three-dimensional structure is arranged in a complex hierarchy of extracellular connective tissue, largely collagen. For modelling purposes the myocardium is usually modelled as an orthotropic material (having three mutually orthogonal directions of distinct material response). This assumption is based on microstructural observations at each point within the myocardium [66].

Mathematical models of total heart function have ranged from axisymmetric shapes with isotropic, homogeneous myocardium [121] to accurate geometries [88] with detailed descriptions of the fibrous micro-structure of myocardium.



This chapter presents the macro-structure (2.1) and micro-structure (2.2) of the myocardium in more detail as required for this study.

## 2.1 Gross Structure

The primary function of the heart is to pump blood throughout the body, delivering nutrients and removing waste from each organ. The thinner-walled atria act as large-volume low-pressure blood reservoirs for the ventricles, which are responsible for the predominant pumping function. Two atrioventricular valves connect each atria to its respective ventricle. The remaining two semilunar valves join the outflow tracts of each ventricle with the great arteries into which the ventricles eject blood.

### 2.1.1 Ventricles

The LV is a thick-walled muscular chamber that pumps blood at physiologically high pressures (up to approximately 15 kPa or 120 mmHg during the normal heart cycle) to distal locations throughout the body. The cavity of the LV resembles a truncated ellipsoid in which both the inflow and outflow tracts are adjacent. In contrast, the RV pumps blood at comparatively low pressures (about one seventh the pressure of the LV) and wraps around the LV in a crescent-like fashion, so that its cavity forms a shallow U-shape. The ventricles are separated by the interventricular septum, which normally functions as part of the LV, and moves toward the LV free wall during systole. See picture 2.1 for an illustration.

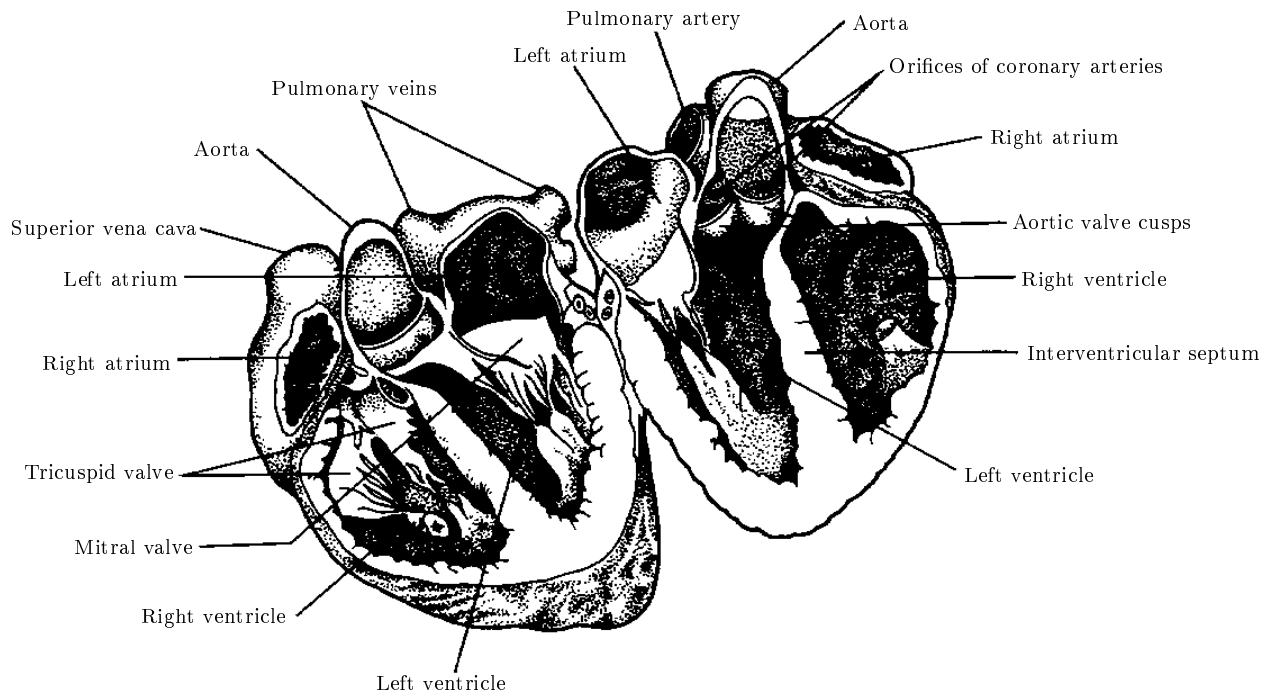


Figure 2.1: Longitudinal cross-section of the heart, from [61].

### 2.1.2 Connective Tissue Network

The endocardial surfaces of the atria and ventricles are covered with connective tissue which also extends over the valves. In addition, ventricular endocardial surfaces include a complex network of cardiac cells that are arranged in discrete bundles called trabeculae. The trabeculae are arranged in such a manner as to form small invaginations which are filled by blood from the cavities during systole. The systolic phase closes these invaginations, forcing the blood back into the main cavity. The pericardium is a fibrous sac that encompasses the entire heart to resist rapid increases in cardiac size. The inner wall of this sac is called parietal pericardium and is continuous with the epicardium or visceral pericardium (the layer of connective tissue

on the outer surface) at the base of the heart, where the great vessels enter and leave. A small amount of fluid within the pericardial sac provides lubrication for the continuous movement of the heart.

## 2.2 Microstructural architecture of the heart

Cardiac muscle cells or myocytes are typically brick-shaped with lengths that range from 80 to  $100\mu m$  and diameters ranging from 10 to  $20\mu m$ . The fundamental contractile unit within each myocyte is the sarcomere, which is about  $2\mu m$  long at rest. The sarcomere spans between adjacent Z-lines along the longitudinal axis of the cell, and contains the contractile apparatus. The contractile apparatus consist of myofibrils that consists of 40–50 sarcomeres in series, with the cells branching and interconnecting end-to-end through intercalated discs junctions. The branching angle is usually acute, so that adjacent cells run almost parallel with one another. In this way the contractile apparatus between cells is aligned for efficient mechanical function. Intercalated discs contain gap junctions, which provide electrical continuity between cells. Consequently, the electrical impulses propagate more rapidly along rather than across the axis of the constituent fibres.

Studies of myocardial architecture date back to the turn of last century when MacCallum [70] and Mall [72] viewed the heart as an assembly of discrete fibre bundles originating at the base of the ventricles and spiraling towards the ventricular apices. More recent studies [114, 4] found a smooth transmural variation of fibre orientation, which led to the predominant view that myocardium is a single muscle mass that is more appropriately describes as a continuum than as discrete muscle bundles. These studies, however, were restricted to measurements at not more than eight sites on a single heart.

It was not until Nielsen et al. [87] and McLean and Prothero [78] that a systematic approach was adopted to characterise the muscle fibre orientation in all regions of the ventricular myocardium.

To date, the most thorough study of cardiac muscle fibre orientation is that of LeGrice [65], who progressively removed fine layers of myocardium from a mounted intact preparation. Muscle fibre orientation was measured together with the absolute coordinates at a large number of sites over successive myocardial surfaces (see [88] for further details). Using this procedure, spatial registration is implicitly preserved and local muscle fibre orientation may be determined with reference to the surrounding myocardium. Measurements from this study confirm the selective findings reported by Streeter et al. [114].

Streeter [113] was one of the researchers who found extensive extracellular gaps within the myocardium, particularly in the midwall. These gaps are called cleavage planes. He also acknowledged that there was substantial discontinuity in the muscular architecture of the ventricles at both the microscopic and macroscopic level. These findings were essentially qualitative until recent anatomical studies of LeGrice and coworkers [66], who report that the ventricular myocardium should not be viewed as a uniformly continuous structure. Their detailed studies reveal that cardiac tissue is a composite of discrete layers of myocardial muscle fibres tightly bound by endomysial collagen, as illustrated in Figure 2.2. These myocardial *laminae* are loosely coupled by perimysial collagen and have the ability to slide over each other with relative ease. Laminae are on average four to six cells thick and continuously branch in each direction throughout the ventricular walls. As for the muscle fibre study of LeGrice [65], sheet orientation was accurately quantified with respect to ventricular geometry, so that the three-dimensional

orthotropic structure of the ventricles could be completely characterised.

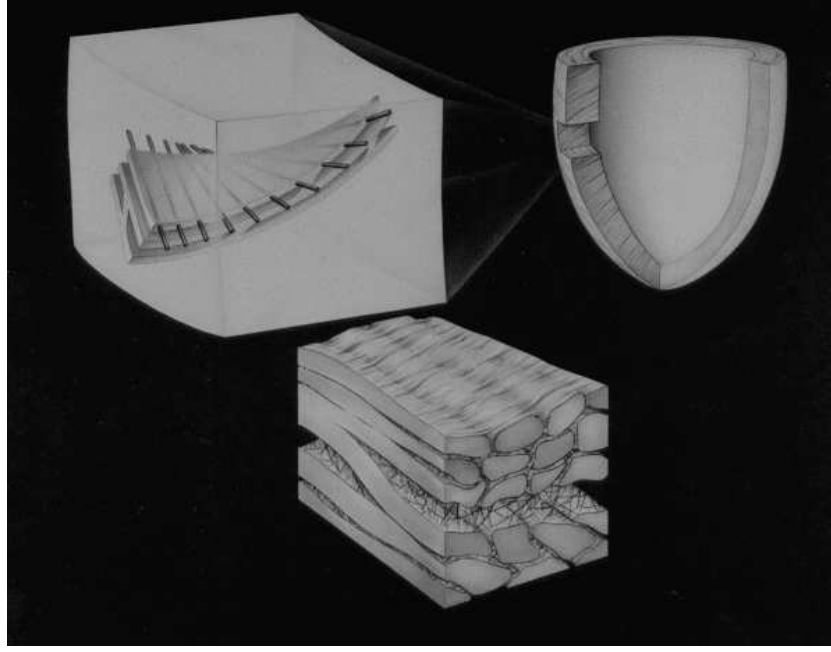


Figure 2.2: Schematic of cardiac micro-structure showing fibre orientation and branching sheet structures, from [66].

For modelling purposes, it is convenient to define a natural set of material directions to characterise the structure of myocardial tissue at an arbitrary point in the heart wall. The first of these directions is referred to as the *fibre axis* and it coincides with the muscle fibre orientation at each point. The *sheet axis* is defined to lie in the plane of the muscle layer and is perpendicular to the fibre direction. The third axis is defined to be orthogonal to the first two and is referred to as the *normal axis* as it is perpendicular to the muscle layer, see Fig.(2.3). This set of micro-structural axes is utilised throughout this study in the formulation of orthotropic material laws. This is described in detail in Chapter 5.

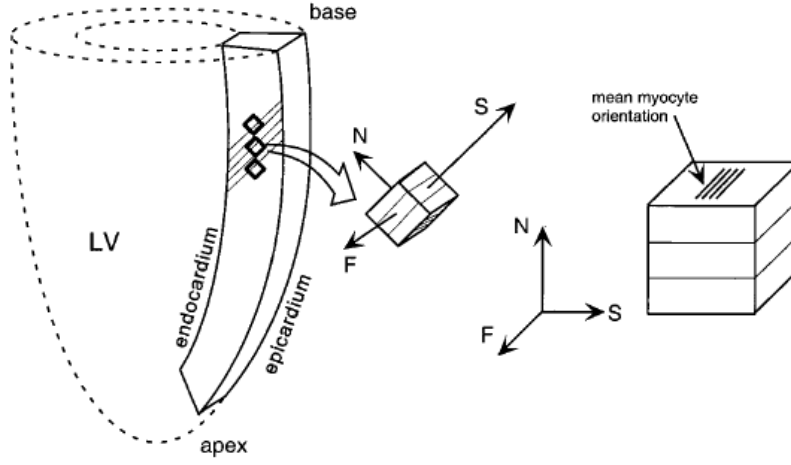


Figure 2.3: Schematic illustrating the three micro-structural axes, from [30].

## 2.3 Tissue Experiments

Knowledge of the myocardial morphology can be very useful in determining the gross features of the mechanical behaviour, i.e. elasticity, viscoelasticity, homogeneity, heterogeneity, isotropy, anisotropy. As discussed in the previous section it is clear that the myocardial microstructure suggests an orthotropic material response differing in varying location of the heart wall, therefore being heterogeneous. To determine whether the response is elastic or viscoelastic, experiments which enable characterisation of these features need to be performed, for further details see also [47, 47].

### 2.3.1 Pressure–Volume Measurements

Quantifying the global mechanical behaviour of whole ventricles, atria, or hearts via simultaneous measurements of cavity pressure and volume has been an extremely useful tool in cardiac physiology and mechanics for many years.

Although appropriate for determining global behaviour and certain features of the characteristic tissue behaviour, pressure–volume studies are not as useful in studying local phenomena such as regional behaviour or a constitutive relation (which are local relations between field quantities). Moriarty [82] and Vogel [119] give further insight into this.

However, recently the determination of transmural strain distribution of *in vivo* behaviour has become available, through the use of Magnetic Resonance Imaging in connection with finite element models. This opens a new field of characterising myocardial material properties [9, 83, 8].

### 2.3.2 Uniaxial Tests

By far the most commonly performed experiment on isolated, excised cardiac tissue is the uniaxial test. More recently tests have been performed on papillary muscles and trabeculae carnae rather than uniaxial strips of myocardium [62]. Uniaxial data have been extremely useful in determining general characteristics of the tissue behaviour, including both the nonlinear quasistatic material behaviour of quiescent muscle and the Frank–Starling behaviour of contracting muscle. The review article by Mirsky [81] can be consulted for details in uniaxial data. Uniaxial tests, however, are insufficient to determine a more complete three–dimensional constitutive relation.

### 2.3.3 Biaxial Tests

Biaxial tests of excised slabs of myocardium can be more useful in identifying three–dimensional mechanical characteristics. Demer and Yin [29] were the first to do so. Also Humprey and coworkers [48] and Smaill and Hunter [107] have reported on data collected from biaxial tests under various protocols.

In particular, the fact that stress–extension relations for uniaxial loading closely resemble those obtained under equibiaxial load indicates that there was little mechanical coupling between the fibre and cross–fibre directions in midmyocardial specimen [107].

### 2.3.4 Triaxial Tests

Biaxial tests are useful in studying the anisotropic material response of myocardium. There are, however, some inherent disadvantages. For example the samples usually need to be very thin to be a membrane for the attachment points. Therefore biaxial tests that quantify the material response in the normal direction continue to elude investigators, since the collagen struts between cleavage planes are easily destroyed in *in vitro* conditions.

Therefore triaxial tests of myocardium without the limitation of a specific thickness would be beneficial in determining the full three–dimensional material response. Furthermore, various studies have proven the importance of shear deformation in myocardial mechanics [5, 67] since certain shear modes provide a mechanism to explain endocardial wall thickening.

Dokos et al. [30] combined these findings in a series of simple shear experiments, which will be described in some detail in the following section.

### 2.3.5 Multiaxial Simple Shear Experiments

The passive shear properties of six pig hearts were determined. Samples ( $\sim 3 \times 3 \times 3$  mm) were cut from adjacent regions of the lateral left ventricular midwall, with sides aligned with the principal material axes ( $f, n, s$ ; fiber, normal, sheet). This position in the midwall ensured a more consistent distribution of fibre and sheet angles. Cycles of sinusoidal shear (shear displacement range  $[-50\%, 50\%]$ ) were applied separately to each specimen



in two orthogonal directions. Three specimens from each heart were tested in two directions, giving all six possible shear modes. Data for the fitting were taken from cycles after strain softening had diminished. The six possible shear modes are presented in Fig.(2.4). Maximum displacement was

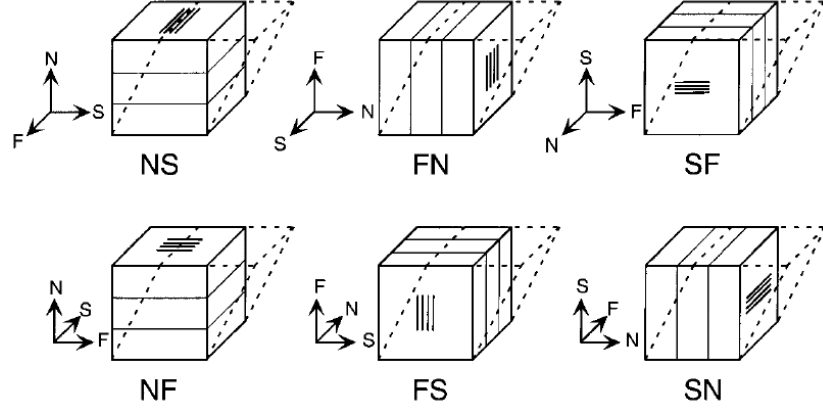


Figure 2.4: A sketch of all six possible shear modes for myocardium. The first letter indicates the normal vector of the face that is shifted, and the second letter indicates the direction in which it is shifted. Narrow lines represent fibres in a sheet. Picture from Dokos et al. [30]

prescribed to be half of the height of the cube, therefore all strain tensors have the same magnitudes. The forces on the top face of the cube were measured and taken as the data for the material parameter optimization. This is described in further detail in Sec.(6).

A typical force displacement curve is presented in Fig.(2.5). Note the typical S- and U-shaped curves.

### 2.3.6 Simple Shear & Uniaxial Extension

The rig used in the study by Dokos and coworkers [30] was only capable of applying simple shear deformations. Since this was thought to be potentially

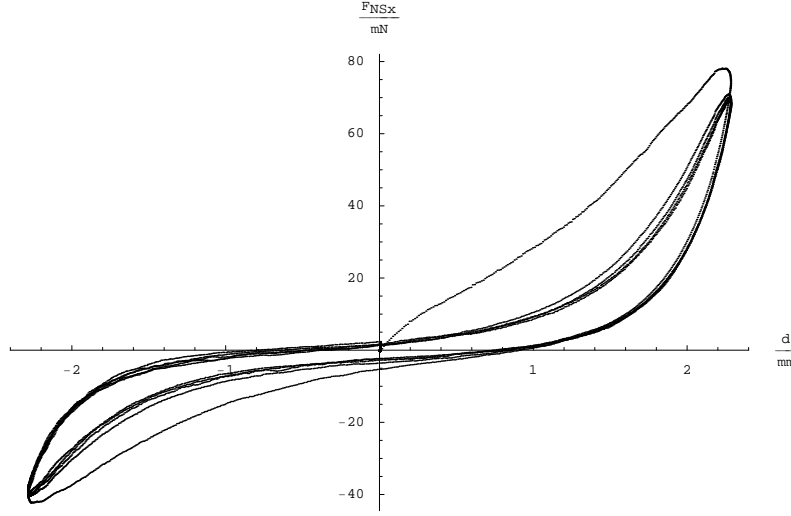


Figure 2.5: The figure shows the force in the  $N$ -direction for the NS-mode throughout the complete experimental loading protocol.

restrictive for the material parameter estimation process, the rig was modified such that it was also possible to apply uniaxial extension.

Samples as in Sec.(2.3.5) underwent firstly simple shear deformation and subsequently uniaxial extension and compression protocols with an extension, compression ratio of 20% of the height of the cube. This ensured that the axial strain components had a comparable magnitude to the shear strains in the simple shear deformation.

A typical extension-compression curve is given in Fig.(2.6), while the simple shear deformation curves remained equivalent to those in Sec.(2.3.5). Note that myocardial tissue exhibits a markedly stiffer behaviour under compression than in extension.

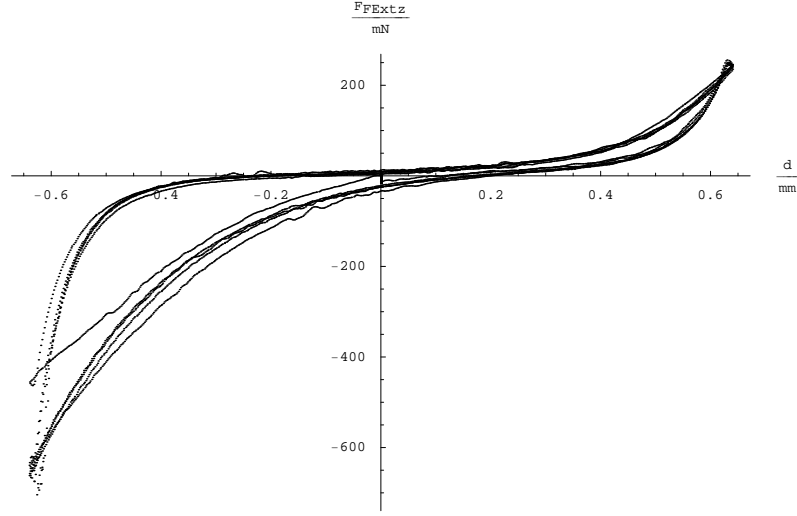


Figure 2.6: The figure shows the force in the  $F$ -direction for uniaxial extension and compression throughout the complete experimental loading protocol.

## 2.4 Summary

This chapter presented the background of the heart anatomy as well as an overview of experimental techniques that allow for a characterisation of the mechanical response of the myocardium. In particular, the simple shear experiments from Dokos et al. [30] were utilised to estimate material parameters for various constitutive equations as outlined in the following chapters. This allowed to determine the three-dimensional mechanical response of the orthotropic myocardium.

Furthermore the uniaxial extension served as additional data to determine the effects of different experimental protocols on the material parameter estimation process. This is presented in Chapter 8.

# Chapter 3

## Continuum Mechanics

This chapter presents a formal description of the mechanical behaviour of a continuous body. This outline is restricted to the case of elastic solids. For a thorough and general treatment, see [13, 44, 75]. First, the geometrical description of body is presented in Sec.(3.1), then in Sec.(3.2) the concept of force and stress as well as the balance concepts are introduced and finally Sec.(3.3) links these three together by introducing the notion of a hyperelastic material.

### 3.1 Kinematics

This section is concerned with describing the deformation or motion of a body from an initial setting, the so-called reference configuration, to a deformed configuration. The movement itself is due to external forces and it fulfills certain balance equation and is described in the subsequent sections.

### 3.1.1 Body & Motion

A body  $\mathcal{B}$  is a set of points  $\mathcal{X}$  with the property that each point  $\mathcal{X}$  can be uniquely identified with a vector in Euclidean 3-space  $\mathbb{R}^3$  for each time  $t$ .

$$\begin{aligned}\chi : \mathcal{B} &\longrightarrow \mathbb{R}^3 \\ \mathcal{X} &\mapsto \mathbf{x} = \chi(\mathcal{X})\end{aligned}\tag{3.1}$$

$\chi$  is called a configuration of  $\mathcal{B}$  if  $\chi^{-1}$  exists and if  $\chi$  and  $\chi^{-1}$  are twice continuously differentiable.

The motion of a body  $\mathcal{B}$  is a set of configurations parametrised by the time  $t$ .

$$\mathbf{x} = \chi_t(\mathcal{X}) \equiv \chi(\mathcal{X}, t)\tag{3.2}$$

describes the location of point  $\mathcal{X}$  at time  $t$ .

### 3.1.2 Configurations

Two special configurations are explicitly defined in this section due to their importance in the subsequent considerations.

The reference configuration of a body  $\mathcal{B}$  is defined as the motion at time  $t = 0$ , i.e.  $\mathcal{B}_0$ . There is no need to define the reference configuration in this manner, however, it is chosen due to its convenience and practicality. A point  $\mathcal{X}$  in  $\mathcal{B}_0$  is denoted as  $\mathbf{X} = \chi(\mathcal{X}, 0)$ .

The current configuration is defined as the motion of  $\mathcal{B}$  at time  $t$ , i.e.  $\mathcal{B}_t$ , and a point  $\mathcal{X}$  in  $\mathcal{B}_t$  is denoted as  $\mathbf{x} = \chi(\mathcal{X}, t)$ .

### 3.1.3 Representation of Functions

Let  $\alpha$  be a time-dependent field quantity on  $\mathcal{B}$ . Then  $\alpha$  can be expressed in three different ways.

- Material Description

The independent variables are  $\mathcal{X}, t$  and  $\alpha$  is expressed as follows:

$$\alpha = \alpha(\mathcal{X}, t) \quad (3.3)$$

- Reference or Lagrangian Description

The independent variables are  $\mathbf{X}, t$  and  $\alpha$  is expressed as follows:

$$\alpha = \alpha(\mathbf{X}, t) \quad (3.4)$$

- Spatial or Eulerian Description

The independent variables are  $\mathbf{x}, t$  and  $\alpha$  is expressed as follows:

$$\alpha = \alpha(\mathbf{x}, t) \quad (3.5)$$

According to Truesdell and Noll [118] there is a fourth description of motion, the so-called relative description.

The material description is usually not utilised since the quantities  $\mathcal{X}$  do not belong to  $\mathbb{R}^3$  but an abstract space of material particles. The Lagrangian description is used in the subsequent sections and a motion is therefore expressed with respect to  $\mathbf{X}$ :  $\mathbf{x} = \chi(\mathbf{X}, t)$ .

The Eulerian representation, on the other hand, is usually used in the context of fluid mechanics. It can, however, be also useful in solid mechanics, indeed this is the most common form in analytical solutions. Also, in finite element solutions, this approach can be very useful in biomechanics [71] because the stress free reference configuration is usually not available clinically.

### 3.1.4 Deformation Gradient Tensor

To characterise the deformation of a body  $\mathcal{B}$  time  $t$  is fixed and the reference and current configuration of  $\mathcal{B}$  are compared. Let  $\mathbf{X}, \mathbf{Y}$  and  $\mathbf{x}, \mathbf{y}$  be the vectors of the points  $\mathcal{X}, \mathcal{Y}$  in the reference and current configuration, respectively. Since  $\mathbf{x} = \boldsymbol{\chi}(\mathbf{X}, t)$  and  $\mathbf{y} = \boldsymbol{\chi}(\mathbf{Y}, t)$ , the difference between  $\mathbf{x}$  and  $\mathbf{y}$  can be written as:

$$\mathbf{y} - \mathbf{x} = \frac{\partial \boldsymbol{\chi}(\mathbf{X}, t)}{\partial \mathbf{X}}(\mathbf{Y} - \mathbf{X}) + \mathbf{r}(\mathbf{X}, \mathbf{Y} - \mathbf{X}) \quad (3.6)$$

where

$$\lim_{\|\mathbf{Y} - \mathbf{X}\| \rightarrow 0} \frac{\mathbf{r}(\mathbf{X}, \mathbf{Y} - \mathbf{X})}{\|\mathbf{Y} - \mathbf{X}\|} = \mathbf{0}. \quad (3.7)$$

Therefore the deformation gradient tensor

$$\mathbb{F} = \frac{\partial \boldsymbol{\chi}(\mathbf{X}, t)}{\partial \mathbf{X}} \quad (3.8)$$

represents a measure to describe the deformation within the vicinity of a body point  $\mathcal{X}$ . It has a few properties that demonstrate how  $\mathbb{F}$  characterises the deformation. These are described below.

#### 3.1.4.1 Transformation of Line Elements

Let  $\mathbf{C}(\lambda)$  be a material line in  $\mathcal{B}_0$  parametrised by  $\lambda \in I, I \subset \mathbb{R}$ . (A material line is a line which consists of the same particles throughout the deformation.) Due to the deformation process  $\mathbf{C}(\lambda)$  deforms into a line  $\mathbf{c}(\lambda)$  in the current configuration:

$$\mathbf{c}(\lambda) = \boldsymbol{\chi}(\mathbf{C}(\lambda), t). \quad (3.9)$$

Let  $\mathbf{X} = \mathbf{C}(\lambda_0), \lambda_0 \in I$  be the vector of a body point in the reference configuration, then  $\mathbf{x} = \mathbf{c}(\lambda_0)$  is the vector of the same body point in the current configuration. Let us now define material line elements with the help of the

tangent vectors on  $\mathbf{C}$  and  $\mathbf{c}$ , respectively:

$$\begin{aligned} d\mathbf{X} &:= \mathbf{C}'(\lambda_0)d\lambda; & \mathbf{C}'(\lambda_0) &= \left. \frac{\partial \mathbf{C}(\lambda)}{\partial \lambda} \right|_{\lambda=\lambda_0} \\ d\mathbf{x} &:= \mathbf{c}'(\lambda_0)d\lambda; & \mathbf{c}'(\lambda_0) &= \left. \frac{\partial \mathbf{c}(\lambda)}{\partial \lambda} \right|_{\lambda=\lambda_0}. \end{aligned} \quad (3.10)$$

Considering

$$\begin{aligned} d\mathbf{x} &= \left. \frac{\partial \mathbf{c}(\lambda)}{\partial \lambda} \right|_{\lambda=\lambda_0} d\lambda \\ &= \underbrace{\left. \frac{\partial \boldsymbol{\chi}(\mathbf{X}, t)}{\partial \mathbf{X}} \right|_{\mathbf{X}=\mathbf{C}(\lambda_0)}}_{=\mathbb{F}} \underbrace{\left[ \left. \frac{\partial \mathbf{C}(\lambda)}{\partial \lambda} \right]_{\lambda=\lambda_0} d\lambda}_{=d\mathbf{X}} \end{aligned} \quad (3.11)$$

$$\implies d\mathbf{x} = \mathbb{F}d\mathbf{X},$$

one can conclude that  $\mathbb{F}$  transforms material line elements of the reference configuration into material line elements in the current configuration. This holds for any arbitrary material line and therefore  $\mathbb{F}$  characterises deformation process, since e.g. a rigid body rotation would imply that  $d\mathbf{x}$  is only rotated with respect to  $d\mathbf{X}$ . In total  $\mathbb{F}$  describes the change in direction and magnitude of  $d\mathbf{X}$ . It is important to note here that  $\mathbb{F}$  is a so-called two point tensor, i.e.:  $\mathbf{F}$  projects tangent vectors at the point  $\mathbf{X}$  to tangent vectors at the point  $\mathbf{x}$ .

### 3.1.4.2 Transformation of normal vectors of material surfaces

Let

$$\Phi(\mathbf{X}) = c = \text{const} \quad (3.12)$$

a material surface in the reference configuration. (A material surface is a surface that consists of the same particles throughout the deformation.) With the help of  $\mathbf{X} = \boldsymbol{\chi}^{-1}(\mathbf{x}, t)$ ,  $\Phi$  can be transformed according to:

$$c = \Phi(\boldsymbol{\chi}^{-1}(\mathbf{x}, t)) =: \phi(\mathbf{x}, t). \quad (3.13)$$



$\phi(\mathbf{x}, t)$  describes the same material surface in the current configuration. When fixing  $t$  one can deduce the following:

$$\begin{aligned} dc &= \frac{\partial \Phi(\mathbf{X})}{\partial \mathbf{X}} \cdot d\mathbf{X} = \frac{\partial \phi(\mathbf{x}, t)}{\partial \mathbf{x}} \cdot d\mathbf{x} \\ &= \frac{\partial \Phi(\mathbf{X})}{\partial \mathbf{x}} \cdot \mathbb{F} d\mathbf{X} = \mathbb{F}^T \frac{\partial \phi(\mathbf{x}, t)}{\partial \mathbf{x}} \cdot d\mathbf{X} \end{aligned} \quad (3.14)$$

or

$$(\text{Grad} \Phi - \mathbb{F}^T \text{grad} \phi) \cdot d\mathbf{X} = 0. \quad (3.15)$$

This equation has to hold for all  $d\mathbf{X}$ , hence the expression within the brackets has to hold by itself,

$$\text{Grad} \Phi = \mathbb{F}^T \text{grad} \phi \iff \text{grad} \phi = \mathbb{F}^{-T} \text{Grad} \Phi. \quad (3.16)$$

The deformation gradient or more precisely the inverse transposed of the deformation gradient  $\mathbb{F}^{-T}$  therefore transforms normal vectors on material surfaces in the reference configuration to normal vectors at the same point in the current configuration. Since this property holds for every material surface,  $\mathbb{F}^{-T}$  can also be utilised as a measure for deformation. A rigid body rotation for example would not alter the magnitude of the normal vector.

### 3.1.4.3 Transformation of Area and Volume Elements

This section will derive the relations between area and volume elements of the reference and current configuration. Firstly, the relation between volume elements is derived from which the area element relation follows immediately.

Let  $d\mathbf{X}, d\mathbf{Y}, d\mathbf{Z}$  be non-coplanar material line elements at a point  $\mathbf{X}$  in the reference configuration with a positive orientation. This can be ensured by the following relation of the triple product:

$$dV := (d\mathbf{X} \times d\mathbf{Y}) \cdot d\mathbf{Z} > 0. \quad (3.17)$$

Then  $dV$  is called the volume element spanned by  $d\mathbf{X}, d\mathbf{Y}, d\mathbf{Z}$ . The three line elements transform into:

$$d\mathbf{x} = \mathbb{F}d\mathbf{X}, \quad d\mathbf{y} = \mathbb{F}d\mathbf{Y}, \quad d\mathbf{z} = \mathbb{F}d\mathbf{Z} \quad (3.18)$$

in the current configuration. There they span the volume element

$$\begin{aligned} dv &:= (d\mathbf{x} \times d\mathbf{y}) \cdot d\mathbf{z} > 0 \\ &= (\mathbb{F}d\mathbf{X} \times \mathbb{F}d\mathbf{Y}) \cdot \mathbb{F}d\mathbf{Z}. \end{aligned} \quad (3.19)$$

From a well-known relation in linear algebra, [112], this can be rewritten as:

$$dv = (\det \mathbb{F})(d\mathbf{X} \times d\mathbf{Y}) \cdot d\mathbf{Z} = (\det \mathbb{F})dV. \quad (3.20)$$

If one requires  $dv > 0$  to physical reasoning then  $\det \mathbb{F} > 0$ , which will always be assumed in the following.

Recalling that the cross-product between two vectors gives the normal of the spanned plane one can utilize Eq.(3.20) to derive the relation between area elements  $d\mathbf{a}$  and  $d\mathbf{A}$  in the current and reference configuration, respectively.

$$\begin{aligned} dv &= (d\mathbf{x} \times d\mathbf{y}) \cdot d\mathbf{z} = d\mathbf{a} \cdot \mathbb{F}d\mathbf{Z} = \mathbb{F}^T d\mathbf{a} \cdot d\mathbf{Z} \\ &= (\det \mathbb{F})(d\mathbf{X} \times d\mathbf{Y}) \cdot d\mathbf{Z} = (\det \mathbb{F})d\mathbf{A} \cdot d\mathbf{Z}. \end{aligned} \quad (3.21)$$

or

$$(\mathbb{F}^T d\mathbf{a} - (\det \mathbb{F})d\mathbf{A}) \cdot d\mathbf{Z} = 0. \quad (3.22)$$

Since this equation has to hold for all  $d\mathbf{X}$  with  $d\mathbf{A} \cdot d\mathbf{X} > 0$  we can conclude that:

$$d\mathbf{a} = (\det \mathbb{F})\mathbb{F}^{-T} d\mathbf{A}. \quad (3.23)$$

This relation is also called Nanson's formula.

Note that if a deformation is isochoric (incompressible) that  $dv = dV$  and therefore  $\det \mathbb{F} \equiv 1$ . Please refer to section 3.3.5 for further details and consequences of incompressibility.

#### 3.1.4.4 Polar Decomposition

Any second order tensor  $\mathbb{F}$  with  $\det \mathbb{F} > 0$  can be decomposed in the following way, see also [44, 75] for proofs of existence and uniqueness:

$$\mathbb{F} = \mathbb{R}\mathbb{U} = \mathbb{V}\mathbb{R} . \quad (3.24)$$

$\mathbb{R}$  is a proper orthogonal second order tensor and describes the rotational part between the reference and current configuration, whereas  $\mathbb{U}$  and  $\mathbb{V}$  are symmetric positive definite second order tensors and are called the right and left stretch tensor, respectively.  $\mathbb{U}$  “lives” in the reference configuration and describes the stretching part of the deformation, i.e. it takes material line elements of the reference configuration and stretches them within the reference configuration.  $\mathbb{R}$  then takes these stretched line elements and rotates them into the current configuration. Equivalent consideration hold for  $\mathbb{V}$  which lives in the current configuration. It is noteworthy that  $\mathbb{R}$  is a two point tensor.

### 3.1.5 Deformation Measures

The polar decomposition clarifies the structure of the deformation gradient tensor. Sensible deformation measures are therefore independent of the rotational tensor  $\mathbb{R}$ , but can be related to either  $\mathbb{U}$  or  $\mathbb{V}$  solely. The next two sections deal with these measures.

#### 3.1.5.1 Right & Left Cauchy–Green Deformation Tensor

Although these two measures are not explicitly utilized in our later studies, it is helpful to discuss these in a bit more detail. The right and left Cauchy–

Green tensors are defined as follows:

$$\begin{aligned}\mathbb{C} &:= \mathbb{F}^T \mathbb{F} = \mathbb{U}^2 && \text{right Cauchy-Green tensor} \\ \mathbb{B} &:= \mathbb{F} \mathbb{F}^T = \mathbb{V}^2 && \text{left Cauchy-Green tensor}.\end{aligned}\tag{3.25}$$

One can show that the eigenvalues of  $\mathbb{C}$  and  $\mathbb{B}$  have the same numerical value which is equivalent to the fact that the invariants have the same numerical values. Furthermore, if  $\mathbf{u}$  is an eigenvector of  $\mathbb{U}$ , then  $\mathbf{v} = \mathbb{R}\mathbf{u}$  is an eigenvector of  $\mathbb{B}$  with the same eigenvalue as  $\mathbf{u}$ . The three invariants are defined as follows:

$$\begin{aligned}I_1 &= \text{tr}(\mathbb{C}) = \text{tr}(\mathbb{B}) \\ I_2 &= \frac{1}{2}(\text{tr}(\mathbb{C})^2 - \text{tr}(\mathbb{C}^2)) = \frac{1}{2}(\text{tr}(\mathbb{B})^2 - \text{tr}(\mathbb{B}^2)) \\ I_3 &= \det(\mathbb{C}) = \det(\mathbb{B}).\end{aligned}\tag{3.26}$$

These three invariants form a so-called integrity basis. They are not unique, rather there exist infinitely many possible integrity bases. The ones presented, however, are the most commonly used ones.

### 3.1.5.2 Green & Almansi Strain Tensor

A common way to measure the strain between the current and the reference configuration is to investigate the following difference  $\Delta$  from which the Green strain tensor is derived:

$$\begin{aligned}\Delta &:= \frac{1}{2}(\|d\mathbf{x}\|^2 - \|d\mathbf{X}\|^2) \\ &= \frac{1}{2}(d\mathbf{x} \cdot d\mathbf{x} - d\mathbf{X} \cdot d\mathbf{X}).\end{aligned}\tag{3.27}$$

With the help of  $d\mathbf{x} = \mathbb{F}d\mathbf{X}$  that gives:

$$\begin{aligned}\Delta &= \frac{1}{2}(\mathbb{F}d\mathbf{X} \cdot \mathbb{F}d\mathbf{X} - d\mathbf{X} \cdot d\mathbf{X}) \\ &= \frac{1}{2}(d\mathbf{X} \cdot \mathbb{F}^T \mathbb{F} d\mathbf{X} - d\mathbf{X} \cdot d\mathbf{X}) \\ &= d\mathbf{X} \cdot \left\{ \frac{1}{2}(\mathbb{F}^T \mathbb{F} - \mathbb{I}) \right\} d\mathbf{X}.\end{aligned}\tag{3.28}$$

The tensor

$$\mathbb{E} = \frac{1}{2}(\mathbb{F}^T \mathbb{F} - \mathbb{I}) = \frac{1}{2}(\mathbb{C} - \mathbb{I})\tag{3.29}$$

is called the Green strain tensor. One can see from Eq.(3.28) that it is a tensor field in the reference configuration. This is sometimes denoted as a Lagrangian tensor field.

One could also utilize the relation  $d\mathbf{X} = \mathbb{F}^{-1}d\mathbf{x}$  in Eq.(3.27) which leads to the following expression:

$$\begin{aligned}\Delta &= \frac{1}{2}(d\mathbf{x} \cdot d\mathbf{x} - \mathbb{F}^{-1}d\mathbf{x} \cdot \mathbb{F}^{-1}d\mathbf{x}) \\ &= \frac{1}{2}(d\mathbf{x} \cdot d\mathbf{x} - d\mathbf{x} \cdot \mathbb{F}^{-\text{T}}\mathbb{F}^{-1}d\mathbf{x}) \\ &= d\mathbf{x} \cdot \left\{ \frac{1}{2}(\mathbb{I} - \mathbb{F}^{-\text{T}}\mathbb{F}^{-1}) \right\} d\mathbf{x}.\end{aligned}\tag{3.30}$$

The tensor

$$\mathbb{A} = \frac{1}{2}(\mathbb{I} - \mathbb{F}^{-\text{T}}\mathbb{F}^{-1}) = \frac{1}{2}(\mathbb{I} - \mathbb{B}^{-1})\tag{3.31}$$

is called the Almansi strain tensor and from Eq.(3.30) it follows that  $\mathbb{A}$  is a tensor field in the current configuration or as sometimes called in the Eulerian setting.

$\mathbb{A}$  and  $\mathbb{E}$  obey the following transformation rule:

$$\mathbb{E} = \mathbb{F}^{\text{T}}\mathbb{A}\mathbb{F}.\tag{3.32}$$

One can also utilise normal vectors on material surfaces rather than material line elements to define strain measures. This results in the so-called Piola strain tensor and the Finger strain tensor.

## 3.2 Stress & Balance Equations

During the movement of a material body  $\mathcal{B}$  the interaction between its various parts and between  $\mathcal{B}$  and its environment is described by means of forces.

### 3.2.1 Forces

There exist three different kinds of forces:

- Contact Forces  $\mathbf{t}$  between various parts of  $\mathcal{B}$
- Contact Forces  $\mathbf{t}$  on the surface of the body  $\partial\mathcal{B}$
- Volume Forces  $\mathbf{b}$  in the interior of  $\mathcal{B}$ , generated by its environment

### 3.2.2 Cauchy's Hypothesis

In the context of contact forces the Cauchy hypothesis is assumed, i.e. there exists a surface–force–density relationship which is called the stress vector  $\mathbf{t}$  and it is defined as follows:

$$\mathbf{t}(\mathbf{n}, \mathbf{x}, t) = \lim_{\Delta a \rightarrow 0} \frac{\Delta \mathbf{F}}{\Delta a}. \quad (3.33)$$

Here  $\mathbf{n}$  defines the normal vector on the infinitesimal surface  $\Delta a$ ,  $\Delta \mathbf{F}$  is the bulk force on  $\Delta a$ ,  $\mathbf{x}$  is the point within  $\mathcal{B}$ , and  $t$  is the time at which the stress vector is evaluated. An equivalent assumption holds for the volume forces  $\mathbf{b} = \mathbf{b}(\mathbf{x}, t)$ . The pair  $(\mathbf{t}, \mathbf{b})$  is called the force system acting on a body  $\mathcal{B}$  or on a part of  $\mathcal{B}$ , i.e.  $\Delta\mathcal{B}$ . The resulting force  $\mathbf{K}(\Delta\mathcal{B}, t)$  on a part  $\Delta\mathcal{B}$  at time  $t$  is then calculated by:

$$\mathbf{K}(\Delta\mathcal{B}, t) := \int_{\partial\Delta\mathcal{B}} \mathbf{t} \, da + \int_{\Delta\mathcal{B}} \mathbf{b} \, dv. \quad (3.34)$$

The resulting angular momentum  $\mathbf{M}_{\mathbf{x}_0}$  with respect to a point  $\mathbf{x}_0$  can be calculated by:

$$\mathbf{M}_{\mathbf{x}_0}(\Delta\mathcal{B}, t) := \int_{\partial\Delta\mathcal{B}} (\mathbf{x} - \mathbf{x}_0) \times \mathbf{t} \, da + \int_{\Delta\mathcal{B}} (\mathbf{x} - \mathbf{x}_0) \times \mathbf{b} \, dv. \quad (3.35)$$

These two quantities now serve as a basis to derive the balance of linear and angular momentum.

### 3.2.3 Balance of Linear & Angular Momentum

Let  $\mathbf{x} = \boldsymbol{\chi}(\mathbf{X}, t)$  be a motion of  $\mathcal{B}$  and  $\mathbf{x}_0$  the vector to an arbitrary fixed point in space. Then

$$\mathbf{I} = \mathbf{I}(\Delta\mathcal{B}, t) := \int_{\Delta\mathcal{B}} \dot{\mathbf{x}} \, dm = \int_{\Delta\mathcal{B}_0} \varrho_0 \dot{\mathbf{x}} \, dV = \int_{\Delta\mathcal{B}_t} \varrho \dot{\mathbf{x}} \, dv \quad (3.36)$$

is called the linear momentum of  $\Delta\mathcal{B}$  in the motion  $\mathbf{x} = \boldsymbol{\chi}(\mathbf{X}, t)$  and

$$\begin{aligned} \mathbf{D}_{\mathbf{x}_0} = \mathbf{D}_{\mathbf{x}_0}(\Delta\mathcal{B}, t) &:= \int_{\Delta\mathcal{B}} (\mathbf{x} - \mathbf{x}_0) \times \dot{\mathbf{x}} \, dm \\ &= \int_{\Delta\mathcal{B}_0} \varrho_0 (\mathbf{x} - \mathbf{x}_0) \times \dot{\mathbf{x}} \, dV \\ &= \int_{\Delta\mathcal{B}_t} \varrho (\mathbf{x} - \mathbf{x}_0) \times \dot{\mathbf{x}} \, dv \end{aligned} \quad (3.37)$$

is called the angular momentum of  $\Delta\mathcal{B}$  with respect to  $\mathbf{x}_0$  in the motion  $\mathbf{x} = \boldsymbol{\chi}(\mathbf{X}, t)$ .  $\rho$  is the mass density and  $dm$  is a mass increment. The actual balance principles are axioms or assumptions and are the equivalent of Newton's second law of motion.

#### 3.2.3.1 Global Form

There exists a reference system, such that the following equations hold relative to it:

$$\begin{aligned} \frac{d}{dt} \mathbf{I}(\Delta\mathcal{B}, t) &= \mathbf{K}(\Delta\mathcal{B}, t) && \text{BLM: balance of linear momentum} \\ \frac{d}{dt} \mathbf{D}_{\mathbf{x}_0}(\Delta\mathcal{B}, t) &= \mathbf{M}_{\mathbf{x}_0}(\Delta\mathcal{B}, t) && \text{BAM: balance of angular momentum.} \end{aligned} \quad (3.38)$$

The balance of linear and angular momentum can be rewritten in the following comprehensive form with respect to the current configuration:

$$\int_{\partial\Delta\mathcal{B}_t} \mathbf{t} \, da + \int_{\Delta\mathcal{B}_t} (\mathbf{b} - \varrho \ddot{\mathbf{x}}) \, dv = \mathbf{0}, \quad (3.39)$$

and

$$\int_{\partial\Delta\mathcal{B}_t} (\mathbf{x} - \mathbf{x}_0) \times \mathbf{t} \, da + \int_{\Delta\mathcal{B}_t} (\mathbf{x} - \mathbf{x}_0) \times (\mathbf{b} - \varrho \ddot{\mathbf{x}}) \, dv = \mathbf{0}. \quad (3.40)$$

### 3.2.4 Cauchy Stress Tensor

The BLM and BAM have two major consequences. Firstly the BLM guarantees that for each point  $\mathbf{x}$  within  $\mathcal{B}$  and each normal vector  $\mathbf{n}(\|\mathbf{n}\| = 1)$  there exists a second order tensor called the Cauchy stress tensor  $\mathbb{T}$  fulfilling the relation:

$$\mathbf{t}(\mathbf{n}, \mathbf{x}, t) = \mathbb{T}(\mathbf{x}, t)\mathbf{n}. \quad (3.41)$$

Secondly the BAM guarantees that the Cauchy stress tensor  $\mathbb{T}$  is symmetric:

$$\mathbb{T} = \mathbb{T}^T. \quad (3.42)$$

Eq.(3.42) represents the “local” form of the BAM. The local form is obtained by applying the divergence theorem for integrals and imposing that the integrand has to hold for arbitrary parts  $\Delta\mathcal{B}$ . The same can be applied to the BLM, which then reads like this:

$$\operatorname{div}\mathbb{T} + \mathbf{b} = \varrho \ddot{\mathbf{x}}. \quad (3.43)$$

The operator “div” is defined as the derivative with respect to the coordinates of the current configuration.

### 3.2.5 1<sup>st</sup> Piola–Kirchhoff Stress Tensor

By defining the first Piola–Kirchhoff stress tensor

$$\mathbb{P} := (\det\mathbb{F})\mathbb{T}\mathbb{F}^{-T}, \quad (3.44)$$

which is a two point tensor, and the body force in the reference configuration  $\mathbf{b}_0 = (\det\mathbb{F})\mathbf{b}$ , one can deduce the local form of the BLM in the reference



configuration:

$$\text{Div} \mathbb{P} + \mathbf{b}_0 = \varrho_0 \ddot{\mathbf{x}}. \quad (3.45)$$

The operator “Div” is defined as the derivative with respect to the coordinates of the reference configuration.

Note that  $\mathbb{P}$  is not a symmetrical tensor.  $\mathbb{P}$  acts on a normal vector of the reference configuration  $\mathbf{N}$  and yields the stress vector  $\mathbf{t}_0$ , which is defined as  $\mathbf{t}_0 = d\mathbf{F}/dA$ .  $dA$  is denoting the area in the reference configuration.  $\mathbf{t}_0$  only equals  $\mathbf{t} = d\mathbf{F}/da$  if the area element  $da$  in the current configuration is the same as  $dA$ . This relationship can be expressed as:

$$\mathbf{t}_0 = \mathbb{P}\mathbf{N}. \quad (3.46)$$

### 3.2.6 2<sup>nd</sup> Piola–Kirchhoff Stress Tensor

Since the first Piola–Kirchhoff stress tensor is not symmetric the second Piola–Kirchhoff stress tensor  $\mathbb{S}$  is introduced:

$$\mathbb{S} := (\det \mathbb{F}) \mathbb{F}^{-1} \mathbb{T} \mathbb{F}^{-T}. \quad (3.47)$$

$\mathbb{S}$  is symmetric and will find use in the formulation of constitutive laws in Sec.(3.3).

Each strain tensor introduced in Sec.(3.1) has its associated stress tensor. The stress tensors are associated to the strain tensors by means of the strain energy density  $W$  function which describes the work done by a certain strain and stress field. This is the topic of the next section.

## 3.3 Constitutive Theory

At this stage three equations of the BLM (3) we have been introduced whereas nine unknowns  $\mathbf{x}$  (3) and  $\mathbb{T}$  (6) remain to be properly constrained. There

are therefore 6 equations missing to have a fully defined system which can be solved. The missing equations are introduced in the subsequent sections in form of a relationship between  $\mathbb{E}$  and  $\mathbb{S}$ . The main objective is to formulate them in a way that they fulfill properties as observed in experiments. Furthermore they have to obey general physical principles.

### 3.3.1 Hyperelasticity

In a very general sense the functional relationship between  $\mathbb{E}$  and  $\mathbb{S}$  can be formulated as:  $\mathbb{S} = f(\mathbb{E})$ . This type of material would be called a Cauchy-elastic material. If one assumes that for an elastic material all deformation is recoverable, then one can postulate the existence of a so-called strain energy density function  $W = W(\mathbb{F})$  which depends on the deformation gradient tensor and serves as a potential. The relationship between the first Piola-Kirchhoff stress tensor and the deformation gradient is presented in various equivalent notations. It can be derived from the second law of thermodynamics [75].

$$\mathbb{P} = \frac{\partial W(\mathbb{F})}{\partial \mathbb{F}} = D_{\mathbb{F}} W(\mathbb{F}) = P_{mn}(F_{ij}) \mathbf{e}_m \otimes \mathbf{e}_n = \frac{\partial W}{\partial F_{mn}}(F_{ij}) \mathbf{e}_m \otimes \mathbf{e}_n. \quad (3.48)$$

### 3.3.2 Objectivity

The principle of material objectivity states that  $W$  must remain the same viewed from different observers which only differ by a rigid body rotation. Let  $(\mathbf{x}, t)$  be an event relative to an observer and let  $(\tilde{\mathbf{x}}, \tilde{t})$  be the same event from an observer with:

$$\tilde{\mathbf{x}} = \mathbb{Q}(t) + \mathbf{c}(t) \quad \text{and} \quad \tilde{t} = t - \hat{t}, \quad (3.49)$$

where  $\mathbb{Q}$  denoted any arbitrary proper orthogonal tensor,  $\mathbf{c}$  a displacement and  $\hat{t}$  a fixed time. Then the form of the material equations and therefore

also  $W$  must be invariant.

$$W(\mathbb{F}) = W(\tilde{\mathbb{F}}) \quad (3.50)$$

By keeping in mind that  $\tilde{\mathbb{F}} = \mathbb{Q}\mathbb{F}$  and starting with

$$\begin{aligned} W(\mathbb{F}) &= W(\tilde{\mathbb{F}}) = W(\mathbb{Q}\mathbb{F}) \\ &= W(\mathbb{Q}\mathbb{R}\mathbb{U}) \end{aligned} \quad (3.51)$$

we can conclude that

$$W(\mathbb{F}) = W(\mathbb{U}), \quad (3.52)$$

since Eq.(3.51) has to hold for an arbitrary  $\mathbb{Q}$  and therefore also for  $\mathbb{Q} = \mathbb{R}^T$ .  $W$  can now also equivalently expressed as being a function of either  $\mathbb{C}$  or  $\mathbb{E}$ , since these also do not depend on the rotational part of  $\mathbb{F}$ .

### 3.3.3 Stress–Strain Relationship

Eq.(3.48) gives the starting point for the derivation of relation between  $\mathbb{S}$  and  $\mathbb{E}$  which is utilised in this work. The reader is referred to Appendix(A) for the detailed derivation of the stress–strain relationship and the requirements imposed for formulating the strain energy density function with respect to the components of the Green strain tensor. Here we just state the relationship for  $\mathbb{S}$  and  $\mathbb{C}$ :

$$\mathbb{S}(\mathbb{C}) = \mathbb{F}^{-1}\mathbb{P}(\mathbb{C}) = 2 \, sym[\mathbb{D}_{\mathbb{C}}W(\mathbb{C})]. \quad (3.53)$$

or for  $\mathbb{S}$  and  $\mathbb{E}$ :

$$\mathbb{S}(\mathbb{E}) = sym[\mathbb{D}_{\mathbb{E}}W(\mathbb{E})]. \quad (3.54)$$

These equations form the correct definition of the stress–strain relationship in symbolic notation. It is, however, necessary to restate it in index notation since Eq.(3.54) will be extensively used in the next chapter. It then reads:

$$S_{ij} = \frac{\partial W}{\partial E_{ij}} \quad (3.55)$$

when complying to the condition

$$\begin{aligned} & W(E_{11}, E_{22}, E_{33}, E_{12}, E_{21}, E_{13}, E_{31}, E_{23}, E_{32}) \\ &= W(E_{11}, E_{22}, E_{33}, E_{21}, E_{12}, E_{31}, E_{13}, E_{32}, E_{23}) \end{aligned} \quad (3.56)$$

for the strain energy density function.

### 3.3.4 Isotropy & Anisotropy

If a body exhibits the same material response within each direction it is said to be isotropic. The strain energy density can therefore only depend on the three invariants of  $\mathbb{C}$ , see Eq.(3.26).

$$W(\mathbb{C}) = W(I_1, I_2, I_3) \quad (3.57)$$

#### 3.3.4.1 Neo-Hookean and Mooney–Rivlin

The simplest strain energy function that can be formulated using these invariants is the so-called Neo-Hookean strain energy function. A material obeying this strain energy function is called a Neo-Hookean material.

$$W(\mathbb{C}) = c_1 \cdot (I_1 - 3) \quad (3.58)$$

Although of high importance for theoretical considerations, this formulation does not prove useful in practical applications.

An extension of this formulation is the so-called Mooney–Rivlin material with the following strain energy density function:

$$W(\mathbb{C}) = c_1 \cdot (I_1 - 3) + c_2 \cdot (I_2 - 3). \quad (3.59)$$

Peng & Chang [94] give an excellent review of these and more general isotropic laws.

### 3.3.4.2 Considerations for myocardium

As pointed out in Secs.(2.2 & 2.3) the myocardium exhibits a clear orthotropic behaviour, both in terms of its microstructure and its macroscopic response. Orthotropy is defined as having three orthogonal directions in which the material exhibits a distinct behaviour. The strain energy density must then incorporate these three directions. Two general approaches are possible to describe this kind of anisotropy.

Firstly one can introduce so-called structural tensors which represent the preferred direction. Depending on the kind of anisotropy a certain number of these structural tensors must be introduced which then form a set of new invariants on which the strain energy density will depend.

The literature existing about the myocardium, however, uses material laws which are formulated with respect to the components of the Green strain tensor. A thorough treatment of the material investigated in this study are presented in the next chapter. Before this presentation, however, a special class of materials is considered and in particular the effect of this class on the stress-strain relationship.

### 3.3.5 Incompressibility

Since the myocardium predominantly consists of water, and since water almost does not change its volume, the myocardium is modelled as being incompressible. This assumption can be justified in the experimental situation where the myocardial cubes are bathed in a physiological solution. Yet it has to be noted that this is only likely to be true after a few loading cycles so that the tissue has equilibrated its state. This assumption might not hold true in vivo where there is blood flow (perfusion) in the heart during the

heart cycle, which will change the volume regionally [43, 19].

As stated in Eq.(3.20) incompressibility can be described by requiring  $\det \mathbb{F} \equiv 1$ . This condition is enforced by means of the hydrostatic pressure  $p = -\frac{1}{3}\text{tr}(\mathbb{T})$ . To account for this a Lagrange multiplier is introduced in the stress-strain relation in Eq.(3.54):

$$\mathbb{S}(\mathbb{E}) = -\lambda \mathbb{C}^{-1} + \text{sym}[\mathbb{D}_{\mathbb{E}} W(\mathbb{E})], \quad (3.60)$$

where  $\lambda$  is the Lagrange multiplier and  $\mathbb{C}^{-1}$  is the equivalent of the identity tensor in the reference configuration, or in other words the “push-back” transformation of the identity tensor in the current configuration into the reference configuration [13].  $\lambda$  will equal the hydrostatic pressure if the strain energy density is restricted to depend on the deviatoric part of  $\mathbb{E}$ ,  $\check{\mathbb{E}}$  only:

$$\check{\mathbb{E}} = \frac{1}{2}(\det \mathbb{F}^{-\frac{2}{3}} \mathbb{C} - \mathbb{I}). \quad (3.61)$$

The numerical implementation of this requirement is discussed in Sec.(4.1.1.1).



# Chapter 4

## Numerical Tools

This chapter briefly summarises the finite element method in Sec.(4.1) as well as some standard optimisation techniques in Sec.(4.2) and statistical measures in Sec.(4.4). Furthermore it introduces a novel objective function in Sec.(4.3) which was utilised throughout this study.

### 4.1 Finite Element Method

To analyse stress in a body undergoing large elastic deformations the equations that govern finite deformation elasticity, developed in chapter 3, must be solved. For materials with regular geometries this may be done analytically, as is presented in section 6.1. However, a more realistic deformation can be modelled by discretising the domain of interest into a number of finite elements (cuboidal hexahedral elements). Thereby the partial differential equation is broken down into a set of algebraic equations. The type of interpolating functions used to interpolate the independent and dependent variables (in this thesis) are tri-linear Lagrange basis functions. See Bathe [11] or Zienkiewicz & Taylor [129] for details of the concept of the finite



element method.

For each element, the equations governing finite elasticity are expressed in terms of known material properties and the unknown displacements of the element vertices or nodes. These equations are formulated as integral equations which are evaluated via Gaussian quadrature.

Element contributions are assembled into a global system of algebraic equations to ensure that the solution is compatible across element boundaries. The system of nonlinear equations are then solved, subject to boundary constraints, to yield a set of deformed nodal coordinates from which deformation patterns are approximated using the specified interpolating functions.

#### 4.1.1 Galerkin Finite Element Equations

Here we sketch the Galerkin weighted residual technique which is derived from integral form of the balance equation Eq.(3.45). We neglect body and inertia forces. Therefore Eq.(3.45) reads:

$$\text{Div} \mathbb{P} = 0 . \quad (4.1)$$

When the displacement variables are approximated by an interpolating function, the equation will not be fulfilled identically and a residual will remain:

$$\text{Div} \hat{\mathbb{P}} = e \quad \Longleftrightarrow \quad R = \text{Div} \hat{\mathbb{P}} - e , \quad (4.2)$$

where  $e$  denotes the error,  $\hat{\mathbb{P}}$  the approximated first Piola–Kirchhoff stress tensor field and  $R$  the residual.

To minimise this residual it is firstly multiplied by  $N_R$  linear independent weighting functions  $\omega_j$  and then integrated over the domain volume. Furthermore it is required that all these integrals vanish:

$$\int_{\mathcal{B}} R \omega_j d\mathcal{B} \stackrel{!}{=} 0 \quad \text{for all } j = 1, \dots, N_R . \quad (4.3)$$

These conditions may then be used to determine the unknown parameters of the approximating function. If the functions  $\omega_j$  are chosen to be the basis functions (the tri-linear basis functions in our case), then it is called the Galerkin method.

#### 4.1.1.1 Incompressibility

The myocardium is typically modelled to be incompressible. There are two main ways of modelling this behaviour: (i) by introducing a Lagrange multiplier that can then be identified with the hydrostatic pressure; or (ii) by modelling the material as being nearly incompressible, and splitting the strain energy density function into volumetric and deviatoric parts. The volumetric part then serves to mimic the nearly incompressible behaviour. Dell & McCulloch [28] reported that this may improve numerical stability for forward solutions using the finite element method.

The finite element code CMISS [124] which was used in this study has a Galerkin incompressibility constraint implemented which is briefly sketched here.

The incompressibility constraint introduces another free variable, the hydrostatic pressure field. The extra constraint necessary to determine the parameters of the hydrostatic pressure field arise from the requirement that  $I_3 = 0$  (see Eq.(3.26) for the definition of  $I_3$ ). This constraint is realised in an element based sense rather than pointwise and modified to reflect volume change:  $\sqrt{I_3} - 1 = 0$ .

To be consistent when calculating stress components and to avoid numerical ill-conditioning, Oden ([90], p.239) suggests that the interpolation scheme chosen to describe the deformed geometric coordinates should be of a higher order than that chosen to approximate the hydrostatic pressure field.

This arises because the strain energy contribution to stress components is related to the first derivatives of the geometric displacement fields, whereas the hydrostatic pressure directly contributes to the stress components. In our case the hydrostatic pressure field is approximated by a element-wise piecewise constant scalar field to satisfy this condition, since the displacement variables are approximated with tri-linear basis functions. Nash & Hunter [84] describe the implementation of this technique into the finite element environment in detail.

The resulting system of nonlinear algebraic equations is then solved using standard solving techniques like the Newton method. It is explained in Sec.(4.2.2), however, it will be explained in the context of material parameter estimation rather in the context of minimising the residual of the finite element equations. The technique itself can be applied equivalently in both cases.

## 4.2 Optimisation Techniques for Parameter Estimation

This section describes the utilisation of experimental  $\mathbf{y}$  and model  $\mathbf{f}(\boldsymbol{\vartheta})$  data for the use of parameter estimation techniques. Here  $\boldsymbol{\vartheta}$  denotes the model parameters, in our case material parameters. A specific estimator will be presented now which is most commonly used, i.e. the least-square objective function. Firstly though, the error  $\mathbf{e}$  is defined as:

$$\mathbf{e}(\boldsymbol{\vartheta}) = \mathbf{y} - \mathbf{f}(\boldsymbol{\vartheta}) \quad \Longleftrightarrow \quad e_m = y_m - f_m(\boldsymbol{\vartheta}). \quad (4.4)$$

From here one can move to the specific estimator.

### 4.2.1 Least-Squares Objective Function

The objective function, which is to be minimised later on, can then be defined as:

$$\Omega(\boldsymbol{\vartheta}) = \frac{1}{2} \mathbf{e}^T \mathbf{e} \iff \Omega(\boldsymbol{\vartheta}) = \frac{1}{2} \sum_m e_m^2. \quad (4.5)$$

This squares the error and for sufficiently smooth data will represent a convex shaped valley, in which parameter estimation can be performed. However, due to the non-linearity of the model the initial guess of the optimisation plays a crucial role. This is addressed in more detail in Chapter 6.

Furthermore a weighted least-square objective function can be defined as:

$$\Omega(\boldsymbol{\vartheta}) = \frac{1}{2} \mathbf{e}^T \mathbf{W} \mathbf{e} \iff \Omega(\boldsymbol{\vartheta}) = \frac{1}{2} \sum_m \sum_n e_m W_{mn} e_n, \quad (4.6)$$

where  $\mathbf{W} \Leftrightarrow W_{mn}$  is the matrix of weights.

Both inner products of the residual vector utilise all existing data points in the region being modelled. In Sec.(4.3) a novel objective function is presented that is based on the idea of a weighted objective function, which reduces the number of data points required by two magnitudes.

Also other objective functions can be defined with various metrics. For the purpose of this study, however, the modified objective function will be applied for all models. The actual optimisation steps are explained in the subsequent sections.

### 4.2.2 Newton Method

To find the minimum of  $\Omega$  we have to find a sequence of steps  $\boldsymbol{\varepsilon}_k$  in the parameter space which successively decreases  $\Omega$ :

$$\Omega(\boldsymbol{\vartheta}_{k+1}) < \Omega(\boldsymbol{\vartheta}_k) \quad \text{with} \quad \boldsymbol{\vartheta}_{k+1} = \boldsymbol{\vartheta}_k + \boldsymbol{\varepsilon}_k. \quad (4.7)$$

It can be shown [10] that this is guaranteed if  $\boldsymbol{\varepsilon}_k$  is chosen to be:

$$\boldsymbol{\varepsilon}_k = -\mathbf{R} \nabla_{\boldsymbol{\vartheta}} \Omega, \quad (4.8)$$

where  $\nabla_{\boldsymbol{\vartheta}} \Omega$  is the gradient of  $\Omega$  and if  $\mathbf{R}$  is a positive definite matrix.

If the valley was parabolic, it would be a natural choice to chose  $\mathbf{R}$  as being the inverse of the Hessian of  $\Omega$ . However, in practical applications this cannot be assumed to be true, especially since the initial guess may lie far outside a convex region. Therefore the Hessian might not be positive definite.

This also highlights the need to find good initial guesses with our method for FEM inverse estimations.

### 4.2.3 Levenberg–Marquardt Method

Levenberg [69] proposed to utilize a modified  $\mathbf{R}$ , namely  $\mathbf{R} = (\mathbf{H} + \Lambda \mathbf{I})^{-1}$ , which allows one to adapt  $\Lambda$  in a way that  $\mathbf{R}$  becomes positive definite. In particular, if  $\Lambda = 0$ , it is the Newton–Raphson method and if  $\Lambda = \infty$ , it is the steepest descent method.

As stopping criteria we chose the difference of two successive steps for the objective function  $|\Delta \Omega|$  and of the length of the material parameter vector  $|\Delta \boldsymbol{\vartheta}|$  to be smaller than  $10^{-5}$ .

## 4.3 A Novel Optimisation Technique

The conventional least squares objective function, Eq.(4.5), would sum over all data points, about  $\sim 5000$  data points for the experiments performed by Dokos et al. [30]. By adding a “weight” to each addend in Eq.(4.6), namely the width  $\Delta x$  of each interval of two successive data points, the objective function approximates the following integral, assuming that the data points imply a

piecewise linear function and that the data stems from a one-dimensional recording.

$$\Omega(\boldsymbol{\vartheta}) = \frac{1}{2} \sum_m e_m^2(\boldsymbol{\vartheta}) \Delta x_m \approx \frac{1}{2} \int_{x_{min}}^{x_{max}} (\mathbf{e}(\boldsymbol{\vartheta}, x))^2 dx \quad (4.9)$$

This weighting was chosen because the integral forms a  $L^2$ -norm in the functional space of squared integrable functions, and can therefore serve as a measure of the *length* of the error. The same holds for the piecewise linear approximating functions and this measure can be interpreted as a "pseudo-energy content" (pseudo, because the dimensions of the integrals in this application are *Joule*<sup>2</sup>/*metre*) and serves as a reference for the minimized objective function to obtain a relative error.

The above formulation suggests that it would be numerically more efficient to approximate the integral via a Gaussian quadrature integration method, see for example [96]. This would then read:

$$\int_{x_{min}}^{x_{max}} (\mathbf{e}(\boldsymbol{\vartheta}, x))^2 dx \approx \sum_{j=1}^M \omega^j (\mathbf{e}(\boldsymbol{\vartheta}, x^j))^2, \quad (4.10)$$

where  $M$  is the number of Gauss quadrature points for over the data range and  $x^j$  are the associated evaluation points. The objective function then reads:

$$\Omega(\boldsymbol{\vartheta}) = \frac{1}{2} \sum_{j=1}^M \omega^j (\mathbf{e}(\boldsymbol{\vartheta}, x^j))^2, \quad (4.11)$$

If  $\mathbf{f}$  in Eq.(4.4) is set to zero, Eq.(4.11) gives the energy content  $\Omega_{EC}$ .

Naturally the question arises whether this modified least square method converges to Eq.(4.9). The convergence analysis is presented in Sec.(6.1.4). For further details the reader is referred to [105].

## 4.4 Statistical Tools

In this section, measures to compare the material laws against each other and amongst experiments are investigated. These measures as well as the least-squares method in the previous section are based on the assumption that the data follows a Gaussian distribution. Yin and coworkers have also investigated the possibility of non-parametric bootstrapping methods rather than simple Gaussian (parametric) statistics [127].

These measures were investigated to see how well they fit to the data for different experimental sets (goodness of fit) and how well they are defined for a given set of experimental data in terms of numerical determinability. These measures are described below.

### 4.4.1 Normalised Standard Deviation

The quantity commonly referred to as “the” mean of a set of values is the arithmetic mean:

$$\mu_x = \frac{1}{n} \sum_{i=1}^N x_i, \quad (4.12)$$

where  $N$  is number of data samples. This measure is also called the (un-weighted) average. The sample variance  $\sigma^2$  is the second sample central moment and is defined by:

$$\sigma_x^2 = \frac{1}{N-1} \sum_{i=1}^N (x_i - \mu_x)^2. \quad (4.13)$$

The square root of the sample variance of a set of  $N$  values is the sample standard deviation:

$$\sigma_x = \sqrt{\frac{1}{N-1} \sum_{i=1}^N (x_i - \mu_x)^2}. \quad (4.14)$$

The coefficient of variation  $CoV$  is defined as:

$$CoV_x = \frac{\sigma_x}{\mu_x}, \quad (4.15)$$

and therefore gives a relative measure of deviation from the mean. The standard error is defined as:

$$s_e = \frac{1}{N} \sigma_x. \quad (4.16)$$

#### 4.4.2 Goodness of Fit

The measure of the objective function value at the optimum  $\Omega(\boldsymbol{\vartheta}_0)$  when normalised by the energy content gives the “relative objective function value”  $\Omega_{rel} = \Omega(\boldsymbol{\vartheta}_0)/\Omega_{EC}$ . We can then calculate the mean values  $\mu_\Omega$  and  $\mu_{\Omega_{rel}}$ , the standard deviation  $\sigma_\Omega$  and  $\sigma_{\Omega_{rel}}$  over all experiments for each material law and thus the coefficient of variation  $CoV_\Omega = \frac{\sigma_\Omega}{\mu_\Omega}$  and  $CoV_{\Omega_{rel}} = \frac{\sigma_{\Omega_{rel}}}{\mu_{\Omega_{rel}}}$  can be formed .

#### 4.4.3 Akaike Information Criterion (AIC)

The relative objective function has limited use as a “goodness of fit” criterion to compare the five models, since it does not take into account the number of parameters of each model. This challenge is usually overcome by introducing an information criterion that reflects both the objective function value and the model complexity via a common measure, see also Nelles [86].

The idea of an information criterion was derived from a similar question. The challenge was to select an approximating model from a set of models. This was overcome by defining a “distance” between two models (similar to the distance between two functions over a given interval), the so-called Kullback–Leibler “distance”. In the mid-1970s Akaike introduced his “*entropy maximisation principle*” in a series of papers [1, 2, 3] as a theoretical



basis for model selection. This principle is a simple relationship between the Kullback–Leibler distance and Fisher’s maximised log-likelihood function. From this Akaike derived *an* information criterion (*AIC*) which is named after him:

$$AIC = N \ln\left(\frac{1}{N} \Omega(\boldsymbol{\vartheta})\right) + 2K. \quad (4.17)$$

The “best” model is defined as the model with the lowest information criterion.  $K$  denotes the number of material parameters and  $N$  the number of data points.

Starting from different statistical assumptions, a number of proposals for the complexity have been made. All of them monotonically increase with the number of parameters in the model. Since it is not clear which information criterion is the best, the Akaike information criterion (*AIC*) as suggested by Burnham et.al. [16] was chosen. The information criterion yields a relative measure and can therefore only act to select the best model within a set of models. However, if all the models were very poor, the criterion would still select the one with the best estimate, but that model may be poor in an absolute sense. This is why the goodness of fit criterion was also utilised.

#### 4.4.4 M– & D–Optimality

The above criteria form a basis for comparing the goodness of fit for the material laws, but it is also important to ask the question whether the material parameters are sensitive to disturbances in the data values, or in other words, how the objective function varies in the neighbourhood of the optimum. For a detailed and thorough discussion of this issue see [64, 85, 10]. Here the basic ideas are described.

Given the optimal point in the parameter space  $\boldsymbol{\vartheta}_0$ , various criteria to measure different aspects of the behaviour of the material in consideration

can be formed. If one considers a small deviation  $\delta\boldsymbol{\vartheta}$  around the optimum  $\boldsymbol{\vartheta}_0$  then the following equation:

$$\delta\boldsymbol{\vartheta}^T \mathbf{H}_0 \delta\boldsymbol{\vartheta} \leq 2\epsilon \quad (4.18)$$

implies an  $K$ -dimensional hyperellipsoid, where  $K$  is the number of material parameters for the material law in consideration and  $\mathbf{H}_0$  is the Hessian at the optimum. This region is sometimes also called the “ $\epsilon$ -indifference region”. The determinant  $\det(\mathbf{H}_0)$  at the optimal point represents the volume of the indifference region and is also referred to as the D-optimality criterion. The higher this number, the lower the variance of the material parameters.

The condition number of the Hessian at the optimum,  $\text{cond}(\mathbf{H}_0)$ , describes the ratio between the highest and the lowest eigenvalue of  $\mathbf{H}_0$  and can be shown to be the square of the eccentricity of the hyperellipsoid. This eccentricity is important to characterise the numerical stability of the optimisation process. It is desirable to have a low eccentricity ([96], p.54 and references above) since it ensures that errors are not overly magnified.

The so-called M-optimality criterion relates the interaction between material parameters. It is defined as:

$$\det(\tilde{\mathbf{H}}_0) \quad \text{where} \quad \tilde{H}_{ij} = \frac{H_{ij}}{H_{ii}H_{jj}} \quad (\text{no sum}), \quad (4.19)$$

and describes the alignment of the hyperellipsoid with the material parameter axes. ( $\tilde{H}_{ij} = \delta_{ij}$  for perfect alignment, corresponding to no correlation between the material parameters.)

#### 4.4.5 Material Parameter Variability amongst Experiments

The statistical analysis of the objective function gives insight into the overall ability of the material law to fit a certain set of experimental data. It

is, however, also important to consider the variability of each individual parameter as well as the overall variability. Therefore calculated the mean  $\mu_{\gamma_i}$  and standard deviation  $\sigma_{\gamma_i}$  of each individual parameter was calculated over all experiments for each material law and thus the coefficient of variation  $CoV_{\gamma_i} = \frac{\sigma_{\gamma_i}}{\mu_{\gamma_i}}$  was formed.

#### 4.4.6 Material Parameter Variability amongst Models

In the comparison of the values between the homogeneous simulations and the FEM simulations or between several refinements of the finite element study for the convergence analysis, it is important to account for the varying magnitudes of the individual parameters. Therefore the following measure  $\Delta_{\kappa}^{m_{\alpha} \setminus m_{\beta}}$  was utilised to compare a specific quantity  $\kappa$  between two different models  $\alpha$  and  $\beta$ :

$$\Delta_{\kappa}^{\alpha \setminus \beta} = \frac{|\kappa_{\alpha} - \kappa_{\beta}|}{\kappa_{\beta}}, \quad (4.20)$$

for example, if  $\kappa$  is the material parameter  $a$ , then  $\Delta_a^{\text{homo} \setminus \text{FEM}}$  would denote the comparison of the material parameter  $a$  of the homogeneous model with the one obtained from the finite element solution, whereas  $\Delta_{\Omega}^{222 \setminus 333}$  denotes the difference in the objective function between two differently refined cubes, i.e. one with  $8 = 2 \times 2 \times 2$  elements (two elements in each direction) and one with  $27 = 3 \times 3 \times 3$  elements (three elements in each direction).

Furthermore it is helpful to employ an overall measure that compares all material parameters:

$$\Delta_{MP}^{\alpha \setminus \beta} = \sum_{i=1}^K \Delta_{\gamma_i}^{\alpha \setminus \beta}, \quad (4.21)$$

where  $K$  denotes the number of material parameters for the given constitutive relation and  $\gamma_i$  a material parameter.

# **Part II**

## **Application**



# Synopsis

This part presents the independent research undertaken during this project. Chapter 5 presents the five material laws that were investigated in this study. The Costa Law (CL), Pole-zero law (PZL) and the Langevin eight chain law (LECL) were chosen as published laws. The separated FUnge-type law (SFL) and the Tangent law (TL) were chosen to investigate whether certain restrictions of the CL and PZL, respectively, could be enhanced.

Chapters 6–8 present the development of the three models. Firstly, the homogeneous simple shear deformation model is derived and the respective results are presented as well as a modified objective function. Secondly, a finite element simple shear model is presented to attain a more realistic description of the deformation process. Furthermore its respective results are also presented. Thirdly, a uniaxial extension model and its results are presented to investigate the effects of a varying experimental protocol on the material parameter estimation. Lastly, Chapter 9 presents the conclusion of this study.



# Chapter 5

## Myocardial Material Laws

The mechanical behaviour of the heart has been modelled over the last 30 years with different material law (ML) concepts, (elastic  $\longleftrightarrow$  viscoelastic, phenomenological  $\longleftrightarrow$  microstructurally based). A brief summary of the attempts to model the passive elastic behaviour of myocardium is given below.

### 5.1 Historical Introduction

Fung [33] was amongst the first to suggest a constitutive relation for the passive myocardial behaviour. The strain energy proposed within there was a combination of a linear and an exponential term. Various modified versions of this original strain energy density function have been used to model the myocardium as being transversely isotropic [39]. Costa et al. [25] extended this to an orthotropic formulation by leaving out the linear term and modifying the exponential term. This law is presented in Sec.(5.2.1). Another micro-structurally motivated yet phenomenological law was introduced by Nash & Hunter [84] and is described in further detail in Sec.(5.2.2). The fact that the myocardium exhibits a “strain-limit” was taken into account into



the formulation of the functional form. These two laws seem to be amongst those most frequently used in the literature to describe the orthotropic passive mechanical response for the myocardium. A constitutive law based on microstructure was introduced by Bischoff et al. [12] which is based on microstructural modelling of macromolecules. It has the advantage of considerably reducing the number of material parameters. This orthotropic law is presented in Sec.(5.2.3). However, other functional forms have been proposed which are described below.

Humphrey et al. [48] introduced a transversely isotropic strain energy based on both theory and experiment in terms of two coordinate invariant measures with five material parameters. This was extended by Holzapfel & Gasser [45] for the orthotropic case applied to arterial walls, but would be applicable for the description of orthotropic myocardium as well. However, the invariant formulation may make inverse material parameter estimation more difficult, since it might be hard to perform experiments that separate the kinematic tensors of the invariants [27]. Criscione [27] proposed a constitutive framework based on the laminar structure of the myocardium. This law was based on the idea to decouple the the kinematic tensors and introduced a series of strain attributes. Finally, it is worth mentioning that Hartmann & Neff [41] introduced the concept of polyconvexity for hyperelastic strain energy functions which guarantees a global optimiser for the finite element equations. This was then extended by Itskov & Aksel [56] for the orthotropic case. Additionally, these polyconvex formulations are based on a different set of invariants which might enhance their suitability for inverse parameter estimations.

Lanir [63] published a micro-structurally based constitutive relation for fibrous connective tissues which extended by Horowitz et al. [46] who took

up this idea and developed a constitutive relation for passive myocardium.

Caillerie et al. [18] proposed a constitutive law for the myocardium based on a cell to muscle homogenisation technique. It was based on the repetitive arrangement of myocytes and did not include the sheet structure and was therefore limited to capture transversely isotropic behaviour. It is to be noted that the concept within this publication could be extended to account for the orthotropic response of myocardium.

## 5.2 Published Laws

The next section will present in detail the strain energy density function for the Costa law (CL) [25], the Pole–Zero law (PZL) [84] and the Langevin eight chain law (LECL) [12]. The CL and PZL were chosen, since they depend on the components of the Green–strain tensor which have physical meaning and therefore enable an interpretation of the material parameters with respect to the underlying micro–structure. The LECL was chosen since it is based on an assumption of micro–structural arrangement and therefore ensured a coverage of different constitutive laws.

Although the theoretically desirable polyconvexity cannot be established under large strain conditions for the following constitutive relations, they do prove in practice to provide very useful parametrisation of experimental data and the material properties. See also Sec.5.3.4.

### 5.2.1 Costa Law

Costa et al. [25] published the following strain energy density function. The polynomial form of the exponent  $Q$  can be considered as the first order terms

of a series expansion of the Green strain components.

$$\Psi_1(E_{ff}, E_{fn}, E_{fs}, E_{nf}, E_{nn}, E_{ns}, E_{sf}, E_{sn}, E_{ss}) = \frac{1}{2}a(e^Q - 1) \quad (5.1)$$

where

$$Q = b_{ff}E_{ff}^2 + 2b_{fn}(\frac{1}{2}(E_{fn} + E_{nf}))^2 + 2b_{fs}(\frac{1}{2}(E_{fs} + E_{sf}))^2 + b_{nn}E_{nn}^2 + 2b_{ns}(\frac{1}{2}(E_{ns} + E_{sn}))^2 + b_{ss}E_{ss}^2$$

Note that the functional form was adapted such that the shear terms are now formulated as the symmetric part of the strain tensor rather than utilizing a product between shear strain terms as proposed by Costa et al. [25]. The meaning of the off-diagonal material parameters, however, remains unchanged.

The material law is based on a general exponential Fung type law, the details of which can be found in [35]. The 1 in the term  $(e^Q - 1)$  is subtracted to ensure that the strain energy density function is zero in the reference configuration, where  $Q = 0$ .

The multiplicative parameter  $a$  couples the other six parameters  $b_{\alpha\beta}$ . Initial simulations indicated that this coupling might decrease the fitting capabilities. Therefore a separated exponential formulation was developed, see Sec.(5.3.1).

Smaill & Hunter [107] found that there was little mechanical coupling between the fiber and sheet direction in midmyocardial specimen in biaxial tests. Since the CL exhibits inherent coupling of all strain components hence also for a biaxial deformation mode, it was believed that this might reduce the capability of the CL to fit a multiaxial set of experimental data. Sec.(5.3.1) therefore presents another exponential Fung-type material law in which this inherent coupling is released and therefore the theoretical capability to fit multiaxial data is enhanced.

### 5.2.2 Pole–Zero Law

A rather different functional form was initially proposed by Hunter [53] (see also Nash & Hunter [84]), called the Pole–zero law (PZL), which is based on the idea that the tissue has a strain or extensibility limit  $a_{ij}$  in each direction, a strength  $k_{ij}$  and parameter  $b_{ij}$  that accounts for the nonlinearity of the stress–strain curve. The parameters  $b_{ij}$  were all set to 2, since this ensured a stable optimization:

$$\begin{aligned} \Psi_3(E_{ff}, E_{fn}, E_{fs}, E_{nf}, E_{nm}, E_{ns}, E_{sf}, E_{sn}, E_{ss}) = \\ \frac{k_{ff} E_{ff}^2}{|a_{ff} - |E_{ff}||^{b_{ff}}} + \frac{k_{fn} (\frac{1}{2}(E_{fn} + E_{nf}))^2}{|a_{fn} - |\frac{1}{2}(E_{fn} + E_{nf})||^{b_{fn}}} + \frac{k_{fs} (\frac{1}{2}(E_{fs} + E_{sf}))^2}{|a_{fs} - |\frac{1}{2}(E_{fs} + E_{sf})||^{b_{fs}}} \\ + \frac{k_{nm} E_{nm}^2}{|a_{nm} - |E_{nm}||^{b_{nm}}} + \frac{k_{ns} (\frac{1}{2}(E_{ns} + E_{sn}))^2}{|a_{ns} - |\frac{1}{2}(E_{ns} + E_{sn})||^{b_{ns}}} + \frac{k_{ss} E_{ss}^2}{|a_{ss} - |E_{ss}||^{b_{ss}}} . \end{aligned} \quad (5.2)$$

### 5.2.3 Langevin Eight–Chain Law

Another law was proposed by Bischoff and coworkers [12]. This constitutive law differs from the two before mentioned in that it is based on micro–structural modelling of macromolecules. Although the macro–molecular model underlying this approach may not reflect the myocardial micro–structure, it may describe orthotropic mechanical behaviour on a macroscopic level.

For the in–depth derivation of the material law please refer to the original paper [12]. Here, we simply restate the major quantities of the law and the strain energy density function. The dimensions  $a, b, c$  were redefined as  $a_f, a_n, a_s$  for orthotropic unit cell in the fiber, normal and sheet direction,  $\mathbf{a}_f, \mathbf{a}_n, \mathbf{a}_s$  are the unit vectors in the direction of the unit cell axes and  $n$  is the density of chain molecules, see Fig.(5.1). The constant  $k$  is the Boltzman constant,  $\theta$  the absolute temperature,  $N$  number of freely jointed links<sup>1</sup> of

---

<sup>1</sup>Please note that the number  $N$  is also used later on for the number of data points.

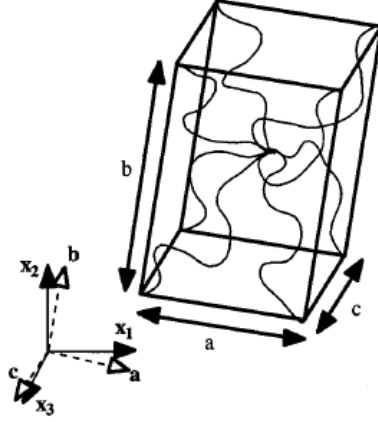


Figure 5.1: Eight-chain, three-dimensional orthotropic unit cell. The eight curved lines in the unit cell represent the constituent macromolecules and the straight lines represent the boundaries of the unit cell. The cell has dimensions  $a \times b \times c$  along the material axes  $\mathbf{a}$ ,  $\mathbf{b}$ ,  $\mathbf{c}$ , respectively, oriented with respect to the reference coordinate system  $\mathbf{X}_i$ . Picture from [12]

length  $l$  in the macromolecule, and  $\Psi_0$  is a constant to ensure zero strain energy at zero strain. The four vectors  $\mathbf{P}^{(1)}, \mathbf{P}^{(2)}, \mathbf{P}^{(3)}, \mathbf{P}^{(4)}$  defined in Eq.(5.3) follows and represent the direction of the start to end point vectors of the macromolecules:

$$\begin{aligned}
 \mathbf{P}^{(1)} &= \frac{a_f}{2}\mathbf{a}_f + \frac{a_n}{2}\mathbf{a}_n + \frac{a_s}{2}\mathbf{a}_s \\
 \mathbf{P}^{(2)} &= \frac{a_f}{2}\mathbf{a}_f + \frac{a_n}{2}\mathbf{a}_n - \frac{a_s}{2}\mathbf{a}_s \\
 \mathbf{P}^{(3)} &= \frac{a_f}{2}\mathbf{a}_f - \frac{a_n}{2}\mathbf{a}_n + \frac{a_s}{2}\mathbf{a}_s \\
 \mathbf{P}^{(4)} &= \frac{a_f}{2}\mathbf{a}_f - \frac{a_n}{2}\mathbf{a}_n - \frac{a_s}{2}\mathbf{a}_s .
 \end{aligned} \tag{5.3}$$

The deformed length of the individual chains are:

$$\rho^{(i)} = \sqrt{\mathbf{P}^{(i)} \cdot \mathbb{C} \cdot \mathbf{P}^{(i)}}, \tag{5.4}$$

where  $\mathbb{C} = 2\mathbb{E} + \mathbb{I}$  is the right Cauchy–Green stretch tensor and with  $\mathbb{E}$  being However,  $N$  with the current meaning is only used in this paragraph for simplicity to adapt the notation from [12].

the Green strain tensor. Let  $\beta_\rho^{(i)} = \mathcal{L}^{-1}(\rho^{(i)}/N)$  be the normalised deformed chain length,  $P = \frac{1}{2}\sqrt{a_f^2 + a_n^2 + a_s^2}$  the normalised undeformed chain length,  $\beta_P = \mathcal{L}^{-1}(P/N)$  and  $\mathcal{L}(x) = \coth(x) - 1/x$  the so-called Langevin function. Finally the strain energy density reads like:

$$\begin{aligned} \Psi_5(E_{ff}, E_{fn}, E_{fs}, E_{nf}, E_{nn}, E_{ns}, E_{sf}, E_{sn}, E_{ss}) = \\ \Psi_0 + \frac{nk\theta}{4} \left( N \sum_{i=1}^4 \left[ \frac{\rho^{(i)}}{N} \beta_\rho^{(i)} + \ln \frac{\beta_\rho^{(i)}}{\sinh \beta_\rho^{(i)}} \right] - \frac{\beta_P}{\sqrt{N}} \ln[\lambda_{\mathbf{a}}^{a^2} \lambda_{\mathbf{b}}^{b^2} \lambda_{\mathbf{c}}^{c^2}] \right) \\ + \frac{B}{\alpha^2} (\cosh[\alpha(J-1)] - 1) . \end{aligned} \quad (5.5)$$

The inverse Langevin function is used during the computation of the stress-strain relationship. Since no closed form of the inverse function exists we utilise the so-called Padé approximant function, see [23]:

$$\mathcal{L}^{-1}(x) = x \frac{3-x^2}{1-x^2} + O(x^6) . \quad (5.6)$$

The symbol  $O(x^6)$  is the Landau symbol, indicating that the error is restricted in the following way:  $0 < \limsup_{x \rightarrow a} \left| \frac{\mathcal{L}^{-1}(x)}{x^6} \right| < \infty$ .

### 5.3 Modified Laws

As mentioned in the above section, the CL and the PZL have theoretical disadvantages due to the coupling and the infinite slope, respectively. In particular preliminary studies had shown that the CL was not able to fit certain modes which was believed to be due to the coupling effect of the term  $Q$ . The pole  $a_{ij}$  of the PZL introduces a limited strain, which is physiologically sensible, however, the infinite slope at the strain limit is not. Furthermore the numerical implementation of such a functional form makes it likely that unreasonably high values might occur during computation.

The following two subsections present the modifications of these laws which were developed to release these limitations.

### 5.3.1 Separated Fung Law

The  $Q$ -term in  $(e^Q - 1)$  in the CL was decoupled in the following way, such that no inherent coupling would exist:

$$\begin{aligned} \Psi_2(E_{ff}, E_{fn}, E_{fs}, E_{nf}, E_{nm}, E_{ns}, E_{sf}, E_{sn}, E_{ss}) = \\ \frac{1}{2}a_{ff}(e^{b_{ff}E_{ff}^2} - 1) + \frac{1}{2}a_{fn}(e^{b_{fn}(\frac{1}{2}(E_{fn} + E_{nf}))^2} - 1) + \frac{1}{2}a_{fs}(e^{b_{fs}(\frac{1}{2}(E_{fs} + E_{sf}))^2} - 1) \\ + \frac{1}{2}a_{nm}(e^{b_{nm}E_{nm}^2} - 1) + \frac{1}{2}a_{ns}(e^{b_{ns}(\frac{1}{2}(E_{ns} + E_{sn}))^2} - 1) + \frac{1}{2}a_{ss}(e^{b_{ss}E_{ss}^2} - 1). \end{aligned} \quad (5.7)$$

This law was termed the separated Fung law (SFL). It is similar to an idea by Choi and Vito [20] for canine pericardium.

### 5.3.2 Tangent Law

The idea of a strain limit was adapted from the PZL. The tangent function  $f(x) = \tan(x)$  also has an infinite slope at  $\pi/2$ . When scaling with two parameters  $a, b$  to  $f(x; a, b) = a \tan(bx)$  the pole can be shifted along the abscissa with the parameter  $b$  and scaled along the ordinate with  $a$ . The infinite slope, however, still exists, which is why the  $\tan$ -function was approximated by its series expansion. Since the stress-strain relationship is the derivative of the strain energy function with respect to the strain we chose the function  $IntTan(x)$ , the indefinite integral of  $\tan(x)$ , and truncated after the fifth term of its Taylor series. This had the effect of removing the infinite slope at the pole – instead the curve monotonically increases. The  $IntTan(x)$  was chosen to comply to the convexity requirements of  $\Psi$ . The functional form

then reads:

$$\begin{aligned}
\Psi_4(E_{ff}, E_{fn}, E_{fs}, E_{nf}, E_{nm}, E_{ns}, E_{sf}, E_{sn}, E_{ss}) = \\
\frac{1}{2}a_{ff}IntTan(b_{ff}E_{ff}^2) + \frac{1}{2}a_{fn}IntTan(b_{fn}(\frac{1}{2}(E_{fn} + E_{nf}))^2) \\
+ \frac{1}{2}a_{fs}IntTan(b_{fs}(\frac{1}{2}(E_{fs} + E_{sf}))^2) + \frac{1}{2}a_{nm}IntTan(b_{nm}E_{nm}^2) \\
+ \frac{1}{2}a_{ns}IntTan(b_{ns}(\frac{1}{2}(E_{ns} + E_{sn}))^2) + \frac{1}{2}a_{ss}IntTan(b_{ss}E_{ss}^2).
\end{aligned} \tag{5.8}$$

Since the tangent function was chosen as the basis for the formulation of this law, it was termed Tangent law (TL).

It is worth noting that the number of addends after which the TL is truncated only plays a minor role. The material parameter estimation was performed for various numbers of addends ranging from 3–20 and they altered the objective function value by less than 0.01%.

### 5.3.3 Theoretical Considerations

There exist a variety of mathematical conditions on the functional form of a given strain energy density function which enhance the numerical performance especially in the context of finite element simulations. For example, the requirement of local convexity [45] of the strain energy density function ensures the quadratic convergence of certain iterative solution techniques that arise when using finite-element methods to solve linearised versions of the equilibrium equations in their weak form (see [44], Sec.(6.6)).

Important consequences also follow from other local convexity properties of the strain energy density function. One can use certain conditions like strong ellipticity as well as the Legendre–Hadamard condition [120] to prove a number of classical results on the local uniqueness and stability of solutions to nonlinear boundary-value problems as well as on the existence, uniqueness, and stability of solutions to the corresponding linearisations of these problems. See for example [40, 91, ?]. For hyperelastic materials, however,



global convexity of the strain energy density function is incompatible, in a certain sense, with frame indifference ([22], Sec(4.8)).

Once having chosen the functional form, it is possible to restrict the range of material parameters even further. Some of these restrictions stem from the strong-ellipticity or the Legendre–Hadamard conditions, [120], Sec.(5). There are also other kinds of restrictions like the Baker–Erickson inequalities [75], p.16, which stem from certain physical considerations. These, however, only hold for isotropic materials. Similar conditions were investigated by Humphrey [49] for a number of transversely isotropic Fung–type laws.

Each of the constitutive relations investigated in this study is convex in each of its components. This ensures some very basic shape requirements of the stress–strain curves. Yet, they do not fulfil the Legendre–Hadamard conditions, see Sec.(5), [120]. Further investigations into the mathematical properties of the constitutive relations presented in this chapter need to be investigated in the future.

In particular, it would be desirable to investigate the restrictions on the material parameters of the e.g. CL, which have negative values for some of the estimates. These investigations would shed more light on the discussions in Sec.(6.2), i.e. whether the material parameters are a result of the experimental data, the deformation model assumptions or the lack of assumptions for the material parameter range.

### 5.3.4 Practical Considerations

It has been recognised only lately that the myocardial microstructure suggest an orthotropic material response. The questions arises whether all components of the functional form are necessary to describe the set of experimental data available.

Therefore a test was performed by leaving out components of the functional form in the homogeneous model as described in Sec.(6.2). For example, the dependence of the CL on the Green strain component  $E_{ff}$  was left out by setting the material parameter  $b_{ff} = 0$ . This was done for all material parameters separately. The increase in the relative objective function error ranged from 11.1% (for setting  $b_m = 0$ ) to 34.8% (for setting  $b_{ff} = 0$ ), indicating that all material parameters were necessary to describe the experimental data. Similar values were obtained for the other material laws.

## 5.4 Summary

This chapter presented the five material laws that were investigated in this study. The CL, PZL and LECL were chosen as published laws. The SFL and TL were chosen to investigate whether certain restrictions of the CL and PZL, respectively, could be enhanced.



# Chapter 6

## Homogeneous Deformation Model

The last chapter introduced the constitutive laws necessary to develop the three models which build on each other.

Firstly, the material parameters for the six simple shear modes of Dokos et al. [30] as described in Sec.(2.3.5) are modelled. A homogeneous deformation as depicted in Fig.(2.4) is assumed. From this assumption the objective function is constructed.

Secondly, parameters for the same data were estimated by releasing the assumption of a homogeneous deformation and by modelling the deformation in the finite element environment, such that Eq.(3.45) were fulfilled. The details of the finite element method is described in Sec.(4.1).

Thirdly, the simple shear experiments were extended to include uniaxial extension data as described in Sec.(2.3.6). This was done to ensure that the material parameters would be validated against another experimental protocol. It is to be noted, however, that the data available with this set of experimental protocol was limited to one experiment, which does not allow

for a statistical analysis, but rather only provides insight into issues that have to be considered for further examinations.

## 6.1 Homogeneous Analytical Deformation Model for Simple Shear

Given the constitutive relations and the homogeneous model assumptions, an analytical form of the top face force in terms of any given displacement was derived. This is presented for one material law (CL) and one shear deformation mode (NS-mode) as an example. A global coordinate system  $(x, y, z)$  is introduced where the direction of shear was aligned with the  $x$ -axis and the normal of the top face with the  $z$ -axis. This serves to obtain an easier expression for the objective function and was also used in Chap.(7) for the finite element model.

### 6.1.1 Derivation of Analytical Model

Assuming material dimensions  $\alpha$ ,  $\beta$  and  $\gamma$  in the  $x, y, z$ -directions or  $f, n, s$ -directions, respectively, the following deformation gradient is obtained:

$$\mathbb{F} = \begin{pmatrix} 1 & 0 & k \\ 0 & 1 & 0 \\ 0 & 0 & 1 \end{pmatrix}_{(x,y,z)} = \begin{pmatrix} 1 & 0 & 0 \\ 0 & 1 & 0 \\ 0 & k & 1 \end{pmatrix}_{(f,n,s)}, \quad (6.1)$$

where now  $k$  ranges between  $-\frac{1}{2}\gamma$  and  $\frac{1}{2}\gamma$ . From that the Green strain tensor in both coordinate systems can be derived:

$$\mathbb{E} = \begin{pmatrix} 0 & 0 & k \\ 0 & 0 & 0 \\ k & 0 & k^2 \end{pmatrix}_{(x,y,z)} = \begin{pmatrix} 0 & 0 & 0 \\ 0 & k^2 & k \\ 0 & k & 0 \end{pmatrix}_{(f,n,s)}. \quad (6.2)$$

The stress strain relationship reads  $\mathbb{S} = -p\mathbb{I} + \frac{\partial\Psi}{\partial\mathbb{E}}$ . Since deformation was constrained to be homogeneous simple shear and was therefore isochoric, the hydrostatic pressure term vanishes as it would only come into play to enforce the volume constraint ( $J = 1$ ). The stress-strain relationship then becomes  $\mathbb{S} = \frac{\partial\Psi}{\partial\mathbb{E}}$ . From this the second Piola-Kirchhoff stress tensor can be derived:

$$\begin{aligned} \mathbb{S} &= \begin{pmatrix} 0 & 0 & \frac{1}{2}a_1b_{ns}ke^{\frac{1}{4}b_{nn}k^4+\frac{1}{2}b_{ns}k^2} \\ 0 & 0 & 0 \\ \frac{1}{2}a_1b_{ns}ke^{\frac{1}{4}b_{nn}k^4+\frac{1}{2}b_{ns}k^2} & 0 & \frac{1}{2}a_1b_{nn}k^2e^{\frac{1}{4}b_{nn}k^4+\frac{1}{2}b_{ns}k^2} \end{pmatrix}_{(x,y,z)} \\ &= \begin{pmatrix} 0 & 0 & 0 \\ 0 & \frac{1}{2}a_1b_{nn}k^2e^{\frac{1}{4}b_{nn}k^4+\frac{1}{2}b_{ns}k^2} & \frac{1}{2}a_1b_{ns}ke^{\frac{1}{4}b_{nn}k^4+\frac{1}{2}b_{ns}k^2} \\ 0 & \frac{1}{2}a_1b_{ns}ke^{\frac{1}{4}b_{nn}k^4+\frac{1}{2}b_{ns}k^2} & 0 \end{pmatrix}_{(f,n,s)}. \end{aligned} \quad (6.3)$$

From this the analytic force on the top face can be derived by means of Nanson's formula Eq.(3.23) :

$$\begin{aligned} \mathbf{t}_{\text{ana}} &= \mathbb{F}\mathbb{S} \cdot \mathbf{N} = \begin{pmatrix} \frac{1}{2}\alpha\beta a_1 \left( b_{ns}ke^{\frac{1}{4}b_{nn}k^4+\frac{1}{2}b_{ns}k^2} b_{nn}k^2e^{\frac{1}{4}b_{nn}k^4+\frac{1}{2}b_{ns}k^2} \right) \\ 0 \\ \frac{1}{2}\alpha\beta a_1 b_{nn}k^2e^{\frac{1}{4}b_{nn}k^4+\frac{1}{2}b_{ns}k^2} \end{pmatrix}_{(x,y,z)} \\ &= \begin{pmatrix} 0 \\ \frac{1}{2}\alpha\beta a_1 b_{nn}k^2e^{\frac{1}{4}b_{nn}k^4+\frac{1}{2}b_{ns}k^2} \\ \frac{1}{2}\alpha\beta a_1 \left( b_{ns}ke^{\frac{1}{4}b_{nn}k^4+\frac{1}{2}b_{ns}k^2} b_{nn}k^2e^{\frac{1}{4}b_{nn}k^4+\frac{1}{2}b_{ns}k^2} \right) \end{pmatrix}_{(f,n,s)}, \end{aligned} \quad (6.4)$$

where  $\mathbf{N} = (0, 0, \alpha\beta)_{(x,y,z)} = (0, \alpha\beta, 0)_{(f,n,s)}$  is the normal vector in the reference configuration multiplied with the area of the top face.

There is an analogue of  $\mathbf{t}_{\text{ana}}$  from the experiment, i.e.  $\mathbf{t}_{\text{exp}}$  the measured force on the top face from the experiment. The number of data points obtained from the experiment are approximately 250 data points over the range of deformations from  $-\frac{1}{2}\gamma$  to  $\frac{1}{2}\gamma$  for each mode.

The usual approach of a least squares objective function is adopted, but modified to account for the expensive numerical computations which arise in inverse parameter estimations as described in Sec.(4.3).

### 6.1.2 Derivation of Objective Function

The conventional least squares objective function would sum over all six modes, all three directions of the top face force and all data points of each mode and force direction, resulting in approximately  $6 \times 3 \times 250 = 4500$  data points:

$$\Omega(\boldsymbol{\vartheta}) = \frac{1}{2} \sum_{\text{modes}} \sum_{\substack{\text{x,y,z-} \\ \text{force}}} \sum_{\substack{\text{data} \\ \text{points}}} |\mathbf{t}_{\text{ana}}(\boldsymbol{\vartheta}) - \mathbf{t}_{\text{exp}}|^2, \quad (6.5)$$

where  $\boldsymbol{\vartheta}$  is the vector of all material parameters. By adding a “weight” to each addend, namely the width  $\Delta x$  of each interval of two successive data points, the objective function approximates the following integral, assuming that the data points imply a piecewise linear function.

$$\begin{aligned} \Omega(\boldsymbol{\vartheta}) &= \frac{1}{2} \sum_{\text{modes}} \sum_{\substack{\text{x,y,z-} \\ \text{force}}} \sum_{\substack{\text{data} \\ \text{points}}} |\mathbf{t}_{\text{ana}}(\boldsymbol{\vartheta}) - \mathbf{t}_{\text{exp}}|^2 \Delta x \\ &\approx \frac{1}{2} \sum_{\text{modes}} \sum_{\substack{\text{x,y,z-} \\ \text{force}}} \int_{-\frac{1}{2}\gamma_i}^{\frac{1}{2}\gamma_i} |\mathbf{t}_{\text{ana}}(\boldsymbol{\vartheta}, x) - \mathbf{t}_{\text{exp}}(x)|^2 dx \end{aligned} \quad (6.6)$$

This weighting was chosen because the integral forms a  $L^2$ -norm in the functional space of squared integrable functions, and can therefore serve as a measure of the *length* of the error. The same holds for the piecewise linear approximating functions and this measure can be interpreted as a “pseudo-energy content” (pseudo, because the dimensions of the integrals are  $J^2/m$ )

and serves as a reference for the minimized objective function to obtain a relative error.

The above formulation suggests that it would be numerically more efficient to approximate the integral via a Gaussian quadrature integration method, see for example [96]. This would then read:

$$\int_{-\frac{1}{2}\gamma_i}^{\frac{1}{2}\gamma_i} |\mathbf{t}_{\text{ana}}(\boldsymbol{\vartheta}, x) - \mathbf{t}_{\text{exp}}(x)|^2 dx \approx \sum_{j=1}^G \omega^j |\mathbf{t}_{\text{ana}}(\boldsymbol{\vartheta}, x^j) - \mathbf{t}_{\text{exp}}(x^j)|^2, \quad (6.7)$$

where  $G$  is the number of Gauss quadrature points for each of the twelve displacement–force curves. The objective function then reads:

$$\Omega(\boldsymbol{\vartheta}) = \frac{1}{2} \sum_{\text{modes}} \sum_{\substack{\mathbf{x}, \mathbf{y}, \mathbf{z} \\ \text{force}}} \sum_{j=1}^G \omega^j |\mathbf{t}_{\text{ana}}(\boldsymbol{\vartheta}, x^j) - \mathbf{t}_{\text{exp}}(x^j)|^2 \quad (6.8)$$

If we choose for example  $G = 12$ , the number of total function evaluations required has been reduced to 144 compared to  $\sim 4500$  in the full model, corresponding to 97% saving.

The change to the Gaussian least squares objective function also has a significant change in meaning, i.e. one now also has a way to obtain a physically meaningful objective measure for each experiment. To be more precise, setting  $\mathbf{t}_{\text{ana}}(\boldsymbol{\vartheta}, x^j) = 0$  in Eq.(6.8) gives the “energy content (EC)”,  $\Omega_{\text{EC}}^G$ . Most importantly this can be used as a way to scale the value of the objective function at the optimal solution  $\boldsymbol{\vartheta}_0$  to  $\Omega_{\text{rel}}^G = \Omega^G(\boldsymbol{\vartheta}_0)/\Omega_{\text{EC}}^G$ , which could then serve as a relative measure to compare amongst experiments [105].

### 6.1.3 Convergence Analysis of Optimisation Technique

Naturally the question arises whether this modified least–squares method converges to Eq.(6.6)<sub>1</sub>, which is examined in this section. For this purpose Eq.(6.6) is denoted as the **Weighted Least Square Objective Function**



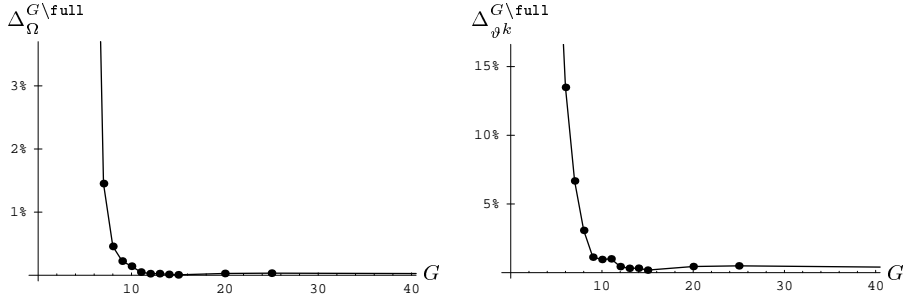


Figure 6.1: Convergence analysis of the objective function  $\Omega_{\text{rel}}^G$  and the difference vector  $\Delta_{\vartheta^k}^{G\backslash\text{full}}$  plotted against the number of Gauss points  $G$ .

(WLSOF) and Eq.(6.8) as the **G**aussian **L**east **S**quare **O**bjective **F**unction (GLSOF). Furthermore the optimal solution of the WLSOF is defined as  $\vartheta_{\text{WLSOF}}$  and the corresponding value of the objective function as  $\Omega_{\text{WLSOF}}$ .

A convergence analysis was performed by plotting (Fig.(6.1)) the number of Gauss points  $G$  used, against the relative error of the GLSOF  $\Omega^G(\vartheta_0)$  with respect to  $\Omega_{\text{WLSOF}}$  of the WLSOF of Eq.(4.6), i.e.  $\Delta_{\Omega}^{G\backslash\text{WLSOF}} = \frac{|\Omega^G(\vartheta_0) - \Omega_{\text{WLSOF}}|}{\Omega_{\text{WLSOF}}}$ . The left graph of Fig.(6.1) shows that 12 Gauss points suffice to give less than 0.01% error compared with the full model approach. The right graph of Fig.(6.1) shows that the relative error in the length of the difference vector of the parameters is below 0.4% when scaled by the absolute length of  $\vartheta_{\text{WLSOF}}$ ,  $\Delta_{\vartheta}^{G\backslash\text{WLSOF}} = \frac{|\vartheta_G - \vartheta_{\text{WLSOF}}|}{|\vartheta_{\text{WLSOF}}|} \leq 0.4\%$

Since the material parameters have different scales it is important to compare the behaviour of each parameter. Therefore the error was computed “point-wise” for each individual parameter  $\Delta_{\vartheta^k}^{G\backslash\text{WLSOF}} = \frac{|\vartheta_G^k - \vartheta_{\text{WLSOF}}^k|}{|\vartheta_{\text{WLSOF}}^k|}$ , and then the mean amongst all of them which resulted in 0.6%, which again confirms the convergence.

The computational time involved for the 12 Gauss point model was 9.6 sec, whereas the full model took 415.6 sec. It was therefore possible to reduce the time by 98% which coincides with the functional evaluation count

in Sec.(6.1.2).

#### 6.1.4 Applicability of Optimisation Technique

A novel optimization kernel has been investigated in order to improve high computational expense typically present in material parameter optimization problems. The kernel was able to reduce the computational time by 98% and maintain accuracy to within 1%.

This saving is critical for inverse material parameter estimation procedures for which the computational time could be reduced to the order of days, which otherwise would easily run into months if all available data were taken into account [54, 104]. Furthermore, this kernel also provides a sound error analysis.

It should be noted that by choosing the number of integration points and its respective integration method, one can easily incorporate any kind of nonlinear behaviour and key features of the curve. Moreover, instead of a Gaussian integration formula, as presented in Eq.(6.7), one could also use other standard integration techniques based on other integration points, e.g. Lagrange or Chebychev polynomials. The big advantage here is that we can make use of a large class of standard numerical integration techniques (e.g. [7]) with well established error analysis. This takes the guess work out of handpicking key points that *could* represent the nonlinear behaviour and therefore gives control over the smoothing error. Furthermore, error analysis of Gaussian integration shows that  $G$  integration points are the minimal number of integration points to exactly integrate polynomials up to degree  $2G - 1$ . No other choice of integration points would deliver the same result.

Furthermore, it is important to note that problems with larger data sets would lead to even further reduction, since the evaluation time is only de-

pendent on the amount of Gauss points necessary to evaluate the integral and not the number of data points. In other words, as a data set would get larger the evaluation of the integral stays more or less constant.

The data of a single force–displacement curve fulfilled two conditions. Firstly, there were numerous data points ( $>250$ ) and secondly, the mean width between two successive data points was below 1% of the total width. This enabled an approximation of the data set by a piecewise linear function. Further theoretical investigations into the precise requirements for the data set would shed more light onto the applicability of this kernel.

### 6.1.5 Determination of Initial Guesses

This section describes the strategy that was employed to find reasonable initial guesses for the estimation process exemplified for the CL.

#### 6.1.5.1 Paired Mode Optimisation

The experimental data was grouped into three pairs of modes (NS,NF), (FN,FS) and (SF,SN) according to Fig.(2.4). The result of this grouping was that only four out of the seven material parameters needed to be estimated, e.g.  $(a, b_{fn}, b_{nm}, b_{ns})$  for the pair (NS,NF). This reduction of material parameters combined with the visual aid of plotting the four relevant curves against the experimental curves ensured that these four material parameters could easily be pre-guessed. It was started with values (1,1,1,1) for these four material parameters and adjusted by hand until the four curves appeared to be in the right range. From there the Levenberg–Marquardt Sec.(4.2.3) method was employed and yielded results for this pair of modes.

The same was repeated for the other two pairs, resulting in the following

three sets of material parameters:

$$\begin{aligned}
 (a, b_{fn}, b_{nm}, b_{ns}) &= (0.427, 1.373, 2.712, 0.957) \\
 (a, b_{ff}, b_{fn}, b_{fs}) &= (0.739, 3.203, 1.115, 1.421) \\
 (a, b_{fs}, b_{ns}, b_{ss}) &= (0.102, 3.657, 2.732, 3.088)
 \end{aligned} \tag{6.9}$$

### 6.1.5.2 Averaging of Paired Estimates

These results were averaged and used as an initial guess for the full optimisation including all six simple shear modes. This strategy usually yielded very good first estimates for all four material laws from which the optimisation converged. For some rare cases this was not the case and the averaged results had to be adjusted by hand until the visual aid of plotting all twelve force–displacement curves suggested that it was more likely to happen.

It can therefore be concluded that this strategy was helpful in finding good initial guesses for the estimation process. However, it was sometimes necessary to employ adjustment by hand.

## 6.2 Results for the Homogeneous Deformation Model

The homogeneous model was solved starting from varying sets of initial values, which yielded identical results for those cases when it converged. To ensure a stable optimisation the Levenberg–Marquardt Sec.(4.2.3) method was employed. The detailed numerical results are given in Tables (6.1)–(6.6). All material parameter values are listed and for each of these entries the mean, standard deviation and coefficient of variation ( $CoV_{\gamma_i} = \frac{\sigma_{\gamma_i}}{\mu_{\gamma_i}}$ ) are presented across the experiments. The total pseudo energy content ( $\Omega_T$ ) is also listed for each experiment in the last column of Table (6.1).

Comparing the mean of the relative goodness of fit amongst all four material laws, the CL obtained the best relative goodness of fit (2.50%), whereas the coefficient of variation for the CL is 54.9%. Comparing the *AIC* confirms this result.

The condition number for all material laws show that the SFL had the highest eccentricity with  $3.2 \cdot 10^{11}$ , whereas LECL was lowest  $5.3 \cdot 10^3$ . Considering the correlation or M-optimality, the CL was best with  $2.8 \cdot 10^{-3}$ . In contrast the result for the TL was dramatically distorted in experiment 2 where the programme suggested that significant numerical errors might occur during the computation of the M-optimality due to a bad condition number. Comparing the variability in terms of the coefficients of variation for each material law over all material parameters shows that LECL has the lowest  $CoV_{Max}$  (40.0%) and SFL has the highest (-246%). The same holds for the  $\mu_{CoV}$  where LECL has the lowest (19.4%) and SFL the highest (79.0%).

It is important to note that experiments 2 and 4 yielded comparably poor results for all material laws. These can be seen in all material laws for the parameters that describe the axial response in the normal direction, which was likely to be the case since the normal modes usually had the smallest partial energy content. In particular,  $b_{nn}$  for the CL,  $a_{nn}$  for the SFL and the TL and  $k_{nn}$  for the PZL have negative values. Note that these values might not be physically sensible. A theoretical way of investigating this would be to extend the Baker-Erickson inequalities to the orthotropic case ([75], p.16 and Sec.(5.3.4)). It is important to point out that the other material parameters seemed to be well within the confidence intervals with respect to the other experiments. The effect of these negative material parameters can also be seen in the graphs in App.(B). Leaving out experiments 2 and 4 would therefore yield a much closer material parameter set for all material laws.

These poor results may be due to heterogeneous variations in the microstructural fiber orientation across the sample. Inverse finite element studies that include this aspect may shed some more light on the possible reasons.

Fig.(6.2) shows all twelve force displacement curves using the CL for experiment 3. The graphs show excellent agreement of the analytical curves (solid) with the experimental data (dotted). Similar results were obtained for all other material laws including LECL which exhibited the highest relative error, Fig.(6.3). A summary of all graphs for all experiments and all laws is given in App.(B.2).

From these results we can see that the CL had both the best fit properties and the best determinability properties of the five laws tested in simple shear, whereas the LECL exhibits the least variance while having worse fitting properties.

| CL          | $\Omega$ | $\Omega_{\text{Rel}}$ | $AIC$ | Rank | $\det(\mathbf{H})$ | $\text{cond}(\mathbf{H})$ | $\det(\tilde{\mathbf{H}})$ | $a$   | $b_{ff}$ | $b_{fn}$ | $b_{fs}$ | $b_{nn}$ | $b_{ns}$ | $b_{ss}$ | $\Omega_T$ |
|-------------|----------|-----------------------|-------|------|--------------------|---------------------------|----------------------------|-------|----------|----------|----------|----------|----------|----------|------------|
| <i>Exp1</i> | 1023     | 2.57%                 | 136.6 | 1    | 1.1E+13            | 1.6E+05                   | 3.1E-03                    | 0.383 | 40.6     | 9.19     | 10.6     | 11.3     | 7.10     | 12.3     | 39747      |
| <i>Exp2</i> | 1359     | 5.18%                 | 154.4 | 1    | 1.0E+12            | 6.5E+05                   | 2.1E-03                    | 0.182 | 31.1     | 14.8     | 13.3     | -3.23    | 13.6     | 33.9     | 26217      |
| <i>Exp3</i> | 128      | 1.59%                 | 6.55  | 1    | 1.8E+09            | 7.8E+05                   | 3.1E-03                    | 0.171 | 34.0     | 11.1     | 12.6     | 19.3     | 9.01     | 13.0     | 8021       |
| <i>Exp4</i> | 183      | 2.17%                 | 29.0  | 1    | 1.9E+09            | 3.6E+05                   | 3.5E-03                    | 0.226 | 39.6     | 9.93     | 9.23     | -0.18    | 9.21     | 10.1     | 8456       |
| <i>Exp5</i> | 558      | 1.97%                 | 98.7  | 1    | 1.1E+12            | 6.1E+05                   | 2.9E-03                    | 0.212 | 38.3     | 9.68     | 9.45     | 10.0     | 6.39     | 16.8     | 28332      |
| <i>Exp6</i> | 204      | 1.50%                 | 35.9  | 1    | 2.4E+10            | 1.8E+06                   | 2.1E-03                    | 0.154 | 71.4     | 10.7     | 10.7     | 9.56     | 8.33     | 25.7     | 13612      |
| $\mu$       | 576      | 2.50%                 |       |      | 2.1E+12            | 7.3E+05                   | 2.8E-03                    | 0.221 | 42.5     | 10.9     | 11.0     | 7.78     | 8.95     | 18.6     | 20731      |
| $\sigma$    | 511      | 1.37%                 |       |      | 4.2E+12            | 5.7E+05                   | 5.9E-04                    | 0.084 | 14.6     | 2.02     | 1.65     | 8.22     | 2.54     | 9.27     | 12746      |
| <i>CoV</i>  | 88.8%    | 54.9%                 |       |      | 197%               | 78.0%                     | 21.1%                      | 37.8% | 34.3%    | 18.6%    | 15.0%    | 106%     | 28.4%    | 49.7%    | 61.5%      |

Table 6.1: Comparison of material parameter estimates for CL across all experiments

| SFL         | $\Omega$ | $\Omega_{\text{Rel}}$ | $AIC$ | Rank | $\det(\mathbf{H})$ | $\text{cond}(\mathbf{H})$ | $\det(\tilde{\mathbf{H}})$ | $a_{ff}$ | $b_{ff}$ | $a_{fn}$ | $b_{fn}$ | $a_{fs}$ | $b_{fs}$ | $a_{nn}$ | $b_{nn}$ | $a_{ns}$ | $b_{ns}$ | $a_{ss}$ | $b_{ss}$ |
|-------------|----------|-----------------------|-------|------|--------------------|---------------------------|----------------------------|----------|----------|----------|----------|----------|----------|----------|----------|----------|----------|----------|----------|
| <i>Exp1</i> | 989      | 2.49%                 | 144.5 | 3    | 3.6E+28            | 4.7E+08                   | 1.9E-11                    | 0.693    | 54.8     | 0.0380   | 25.1     | 0.0411   | 26.3     | 0.0378   | 93.0     | 0.0408   | 20.0     | 0.0505   | 94.8     |
| <i>Exp2</i> | 1545     | 5.89%                 | 172.4 | 3    | 7.3E+27            | 1.9E+12                   | 9.5E-12                    | 0.073    | 116      | 0.0494   | 24.5     | 0.0706   | 21.6     | -0.0005  | 234.2    | 0.0843   | 19.0     | 0.2863   | 66.2     |
| <i>Exp3</i> | 127      | 1.58%                 | 16.0  | 2    | 2.9E+23            | 1.1E+09                   | 2.3E-11                    | 0.279    | 56.7     | 0.0514   | 19.6     | 0.0382   | 24.2     | 0.0761   | 70.9     | 0.0458   | 17.1     | 0.0132   | 127      |
| <i>Exp4</i> | 165      | 1.95%                 | 32.6  | 3    | 2.9E+20            | 2.2E+10                   | 1.4E-11                    | 0.257    | 70.1     | 0.0507   | 20.2     | 0.0615   | 17.8     | -51.86   | 0.0366   | 0.0709   | 16.3     | 0.0137   | 118      |
| <i>Exp5</i> | 569      | 2.01%                 | 110.0 | 3    | 1.4E+28            | 8.7E+08                   | 2.7E-11                    | 0.269    | 63.2     | 0.0328   | 22.7     | 0.0326   | 22.6     | 0.0232   | 90.3     | 0.0358   | 16.6     | 0.0376   | 86.9     |
| <i>Exp6</i> | 316      | 2.32%                 | 73.1  | 3    | 6.4E+23            | 5.0E+08                   | 2.1E-11                    | 0.254    | 102      | 0.0446   | 18.7     | 0.0465   | 19.9     | 0.0928   | 34.9     | 0.0421   | 16.4     | 0.0738   | 78.9     |
| $\mu$       | 618      | 2.71%                 |       |      | 9.6E+27            | 3.2E+11                   | 1.9E-11                    | 0.304    | 77.0     | 0.0445   | 21.8     | 0.0484   | 22.1     | -8.60    | 87.2     | 0.0533   | 17.5     | 0.0792   | 95.3     |
| $\sigma$    | 554      | 1.59%                 |       |      | 1.4E+28            | 7.8E+11                   | 6.3E-12                    | 0.205    | 25.5     | 0.0076   | 2.68     | 0.0147   | 3.01     | 21.2     | 80.3     | 0.0196   | 1.54     | 0.1040   | 23.3     |
| <i>CoV</i>  | 89.7%    | 58.8%                 |       |      | 147%               | 241%                      | 33.3%                      | 67.6%    | 33.0%    | 17.1%    | 12.3%    | 30.3%    | 13.6%    | -246%    | 92.1%    | 36.8%    | 8.75%    | 131%     | 24.4%    |

Table 6.2: Comparison of material parameter estimates for SFL across all experiments

| PZL         | $\Omega$ | $\Omega_{\text{Rel}}$ | $AIC$ | Rank | $\det(\mathbf{H})$ | $\text{cond}(\mathbf{H})$ | $\det(\tilde{\mathbf{H}})$ | $k_{ff}$ | $a_{ff}$ | $k_{fn}$ | $a_{fn}$ | $k_{fs}$ | $a_{fs}$ | $k_{nn}$ | $a_{nn}$ | $k_{ns}$ | $a_{ns}$ | $k_{ss}$ | $a_{ss}$ |
|-------------|----------|-----------------------|-------|------|--------------------|---------------------------|----------------------------|----------|----------|----------|----------|----------|----------|----------|----------|----------|----------|----------|----------|
| <i>Exp1</i> | 944      | 2.37%                 | 141.6 | 2    | 1.3E+53            | 8.3E+04                   | 1.1E-11                    | 2.14     | 0.393    | 0.0760   | 0.357    | 0.0867   | 0.351    | 0.0845   | 0.271    | 0.0728   | 0.392    | 0.109    | 0.266    |
| <i>Exp2</i> | 1529     | 5.83%                 | 171.7 | 2    | 1.9E+54            | 4.5E+04                   | 1.3E-11                    | 0.146    | 0.236    | 0.0985   | 0.361    | 0.133    | 0.380    | -0.0013  | 0.173    | 0.153    | 0.404    | 0.771    | 0.341    |
| <i>Exp3</i> | 142      | 1.95%                 | 23.3  | 4    | 3.1E+47            | 1.1E+04                   | 8.8E-12                    | 0.670    | 0.361    | 0.0859   | 0.391    | 0.0769   | 0.371    | 0.194    | 0.325    | 0.0728   | 0.416    | 0.027    | 0.224    |
| <i>Exp4</i> | 162      | 1.91%                 | 31.3  | 2    | 2.5E+24            | 1.2E+18                   | 1.5E-12                    | 0.669    | 0.328    | 0.0906   | 0.390    | 0.109    | 0.414    | -2.5E+05 | 513.8    | 0.128    | 0.434    | 0.026    | 0.231    |
| <i>Exp5</i> | 548      | 1.93%                 | 107.5 | 2    | 1.3E+52            | 8.7E+03                   | 8.1E-12                    | 0.759    | 0.354    | 0.0606   | 0.370    | 0.0596   | 0.370    | 0.0525   | 0.276    | 0.0644   | 0.431    | 0.085    | 0.282    |
| <i>Exp6</i> | 308      | 2.26%                 | 71.5  | 2    | 5.7E+45            | 1.0E+06                   | 3.1E-12                    | 0.520    | 0.253    | 0.0808   | 0.407    | 0.0854   | 0.394    | 0.414    | 0.565    | 0.0771   | 0.435    | 0.175    | 0.300    |
|             | 605      | 2.71%                 |       |      | 3.5E+53            | 1.9E+17                   | 7.7E-12                    | 0.817    | 0.321    | 0.0821   | 0.379    | 0.0917   | 0.380    | -4.2E+04 | 85.9     | 0.0947   | 0.419    | 0.199    | 0.274    |
| $\sigma$    | 542      | 1.54%                 |       |      | 7.9E+53            | 4.7E+17                   | 4.6E-12                    | 0.684    | 0.063    | 0.0131   | 0.020    | 0.0256   | 0.0218   | 1.0E+05  | 209.6    | 0.0366   | 0.018    | 0.286    | 0.044    |
| <i>CoV</i>  | 89.6%    | 56.8%                 |       |      | 225%               | 245%                      | 59.7%                      | 83.7%    | 19.6%    | 15.9%    | 5.2%     | 28.0%    | 5.8%     | -244.9%  | 244.0%   | 38.7%    | 4.27%    | 144%     | 16.0%    |

Table 6.3: Comparison of material parameter estimates for PZL across all experiments

| TL          | $\Omega$ | $\Omega_{\text{Rel}}$ | $AIC$ | Rank | $\det(\mathbf{H})$ | $\text{cond}(\mathbf{H})$ | $\det(\tilde{\mathbf{H}})$ | $a_{ff}$ | $b_{ff}$ | $a_{fn}$ | $b_{fn}$ | $a_{fs}$ | $b_{fs}$ | $a_{nn}$ | $b_{nn}$ | $a_{ns}$ | $b_{ns}$ | $a_{ss}$ | $b_{ss}$ |
|-------------|----------|-----------------------|-------|------|--------------------|---------------------------|----------------------------|----------|----------|----------|----------|----------|----------|----------|----------|----------|----------|----------|----------|
| <i>Exp1</i> | 1034     | 2.60%                 | 147.3 | 4    | 4.7E+30            | 2.9E+05                   | 7.1E-10                    | 3.17     | 15.5     | 0.1155   | 13.1     | 0.123    | 13.5     | 0.269    | 18.7     | 0.114    | 11.6     | 0.362    | 18.9     |
| <i>Exp2</i> | 1577     | 6.01%                 | 173.7 | 4    | -5.0E+27           | 2.6E+04                   | -7.6E+42                   | 0.620    | 20.4     | 0.1606   | 12.7     | 0.201    | 12.1     | -3.1E-13 | 3.1E-13  | 0.227    | 11.3     | 1.51     | 16.7     |
| <i>Exp3</i> | 133      | 1.65%                 | 18.8  | 3    | 1.1E+26            | 4.4E+05                   | 2.6E-09                    | 1.30     | 15.8     | 0.1407   | 11.5     | 0.119    | 12.7     | 0.425    | 17.1     | 0.112    | 10.9     | 0.124    | 21.0     |
| <i>Exp4</i> | 172      | 2.03%                 | 35.1  | 4    | 4.6E+22            | 8.9E+06                   | 1.1E-09                    | 1.40     | 17.1     | 0.1443   | 11.7     | 0.156    | 11.1     | -5.34    | 0.410    | 0.169    | 10.7     | 0.123    | 20.4     |
| <i>Exp5</i> | 597      | 2.11%                 | 112.9 | 4    | 5.7E+30            | 5.3E+05                   | 3.2E-09                    | 1.36     | 16.4     | 0.0994   | 12.3     | 0.100    | 12.3     | 0.162    | 18.5     | 0.085    | 10.8     | 0.249    | 18.4     |
| <i>Exp6</i> | 333      | 2.45%                 | 76.4  | 4    | 4.8E+26            | 1.4E+06                   | 4.1E-09                    | 1.90     | 19.5     | 0.1160   | 11.3     | 0.127    | 11.7     | 0.311    | 12.9     | 0.097    | 10.8     | 0.451    | 17.7     |
| $\mu$       | 641      | 2.81%                 |       |      | 1.7E+30            | 1.9E+06                   | -1.3E+42                   | 1.62     | 17.5     | 0.1294   | 12.1     | 0.138    | 12.2     | -0.695   | 11.3     | 0.134    | 11.0     | 0.471    | 18.8     |
| $\sigma$    | 567      | 1.60%                 |       |      | 2.7E+30            | 3.5E+06                   | 3.1E+42                    | 0.859    | 2.04     | 0.0228   | 0.702    | 0.0358   | 0.83     | 2.28     | 8.82     | 0.054    | 0.374    | 0.528    | 1.64     |
| <i>CoV</i>  | 88.4%    | 57.1%                 |       |      | 156%               | 178%                      | -245%                      | 52.9%    | 11.7%    | 17.6%    | 5.80%    | 26.0%    | 6.76%    | -328%    | 78.2%    | 40.1%    | 3.40%    | 112%     | 8.71%    |

Table 6.4: Comparison of material parameter estimates for TL across all experiments



| LECL        | $\Omega$ | $\Omega_{\text{Rel}}$ | $AIC$ | Rank | $\det(\mathbf{H})$ | $\text{cond}(\mathbf{H})$ | $\det(\tilde{\mathbf{H}})$ | $a_f$ | $a_n$ | $a_s$ | $n$                   |
|-------------|----------|-----------------------|-------|------|--------------------|---------------------------|----------------------------|-------|-------|-------|-----------------------|
| <i>Exp1</i> | 1807     | 4.55%                 | 166.2 | 5    | 2.8E+18            | 9.7E+03                   | 1.4E-04                    | 1.98  | 1.06  | 1.12  | $2.34 \cdot 10^{20}$  |
| <i>Exp2</i> | 2859     | 10.90%                | 194.9 | 5    | 9.1E+19            | 4.9E+03                   | 7.4E-04                    | 1.44  | 1.34  | 1.42  | $1.26 \cdot 10^{20}$  |
| <i>Exp3</i> | 283      | 3.88%                 | 50.3  | 5    | 1.0E+18            | 1.9E+03                   | 5.9E-04                    | 1.58  | 1.32  | 1.33  | $0.881 \cdot 10^{20}$ |
| <i>Exp4</i> | 530      | 6.27%                 | 89.5  | 5    | 1.5E+16            | 3.2E+03                   | 1.7E-04                    | 2.01  | 1.07  | 1.06  | $1.28 \cdot 10^{20}$  |
| <i>Exp5</i> | 1147     | 4.05%                 | 137.8 | 5    | 1.4E+18            | 2.8E+03                   | 1.1E-04                    | 2.02  | 1.07  | 1.06  | $1.21 \cdot 10^{20}$  |
| <i>Exp6</i> | 1211     | 8.90%                 | 141.2 | 5    | 2.7E+19            | 9.6E+03                   | 1.3E-04                    | 1.75  | 1.21  | 1.22  | $0.949 \cdot 10^{20}$ |
| $\mu$       | 1306     | 6.42%                 |       |      | 2.1E+19            | 5.3E+03                   | 3.1E-04                    | 1.80  | 1.18  | 1.20  | $1.32 \cdot 10^{20}$  |
| $\sigma$    | 932      | 2.89%                 |       |      | 3.6E+19            | 3.5E+03                   | 2.8E-04                    | 0.250 | 0.131 | 0.151 | $0.528 \cdot 10^{20}$ |
| <i>CoV</i>  | 71.4%    | 45.0%                 |       |      | 175%               | 65.0%                     | 89.0%                      | 13.9% | 11.1% | 12.6% | 40.0%                 |

Table 6.5: Comparison of material parameter estimates for LECL across all experiments

|      | $\Omega_{\text{Rel}}$ | $\det(\mathbf{H})$ | $\text{cond}(\mathbf{H})$ | $\det(\tilde{\mathbf{H}})$ | $CoV_{Max}$ | $\mu_{CoV}$ |
|------|-----------------------|--------------------|---------------------------|----------------------------|-------------|-------------|
| CL   | 2.50%                 | 2.1E+12            | 7.3E+05                   | 2.8E-03                    | 106%        | 41.4%       |
| SFL  | 2.71%                 | 9.6E+27            | 3.2E+11                   | 1.9E-11                    | -246%       | 79.0%       |
| PZL  | 3.35%                 | 8.2E+53            | 2.7E+08                   | 9.4E-10                    | -94.7%      | 47.0%       |
| TL   | 2.81%                 | 1.7E+30            | 1.9E+06                   | -1.3E+42                   | -328%       | 57.6%       |
| LECL | 6.42%                 | 2.1E+19            | 5.3E+03                   | -3.1E-04                   | 40.0%       | 19.4%       |

Table 6.6: Comparison of all material laws

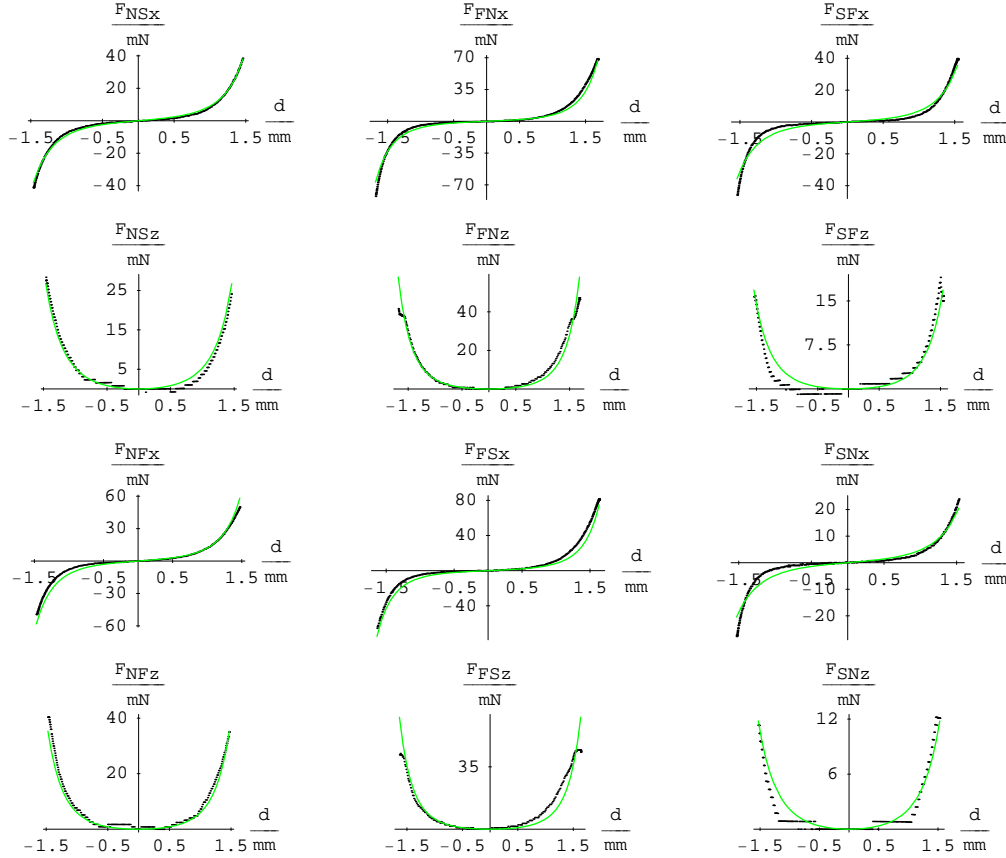


Figure 6.2: The table depicts the experimental (dotted) and fitted force–displacement curves (solid) of the Costa–law for all six modes for experiment 3. It is grouped according to Fig.2.4, whereas groups of two pictures show the x– and z–force, respectively. The y–force is left out due its negligible energy content. The overall relative error is 1.59%. Note the different scales on each graph. The abscissa shows the displacement in  $mm$ , whereas the ordinate shows the top face force in  $mN$ , where e.g.  $F_{NS_x}$  indicates the x–force for the NS–mode.

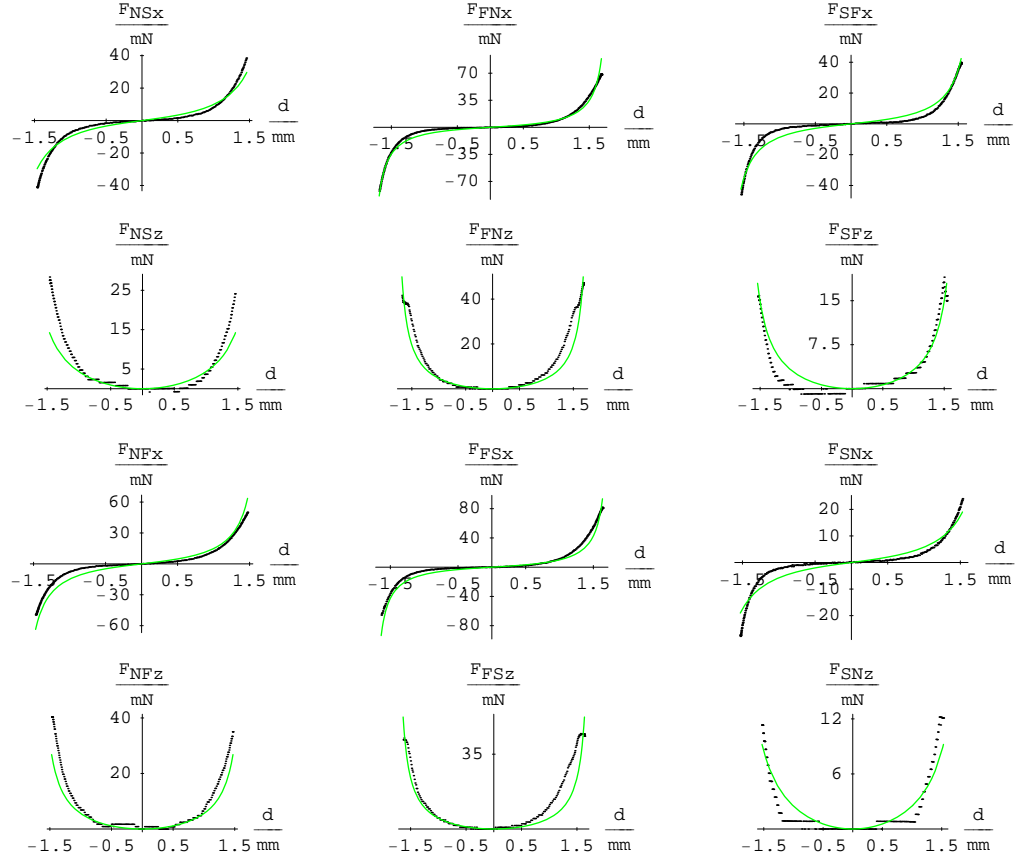


Figure 6.3: The table depicts the experimental (dotted) and fitted force–displacement curves (solid) of the Langevin Eight–Chain–law for all six modes for experiment 3. It is grouped according to Fig.2.4, whereas groups of two pictures show the x– and z–force, respectively. The y–force is left out due its negligible energy content. The overall relative error is 3.88%. Note the different scales on each graph. The abscissa shows the displacement in  $mm$ , whereas the ordinate shows the top face force in  $mN$ , where e.g.  $F_{NS_x}$  indicates the x–force for the NS–mode.

## 6.3 Discussion

The optimisation for CL, SFL and TL could be started from a wide variety of initial guesses, whereas for the PZL and LECL a more elaborate strategy had to be applied.

For the PZL and LECL the optimisation was initially setup for so-called paired-mode optimisation was carried out, where the material parameters were fitted to only two out of the six modes. The analytical equation of the PZL for the top-face force indicated that it would be advantageous to estimate for the NS & NF, FS & FN or SN & SF modes together, since in these pairs similar parameters would be “active”. For example, first estimates could be obtained for the material parameters  $a_{ff}, k_{ff}, a_{fn}, k_{fn}, a_{fs}$  and  $k_{fs}$  for PZL when fitting for the FS & FN mode only. When done for all paired modes the mean of the parameters was computed and used as the initial guess for the full optimisation. This typically proved to be a successful technique to obtain globally minimising material parameters.

A similiar technique was applied for the LECL although all material parameters were “active” in all paired modes. Nevertheless the procedure gave reliably good first estimates to find the global optimum. The optimum, however, did not provide a good fit to all twelve force-displacement curves, Fig.(6.3), see also App.(B.2).

## 6.4 Summary

This chapter develops the homogeneous model to estimate myocardial material parameters. It is clear from Sec.(6.2) that the CL is the most suitable constitutive law to model passive myocardial mechanics in homogeneous simple shear.

The major limitation of this model was that in a real experiment the edges of the cubes do not remain straight, rather they bulge and the overall deformation is non-homogeneous. The next chapter relaxes this and introduces a finite element model for inverse material parameter estimation.

# Chapter 7

## Non–Homogeneous Finite Element Deformation Model for Simple Shear

The last chapter presented the homogeneous deformation model. The very assumption of a homogeneous deformation, however, does account for bulging (Poynting) effects that are observed in simple shear experiments [95]. To allow for this, a finite element model for each of the 3 separate tissue blocks in each of the 6 sets of experiments was created to account for the non–homogeneous deformation. Each block was given a cuboid geometry with the recorded dimensions. Two shear modes were applied in each block in order to cover the 6 different shear modes for each experiment.

### 7.1 Development of FE Model

The forward solution of the finite elasticity equations of the mathematical representations of the ventricular myocardium were solved using the Galerkin

finite element method incorporating tri-linear 8-node elements. Fig.(7.1) shows a sample finite element model used in this study. The simple shear deformation was modelled as a  $xz$ -shear, i.e. the top face with a normal in the  $z$ -direction was displaced in the  $x$ -direction. The mesh incorporated the fibre and the sheet orientation of the tissue equivalent to the experimental tests by assigning a globally homogeneous fibre, sheet, normal distribution throughout the cube for each mode. A variety of mesh resolutions were analysed and the results of the convergence analysis are presented in Sec(7.1.3). The incompressibility constraint was implemented via the backend of CMISS

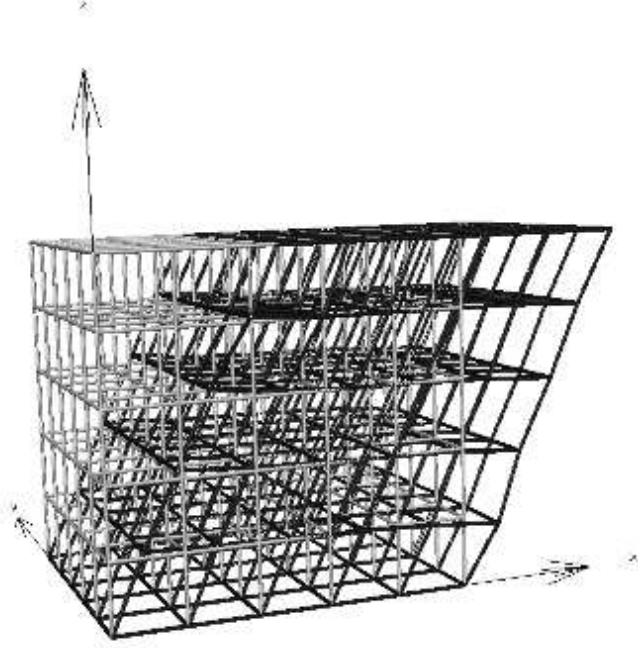


Figure 7.1: This graph shows the undeformed and deformed finite element mesh. The mesh has five elements in each direction. The boundary conditions are imposed on the bottom and top surface. The bottom surface is fixed and the top surface is displaced into the positive  $x$ -direction by half the height of the cube.

as explained in [84], see also Sec.(4.1.1.1).

### 7.1.1 Validation of constitutive laws

The constitutive relations were implemented by means of an XML based markup language called CellML [123], which is compatible with the finite element environment. All laws were validated against the same functional form of the stress–strain relationship using the mathematical computational tool Matlab [125].

### 7.1.2 Optimisation Kernel

A sequential quadratic programming (SQP) algorithm was used to optimise the material parameters for each constitutive law. SQP involves the solution of a quadratic problem at each step in the optimisation process with linear constraints for each material parameter. This has an analytic solution that can be solved directly. In addition, the algorithm performs a line search to find an improved position. The Hessian was approximated using the local gradient, as is common for sums of squares problems. The derivatives of the objective function with respect to the optimisation variables (the material parameters) was performed using one–sided differences. Initial estimates of the material parameters were taken from the homogeneous solutions [103] and tables (7.1–7.4). Constraints in terms of interval bounds on the material parameters were imposed to ensure a valid forward solution. For each optimisation iteration, a series of finite elasticity problems was solved. One for the current solution, and one for each finite difference derivative approximation. In each of these finite element solutions the solver was started from the previous mechanics solution.



### 7.1.3 Convergence Analysis

Tri-linear cubes were used with an equal number of elements in each direction from an eight element cube (222cube) (two elements in each direction) up to an 888cube (512 elements). Convergence was checked with respect to two criteria: the objective function value and  $\Delta_{MP}^{m_\alpha \setminus m_\beta}$ , see Sec.(4.4.6).

The sequence was repeated with differing starting values and limits, until a minimum least-squares error between the predicted and observed reaction forces was obtained. The initial estimates from the homogeneous study proved to be very close to the optimum for almost all cases.

The detailed tables of the convergence analysis are shown in App.(C.2) and suggest that a 555cube was sufficient to capture the main criteria of the deformation.

The LECL did not converge for any of the experiments when starting from the homogeneous values. Even considerable tests from varying initial parameters did not result in a successful optimisation. The LECL was therefore not studied using the FEM model.

## 7.2 Results for the Non-Homogeneous Finite Element Model during Simple Shear

The detailed numerical results for all material laws are given in Tables (7.1–7.4). All material parameter values are listed and for each of these entries the mean, standard deviation, and coefficient of variation ( $\text{CoV} = \frac{\sigma}{\mu}$ ) across the experiments are presented. We also list the total pseudo energy content ( $\Omega_T$ ) for each experiment is also listed in the last column of Table (7.1).

| CL          | $\Omega$ | $\Omega_{\text{Rel}}$ | $AIC$ | Rank | $\det(\mathbf{H})$ | $\text{cond}(\mathbf{H})$ | $\det(\hat{\mathbf{H}})$ | $a$   | $b_{ff}$ | $b_{fn}$ | $b_{fs}$ | $b_{nn}$ | $b_{ns}$ | $b_{ss}$ | $\Omega_T$ |
|-------------|----------|-----------------------|-------|------|--------------------|---------------------------|--------------------------|-------|----------|----------|----------|----------|----------|----------|------------|
| <i>Exp1</i> | 982.4    | 2.5%                  | 134.1 | 3    | 2.2E+22            | 4.1E+08                   | 1.4E-14                  | 0.41  | 36.3     | 10.7     | 12.7     | 12.3     | 7.96     | 11.4     | 39748      |
| <i>Exp2</i> | 1798     | 6.9%                  | 171.9 | 3    | -2.4E+18           | 5.4E+08                   | -1.6E-09                 | 0.33  | 20.7     | 14.4     | 11.3     | 0.00     | 17.0     | 33.8     | 26217      |
| <i>Exp3</i> | 123.9    | 1.5%                  | 4.6   | 4    | 2.6E+20            | 2.1E+09                   | 4.0E-11                  | 0.19  | 30.5     | 12.1     | 13.9     | 17.8     | 9.86     | 13.6     | 8021       |
| <i>Exp4</i> | 222.8    | 2.6%                  | 41.3  | 3    | 6.6E+18            | 3.4E+08                   | 2.3E-11                  | 0.23  | 38.0     | 11.3     | 11.5     | 4.43     | 11.2     | 9.60     | 8457       |
| <i>Exp5</i> | 432.4    | 1.5%                  | 82.8  | 4    | -1.3E+22           | 1.1E+10                   | -2.0E-12                 | 0.20  | 35.7     | 11.4     | 10.5     | 13.0     | 8.35     | 18.9     | 28332      |
| <i>Exp6</i> | 175.2    | 1.3%                  | 26.3  | 1    | -1.4E+21           | 1.2E+09                   | -2.4E-12                 | 0.18  | 62.3     | 12.0     | 12.3     | 7.06     | 10.9     | 26.3     | 13613      |
| $\mu$       | 622.4    | 2.7%                  | 76.8  |      | 1.2E+21            | 2.6E+09                   | -2.5E-10                 | 0.26  | 37.2     | 12.0     | 12.0     | 9.11     | 10.9     | 18.9     | 20731      |
| $\sigma$    | 656.5    | 2.1%                  | 65.4  |      | 1.1E+22            | 4.3E+09                   | 6.4E-10                  | 0.091 | 13.8     | 1.30     | 1.21     | 6.49     | 3.28     | 9.46     | 12746      |
| <i>CoV</i>  | 105.5%   | 77.2%                 | 85.1% |      | 904.8%             | 161.1%                    | -256.6%                  | 35.8% | 37.0%    | 10.9%    | 10.1%    | 71.2%    | 30.1%    | 50.0%    | 61.5%      |

Table 7.1: Comparison of material parameter estimates for CL across all experiments

| SFL         | $\Omega$ | $\Omega_{\text{Rel}}$ | $AIC$ | Rank | $\det(\mathbf{H})$ | $\text{cond}(\mathbf{H})$ | $\det(\hat{\mathbf{H}})$ | $a_{ff}$ | $b_{ff}$ | $a_{fn}$ | $b_{fn}$ | $a_{fs}$ | $b_{fs}$ | $a_{nn}$ | $b_{nn}$ | $a_{ns}$ | $b_{ns}$ | $a_{ss}$ | $b_{ss}$ |
|-------------|----------|-----------------------|-------|------|--------------------|---------------------------|--------------------------|----------|----------|----------|----------|----------|----------|----------|----------|----------|----------|----------|----------|
| <i>Exp1</i> | 742.4    | 1.9%                  | 126.6 | 1    | 4.2E+61            | 4.0E+07                   | 2.8E-35                  | 0.85     | 42.2     | 0.024    | 58.4     | 0.014    | 75.2     | 0.0087   | 157.9    | 0.040    | 35.8     | 1.02     | 11.7     |
| <i>Exp2</i> | 1499     | 5.7%                  | 170.5 | 2    | 2.1E+56            | 1.2E+11                   | 4.3E-20                  | 0.12     | 66.6     | 0.012    | 75.7     | 0.059    | 45.4     | 2.95     | 0.38     | 0.082    | 52.0     | 0.78     | 34.2     |
| <i>Exp3</i> | 94.2     | 1.2%                  | -2.5  | 1    | 5.9E+54            | 2.4E+12                   | 4.7E-10                  | 0.28     | 50.3     | 0.017    | 51.6     | 0.022    | 55.0     | 0.18     | 36.4     | 0.015    | 46.1     | 0.045    | 56.8     |
| <i>Exp4</i> | 188.7    | 2.2%                  | 40.9  | 2    | 1.5E+47            | 3.3E+13                   | 6.0E+01                  | 0.22     | 73.7     | 0.051    | 37.9     | 0.025    | 48.8     | 0.00     | 100.0    | 0.058    | 33.0     | 0.011    | 89.1     |
| <i>Exp5</i> | 301.2    | 1.1%                  | 70.2  | 2    | 9.7E+61            | 9.0E+12                   | 6.6E-15                  | 0.27     | 57.6     | 0.016    | 54.1     | 0.018    | 47.5     | 0.10     | 39.6     | 0.0066   | 57.0     | 0.017    | 123.2    |
| <i>Exp6</i> | 175.7    | 1.3%                  | 36.4  | 2    | 5.9E+57            | 7.2E+10                   | 2.5E-22                  | 0.25     | 98.4     | 0.0061   | 70.3     | 0.021    | 51.3     | 1.49     | 2.61     | 0.0090   | 59.3     | 0.15     | 53.8     |
| $\mu$       | 500.2    | 2.2%                  | 73.7  |      | 2.3E+61            | 7.4E+12                   | 9.9E+00                  | 0.33     | 64.8     | 0.021    | 58.0     | 0.026    | 53.9     | 0.79     | 56.1     | 0.035    | 47.2     | 0.34     | 61.5     |
| $\sigma$    | 540.9    | 1.8%                  | 64.0  |      | 4.0E+61            | 1.3E+13                   | 2.4E+01                  | 0.26     | 19.9     | 0.016    | 13.6     | 0.016    | 11.0     | 1.20     | 61.5     | 0.030    | 10.9     | 0.44     | 39.7     |
| <i>CoV</i>  | 108.1%   | 79.5%                 | 86.8% |      | 171.8%             | 174.6%                    | 244.9%                   | 78.0%    | 30.7%    | 76.5%    | 23.5%    | 62.0%    | 20.4%    | 152.6%   | 109.6%   | 87.2%    | 23.2%    | 131.9%   | 64.6%    |

Table 7.2: Comparison of material parameter estimates for SFL across all experiments

| PZL         | $\Omega$ | $\Omega_{\text{Rel}}$ | $AIC$ | Rank | $\det(\mathbf{H})$ | $\text{cond}(\mathbf{H})$ | $\det(\hat{\mathbf{H}})$ | $k_{ff}$ | $a_{ff}$ | $k_{fn}$ | $a_{fn}$ | $k_{fs}$ | $a_{fs}$ | $k_{nn}$ | $a_{nn}$ | $k_{ns}$ | $a_{ns}$ | $k_{ss}$ | $a_{ss}$ |
|-------------|----------|-----------------------|-------|------|--------------------|---------------------------|--------------------------|----------|----------|----------|----------|----------|----------|----------|----------|----------|----------|----------|----------|
| <i>Exp1</i> | 804.4    | 2.0%                  | 131.6 | 2    | -3.E+107           | 9.5E+10                   | -5.E-61                  | 2.46     | 0.43     | 0.049    | 0.34     | 0.038    | 0.31     | 0.050    | 0.24     | 0.032    | 0.37     | 10.9     | 1.37     |
| <i>Exp2</i> | 1698     | 6.5%                  | 178.3 | 4    | 6.E+101            | 5.2E+06                   | 1.E-86                   | 0.098    | 0.24     | 0.040    | 0.32     | 0.189    | 0.43     | 0.000    | 0.58     | 0.51     | 0.49     | 0.80     | 0.34     |
| <i>Exp3</i> | 96.8     | 1.2%                  | -0.8  | 2    | 2.E+113            | 9.5E+04                   | 6.E-97                   | 0.79     | 0.39     | 0.037    | 0.36     | 0.039    | 0.34     | 0.35     | 0.39     | 0.031    | 0.38     | 0.16     | 0.36     |
| <i>Exp4</i> | 183.2    | 2.2%                  | 39.0  | 1    | 1.E+117            | 1.2E+07                   | 3.E-107                  | 0.59     | 0.32     | 0.080    | 0.40     | 0.040    | 0.35     | 0.000    | 0.24     | 0.106    | 0.44     | 0.031    | 0.28     |
| <i>Exp5</i> | 283.3    | 1.0%                  | 66.3  | 1    | 7.E+123            | 2.3E+06                   | 3.E-109                  | 0.83     | 0.38     | 0.029    | 0.34     | 0.031    | 0.36     | 0.30     | 0.46     | 0.011    | 0.33     | 0.037    | 0.23     |
| <i>Exp6</i> | 178.9    | 1.3%                  | 37.6  | 3    | 7.E+115            | 1.4E+07                   | 2.E-91                   | 0.55     | 0.26     | 0.015    | 0.31     | 0.037    | 0.35     | 0.34     | 0.60     | 0.021    | 0.34     | 0.43     | 0.38     |
| $\mu$       | 540.8    | 2.4%                  | 75.3  |      | 1.E+123            | 1.6E+10                   | -9.E-62                  | 0.89     | 0.34     | 0.04     | 0.35     | 0.06     | 0.36     | 0.17     | 0.42     | 0.12     | 0.39     | 2.05     | 0.49     |
| $\sigma$    | 621.4    | 2.1%                  | 66.9  |      | 3.E+123            | 3.9E+10                   | 2.E-61                   | 0.81     | 0.08     | 0.02     | 0.03     | 0.06     | 0.04     | 0.17     | 0.16     | 0.20     | 0.06     | 4.32     | 0.43     |
| <i>CoV</i>  | 114.9%   | 87.4%                 | 88.8% |      | 244.9%             | 244.8%                    | -244.9%                  | 91.8%    | 22.7%    | 52.7%    | 8.7%     | 100.1%   | 10.7%    | 100.0%   | 38.1%    | 164.5%   | 15.9%    | 210.7%   | 87.8%    |

Table 7.3: Comparison of material parameter estimates for PZL across all experiments

| TL          | $\Omega$ | $\Omega_{\text{Rel}}$ | $AIC$ | Rank | $\det(\mathbf{H})$ | $\text{cond}(\mathbf{H})$ | $\det(\hat{\mathbf{H}})$ | $a_{ff}$ | $b_{ff}$ | $a_{fn}$ | $b_{fn}$ | $a_{fs}$ | $b_{fs}$ | $a_{nn}$ | $b_{nn}$ | $a_{ns}$ | $b_{ns}$ | $a_{ss}$ | $b_{ss}$ |
|-------------|----------|-----------------------|-------|------|--------------------|---------------------------|--------------------------|----------|----------|----------|----------|----------|----------|----------|----------|----------|----------|----------|----------|
| <i>Exp1</i> | 1034     | 2.6%                  | 147.3 | 4    | 1.4E+62            | 1.2E+08                   | 2.4E-36                  | 3.32     | 14.6     | 0.16     | 13.7     | 0.11     | 14.8     | 0.31     | 18.7     | 0.092    | 12.9     | 1.08     | 11.2     |
| <i>Exp2</i> | 1470     | 5.6%                  | 169.3 | 1    | -8.4E+68           | 1.3E+11                   | -1.3E-40                 | 0.53     | 18.1     | 0.043    | 17.5     | 0.21     | 14.1     | 0.00     | 18.1     | 0.49     | 13.4     | 3.62     | 9.91     |
| <i>Exp3</i> | 102.6    | 1.3%                  | 2.8   | 3    | 1.9E+65            | 1.1E+09                   | 2.4E-34                  | 1.25     | 14.6     | 0.11     | 13.1     | 0.15     | 13.5     | 0.71     | 12.3     | 0.078    | 12.7     | 0.23     | 14.8     |
| <i>Exp4</i> | 193.8    | 2.3%                  | 42.6  | 4    | -2.8E+65           | 2.1E+09                   | -1.0E-30                 | 1.26     | 17.4     | 0.26     | 11.4     | 0.15     | 12.8     | 0.0087   | 19.2     | 0.23     | 11.2     | 0.11     | 16.9     |
| <i>Exp5</i> | 323.9    | 1.1%                  | 74.7  | 3    | 5.6E+69            | 1.1E+09                   | 8.6E-38                  | 1.30     | 15.7     | 0.10     | 13.5     | 0.11     | 12.7     | 0.36     | 13.4     | 0.049    | 13.6     | 0.16     | 20.7     |
| <i>Exp6</i> | 250.2    | 1.8%                  | 58.6  | 4    | 8.9E+60            | 1.1E+08                   | 3.1E-34                  | 1.84     | 19.7     | 0.039    | 14.6     | 0.17     | 12.0     | 0.69     | 6.44     | 0.089    | 12.7     | 0.62     | 17.4     |
| $\mu$       | 562.5    | 2.5%                  | 82.5  |      | 8.0E+68            | 2.2E+10                   | -1.7E-31                 | 1.58     | 16.7     | 0.12     | 14.0     | 0.15     | 13.3     | 0.35     | 14.7     | 0.17     | 12.7     | 0.97     | 15.2     |
| $\sigma$    | 556.5    | 1.6%                  | 63.7  |      | 2.4E+69            | 5.1E+10                   | 4.3E-31                  | 0.95     | 2.06     | 0.084    | 2.00     | 0.038    | 1.03     | 0.31     | 4.96     | 0.17     | 0.84     | 1.35     | 4.05     |
| <i>CoV</i>  | 98.9%    | 66.7%                 | 77.2% |      | 299.2%             | 234.5%                    | -245.1%                  | 59.9%    | 12.4%    | 70.5%    | 14.3%    | 25.2%    | 7.7%     | 90.0%    | 33.8%    | 98.5%    | 6.6%     | 138.9%   | 26.7%    |

Table 7.4: Comparison of material parameter estimates for TL across all experiments

Before making any comparison, it is important to note that experiments 2 and 4 yielded comparably poor results for all material laws. Leaving out these experiments would therefore yield a much closer material parameter set for all material laws. These poor results may be due to heterogeneous variations in the micro-structural fiber orientation across the sample. Inverse finite element studies that include this aspect may shed some more light on the possible reasons. However, the Dokos experimental studies did not measure this so assumptions of straight fibres were necessary.

Comparing the mean of the relative goodness of fit of the finite element study amongst all four material laws, the SFL obtained the best relative goodness of fit (2.2%), whereas the coefficient of variation of the objective function was lowest for the TL (66.7%). The *AIC* confirms the result for the SFL.

Comparing the CoV of material parameters for all laws we find that the CL has the lowest (71.2%) for the parameter  $b_{nn}$  whereas PZL has the highest (210%) for  $a_{nn}$ .

The CL converged without any complications and took the shortest time ( $\sim 8$ hrs) on an IBM 1.9GHz Power 5 Processor when starting from the homogeneous values. Varying the initial starting point of  $\boldsymbol{\vartheta}$  had no effect on the final outcome and we could therefore conclude that the CL was very stable for the estimation process. The SFL was rather unstable and needed considerable additional strategies to converge. It was necessary to start at the 222cube while fixing the axial parameters and only optimising for the shear parameters. Subsequently, the shear parameters were fixed and the model was optimised by varying the axial parameters. Then a converged solution for the 222cube was obtained when optimising for all material parameters. Furthermore it was necessary to do that for all intermediate meshes as well to

finally obtain a fully converged 555cube. A similar procedure was necessary for the PZL. The TL also converged after choosing the homogeneous values as initial values. However, the step size in the parameter space needed to be decreased for a stable optimisation which resulted in an optimisation time of between 4–8 days.

The D-optimality for all laws reflects the stability of the optimisation process. The higher the numbers, the worse the convergence. The condition number for all material laws showed that the SFL had the highest eccentricity with  $7.4 \cdot 10^{12}$  whereas CL was lowest  $2.6 \cdot 10^9$ . The M-optimality showed that the CL had the lowest material parameter correlation whereas the PZL had the highest.

One of the advantages of the homogeneous model were thought to be that it gives good first estimates for more realistic finite element studies. It is therefore also useful to comment on the performance of the material laws with respect to the convergence behaviour and the computational time involved when compared to the homogeneous model. This is done in Sec.(7.4).

Guccione and coworkers [39] published a transversely isotropic material which we also fitted to all six experiments. It exhibited very poor behaviour since it was only able to fit three out of the six modes, those with the highest partial energy content. It can therefore be concluded that a transversely isotropic material is not suitable to model the passive myocardial behaviour in simple shear.

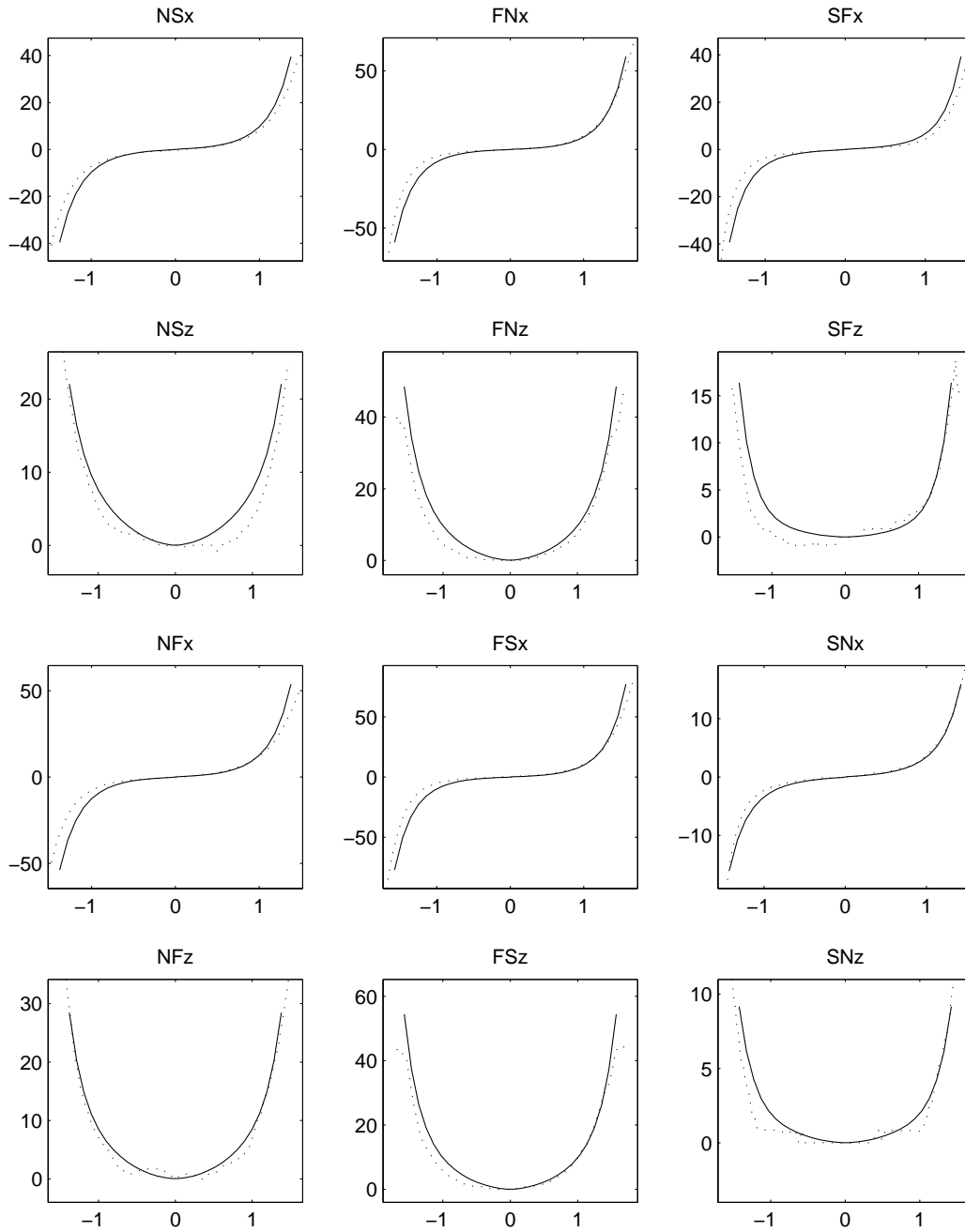


Figure 7.2: The graphs depict the experimental (dotted) and fitted force–displacement curves (solid) of the SFL for all six modes for experiment 3. They are grouped according to Fig.2.4, where groups of two pictures show the x– and z–force, respectively. The overall error is 1.2%. Note the different scales on each graph. The abscissa shows the displacement in  $mm$ , whereas the ordinate shows the top face force in  $mN$ , where e.g.  $NS_x$  indicates the x–force for the NS–mode.

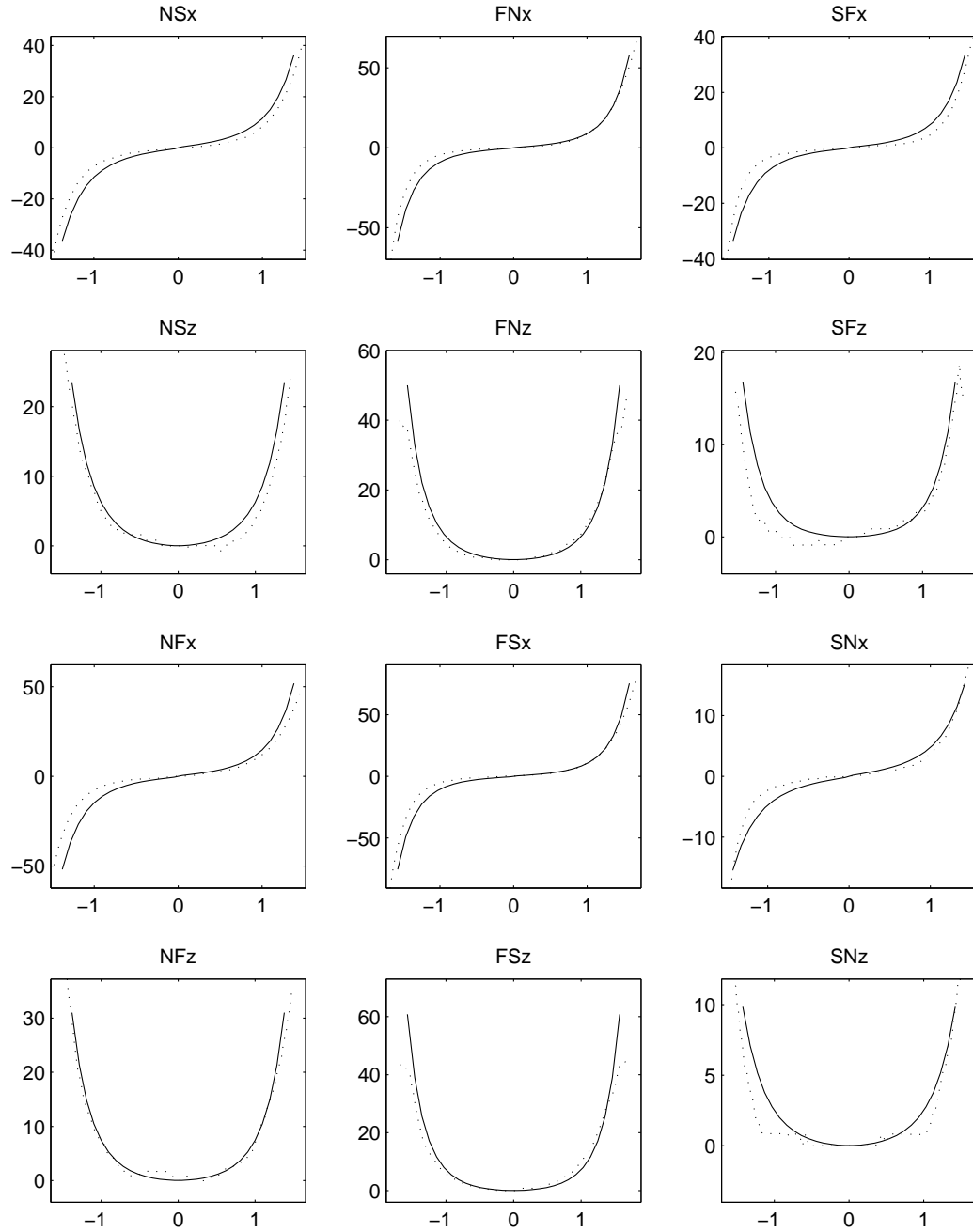


Figure 7.3: The graphs depict the experimental (dotted) and fitted force-displacement curves (solid) of the CL for all six modes for experiment 3. They are grouped according to Fig. 2.4, where groups of two pictures show the x- and z-force, respectively. The overall error is 1.5%. Note the different scales on each graph. The abscissa shows the displacement in  $mm$ , whereas the ordinate shows the top face force in  $mN$ , where e.g.  $NS_x$  indicates the x-force for the NS-mode.

## 7.3 Discussion

The results show that the CL performed best for both homogeneous simulations and inverse finite element material parameter estimations. This is clear from the fact that although the goodness of fit and AIC of the SFL is slightly better than that for the CL in the FEM study (see Figs.(7.2 & 7.3)), the CL has by far the highest material parameter consistency, see Fig.(7.4) and the lowest computational time involved when compared to the other laws. For the graphs of the other laws and experiments the reader is referred to App.(C.3).

There are some comments to be made about the CL. It exhibits a theoretical cross-coupling of strain terms for each stress component, whereas that is not the case for the other three laws. In the homogeneous simulation (which has a sparsely populated strain tensor), this cross-coupling did not occur in the analytic expression of the top face force. Therefore caution was paid to the fact that this might differentiate the CL from the other three laws when using FEM inverse parameter estimations, especially with more complex deformation modes. The results of the finite element study indicate that the cross-coupling does not play a major role for the finite element simulations. Smaill & Hunter [107] found that there was little mechanical coupling between the fiber and sheet direction in midmyocardial specimen in biaxial tests. It therefore remains an open question whether results for the constitutive relations of inverse material parameter estimation procedures would differ in biaxial extension tests.



## 7.4 Comparison of FE and Homogeneous Model

When we compare the homogeneous study with the FEM study we find that the difference in information by adding the finite element study in terms of the mean of the goodness of fit criterion  $\Delta_{\Omega}^{\text{homo}\backslash\text{FEM}}$  was lowest for the CL (8.19%) and highest for the SFL (21.7%). The same holds for the mean increase in the  $\Delta_{AIC}^{\text{homo}\backslash\text{FEM}}$ , where CL has the lowest value (0.05%) and the SFL the highest (24.1%). These numbers are obtained by comparison of the tables listing the results of the homogeneous model in [103].

When comparing the individual  $\Delta_{\gamma_i}^{\text{homo}\backslash\text{FEM}}$  the SFL, PZL and TL have one outlier in the order of  $10^5$  and higher for  $a_{nn}, k_{nn}, a_{nn}$  for the fourth experiment, respectively. The CL also has the highest  $\Delta_{\gamma_i}^{\text{homo}\backslash\text{FEM}}$  for  $b_{nn}$  for the fourth experiment (104.1%). However, the confidence intervals for both studies were very similar. They are presented in Fig.(7.4).

The results of the other laws are pointing towards the poorer material parameter estimation capability of the homogeneous simulations, since it usually reached large negative values for experiments 2 and 4, as well as towards the fact that the optimisation package of the finite element environment reached the lower bound imposed on the material parameter. (The lower bound was zero for all material parameters of the CL, SFL and TL as well as for  $k_{\alpha\beta}$  for the PZL. The lower bound for the parameters  $k_{\alpha\beta}$  of the PZL was chosen to be 0.125, since this was the lowest entry of the Green-strain tensor for the homogeneous case.) Furthermore this points towards the fact that the parameters of the normal direction are those being most difficult to estimate due to the lowest partial energy content of the NF-mode (4.0%) vs (44.9%) in the FN-mode.

The comparison of  $\Delta_{\Omega_{rel}}^{\text{homo}\backslash\text{FEM}}$  and  $\Delta_{AIC}^{\text{homo}\backslash\text{FEM}}$  may be interpreted the following way. Firstly it means that the SFL is ideally used in the finite element environment where it performs best. The CL, however, seems to perform almost identically in the homogeneous simulations and in the finite element simulations, while performing almost as well as the SFL in terms of the goodness of fit criteria.

When comparing the material parameter consistency by looking at the mean of all  $\Delta_{\gamma_i}^{\text{homo}\backslash\text{FEM}}$  then CL performs best with 15.3%. If one disregards the second and fourth experiment, then  $\Delta_{\gamma_i}^{\text{homo}\backslash\text{FEM}}$  for the TL (27.1%) and it therefore also performs well. The PZL and SFL, however, have values of 67.7% and 138.0%, respectively.

## 7.5 Summary

This chapter introduced the finite element model to estimate myocardial material parameters. It is clear from Sec.(7.2) that the CL is the most suitable constitutive law to model passive myocardial mechanics in non-homogeneous simple shear.

The experimental protocol in this study consisted of six simple shear modes. As a consequence the maximal axial entries in the Green-strain tensor were limited to 0.125 compared to 0.25 for the shear entries. To obtain similar magnitudes for both axial and shear entries, the experimental protocol was extended to include uniaxial extension modes with axial entries of 0.22. This promised to result in more realistic estimates for the material parameters.

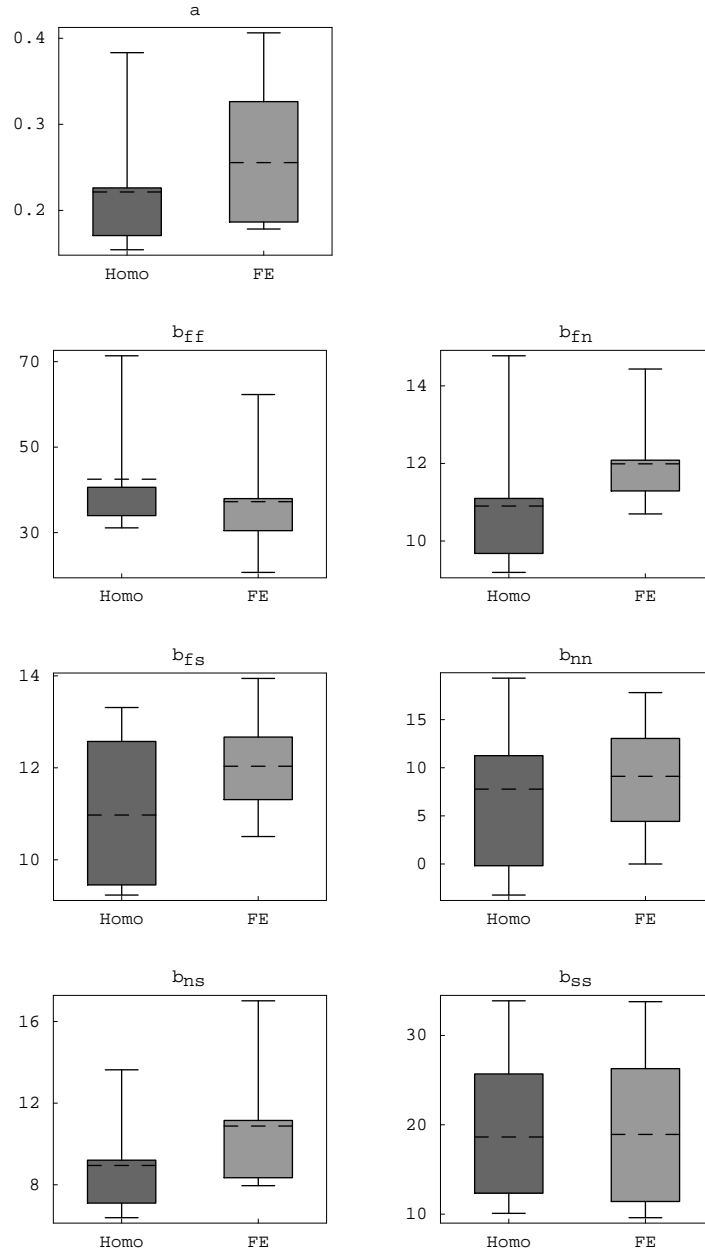


Figure 7.4: Modified box whisker plots of all material parameters of the CL. Each graph compares the homogeneous data set (left, dark grey) and the FE data set (right, light grey). The dashed line indicates the mean of the material parameter. The box encapsulates all values between the lower and upper quartile and the “whiskers” indicate the lowest and highest value. The graphs indicate the good agreement between homogeneous and finite element values.

## Chapter 8

# Non–Homogeneous Finite Element Deformation Model for Simple Shear & Uniaxial Extension

The previous chapter introduced the finite element model for the estimation of material parameters of all material laws. The estimation procedure, however, was limited to the set of simple shear experiments.

An extension of the experimental protocol analysing from six simple shear modes to six shear modes plus three uniaxial extension modes along the three preferred directions of material response was presented in Sec.(2.3.6). The additional uniaxial extension modes were included to provide extension data uncoupled from shear, since simple shear modes result in both shear and axial extension. The axial extension modes contributed to the objective function with axial strain values (0.22) very close to the shear strain values of the shear modes (0.25), rather than one half of the shear strain as in simple

shear (0.125).

Although data from only one animal was obtained with all axial and all shear modes, the result from the FE model may indicate whether data from axial modes effect the resulting material parameters.

## 8.1 Development of FE Model

To estimate material parameters for all these modes the same model as in Chap.(7) was used. However, the boundary conditions for the three uniaxial extension were adapted and the modified objective functions for these modes were added to Eq.(6.8).

Fig.(8.1) depicts the deformed model under a finite element mesh for uniaxial extension. Material parameters obtained from the homogeneous model as described in Chap.(6) were chosen as initial values for the optimisation process. This is described in detail in the following sections.

## 8.2 Estimation Strategy

This section describes the elaborate estimation strategy that was necessary for obtaining an optimal set of material parameters. This strategy was applied for all four material laws (CL, SFL, PZL, TL). It is explained in detail for the CL. The same strategy was applied for all other laws and the results for all material laws are presented in Sec.(8.3).

Initially it was attempted to start off with estimating the material parameters (MP's) with the homogeneous model and then fit all material parameters to all fifteen curves (6 shear modes  $\times$   $x, z$ -forces & 3 uniaxial extension modes,  $z$ -forces) within the finite element environment. This, however, did

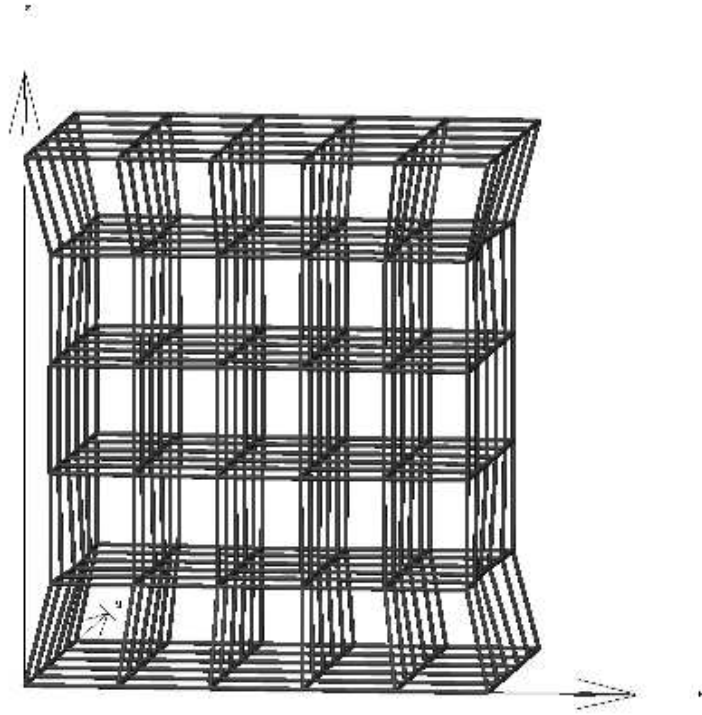


Figure 8.1: The deformed finite element mesh under uniaxial extension. The mesh has five elements in each direction. The boundary conditions are imposed on the bottom and top surface. The bottom surface was fixed and the top surface was displaced in the positive  $z$ -directions 20% of the height of the cube.

not prove to be successful. In particular the three uniaxial extension modes were exhibiting high errors.

It was found that the following estimation strategy was successful in finding good material parameter fits for the CL, SFL and TL, whereas it was not possible to obtain a converged solution for the PZL in the last optimisation step.

### 8.2.1 All Parameters to Shear Modes

For the sake of clarity, a notation is introduced to indicate three factors involved in each step.

$$\text{MP}_{\text{MP}}^{\text{start} \setminus \text{end}}, \quad (8.1)$$

so that

$$\text{MP}_{\text{ALL}}^{\text{HOMO} \setminus \text{SHEAR}}, \quad (8.2)$$

indicates that in the initial step all (ALL) MP's were fitted to all shear (SHEAR) modes starting from the homogeneous (HOMO) set of MP's.

After each estimation step the residual for the shear modes and for the axial modes was computed as well as the total residual. The complete tables for all material laws are presented in Sec.(8.3).

| CL  | Modes | EC     | $\Omega$ | $\Omega_{rel}$ |
|---|-------|--------|----------|----------------|
| $\text{MP}_{\text{ALL}}^{\text{HOMO} \setminus \text{SHEAR}}$ | Shear | 4378.7 | 101.54   | 2.32%          |
|   | Axial | 2494.3 | 4338.87  | 173.95%        |
|   | Full  | 6872.9 | 4440.41  | 64.61%         |

Table 8.1: Results of the first material parameter estimation step. The relative residual  $\Omega_{rel}$  of the axial modes is 173.95% indicating that the axial parameters are overestimated, or that the estimation space is not properly constraining the axial parameters.

It is clear from Tab.(8.1) that the estimation yields very good results for the shear modes with a relative error of 2.32% indicating that the result lies in the range of those from the previous chapter. The second row, however, with an relative error of 173.95% indicates that the the axial parameters are clearly overestimated in this step (see also (Fig.(8.3)(a)) or in other words that the shear modes are not properly constraining the axial parameters.

The total relative error for all fifteen modes of 64.61% was not an acceptable error and further estimations had to be undertaken.

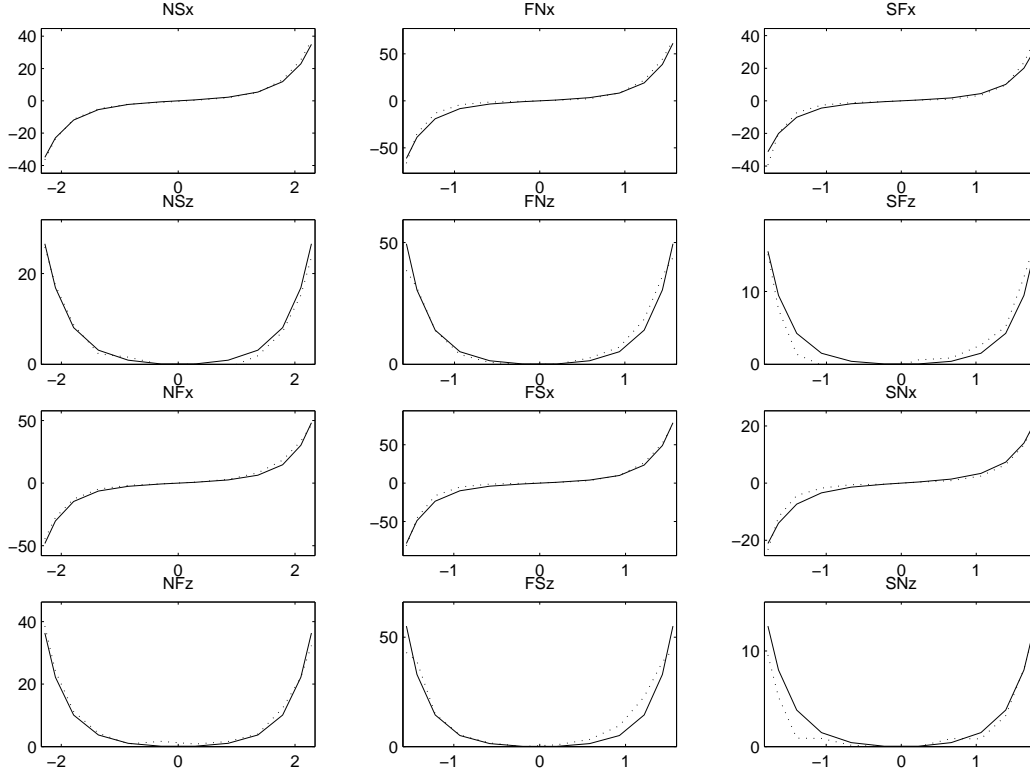


Figure 8.2: These graphs show the force–displacement curves for the shear modes after the first optimisation step. The relative error is 2.32%. Experimental data: (*dotted*); Model data: (*solid*).

### 8.2.2 Axial Parameters to Uniaxial Extension Modes

The next step used the MP's from the previous section and fitted just the axial parameters to the axial modes whereas the shear parameters remained fixed. Using the notation above, this is denoted:

$$\text{MP}_{\text{AXIAL}}^{\text{SHEAR} \setminus \text{AXIAL}}. \quad (8.3)$$



As can be seen from the axial residual of 173.95% after the first step in Tab.(8.1) and also from Fig.(8.3)(a), the axial model force was substantially different from the experimental measurement. To ensure a stable optimisation, the axial parameters were adjusted by hand to an extent that eyeballing the data would ensure a noticeable similarity between model and experimental data. After this adjustment by hand the optimisation was stable and yielded the results as listed in Table(8.2), see also Fig.(8.4).

| CL   | Modes | EC     | $\Omega$ | $\Omega_{rel}$ |
|--|-------|--------|----------|----------------|
| MP <sup>SHEAR\AXIAL</sup> <sub>AXIAL</sub> | Shear | 4378.7 | 667.56   | 15.25%         |
|  | Axial | 2494.3 | 69.02    | 2.77%          |
|  | Full  | 6872.9 | 736.59   | 10.72%         |

Table 8.2: Results of the second material parameter estimation step. The relative residual  $\Omega_{rel}$  of the shear modes is 15.25% indicating that the estimation step yielded axial parameters which did not optimally fit the shear modes. The axial relative error 2.77%, however, indicates that the new set of MP's fits the axial modes very well. Additionally the total relative error was reduced down to 10.72%.

Results of the first material parameter estimation step show that the relative residual  $\Omega_{rel}$  of the shear modes is 15.25%, indicating that the estimation step yielded axial parameters which did not optimally fit the shear modes. The axial relative error 2.77%, however, indicates that the new set of MP's fits the axial modes very well. Interestingly, the total relative error could be reduced down to 10.72% from 64.61% of the previous step.

### 8.2.3 All Parameters to All Modes

The last step used the MP's from Sec.(8.2.2) and fitted all parameters to the full set of all fifteen modes. This was denoted:

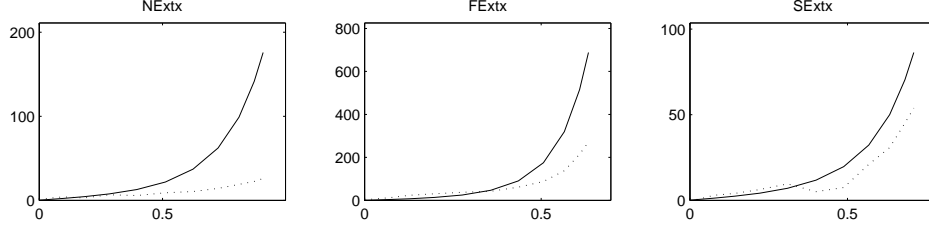
$$\text{MP}_{\text{ALL}}^{\text{AXIAL} \setminus \text{FULL}}. \quad (8.4)$$

This estimation step resulted in the set of residuals as listed in Table(8.3):

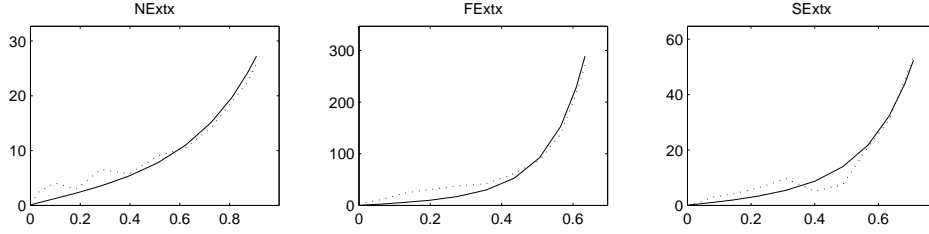
| CL  | Modes | EC     | $\Omega$ | $\Omega_{rel}$ |
|---|-------|--------|----------|----------------|
| $\text{MP}_{\text{ALL}}^{\text{AXIAL} \setminus \text{FULL}}$ | Shear | 4378.7 | 209.77   | 4.79%          |
|   | Axial | 2494.3 | 93.68    | 3.76%          |
|   | Full  | 6872.9 | 303.45   | 4.42%          |

Table 8.3: Results of the last material parameter estimation step. The relative residual  $\Omega_{rel}$  of the shear modes is 4.79% indicating that the estimation step yielded MP's fit that the shear modes considerably better than the previous step. The axial relative error 3.76% indicates that the new set of MP's still fit the axial modes very well. Additionally the total relative error was reduced down to 4.42%.

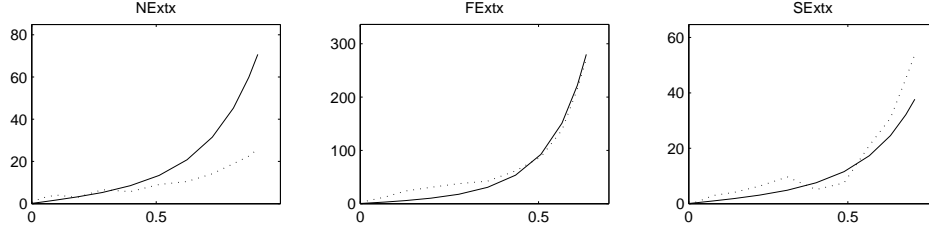
Results of the last material parameter estimation step show that the relative residual  $\Omega_{rel}$  of the shear modes is 4.79% indicating that the estimation step yielded MP's fit the shear modes considerably better than the previous step. The axial relative error 3.76% indicates that the new set of MP's still fit the axial modes very well. Additionally the total relative error could be reduced down to 4.42%.



(a) Axial Graphs First Step



(b) Axial Graphs Second Step



(c) Axial Graphs Last Step

Figure 8.3: (a) Axial force displacement curves for the CL with MP's fitted to just the shear modes has been done in the previous chapters. The relative error of these modes is 173.95%. The overestimated axial parameters can be clearly seen. (b) The same curves after the axial parameters have been fitted to the axial modes. The relative error for these modes is now 2.77%. (c) The curves after all MP's have been fitted to all fifteen modes. The relative error of the axial modes is now 3.76%. Note the significant change in the N-modes due to the altered parameter  $b_{nn}$ . This is due to the higher energy content of the N-extension mode. Experimental data: (*dotted*); Model data: (*solid*).

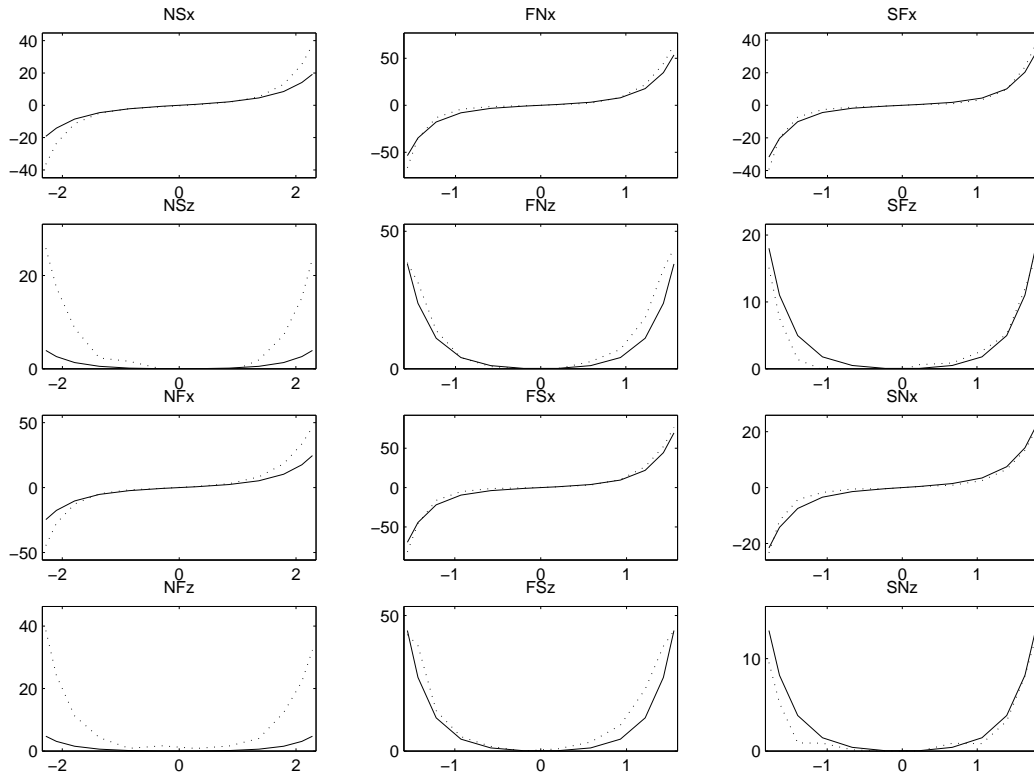


Figure 8.4: Force–displacement curves for the shear modes after the second optimisation step. The relative error is 15.25%. Experimental data: (*dotted*); Model data: (*solid*).

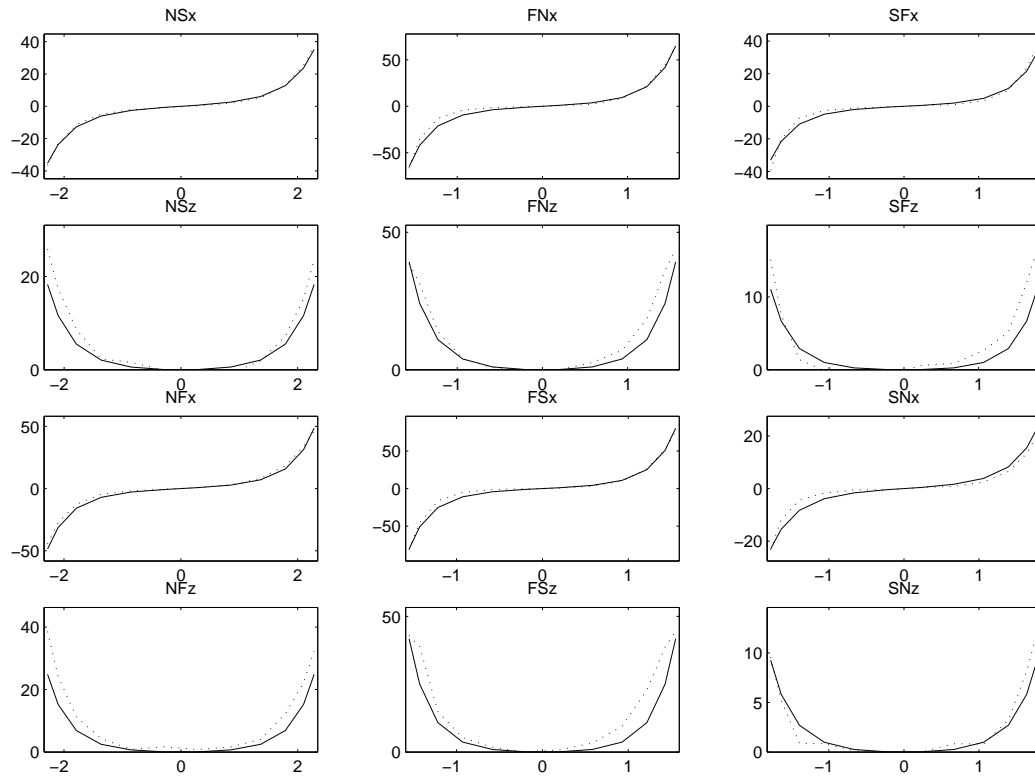


Figure 8.5: Force–displacement curves for the shear modes after the second optimisation step. The relative error is 4.79%. Note that the N-modes are yet the ones worst fitted. Experimental data: (*dotted*); Model data: (*solid*)

In summary this 3-step estimation strategy was found to be suitable for obtaining a set of globally optimal MP's.

### 8.3 Results Full FE Model

The previous sections detailed the 3-step estimation strategy for obtaining a material parameter set for fitting all fifteen force-displacement curves and demonstrated the process for the CL. The same strategy was applied to all material laws and the full set of tables including the relative errors and the set of material parameters is presented in Tables (8.4)–(8.7).

It was found for all material laws that the shear parameters remained in the same range whereas the axial parameters considerably changed of the three steps. The final set of shear parameters of the CL stayed within 13% of their original values. The axial parameters, however, all decreased by 25% or more. The axial parameters  $b_{ff}$ ,  $b_{nn}$ ,  $b_{ss}$  of the SFL and the TL all decreased by  $\sim 50\%$ . For the PZL both axial parameters  $k_{ff}$ ,  $a_{ff}$  changed by more than 50% whereas the parameters  $k_{ss}$ ,  $a_{ss}$  did not change as significantly. The parameters  $k_{nn}$ ,  $a_{nn}$ , however, both changed substantially and  $k_{nn}$  reached its upper bound of 5 imposed by the optimisation package. It was not possible for the PZL to obtain a fully converged set of material parameters, which is also reflected by the increased relative objective function value of 43.04%.

Note also the tradeoff between the pair of material parameters for the SFL, PZL and the TL. For example, while the parameter  $a_{ff}$  of the SFL almost doubled from 0.130 to 0.206, the parameter  $b_{ff}$  more than halved from 59.0 to 27.3.

| CL   | Modes | EC     | $\Omega$ | $\Omega_{rel}$ | $a$   | $b_{ff}$ | $b_{fn}$ | $b_{fs}$ | $b_{nn}$ | $b_{ns}$ | $b_{ss}$ |
|--|-------|--------|----------|----------------|-------|----------|----------|----------|----------|----------|----------|
| MP <sup>HOMO\</sup> <sub>ALL</sub> <sup>SHEAR</sup>    | Shear | 4378.7 | 101.54   | 2.32%          | 0.101 | 32.8     | 10.8     | 12.7     | 31.6     | 10.5     | 22.8     |
|  | Axial | 2494.3 | 4338.87  | 173.95%        |       |          |          |          |          |          |          |
|  | Full  | 6872.9 | 4440.41  | 64.61%         |       |          |          |          |          |          |          |
| MP <sup>SHEAR\</sup> <sub>AXIAL</sub> <sup>AXIAL</sup> | Shear | 4378.7 | 667.56   | 15.25%         | 0.101 | 27.8     | 10.8     | 12.7     | 9.4      | 10.5     | 23.7     |
|  | Axial | 2494.3 | 69.02    | 2.77%          |       |          |          |          |          |          |          |
|  | Full  | 6872.9 | 736.59   | 10.72%         |       |          |          |          |          |          |          |
| MP <sup>AXIAL\</sup> <sub>ALL</sub> <sup>FULL</sup>    | Shear | 4378.7 | 209.77   | 4.79%          | 0.102 | 24.8     | 12.4     | 14.0     | 22.2     | 11.9     | 16.8     |
|  | Axial | 2494.3 | 93.68    | 3.76%          |       |          |          |          |          |          |          |
|  | Full  | 6872.9 | 303.45   | 4.42%          |       |          |          |          |          |          |          |

Table 8.4: Results of all material parameter estimation steps for the CL. The total relative error decreases from 64.61% to 10.72% in the second and 4.42% in the last step.

| SFL  | Modes | EC     | $\Omega$ | $\Omega_{rel}$ | $a_{ff}$ | $b_{ff}$ | $a_{fn}$ | $b_{fn}$ | $a_{fs}$ | $b_{fs}$ | $a_{nn}$ | $b_{nn}$ | $a_{ns}$ | $b_{ns}$ | $a_{ss}$ | $b_{ss}$ |
|--|-------|--------|----------|----------------|----------|----------|----------|----------|----------|----------|----------|----------|----------|----------|----------|----------|
| MP <sup>HOMO\</sup> <sub>ALL</sub> <sup>SHEAR</sup>    | Shear | 4378.7 | 84.45    | 1.93%          | 0.130    | 59.0     | 0.0146   | 41.2     | 0.00913  | 53.2     | 0.0685   | 78.6     | 0.0202   | 36.1     | 0.0222   | 108.7    |
|  | Axial | 2494.3 | 163100   | 6539%          |          |          |          |          |          |          |          |          |          |          |          |          |
|  | Full  | 6872.9 | 163185   | 2374%          |          |          |          |          |          |          |          |          |          |          |          |          |
| MP <sup>SHEAR\</sup> <sub>AXIAL</sub> <sup>AXIAL</sup> | Shear | 4378.7 | 969.8    | 22.15%         | 0.123    | 29.4     | 0.0146   | 41.2     | 0.00913  | 53.2     | 0.0379   | 28.4     | 0.0202   | 36.1     | 0.0095   | 61.5     |
|  | Axial | 2494.3 | 197.4    | 7.91%          |          |          |          |          |          |          |          |          |          |          |          |          |
|  | Full  | 6872.9 | 1167.2   | 16.98%         |          |          |          |          |          |          |          |          |          |          |          |          |
| "MP <sup>AXIAL\</sup> <sub>ALL</sub> <sup>FULL</sup> " | Shear | 4378.7 | 530.2    | 12.11%         | 0.206    | 27.3     | 0.0221   | 38.7     | 0.01073  | 53.4     | 0.1281   | 29.4     | 0.0201   | 40.2     | 0.0159   | 55.8     |
|  | Axial | 2494.3 | 109.3    | 4.38%          |          |          |          |          |          |          |          |          |          |          |          |          |
|  | Full  | 6872.9 | 639.54   | 9.31%          |          |          |          |          |          |          |          |          |          |          |          |          |

Table 8.5: Results of all material parameter estimation steps for the SFL. The total relative error decreases from 2374% in the first step to 16.98% in the second and 9.31% in the last step.

| PZL  | Modes | EC     | $\Omega$ | $\Omega_{rel}$ | $k_{ff}$ | $a_{ff}$ | $k_{fn}$ | $a_{fn}$ | $k_{fs}$ | $a_{fs}$ | $k_{nn}$ | $a_{nn}$ | $k_{ns}$ | $a_{ns}$ | $k_{ss}$ | $a_{ss}$ |
|--|-------|--------|----------|----------------|----------|----------|----------|----------|----------|----------|----------|----------|----------|----------|----------|----------|
| MP <sup>HOMO\Shear</sup> <sub>ALL</sub>    | Shear | 4378.7 | 78.36    | 1.79%          | 0.41     | 0.381    | 0.0263   | 0.386    | 0.019    | 0.347    | 0.167    | 0.304    | 0.0374   | 0.415    | 0.0430   | 0.243    |
|  | Axial | 2494.3 | 799962   | 32072%         |          |          |          |          |          |          |          |          |          |          |          |          |
|  | Full  | 6872.9 | 800041   | 11640%         |          |          |          |          |          |          |          |          |          |          |          |          |
| MP <sup>SHeAR\AXIAL</sup> <sub>AXIAL</sub> | Shear | 4378.7 | 828.8    | 18.93%         | 0.48     | 0.507    | 0.0263   | 0.386    | 0.019    | 0.347    | 0.822    | 1.01     | 0.0374   | 0.415    | 0.0868   | 0.393    |
|  | Axial | 2494.3 | 53.9     | 2.16%          |          |          |          |          |          |          |          |          |          |          |          |          |
|  | Full  | 6872.9 | 882.7    | 12.84%         |          |          |          |          |          |          |          |          |          |          |          |          |
| MP <sup>AXIAL\FULL</sup> <sub>ALL</sub>    | Shear | 4378.7 | 2822.7   | 64.47%         | 1.85     | 0.733    | 0.0162   | 0.350    | 0.015    | 0.332    | 5.00     | 1.39     | 0.0147   | 0.346    | 0.0637   | 0.381    |
|  | Axial | 2494.3 | 135.6    | 5.44%          |          |          |          |          |          |          |          |          |          |          |          |          |
|  | Full  | 6872.9 | 2958.3   | 43.04%         |          |          |          |          |          |          |          |          |          |          |          |          |

Table 8.6: Results of all material parameter estimation steps for the PZL. The total relative error decreases from  $\sim 10^5\%$  in the first step to 12.84% in the second and increases to 43.04% in the last step.

| TL   | Modes | EC     | $\Omega$ | $\Omega_{rel}$ | $a_{ff}$ | $b_{ff}$ | $a_{fn}$ | $b_{fn}$ | $a_{fs}$ | $b_{fs}$ | $a_{nn}$ | $b_{nn}$ | $a_{ns}$ | $b_{ns}$ | $a_{ss}$ | $b_{ss}$ |
|--|-------|--------|----------|----------------|----------|----------|----------|----------|----------|----------|----------|----------|----------|----------|----------|----------|
| MP <sup>HOMO\Shear</sup> <sub>ALL</sub>    | Shear | 4378.7 | 239.89   | 5.48%          | 0.229    | 14.76    | 0.121    | 7.43     | 0.368    | 6.43     | 0.379    | 12.33    | 0.116    | 7.44     | 0.151    | 14.2077  |
|  | Axial | 2494.3 | 11259574 | 451415%        |          |          |          |          |          |          |          |          |          |          |          |          |
|  | Full  | 6872.9 | 11259814 | 163828%        |          |          |          |          |          |          |          |          |          |          |          |          |
| MP <sup>SHeAR\AXIAL</sup> <sub>AXIAL</sub> | Shear | 4378.7 | 709.8    | 16.21%         | 1.31     | 6.09     | 0.121    | 7.43     | 0.368    | 6.43     | 0.532    | 4.92     | 0.116    | 7.44     | 0.400    | 7.37013  |
|  | Axial | 2494.3 | 40.8     | 1.64%          |          |          |          |          |          |          |          |          |          |          |          |          |
|  | Full  | 6872.9 | 750.6    | 10.92%         |          |          |          |          |          |          |          |          |          |          |          |          |
| MP <sup>AXIAL\FULL</sup> <sub>ALL</sub>    | Shear | 4378.7 | 390.4    | 8.92%          | 1.68     | 5.61     | 0.0620   | 8.62     | 0.0481   | 9.35     | 0.800    | 5.69     | 0.052    | 8.82     | 0.239    | 7.86137  |
|  | Axial | 2494.3 | 77.0     | 3.09%          |          |          |          |          |          |          |          |          |          |          |          |          |
|  | Full  | 6872.9 | 467.4    | 6.80%          |          |          |          |          |          |          |          |          |          |          |          |          |

Table 8.7: Results of all material parameter estimation steps for the TL. The total relative error decreases from  $\sim 10^6\%$  in the first step to 10.92% in the second and 6.80% in the last step.



## 8.4 Discussion

After applying the estimation strategy the results show that the CL is most suitable for estimating myocardial material properties for a combined experimental protocol of simple shear and uniaxial deformation. This becomes clear from analysing Tables(8.4)–(8.7), which shows that the CL has the lowest total relative error of 4.42%. Note that the axial material parameters for the CL in Tab.(8.4) demonstrate very clearly that they are overestimated in the simple shear finite element model.

The SFL and the TL seemed to be able to produce acceptable fits for the full FE model that but they are worse than those of the CL. It is possible that the decoupling of the SFL and the TL decrease the suitability fit inverse material parameter estimation for the full model.

For the PZL it was not possible to obtain a converged solution for the full FE model. This might be due to the highly non-linear nature of the overall estimation process. More specifically, Table(7.3) shows for a mean of 0.17 the MP  $k_{nn}$ . For this experiment this value is very close, 0.167 for the first estimation step, see Table(8.6). For the subsequent steps, however, it increases dramatically and reaches its upper bound in the last step. As can be seen in Fig.(8.3)(c) for the CL as well, the energy content of the N-shear modes and the N-axial mode seemed to be incompatible, which is a possible reason that the material parameters  $k_{nn}$  and  $a_{nn}$  drifted off in the last estimation step.

Overall, caution must be paid to these observations since they are only based on one experimental data set. Further studies will be necessary to obtain statistically sound results. However, it appears that both uniaxial extension and simple shear data are needed to characterise all material parameters.

## 8.5 Summary

This chapter presented the finite element model to estimate myocardial material parameters under simple shear and uniaxial extension. It is clear from Sec.(8.3) that the CL is the most suitable constitutive law to model passive myocardial mechanics in non-homogeneous simple shear and uniaxial extension.

Future improvements for comparative studies would involve the measurement of the non-homogeneous fibre distribution.



# Chapter 9

## Conclusion

This study investigated the suitability of a number constitutive laws in the context of material parameter estimation. Three models were examined and compared. Firstly, a homogeneous deformation model that fitted material parameters to a set of six simple shear modes. Secondly, the deformation was modelled more accurately with a finite element model to the same experimental protocol. Lastly, the same finite element model was used to estimate material parameters for a combined experimental protocol of simple shear and uniaxial extension modes.

The homogeneous and the FE shear models showed that the CL is the most suitable law for inverse material parameter estimations. In particular the set of material parameters was very close and it could be concluded that the homogeneous model serves very well to obtain computationally cheap initial estimates, which is a crucial advantage in inverse material parameter estimation. The CL was very stable for the forward solution and only required a minimal number of load steps to converge to the final solutions. This appeared to be almost independent of the choice of material parameters. Similarly, for inverse material parameter estimation the CL converged

for seemingly any possible starting point to the same solution. This is a markedly important feature which cannot be overstressed in light of the difficulties experienced with the other constitutive relations.

Most findings could also be supported by the study which included both the simple shear deformations and the uniaxial extension data. The only marked difference is that the axial material parameters changed due to the different energy content of the axial modes.

Initial concerns that the theoretical cross-coupling of the CL might constrain the fitting abilities could not be confirmed. Rather the opposite seems to hold, i.e. the coupling constrains the MP's in a reasonable way such that it seems to stabilise both the forward solution and the estimation procedure for all three models.

The SFL and TL exhibited very good fitting properties especially for the finite element shear model. However, it was obvious from the full finite element model that the axial material parameters were markedly overestimated. It is therefore important to supply these material laws with a complete set of experimental protocols which ensures that the strain values for all entries of the Green strain have similar magnitudes.

The PZL had excellent fitting properties for the homogeneous model. For the finite element models, however, it was clear that this behaviour could not be reproduced. Even with considerable extra effort in the choice of initial parameters and estimation parameters (such as step size) in the parameter space could not ensure a stable optimisation. Moreover, the material parameters exhibited a great variance.

The LECL had the worst fitting properties for the homogeneous model and it was not possible to fit it to any of the other two models. It is possible that the underlying micro-structural assumption underpinning the construc-

tion of this model is not valid for the simulation of myocardial mechanics.

The transversely isotropic material law from Guccione et al. [39] exhibited very poor behaviour in the FE shear model since it was only capable of fitting three out of the six modes, those with the highest partial energy content. It can therefore be concluded that a transversely isotropic material is not suitable to model the passive myocardial behaviour in simple shear.

Future work will include the investigation of two other kinds of material laws. The fibre splay model as introduced by Lanir [63] and the polyconvex formulations by Itskov & Aksel [56].

Novak et al. [89] investigated regional differences in the passive canine myocardial behaviour in four regions, interventricular septum and the inner, middle and outer layers of the lateral left ventricular free wall. An existing (transversely isotropic) three-dimensional constitutive relation described the nonlinear and anisotropic behaviour exhibited in the four regions equally well. The anisotropy was similar in each region. There were, however, regional differences in the strain energy stored by specimens during identical finite deformations. In particular, specimen from subendocardial and subepicardial regions tended to be stiffer than those from the midwall and septum.

It remains to quantify these regional differences for an orthotropic constitutive relation. This quantification will be impeded by the fact that the change in fiber, sheet and normal direction are varying to a larger extent in the subendo- and subepicardial regions, such that extractions of small cubes aligned with these directions will be almost impossible.

New experimental techniques are needed to extract these regional differences. Also improved imaging techniques would enhance the model building process, ideally enabling one to include the variations of the orthotropic vari-

ations within a specimen.

Lastly, it remains to determine these material parameters in vivo. Again, improved experimental as well as imaging techniques are necessary for this.

Furthermore, all these laws are phenomenological formulations and it is desirable to investigate the relation between these material parameters and the underlying microstructural constituents like collagen and elastin. A framework for the determination of such a relation and initial investigations of the microstructural topoplogy are presented in the next chapter.

## Part III

# Outlook: Microstructural Models





# Synopsis

This part presents a multi-scale framework that associates macrostructural material parameters with underlying microstructural topology and constituents. In particular, a system identification process is presented and an algorithm that quantifies the topology of cardiac myocytes.



# Chapter 10

## Multi-Scale Modeling Framework

Part II examined suitability of several constitutive relations for describing and quantifying the macroscopic mechanical response in relation to the myocardial laminar structure [66].

Ideally, spatially varying material properties should be taken into account as occurs, for example, with transmural changes in the collagen content [66, 128]. Measuring the spatially varying material properties in a quantifiable way is not yet feasible. However, it is possible to observe structure on various length scales, and therefore establish a relationship between the mechanical behaviour and structure.

Sands et al. [99], were able to image extended volumes of myocardial microstructure which enabled them to utilize an anatomically realistic representation of the cleavage planes to simulate wave propagation throughout a myocardial block [100, 116]. These advances in imaging make it possible to firstly take spatial variation of mechanical properties into account and secondly attribute physiological meaning to the macro-scale parameters. A

common approach is to consider compartments on the micro-scale and use homogenization techniques to relate the micro parameters to those on the macro-scale. This, however, requires a certain repeatability of this compartment and is therefore not a feasible approach for the myocardium which exhibits marked heterogeneities on several scales (see Figs.(10.1),(10.2)).

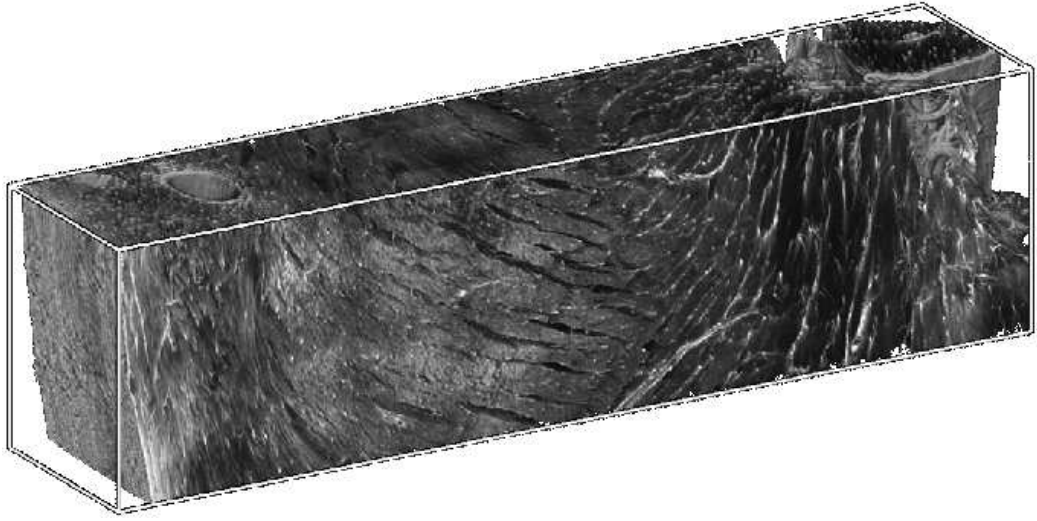


Figure 10.1: A transmural block of rat myocardium

For the mechanical constitutive relations it remains to characterise the connection between the material parameters at the macro-scale and the microstructural constituents. The next section proposes a multi-scale framework in the context of mechanical behaviour that allows one to identify such connections, [102]. These ideas are also applicable for modelling electrical properties of myocardium [108, 111].

Firstly, the underlying experimental data from Sands and coworkers [99] is briefly summarised and a broad concept of a system identification process is presented. This is followed by the results of a digitisation process of the image data, the subsequent statistical analysis, and finally by an algorithm that accurately captures the myocardial topology.

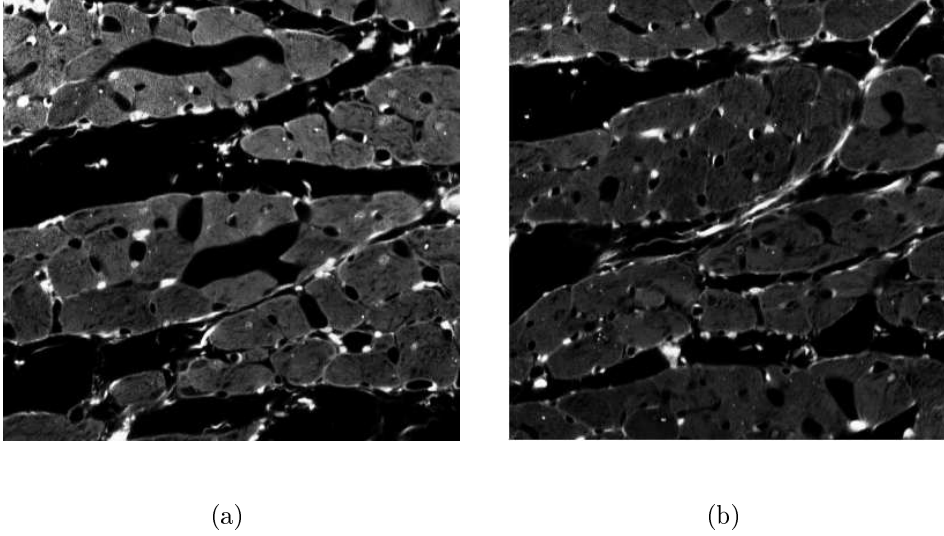


Figure 10.2: These images show magnified samples of cross-sectional areas of rat myocardium orthogonal to the fiber direction. The dimension are  $200 \times 200 \mu m$ . Individual myocytes and sheets can easily be recognised. These fluorescent images were stained with picosirius red to highlight perimysial collagen bundles (white).

## 10.1 Topology of Myocardial Microstructure and its Role in Mechanical Function

Fig.(10.1) shows a transmural block of rat myocardium and the heterogeneity can easily be discerned. Furthermore Fig.(10.3) depicts the transmural collagen distribution of the same sample. It is clear that the mechanical response will dramatically change between subepicardial, midwall and subendocardial regions. For this purpose it is helpful to consider microstructural collagenous components and their respective mechanical function. Figs.(10.2) show highly magnified cross-sectional samples of rat myocardium in the mid-wall which are orthogonal to the fibre direction. The myocardial connective tissue, like that in skeletal muscle, is generally considered to be organised in three levels. Epimysium is the sheath that surrounds the entire muscle,

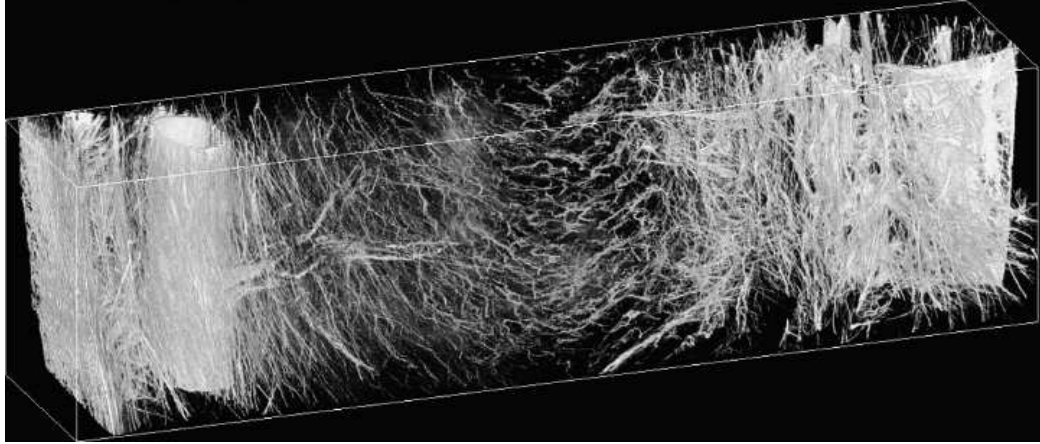


Figure 10.3: Transmurular collagen distribution

endomysium is the fine connective tissue that surrounds and interconnects individual cells, and perimysium is associated with groups or bundles of cells [97].

A digitisation of these levels of collagen will enable one to determine a functional connection between these levels and macro-structural constitutive parameters. It is critical to understand the topology of myocyte and sheet branching since the collagen matrix and the topology interact geometrically.

Furthermore, it has been reported that an increase in interstitial collagen concentration, secondary to pressure overload, results in an increase of stiffness in myocardium [58]. In contrast, a reduction in collagen concentration characterised by a disruption and disappearance of fibrillar collagen leads to a markedly dilated left ventricle that is significantly more compliant. With a model that connects the microstructural constituents and the macrostructural material parameters, it will be possible to model these effects as well as growth phenomena in general.

## 10.2 System Identification Model

The digitisation of the myocardial topology and the collageneous constituents are necessary to connect the micro– and macro–scales. The topology and the collagen distribution have been described in terms of algorithms which are parametrised by two sets of parameters:  $\tau$  for the topology and  $\kappa$  for the collagen distribution. These algorithms are based on the digitised statistical data and need to be replicable. Such an algorithm would be the base to easily generate numerous models with varying parameters.

It is assumed that the mechanical behaviour on the macro–level is described by, see Eq.(3.48):

$$\mathbb{P}(\mathbb{F}, \xi) = \frac{\partial W(\mathbb{F}), \xi}{\partial \mathbb{F}}, \quad (10.1)$$

where  $\xi$  are the material parameters, e.g. the material parameters of the CL, Sec.(5.2.1).

The relationship  $g$  between the macro–material parameters  $\xi$  and the micro–parameters for the topology  $\tau$  and the collagen distribution  $\kappa$ ,

$$\xi = g(\tau, \kappa) \quad (10.2)$$

can be determined by a “black box” system identification process as outlined in detail by Sjöberg et al. [106], and Ghoniem et al. [36].

The nonlinear black box situation, as is the case here, is hard to compute as a very rich spectrum of model descriptions must be handled. The area is quite diverse and covers topics from mathematical approximation theory, via estimation theory and regression analysis to neural networks, wavelets and fuzzy logic models. If the principle of parsimony is applied in the sense of simplicity then one can start the identification process by setting up polynomial relationships between the micro– and macro–parameters determining the parameters via a nonlinear least square minimization method. If this approach



is either too restricted or requires too many parameters, techniques such as radial basis functions or genetic algorithms remain as other possibilities [15].

It is important to note that other descriptions for the macro-scale need to be considered. This is the case, since one of the major assumptions of continuum mechanics is that the body consists of the same material particles throughout the deformation process. Several factors like development, aging, healing, growth, atrophy and remodelling [93, 17], however, influence the makeup of the tissue in consideration. Theories that are capable of dealing with these kind of continuously altering composition on the micro-scale are therefore crucial in modelling the above mentioned mechanisms. One of the possible candidates to describe these, mixture theory, were introduced in the context of biomechanics by Humphrey and Rajagopal [51, 52]. This theory allows for a number of constituents with changing densities at each point in the mathematical space. It is therefore suitable to model their homeostatic tendency to adapt in response to changes in their mechanical environment.

Furthermore, other theories need to be developed to describe competing hypothesis on the various spatial and temporal scales.

### 10.3 Digitisation of Myocardial Topology

The last section sketched the process of quantifying the relation between the micro- and macro-parameters. The myocardial microstructure is believed to be comprised of three parts forming a sensible structural hierarchy. These are the cleavage planes, the myocytes and the collagenous network. Trew and coworkers [116] were able to digitise the cleavage planes. It remains, however, to perform a statistical analysis of these planes.

This section presents a geometrical digitisation process of a tissue block

$200 \times 200 \times 200 \mu m$ , which is used to create an algorithm capable of replicating the major features of the myocyte topology.

### 10.3.1 Digitisation of Myocyte Topology

Fig.(10.4) depicts the specimen that was digitised. The left shows a 3D rendered volume image and the right one of its collagenous networks. The

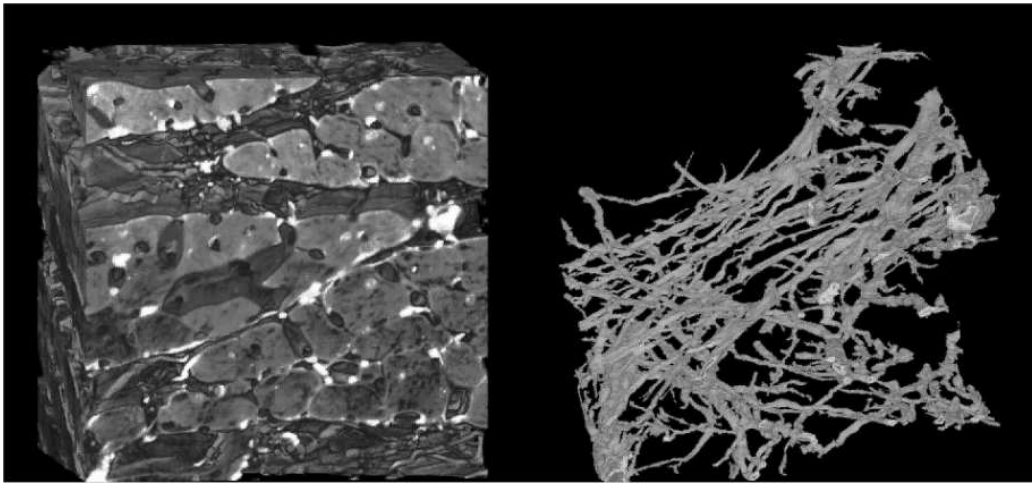
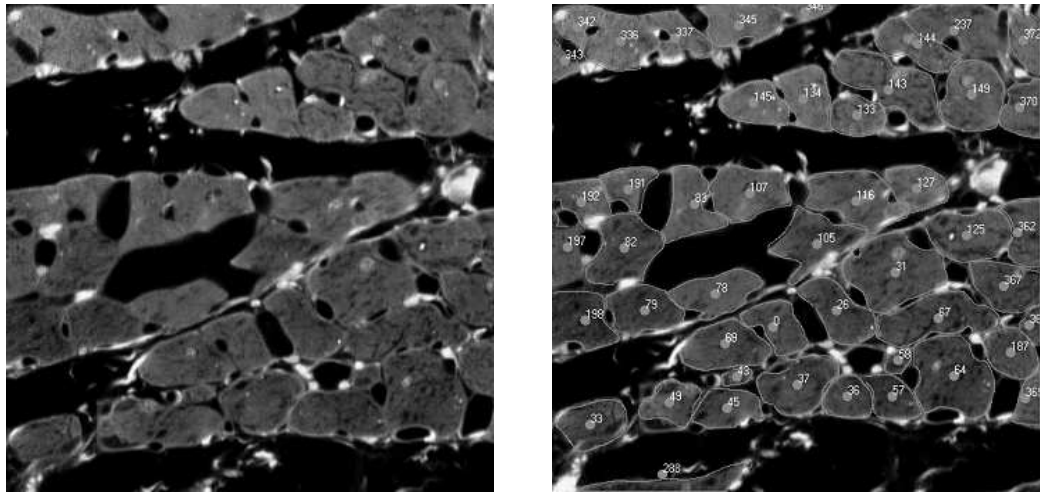


Figure 10.4: Left, shows a 3D rendered volume image of the block that was digitized; right, one of its corresponding collagenous branching networks.

image data consisted of 492 two-dimensional images aligned with the fibre direction. The resolution of these images was  $0.4 \mu m / \text{voxel}$ . Fig.(10.5) depicts the digitisation process for these images. This was done manually using the tool Labview [126].



(a)

(b)

Figure 10.5: Left: a cross sectional image showing myocyte areas and the sheet structure; right: the digitised image, including cell boundaries, centroids and cell numbers.

The images were digitised to extract information about the connectivity pattern, the mean length of myocyte segments, their direction and cross-sectional area. Myocytes form a complex network and branch and connect with each other. This braching and connecting pattern was termed “splitting” and “merging”. Note that this is an arbitrary terminology depending on the direction one views the network from. A split or merge was defined when the endomysial collagen changed from one contour into two contours from one image to the subsequent one, or vice versa. The straight line between the centroids of the start and end contour is denoted as a fibre or myocyte segment. These segments do not coincide with actual myocardial cells, since the images were stained for collagen. Other staining techniques would allow to identify the intercalated disks and therefore for myocardial cells. The whole block yielded a total number of 287 segments which gave a solid basis for a statistical analysis of directional data [74]. Furthermore the mean laminae orientation was extracted.

The statistical analysis yielded a number of distributions. For example, Fig.(10.6)(a) shows the length distribution of the fibre segments. This distribution is displayed as a histogram as well as a continuous distribution which was found to be the optimal distribution by the Statistical Toolbox from Matlab [125]. This distribution quantifies the geometrical arrangement within the mean fibre direction. For a complete description of the topology it is also important to obtain information about the geometrical arrangement within the sheet-normal plane. This is described in Sec.(10.3.2).

The direction of the segments and sheets were averaged and the images were rotated so that they were precisely aligned with the microstructural  $f, n, s$  coordinate system. This enabled a precise computation of the cross-sectional area and angles between centroids.

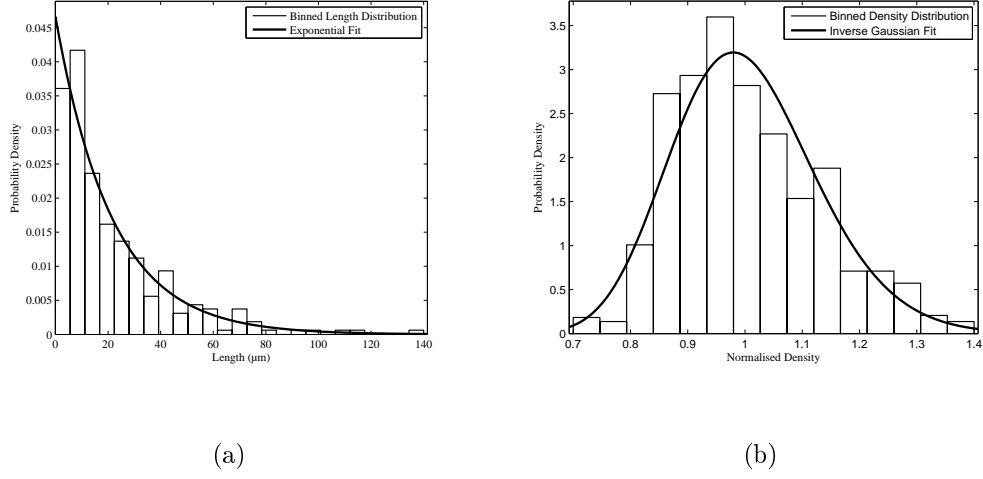


Figure 10.6: Left: length distribution of the fibre segments with mean  $\mu_L = 21.4\mu m$ ; right: normalised area distribution of the Voronoi cells across all images with mean  $\mu_A = 600\mu m^2$ .

### 10.3.2 Voronoi Cells

As mentioned above it is important to obtain information about the arrangement of the centroids in the sheet-normal plane. Voronoi cells are a standard tool for such a two dimensional analysis [92].

The sheet boundaries and the centroids as displayed in Fig.(10.7)(a) were utilised to create Voronoi meshes [14] as can be seen in Fig.(10.7)(b). Even though the boundaries of the Voronoi cells do not exactly match the digitised boundaries, they do resemble the gross density pattern of the distribution of cross-sectional areas within a sheet. With these data it was possible to perform a statistical analysis on a number of variables like area and orientation of the cells that characterise the in-plane topology of the myocardial segments. Fig.(10.6)(b) shows the Voronoi cell area distribution across all images with a mean of  $\mu_A = 600\mu m^2$ . The mean is calculated by the area of the sheet divided by the number of cells in the sheet.

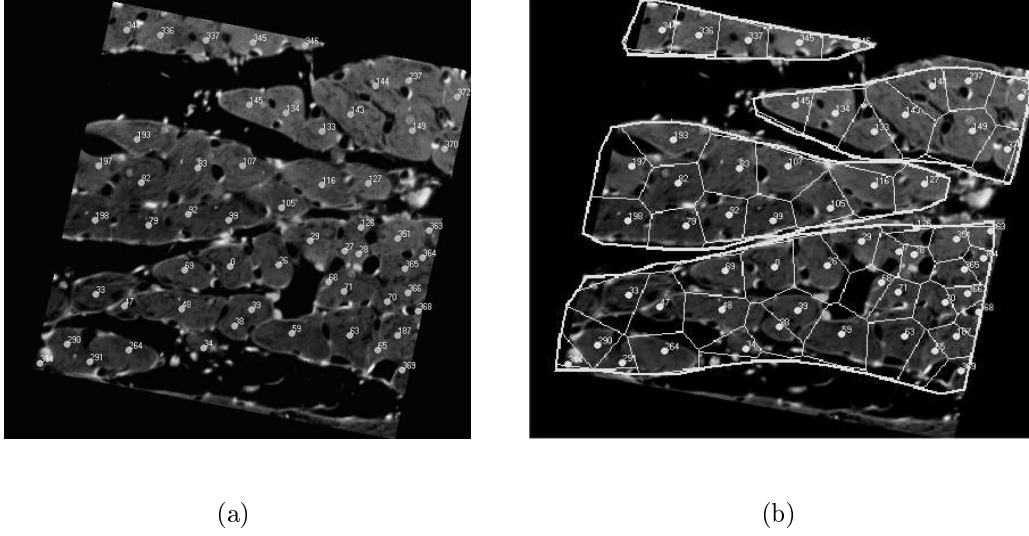


Figure 10.7: Left: shows a rotated image with just centroids; right shows the Voronoi cells of this image.

The detailed list of variables and the regression analysis based on these are presented in the subsequent sections.

## 10.4 Algorithm of Myocyte Topology

This section presents the regression model used to decide which microstructural variables best explain the branching pattern of myocardial segments. Furthermore an algorithm is presented for generating a sequence of two-dimensional Voronoi meshes. This algorithm is calibrated to our image data and run repeatedly to verify its validity and the accuracy of the regression model.

The branching pattern of the segments can be viewed as either a split or a merge depending on the orientation of the coordinate system. For this case the orientation was fixed and the resulting number of splits and merges was

almost equal, indicating that the other viewing direction should have yielded very similar results.

For the merging regression model every possible merge combination in all 519 rotated images was included. A merge was deemed possible for any two adjacent cells  $i$  and  $j$  within a sheet. This yielded a total of  $\sim 5 \cdot 10^4$  possible merge combinations out of which 110 merges occurred. The response variable for this model was  $M_{ij}$ , a boolean variable (true/false) indicating whether the combination merged. The following explanatory variables ( $A_{ij}^M$ ,  $R_{ij}^M$ ,  $\gamma_{ij}^M$ ,  $\tau_{ij}^M$ ) were considered for the regression model:

$A_{ijk}^M$ :  $A_{ijk}^M = \frac{A_{ik} + A_{jk}}{\mu_A}$ , normalised area of the two Voronoi cells  $i, j$  in image  $k$ .

$R_{ijk}^M$ :  $R_{ijk}^M = \frac{A_{ik}}{A_{jk}}$ , ratio of area small/large in image  $k$ .

$\gamma_{ijk}^M$ :  $\gamma_{ijk}^M = \arctan\left(\frac{y_{jk} - y_{ik}}{x_{jk} - x_{ik}}\right)$ , alignment of line connecting centroids with respect to sheet direction ( $x$ -axis),  $(x_i^k, y_i^k)$ ,  $(x_j^k, y_j^k)$  are the coordinates in the image plane of the points  $i$  and  $j$  in image  $k$ , respectively.

$\tau_{ijk}^M$ :  $\tau_{ijk}^M = \frac{\sqrt{(x_j^k - x_i^k)^2 + (y_j^k - y_i^k)^2}}{\sqrt{(x_j^{k+1} - x_i^{k+1})^2 + (y_j^{k+1} - y_i^{k+1})^2}}$ , measure whether centroids move towards each other in two successive images  $k$  and  $k + 1$ .

For the splitting regression model a total of  $\sim 2.5 \cdot 10^4$  individual segments over all images were considered out which 123 splits occurred. The response variable for this model was  $S_i$ , a boolean variable (true/false) indicating whether the segment split. Below is a list of the response variables ( $A_i^S$ ,  $R_i^S$ ,  $\beta_i^S$ ) that were considered as possible factors explaining the response of a split ( $S_i$ ) of a segment:

$A_{ik}^S$ :  $A_{ik}^S = \frac{A_{ik}}{\mu_A}$ , normalised area of the Voronoi cell  $i$  in image  $k$ .

$R_{ik}^S$ :  $R_{ik}^S = \frac{d_{\min}}{d_{\max}}$ , ratio of minor  $d_{\min}$  and major  $d_{\max}$  axes of Voronoi cell  $i$  in image  $k$ .

$\beta_{ik}^S$ :  $\beta_{ik}^S = \angle(\vec{d}_{\max}, \vec{s})$ , angle between direction of major axis  $\vec{d}_{\max}$  of the cell with respect to sheet direction  $\vec{s}$  in image  $k$ .

The area was considered to be an important explanatory variable, since it was believed that a high density of cells would increase the chance of merging and that an large cross-sectional area of a cell would increase the chance of splitting.

The variables presented in these lists were used in the regression models that are presented in the next section.

#### 10.4.1 Regression Analysis

A logistical regression model was fit to the data using a combination of forward and backward regression [79] as implemented in the program  $\mathcal{R}$  [26]. The initial model in forward regression contains the response variable but no explanatory variables (referred to as the null model). All explanatory variables are iteratively included in the model in a greedy manner, so as to improve some measure of fit (such as the Akaike Information Criterion). The algorithm terminates when the inclusion of no remaining explanatory variable will improve the fit by a predefined minimum tolerance, or when all explanatory variables are included into the model (referred to as the full model). In backward regression one starts with the full model and iteratively removes explanatory variables so as to reduce the measure of the fit by as little as possible. The algorithm terminates when no variable can be removed without reducing the measure of the fit by some predetermined maximum tolerance, or when the null model is reached.



From these models, the probability  $\pi_{ij}^M$  that two adjacent segments  $i$  and  $j$  will merge is given by [31]:

$$\pi_{ij}^M = \frac{e^{k_{ij}}}{1 + e^{k_{ij}}} , \quad (10.3)$$

where

$$\begin{aligned} k_{ij} = & -4.70 - 1.34A_{ij}^M + 1.00R_{ij}^M \\ & -0.182\gamma_{ij}^M + 3.61\tau_{ij}^M . \end{aligned} \quad (10.4)$$

The probability  $\pi_i^S$  that segment  $i$  will split in the next image is given by:

$$\pi_i^S = \frac{e^{k_i}}{1 + e^{k_i}} , \quad (10.5)$$

where

$$k_i = -5.96 - 0.52A_i^S . \quad (10.6)$$

The values in Eqs.(10.4)&(10.6) are the coefficients of the explanatory variables determined by the corresponding logistical regression. There was strong evidence that  $A_{ij}^M, \tau_{ij}^M$  explained the merging of two cells, with p-values of  $3.8 \cdot 10^{-13}, 4.9 \cdot 10^{-13}$ . Furthermore there was weak evidence that  $R_{ij}^M, \gamma_{ij}^M$  explained the merging of two cells with p-values of 0.11 and 0.12, respectively. For the splitting only the variable  $A_i^S$  seemed to explain the split of any given cell with a p-value of 0.049.

### 10.4.2 Algorithm for Segment Topology

Utilising the results of the regression analysis, a model was built to replicate the arrangement of myocytes within a sheet. Since the data set created from the images produced by Sands et al. [99] is based on two dimensional slices through the ventricular wall, the model was designed to replicate these two dimensional slices.

Starting with a defined sheet boundary an initial grid of seed points within the sheet boundary was generated that corresponds to the centroids of the myocyte segments. This was achieved by first generating an initial field of randomly generated points. To create the required area distribution Matern's hard core process with a parameter  $p = 0.2$  was used [42]. The statistics of fibre deviation from mean fibre direction were used to attribute a random degree of deviation from the mean fibre direction and direction in the sheet normal plane for each segment.

This initial sheet slice served to generate a Voronoi mesh of the points within the sheet using the sheet boundary as the external boundary for all Voronoi cells with an external edge as above. The mean area of this initial grid was very stable with  $596.6 \pm 37.6 \mu m^2$  compared to  $600.0 \pm 61.9 \mu m^2$  of the experimental mean area. Using the equation from the regression model the probability that a segment cell within the mesh would split or merge was calculated. These probabilities were used in combination with a random number generator to decide whether splitting or merging would occur for the next image.

The algorithm stepped forward in space along the mean fibre direction and positions of cell centroids were updated based on their allocated directions. If a cell or cell pair had been designated to split or merge a new segment centroid was generated accordingly. Its direction was assigned according to the distribution of the fibre direction.

Two pictures of a typical run of the model can be seen in Fig.(10.8).

### 10.4.3 Preliminary Results

The model was run ten times with the probabilities from the regression model. The same statistical analysis as for the original image set was per-

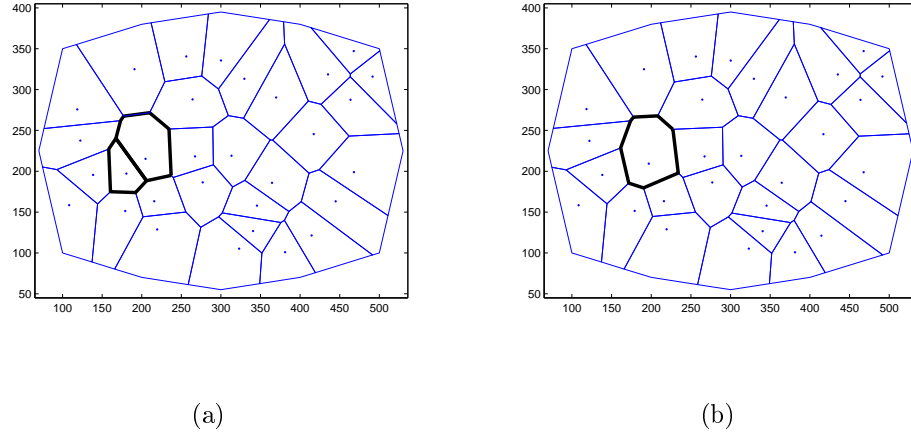


Figure 10.8: Two consecutive images in a typical model run. Left: a sheet sample with two highlighted Voronoi cells that are about to merge; right: the same sheet with these two Voronoi cells having merged into one.

formed, i.e. the mean, the standard deviation, as well as the standard error were computed for the length and density distributions.

Fig.(10.9) shows a typical set of fitted distributions and the similarity between these can easily be recognised. For an easier visual comparison it is helpful to fit continuous distributions to both the discrete sample and model distribution for length and density. It is clear that the length distribution of the model is very close to this of the sample distribution. The area distribution of the model, however, exhibits a lower standard deviation from the mean and seems to be related to the area distribution of the initial grid. Therefore, further investigations are necessary to obtain a closer resemblance between sample and model.

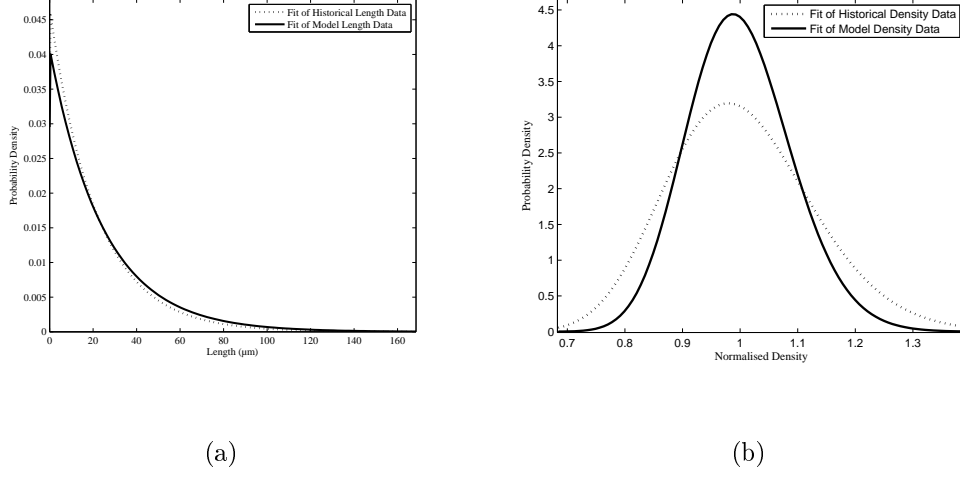


Figure 10.9: Left: the fitted sample (dotted) and model (solid) length distributions; right: the fitted sample (dotted) and model (solid) density distributions

## 10.5 Discussion

The algorithm in the previous chapter presented a critical milestone towards a multi-scale model of myocardial mechanics that allows one to mutually identify micro-constituents and macro-material parameters.

Further steps involve the digitisation of more samples and a cross-sample statistical analysis. This will be done for samples of the same region of other animals of the same health and compared with distributions from diseased samples. This will enable the identification of the dependence of the algorithm parameters on pathological conditions and therefore the influence of disease on the mechanical performance at the different scales.

## 10.6 Summary

This chapter presented the multi-scale modelling framework that allows one to identify macro-structural material parameters as those of the CL with micro-structural constituents and their topological arrangement. This was done by presenting a system identification process as well as a first step towards an anatomically realistic algorithm to create artificial myocardial blocks.

Further steps will involve the development of algorithms for the sheet structure as well as the collagenous network. Finally, a finite element model will be created that combines these three algorithms.

## Part IV

# Appendices



# Synopsis

This part presents additional research that was undertaken during this study as well as additional data and sample files for the three models presented Part II: Application.

Appendix A presents the detailed derivation of the stress–strain relationship (Eq.(3.54)) depending on the formulation of the functional form of the strain energy density function. Appendix B lists a sample file for the homogeneous model as well as all graphs for all laws and all experiments. Appendix C lists a sample file for the FE model as well as all graphs for all laws and all experiments.





# Appendix A

## Ambiguities in Hyperelastic Constitutive Law Formulations

Within the framework of continuum mechanics materials are said to be hyperelastic or Green–elastic, when work done on the boundaries and by body forces can be fully recovered from a stored strain energy density function.

There is, however, ambiguity in the literature on how the strain energy density function should be formulated with respect to the components of the strain measure when using certain stress strain relationships. This section clarifies the requirements that yield consistent formulations, refer to Sec.(3.3.3).

### A.1 Introduction

Among the first authors to introduce the concept of the strain energy density function (SEDF) and the corresponding stress–strain relationship (SSR) are Green & Zerna, 1954, [38]. Since 1954 numerous books and articles have been published on these so-called “hyperelastic” or “Green–elastic” materials, but

frequently with different ways of expressing the dependence on the shear strain components. The underlying risks of using an inconsistent pairing of SEDF and related SSR can lead to errors of a factor two for the shear strain components. The last years in the biomechanical treatise of material laws have shown that it is crucial to formulate ever new constitutive laws to cover the wide range of biological tissue; this is especially the case for formulating them in terms of the actual components rather than the usual invariants, see [39, 84, 25], and that is where potential errors occur.

In Fung, [35], we can find two different requirements for the SEDF although the same SSR is used. This can lead to erroneous results for the shear strain components.

On page 269 he writes:

Example A: *“If a material is elastic and has a strain energy function  $W$ , which is a function of the strain components  $e_{11}, e_{22}, e_{33}, e_{12}, e_{23}, e_{31}$ , then the stress can be obtained from the strain energy function by differentiation:*  

$$\sigma_{ij} = \frac{\partial \Psi}{\partial e_{ij}}$$
”

Whereas on page 300 he writes:

Example B: *“Let  $\Psi$  be expressed in terms of the nine strain components  $E_{11}, E_{12}, E_{13}, E_{21}, E_{22}, E_{23}, E_{31}, E_{32}, E_{33}$ , and be written in a form that is symmetric in the symmetric components  $E_{12}$  and  $E_{21}$ ,  $E_{23}$  and  $E_{32}$ ,  $E_{13}$  and  $E_{31}$ . The nine strain components are treated as independent variables when partial derivatives of  $W$  are formed.”* Here the same SSR is used.

Let us now consider a simple example of a linear elastic material described by the following SEDF and let them be expressed according to both examples above:

Example A:

$$\Psi_A(E_{ij}) = a_{11}E_{11}^2 + a_{22}E_{22}^2 + a_{33}E_{33}^2 + a_{12}E_{12}^2 + a_{23}E_{23}^2 + a_{31}E_{31}^2 \quad (\text{A.1})$$

Example B:

$$\begin{aligned} \Psi_B(E_{ij}) = & a_{11}E_{11}^2 + a_{22}E_{22}^2 + a_{33}E_{33}^2 + \\ & a_{12} \left( \frac{1}{2}(E_{12} + E_{21}) \right)^2 + a_{23} \left( \frac{1}{2}(E_{23} + E_{32}) \right)^2 + a_{31} \left( \frac{1}{2}(E_{31} + E_{13}) \right)^2 \end{aligned} \quad (\text{A.2})$$

Note that both SEDF's would now have the same value if being evaluated at the same strain state, for all possible  $\mathbb{E}$ . If we now apply the derivative formula without scrutinizing the underlying mathematical implications of the symmetry of  $\mathbb{E}$  we obtain the following results.

Example A: Using the SSR  $S_{ij} = \frac{\partial \Psi}{\partial E_{ij}}$  then, for  $S_{12}$ , we obtain:

$$S_{12}^A = 2a_{12}E_{12} \quad (\text{A.3})$$

Example B: Using the same SSR, we obtain for  $S_{12}$

$$S_{12}^B = a_{12}E_{12} \quad (\text{A.4})$$

Clearly we get a different result for  $S_{12}$  even though the SEDF's are numerically equal for all  $\mathbb{E}$ . In actuality, we must change the SSR for the SEDF in example A. The authors believe that it is therefore necessary to present a detailed derivation of existing SSR's and the related requirements for the SEDF's.

## A.2 Derivation of Stress–Strain Relations

Here we derive the two existing forms of the SSR and corresponding requirements for the functional form of the SEDF. This derivation is based on the generalized version of the directional derivative, see also [13, 24]. It was chosen because it clarifies the connections between the various stress and strain measures, where they are all considered as  $3 \times 3$ -matrices; initially, we chose to derive the relationship between the first Piola–Kirchhoff stress tensor  $\mathbb{P}$

and the right Cauchy–Green stretch tensor  $\mathbb{C}$ , based on the relationship between the first Piola–Kirchhoff stress tensor  $\mathbb{P}$  and the deformation gradient tensor  $\mathbb{F}$ . Then the SSR between  $\mathbb{S}$  and  $\mathbb{C}$  is obtained and eventually the relation between  $\mathbb{S}$  and  $\mathbb{E}$  is then easily obtained in the end by a factor of 2.

We start with the first Piola–Kirchhoff stress tensor  $\mathbb{P}$ , which can be identified as the first part of a Taylor series expansion of the SEDF  $\Psi = \Psi(\mathbb{F})$ .

$$\Psi(\mathbb{F} + \mathbb{H}) = \Psi(\mathbb{F}) + \langle D_{\mathbb{F}}\Psi(\mathbb{F}), \mathbb{H} \rangle + \text{higher order terms} \quad (\text{A.5})$$

$\langle \mathbb{A}, \mathbb{B} \rangle = \text{tr}(\mathbb{A}^T \mathbb{B})$  describes the inner product of two  $3 \times 3$ -matrices. Therefore

$$\mathbb{P}(\mathbb{F}) = D_{\mathbb{F}}\Psi(\mathbb{F}), \quad (\text{A.6})$$

which reads as follows in index notation:

$$\mathbb{P}(\mathbb{F}) = P_{mn}(F_{ij}) \mathbf{e}_m \otimes \mathbf{e}_n = \frac{\partial \Psi}{\partial F_{mn}}(F_{ij}) \mathbf{e}_m \otimes \mathbf{e}_n, \quad (\text{A.7})$$

where  $\otimes$  defines the dyadic product and  $\mathbf{e}_m$  are the base vectors of Euclidean 3-space. The above relationship, in particular the Taylor expansion can be found in e.g. [75], pp.180 and is also connected to a consideration of the Clausius–Duhem inequality, which we leave out here, since it suffices to consider the relationship between  $\mathbb{P}$  and  $\mathbb{F}$ . The differential operator  $D_{\mathbb{F}}(\cdot)$  cannot be misinterpreted since  $\mathbb{F}$  in general is a non-symmetric fully populated matrix and could therefore equally well be expressed in component form where the components are formed as partial derivatives  $P_{ij} = \frac{\partial \Psi}{\partial F_{ij}}$  as given in Eq.(A.7).

If we now want to deduce the relationship between the second Piola–Kirchhoff stress tensor and say the right Cauchy–Green stretch tensor  $\mathbb{C} = \mathbb{F}^T \mathbb{F}$  then we start with the inner product of the above series expansion and gradually perform changes which eventually lead to the desired relationship.

If we recall the principle of material objectivity, see [75], p.152, then the SEDF,  $\Psi$  can be rewritten as  $\Psi = \hat{\Psi}(\mathbb{F}^T \mathbb{F}) = \hat{\Psi}(\mathbb{C})$ . Before we proceed let us first define the symmetry operator  $\text{sym}[\mathbb{A}] = \frac{\mathbb{A} + \mathbb{A}^T}{2}$ . Then the inner product, which is the directional derivative then reads:

$$\begin{aligned}
 \langle D_{\mathbb{F}} \hat{\Psi}(\mathbb{F}^T \mathbb{F}), \mathbb{H} \rangle &= \langle D_{\mathbb{C}} \hat{\Psi}(\mathbb{C}), \mathbb{F}^T \mathbb{H} + \mathbb{H}^T \mathbb{F} \rangle \\
 &= 2 \langle D_{\mathbb{C}} \hat{\Psi}(\mathbb{C}), \frac{\mathbb{F}^T \mathbb{H} + \mathbb{H}^T \mathbb{F}}{2} \rangle \\
 &= 2 \langle D_{\mathbb{C}} \hat{\Psi}(\mathbb{C}), \text{sym}[\mathbb{F}^T \mathbb{H}] \rangle \\
 &= 2 \langle \text{sym}[D_{\mathbb{C}} \hat{\Psi}(\mathbb{C})], \mathbb{F}^T \mathbb{H} \rangle \\
 &= 2 \langle \mathbb{F} \text{sym}[D_{\mathbb{C}} \hat{\Psi}(\mathbb{C})], \mathbb{H} \rangle.
 \end{aligned} \tag{A.8}$$

Again identifying the first Piola–Kirchhoff stress tensor leads to

$$\mathbb{P}(\mathbb{F}) = D_{\mathbb{F}} \hat{\Psi}(\mathbb{F}^T \mathbb{F}) = 2 \mathbb{F} \text{sym}[D_{\mathbb{C}} \hat{\Psi}(\mathbb{C})] = \mathbb{P}(\mathbb{C}) \tag{A.9}$$

and finally to the second Piola–Kirchhoff stress tensor reads:

$$\mathbb{S}(\mathbb{C}) = \mathbb{F}^{-1} \mathbb{P}(\mathbb{C}) = 2 \text{sym}[D_{\mathbb{C}} \hat{\Psi}(\mathbb{C})]. \tag{A.10}$$

We will now discuss the component formulation since this is where potential errors occur. The principle of material objectivity gives as stated above that  $\Psi = \hat{\Psi}(\mathbb{F}^T \mathbb{F}) = \hat{\Psi}(\mathbb{C})$  and therefore if  $\Psi$  is expressed in terms of  $\mathbb{C}$  that  $\hat{\Psi}(\mathbb{C}) = \hat{\Psi}(\mathbb{C}^T)$ , which in component form e.g. reads:

$$\begin{aligned}
 &\hat{\Psi}(C_{11}, C_{22}, C_{33}, C_{12}, C_{21}, C_{13}, C_{31}, C_{23}, C_{32}) \\
 &= \hat{\Psi}(C_{11}, C_{22}, C_{33}, C_{21}, C_{12}, C_{31}, C_{13}, C_{32}, C_{23}).
 \end{aligned} \tag{A.11}$$

The order of the components can of course be chosen arbitrarily; we chose this specific one, so that the transposition operation can be easily identified, since  $\Psi$  can now be understood as a scalar function of nine components, rather than a matrix.

Eq.(A.10) implies that the second Piola–Kirchhoff stress tensor can be expressed in the following component form:

$$S_{ij} = \left( \frac{\partial \hat{\Psi}}{\partial C_{ij}} + \frac{\partial \hat{\Psi}}{\partial C_{ji}} \right) (C_{ij}) \quad (\text{A.12})$$

but since Eq.(A.11) holds this can be simplified to the following formula, which is prevalent in the current continuum mechanics literature:

$$\mathbb{S} = 2 \frac{\partial \hat{\Psi}}{\partial \mathbb{C}}(\mathbb{C}) \quad \Longleftrightarrow \quad S_{ij} = 2 \frac{\partial \hat{\Psi}}{\partial C_{ij}}(C_{ij}). \quad (\text{A.13})$$

Note that the symmetric nature of the differential operator still holds although it cannot be seen anymore and that a symmetric stress is generated independent of the conservation of angular momentum.

Of course, the SEDF can be expressed in terms of only six independent components of  $\mathbb{C}$  like in example A of the introduction. This can be expressed in the following way (There are others as well and none is correct or wrong, just different.):

$$\begin{aligned} & \hat{\Psi}(C_{11}, C_{22}, C_{33}, C_{12}, C_{21}, C_{13}, C_{31}, C_{23}, C_{32}) \\ &= \tilde{\Psi}(C_{11}, C_{22}, C_{33}, 2C_{12}, 0, 2C_{13}, 0, 2C_{23}, 0) \\ &= \tilde{\Psi}(C_1, C_2, C_3, C_4, C_5, C_6) \end{aligned} \quad (\text{A.14})$$

Here we chose to rename the components to avoid ambiguity. But then Eq.(A.11) does not hold anymore or in other words there are only six components left:

$$\tilde{\Psi}(\mathbb{C}) \neq \tilde{\Psi}(\mathbb{C}^T), \quad (\text{A.15})$$

and we cannot perform the above simplification of the differential operator anymore and therefore the SSR for  $\Psi = \tilde{\Psi}(\tilde{\mathbb{C}})$  reads:

$$\mathbb{S}(\mathbb{C}) = 2 \, sym[D_{\mathbb{C}} \tilde{\Psi}(\mathbb{C})]. \quad (\text{A.16})$$

or in index notation

$$S_{ij} = \left( \frac{\partial \tilde{\Psi}}{\partial C_{ij}} + \frac{\partial \tilde{\Psi}}{\partial C_{ji}} \right) (C_{ji}). \quad (\text{A.17})$$

We complete the discussion by introducing the SSR between  $\mathbb{S}$  and  $\mathbb{E}$  when the SEDF is expressed in terms of  $\mathbb{E}$  with  $\tilde{\Psi}(\mathbb{E}) \neq \tilde{\Psi}(\mathbb{E}^T)$ . Then Eqs.(A.16&A.17) only differ by a factor 2 since  $\mathbb{E} = \frac{1}{2}(\mathbb{C} - \mathbb{I})$ .

$$\mathbb{S}(\mathbb{E}) = \text{sym}[\mathbb{D}_{\mathbb{E}} \tilde{\Psi}(\mathbb{E})], \quad (\text{A.18})$$

or in index notation

$$S_{ij} = \frac{1}{2} \left( \frac{\partial \tilde{\Psi}}{\partial E_{ij}} + \frac{\partial \tilde{\Psi}}{\partial E_{ji}} \right) (E_{ij}). \quad (\text{A.19})$$

The above equation is exactly the SSR as introduced by Green & Zerna, 1954, [38]. It is important to note that no mistake is introduced when the SSR Eq.(A.18&A.19) are used even if the SEDF is not changed down to six components.

To finish the discussion it is helpful to apply Eq.(A.19) to example A of the introduction to show that it works. We therefore remind ourselves about the form of the SEDF of example A.

Example A:

$$\Psi_A(E_{ij}) = a_{11}E_{11}^2 + a_{22}E_{22}^2 + a_{33}E_{33}^2 + a_{12}E_{12}^2 + a_{23}E_{23}^2 + a_{31}E_{31}^2 \quad (\text{A.20})$$

And now we can apply the SSR Eq.(A.19), then, for  $S_{12}$ , we obtain:

$$S_{12}^A = \frac{1}{2} \left( \frac{\partial \Psi_A}{\partial E_{12}} + \frac{\partial \Psi_A}{\partial E_{21}} \right) (E_{12}) = \frac{1}{2} (2a_{12}E_{12} + 0) (E_{12}) = a_{12}E_{12} \quad (\text{A.21})$$

which now coincides with the result from example B.



### A.3 Conclusion

We have shown that the erroneous use of SEDF's and SSR's may lead to a false result by a factor of two. It is straightforward, though not trivial, which SSR to use depending on the functional form of the SEDF. As a summary we give a table of consistent, inconsistent and potentially ambiguous formulæ in the literature, see Table A.1.

### A.4 Nomenclature for this Section

$\mathbb{C}$  right Cauchy–Green stretch tensor

$\mathbb{E}$  Green strain tensor

$\mathbb{P}$  1<sup>st</sup> Piola–Kirchhoff stress tensor

$\mathbb{S}$  2<sup>nd</sup> Piola–Kirchhoff stress tensor

$\Psi$  strain energy density function in its general sense

$\hat{\Psi}$  strain energy density function dependent on nine independent tensor components

$\tilde{\Psi}$  strain energy function dependent on six independent components of  $\mathbb{C}$

$\tilde{\tilde{\Psi}}$  strain energy function dependent on six independent components of  $\mathbb{E}$

Table A.1: A non-exhaustive summary of consistent, inconsistent and potentially ambiguous formulæ

|   |
|---|
| <b>1.) Consistent formulæ</b>                 |
| Atkin & Fox, 1980, [6], pp.62, 63             |
| Chung, 1996, [21], p.102                      |
| Fung, 1965, [32], p.449                       |
| Fung, 1993, [35], pp.300, 301                 |
| Green & Adkins, 1960, [37], pp.5-28           |
| Green & Zerna, 1954, [38], p.71               |
| Lemaitre & Chaboche, 1990, [68], pp. 122, 123 |
| Malvern, 1969, [73], pp.283, 284              |
| Marsden & Hughes, 1983, [75], pp.197–217      |
| Spencer, 1980, [110], pp.138, 139             |
| Truesdell, 1966, [117], pp.54, 55             |
| <b>2.) Inconsistent formulæ</b>               |
| Fung, 1993, [35], p.269                       |
| Holzapfel, 2000, [44], pp.209, 210            |
| <b>3.) Potentially ambiguous formulæ</b>      |
| Humphrey, 2002, [50], pp.91–92                |
| Hunter, 1976, [55], pp.152–154                |
| Jaunzemis, 1967, [60], p.299                  |
| Mase, 1970, [76], p.141                       |
| Sokolnikoff, 1964, [109], p.339               |



# Appendix B

## Additional Data for Homogeneous Model

This chapter gives additional data for the homogeneous model, i.e. Sec.(B.1) shows a sample file of the homogeneous model for experiment 3 in Mathematica format (comments are in capital letters), version 5.1, whereas Sec.(B.2) shows all graphs for all laws and all experiments.

### B.1 Example File for Homogeneous Model

ZX SHEAR, "Z" INDICATES THE NORMAL OF THE TOP FACE, AND "X" INDICATES THE DIRECTION IN WHICH THIS FACE IS SHEARED. ALL IS DESCRIBED IN THE FNS (MNS) SYSTEM

```
Off[General::spell1]
Off[General::spell]
<<LinearAlgebra`MatrixManipulation`

DEFORMATION GRADIENT AND GREEN STRAIN

FNS = 1, 0, 0, 0, 1, 0, 0, k, 1;
FNF = 1, k, 0, 0, 1, 0, 0, 0, 1;
FFN = 1, 0, 0, k, 1, 0, 0, 0, 1;
FFS = 1, 0, 0, 0, 1, 0, k, 0, 1;
FSF = 1, 0, k, 0, 1, 0, 0, 0, 1;
FSN = 1, 0, 0, 0, 1, k, 0, 0, 1;

EENS = (1/2)*(Transpose[FNS] . FNS - IdentityMatrix[3]);
EENF = (1/2)*(Transpose[FNF] . FNF - IdentityMatrix[3]);
EEFN = (1/2)*(Transpose[FFN] . FFN - IdentityMatrix[3]);
EEFS = (1/2)*(Transpose[FFS] . FFS - IdentityMatrix[3]);
EESF = (1/2)*(Transpose[FSF] . FSF - IdentityMatrix[3]);
EESN = (1/2)*(Transpose[FSN] . FSN - IdentityMatrix[3]);
```

GENERAL STRAIN ENERGY FUNCTION — COSTA LAW

```

W[Emm_, Emn_, Ems_, Enm_, Enn_, Ens_, Esm_, Esn_, Ess_] :=
(1/2)*c1*Exp[
    cmm*Emm2 + cnn*Enn2 + css*Ess2 + 2*cmn*((1/2)*(Emn + Enm))2 +
    2*cms*((1/2)*(Ems + Esm))2 + 2*cns*((1/2)*(Ens + Esn))2
]

STRESS-STRAIN-RELATIONSHIP

SS[{Emm_, Emn_, Ems_}, {Enm_, Enn_, Ens_}, {Esm_, Esn_, Ess_}] :=
{{D[W[Emm, Emn, Ems, Enm, Enn, Ens, Esm, Esn, Ess], Emn],
D[W[Emm, Emn, Ems, Enm, Enn, Ens, Esm, Esn, Ess], Esm],
D[W[Emm, Emn, Ems, Enm, Enn, Ens, Esm, Esn, Ess], Ems]},
{D[W[Emm, Emn, Ems, Enm, Enn, Ens, Esm, Esn, Ess], Enm],
D[W[Emm, Emn, Ems, Enm, Enn, Ens, Esm, Esn, Ess], Enn],
D[W[Emm, Emn, Ems, Enm, Enn, Ens, Esm, Esn, Ess], Ens]},
{D[W[Emm, Emn, Ems, Enm, Enn, Ens, Esm, Esn, Ess], Esm],
D[W[Emm, Emn, Ems, Enm, Enn, Ens, Esm, Esn, Ess], Esn],
D[W[Emm, Emn, Ems, Enm, Enn, Ens, Esm, Esn, Ess], Ess]}}

SSEval[{Emm_, Emn_, Ems_}, {Enm_, Enn_, Ens_}, {Esm_, Esn_, Ess_}] :=
Evaluate[SS[{Emm, Emn, Ems}, {Enm, Enn, Ens}, {Esm, Esn, Ess}]]

SSEvalNS = SSEval[EENS];
SSEvalNF = SSEval[EENF];
SSEvalFN = SSEval[EEFN];
SSEvalFS = SSEval[EEFS];
SSEvalSF = SSEval[EESF];
SSEvalSN = SSEval[EESN];

CALCULATION OF FIRST PK

PPNS = FNS . SSEvalNS;
PPNF = FNF . SSEvalNF;
PPFN = FFN . SSEvalFN;
PPFS = FFS . SSEvalFS;
PPSF = FSP . SSEvalSF;
PPSN = FSN . SSEvalSN;

FORCE CALCULATION ON TOP FACE, AREA TO BE DEFINED LATER ON

NormalVectorNS = 0, AreaNS, 0;
NormalVectorNF = 0, AreaNF, 0;
NormalVectorFN = AreaFN, 0, 0;
NormalVectorFS = AreaFS, 0, 0;
NormalVectorSF = 0, 0, AreaSF;
NormalVectorSN = 0, 0, AreaSN;

tNS = PPNS . NormalVectorNS;
tNF = PPNF . NormalVectorNF;
tFN = PPFN . NormalVectorFN;
tFS = PPFS . NormalVectorFS;
tSF = PPSF . NormalVectorSF;
tSN = PPSN . NormalVectorSN;

tNSFunct[khelp_] := Evaluate[tNS /. {k -> khelp}];
tNSFunctX[k_] := Evaluate[tNSFunct[khelp] /. {khelp -> k}][[3]];
tNSFunctZ[k_] := Evaluate[tNSFunct[khelp] /. {khelp -> k}][[2]];
tNFFunct[khelp_] := Evaluate[tNF /. {k -> khelp}];
tNFFunctX[k_] := Evaluate[tNFFunct[khelp] /. {khelp -> k}][[1]];
tNFFunctZ[k_] := Evaluate[tNFFunct[khelp] /. {khelp -> k}][[2]];
ModelOutcomeForceNS[{γ1_, γnn_, γns_}, k_] :=
    Evaluate[tNS /. {c1 -> γ1, cnn -> γnn, cns -> γns}]
ModelOutcomeForceNF[{γ1_, γnn_, γns_}, k_] :=
    Evaluate[tNF /. {c1 -> γ1, cmn -> γnn, cnn -> γnn}]

tFNFunct[khelp_] := Evaluate[tFN /. {k -> khelp}];
tFNFunctX[k_] := Evaluate[tFNFunct[khelp] /. {khelp -> k}][[2]];
tFNFunctZ[k_] := Evaluate[tFNFunct[khelp] /. {khelp -> k}][[1]];
tFSFunct[khelp_] := Evaluate[tFS /. {k -> khelp}];
tFSFunctX[k_] := Evaluate[tFSFunct[khelp] /. {khelp -> k}][[3]];
tFSFunctZ[k_] := Evaluate[tFSFunct[khelp] /. {khelp -> k}][[1]];
ModelOutcomeForceFN[{γ1_, γmm_, γmn_}, k_] :=
    Evaluate[tFN /. {c1 -> γ1, cmm -> γmm, cmn -> γmn}]
ModelOutcomeForceFS[{γ1_, γmm_, γms_}, k_] :=
    Evaluate[tFS /. {c1 -> γ1, cmm -> γmm, cms -> γms}]

tSFFunct[khelp_] := Evaluate[tSF /. {k -> khelp}];
tSFFunctX[k_] := Evaluate[tSFFunct[khelp] /. {khelp -> k}][[1]];
tSFFunctZ[k_] := Evaluate[tSFFunct[khelp] /. {khelp -> k}][[3]];
tSNFunct[khelp_] := Evaluate[tSN /. {k -> khelp}];
tSNFunctX[k_] := Evaluate[tSNFunct[khelp] /. {khelp -> k}][[2]];
tSNFunctZ[k_] := Evaluate[tSNFunct[khelp] /. {khelp -> k}][[3]];
ModelOutcomeForceSF[{γ1_, γms_, γss_}, k_] :=

```

```

Evaluate[tSF /. {c1 ->  $\gamma_1$ , cms ->  $\gamma_{ms}$ , css ->  $\gamma_{ss}$ }]
ModelOutcomeForceSN[{ $\gamma_1$ _,  $\gamma_{ms}$ _,  $\gamma_{ss}$ _}, k_] :=
Evaluate[tSN /. {c1 ->  $\gamma_1$ , cns ->  $\gamma_{ns}$ , css ->  $\gamma_{ss}$ }]

DIMENSIONS FOR THE CUBES, MNS COORDINATE SYSTEM, EXPERIMENTAL FORCE GENERATION

MdimNS = 3.4; NdimNS = 3.; SdimNS = 4.6; AreaNS = MdimNS*SdimNS;
MdimNS = 3.4; NdimNS = 3.; SdimNS = 4.6; AreaNF = MdimNS*SdimNS;
MdimFN = 3.4; NdimFN = 3.4; SdimFN = 3.4; AreaFN = NdimFN*SdimFN;
MdimFS = 3.4; NdimFS = 3.4; SdimFS = 3.4; AreaFS = MdimFS*SdimFS;
MdimSF = 3.2; NdimSF = 2.7; SdimSF = 3.1; AreaSF = MdimSF*SdimSF;
MdimSN = 3.2; NdimSN = 2.7; SdimSN = 3.1; AreaSN = MdimSN*SdimSN;

SetDirectory["E:\\Mathematica\\ HomogeneousFitting\\ SP17"];

NSFullExperimentalData = Import["NSFullExperimentalData.txt", "Table"];
NFFullExperimentalData = Import["NFFullExperimentalData.txt", "Table"];
FNFullExperimentalData = Import["FNFullExperimentalData.txt", "Table"];
FSFullExperimentalData = Import["FSFullExperimentalData.txt", "Table"];
SFFullExperimentalData = Import["SFFullExperimentalData.txt", "Table"];
SNFullExperimentalData = Import["SNFullExperimentalData.txt", "Table"];

NSExperimentalDisplacement = Transpose[NSFullExperimentalData][[1, All]];
NSExperimentalXForce = Transpose[NSFullExperimentalData][[2, All]];
NSExperimentalZForce = Transpose[NSFullExperimentalData][[3, All]];
NFFExperimentalDisplacement = Transpose[NFFullExperimentalData][[1, All]];
NFFExperimentalXForce = Transpose[NFFullExperimentalData][[2, All]];
NFFExperimentalZForce = Transpose[NFFullExperimentalData][[3, All]];
FNExperimentalDisplacement = Transpose[FNFullExperimentalData][[1, All]];
FNExperimentalXForce = Transpose[FNFullExperimentalData][[2, All]];
FNExperimentalZForce = Transpose[FNFullExperimentalData][[3, All]];
FSExperimentalDisplacement = Transpose[FSFullExperimentalData][[1, All]];
FSExperimentalXForce = Transpose[FSFullExperimentalData][[2, All]];
FSExperimentalZForce = Transpose[FSFullExperimentalData][[3, All]];
SFFExperimentalDisplacement = Transpose[SFFullExperimentalData][[1, All]];
SFFExperimentalXForce = Transpose[SFFullExperimentalData][[2, All]];
SFFExperimentalZForce = Transpose[SFFullExperimentalData][[3, All]];
SNExperimentalDisplacement = Transpose[SNFullExperimentalData][[1, All]];
SNExperimentalXForce = Transpose[SNFullExperimentalData][[2, All]];
SNExperimentalZForce = Transpose[SNFullExperimentalData][[3, All]];

NSMaxExperimentalDisplacement = Max[Abs[NSFullExperimentalData][[All, 1]]];
NFMMaxExperimentalDisplacement = Max[Abs[NFFullExperimentalData][[All, 1]]];
FNMMaxExperimentalDisplacement = Max[Abs[FNFullExperimentalData][[All, 1]]];
FSMMaxExperimentalDisplacement = Max[Abs[FSFullExperimentalData][[All, 1]]];
SFMMaxExperimentalDisplacement = Max[Abs[SFFullExperimentalData][[All, 1]]];
SNMMaxExperimentalDisplacement = Max[Abs[SNFullExperimentalData][[All, 1]]];

GRAPHS

t1 = 0.015;

NSExpPlot = ListPlot[Transpose[{NSExperimentalDisplacement,
NSExperimentalXForce}], AxesLabel -> {d/mm, Subscript[F, NSx]/mN},
TextStyle -> {FontSize -> 5},
Ticks -> {{{-1.5, -1.5, t1}, {-0.5, -0.5, t1}, {0.5, 0.5, t1},
{1.5, 1.5, t1}}, {{-40, -40, t1}, {-20, -20, t1}, {20, 20, t1}, {40, 40, t1}}];
NSExpZPlot = ListPlot[Transpose[{NSExperimentalDisplacement,
NSExperimentalZForce}], AxesLabel -> {d/mm, Subscript[F, NSz]/mN},
TextStyle -> {FontSize -> 5},
Ticks -> {{{-1.5, -1.5, t1}, {-0.5, -0.5, t1}, {0.5, 0.5, t1},
{1.5, 1.5, t1}}, {{5, 5, t1}, {15, 15, t1}, {25, 25, t1}}];
NFFExpPlot = ListPlot[Transpose[{NFFExperimentalDisplacement,
NFFExperimentalXForce}], AxesLabel -> {d/mm, Subscript[F, NFX]/mN},
TextStyle -> {FontSize -> 5},
Ticks -> {{{-1.5, -1.5, t1}, {-0.5, -0.5, t1}, {0.5, 0.5, t1},
{1.5, 1.5, t1}}, {{-60, -60, t1}, {-30, -30, t1}, {30, 30, t1}, {60, 60, t1}}];
NFFExpZPlot = ListPlot[Transpose[{NFFExperimentalDisplacement,
NFFExperimentalZForce}], AxesLabel -> {d/mm, Subscript[F, NFz]/mN},
TextStyle -> {FontSize -> 5},
Ticks -> {{{-1.5, -1.5, t1}, {-0.5, -0.5, t1}, {0.5, 0.5, t1},
{1.5, 1.5, t1}}, {{20, 20, t1}, {40, 40, t1}}];
FNExpPlot = ListPlot[Transpose[{FNExperimentalDisplacement,
FNExperimentalXForce}], AxesLabel -> {d/mm, Subscript[F, FNx]/mN},
TextStyle -> {FontSize -> 5},
Ticks -> {{{-1.5, -1.5, t1}, {-0.5, -0.5, t1}, {0.5, 0.5, t1},
{1.5, 1.5, t1}}, {{-70, -70, t1}, {-35, -35, t1}, {35, 35, t1}, {70, 70, t1}}];
FNExpZPlot = ListPlot[Transpose[{FNExperimentalDisplacement,
FNExperimentalZForce}], AxesLabel -> {d/mm, Subscript[F, FNz]/mN},
TextStyle -> {FontSize -> 5},
Ticks -> {{{-1.5, -1.5, t1}, {-0.5, -0.5, t1}, {0.5, 0.5, t1},
{1.5, 1.5, t1}}, {{20, 20, t1}, {40, 40, t1}}];
FSExpPlot = ListPlot[Transpose[{FSExperimentalDisplacement,
FSExperimentalXForce}], AxesLabel -> {d/mm, Subscript[F, FSx]/mN},
TextStyle -> {FontSize -> 5},
Ticks -> {{{-1.5, -1.5, t1}, {-0.5, -0.5, t1}, {0.5, 0.5, t1},
{1.5, 1.5, t1}}, {{20, 20, t1}, {40, 40, t1}}];
FSExpZPlot = ListPlot[Transpose[{FSExperimentalDisplacement,
FSExperimentalZForce}], AxesLabel -> {d/mm, Subscript[F, FSz]/mN},
TextStyle -> {FontSize -> 5},
Ticks -> {{{-1.5, -1.5, t1}, {-0.5, -0.5, t1}, {0.5, 0.5, t1},
{1.5, 1.5, t1}}, {{20, 20, t1}, {40, 40, t1}}];

```

```

FSExpZPlot = ListPlot[Transpose[{FSExpZPlotDisplacement,
FSExpZPlotForce}], AxesLabel -> {d/mm, Subscript[F, FSz]/mN},
TextStyl -> {FontSize -> 5},
Ticks -> {{{-1.5, -1.5, t1}, {-0.5, -0.5, t1}, {0.5, 0.5, t1},
{1.5, 1.5, t1}}, {{-80, -80, t1}, {-40, -40, t1}, {40, 40, t1}, {80, 80, t1}}];
FSExpXPlot = ListPlot[Transpose[{FSExpXPlotDisplacement,
FSExpXPlotForce}], AxesLabel -> {d/mm, Subscript[F, FSx]/mN},
TextStyl -> {FontSize -> 5},
Ticks -> {{{-1.5, -1.5, t1}, {-0.5, -0.5, t1}, {0.5, 0.5, t1},
{1.5, 1.5, t1}}, {{35, 35, t1}, {70, 70, t1}}];
SFExpZPlot = ListPlot[Transpose[{SFExpZPlotDisplacement,
SFExpZPlotForce}], AxesLabel -> {d/mm, Subscript[F, SFz]/mN},
TextStyl -> {FontSize -> 5},
Ticks -> {{{-1.5, -1.5, t1}, {-0.5, -0.5, t1}, {0.5, 0.5, t1},
{1.5, 1.5, t1}}, {{-40, -40, t1}, {-20, -20, t1}, {20, 20, t1}, {40, 40, t1}}];
SFExpXPlot = ListPlot[Transpose[{SFExpXPlotDisplacement,
SFExpXPlotForce}], AxesLabel -> {d/mm, Subscript[F, SFx]/mN},
TextStyl -> {FontSize -> 5},
Ticks -> {{{-1.5, -1.5, t1}, {-0.5, -0.5, t1}, {0.5, 0.5, t1},
{1.5, 1.5, t1}}, {{7.5, 7.5, t1}, {15, 15, t1}}];
SNExpZPlot = ListPlot[Transpose[{SNExpZPlotDisplacement,
SNExpZPlotForce}], AxesLabel -> {d/mm, Subscript[F, SNz]/mN},
TextStyl -> {FontSize -> 5},
Ticks -> {{{-1.5, -1.5, t1}, {-0.5, -0.5, t1}, {0.5, 0.5, t1},
{1.5, 1.5, t1}}, {{-40, -40, t1}, {-20, -20, t1}, {20, 20, t1}, {40, 40, t1}}];
SNExpXPlot = ListPlot[Transpose[{SNExpXPlotDisplacement,
SNExpXPlotForce}], AxesLabel -> {d/mm, Subscript[F, SNx]/mN},
TextStyl -> {FontSize -> 5},
Ticks -> {{{-1.5, -1.5, t1}, {-0.5, -0.5, t1}, {0.5, 0.5, t1},
{1.5, 1.5, t1}}, {{-20, -20, t1}, {-10, -10, t1}, {10, 10, t1}, {20, 20, t1}}];
NSModelXPlot = Plot[ModelOutcomeForceNS[θInitGuessNS,
k/(2*NSMaxExperimentalDisplacement)][[3]],
{k, -NSMaxExperimentalDisplacement, NSMaxExperimentalDisplacement}];
NSModelZPlot = Plot[ModelOutcomeForceNS[θInitGuessNS,
k/(2*NSMaxExperimentalDisplacement)][[2]],
{k, -NSMaxExperimentalDisplacement, NSMaxExperimentalDisplacement}];
NFModelXPlot = Plot[ModelOutcomeForceNF[θInitGuessNF,
k/(2*NFMaxExperimentalDisplacement)][[3]],
{k, -NFMaxExperimentalDisplacement, NFMaxExperimentalDisplacement}];
NFModelZPlot = Plot[ModelOutcomeForceNF[θInitGuessNF,
k/(2*NFMaxExperimentalDisplacement)][[2]],
{k, -NFMaxExperimentalDisplacement, NFMaxExperimentalDisplacement}];
FNModelXPlot = Plot[ModelOutcomeForceFN[θInitGuessFN,
k/(2*FNMaxExperimentalDisplacement)][[3]],
{k, -FNMaxExperimentalDisplacement, FNMaxExperimentalDisplacement}];
FNModelZPlot = Plot[ModelOutcomeForceFN[θInitGuessFN,
k/(2*FNMaxExperimentalDisplacement)][[2]],
{k, -FNMaxExperimentalDisplacement, FNMaxExperimentalDisplacement}];
FSModelXPlot = Plot[ModelOutcomeForceFS[θInitGuessFS,
k/(2*FSMaxExperimentalDisplacement)][[3]],
{k, -FSMaxExperimentalDisplacement, FSMaxExperimentalDisplacement}];
FSModelZPlot = Plot[ModelOutcomeForceFS[θInitGuessFS,
k/(2*FSMaxExperimentalDisplacement)][[2]],
{k, -FSMaxExperimentalDisplacement, FSMaxExperimentalDisplacement}];
SFModelXPlot = Plot[ModelOutcomeForceSF[θInitGuessSF,
k/(2*SFMMaxExperimentalDisplacement)][[3]],
{k, -SFMMaxExperimentalDisplacement, SFMMaxExperimentalDisplacement}];
SFModelZPlot = Plot[ModelOutcomeForceSF[θInitGuessSF,
k/(2*SFMMaxExperimentalDisplacement)][[2]],
{k, -SFMMaxExperimentalDisplacement, SFMMaxExperimentalDisplacement}];
SNModelXPlot = Plot[ModelOutcomeForceSN[θInitGuessSN,
k/(2*SNMMaxExperimentalDisplacement)][[3]],
{k, -SNMMaxExperimentalDisplacement, SNMMaxExperimentalDisplacement}];
SNModelZPlot = Plot[ModelOutcomeForceSN[θInitGuessSN,
k/(2*SNMMaxExperimentalDisplacement)][[2]],
{k, -SNMMaxExperimentalDisplacement, SNMMaxExperimentalDisplacement}];

NSXCombPlot = Show[{NSExpZPlot, NSModelXPlot}, DisplayFunction -> Identity];
NSZCombPlot = Show[{NSExpXPlot, NSModelZPlot}, DisplayFunction -> Identity];
NFXCombPlot = Show[{NFExpZPlot, NFModelXPlot}, DisplayFunction -> Identity];
NFZCombPlot = Show[{NFExpXPlot, NFModelZPlot}, DisplayFunction -> Identity];
FNXCombPlot = Show[{FNExpZPlot, FNModelXPlot}, DisplayFunction -> Identity];
FNZCombPlot = Show[{FNExpXPlot, FNModelZPlot}, DisplayFunction -> Identity];
FSXCombPlot = Show[{FSExpZPlot, FSModelXPlot}, DisplayFunction -> Identity];
FSZCombPlot = Show[{FSExpXPlot, FSModelZPlot}, DisplayFunction -> Identity];
SFXCombPlot = Show[{SFExpZPlot, SFModelXPlot}, DisplayFunction -> Identity];
SFZCombPlot = Show[{SFExpXPlot, SFModelZPlot}, DisplayFunction -> Identity];

```

```

SFZCombPlot = Show[{SFExpZPlot, SFModelZPlot}, DisplayFunction -> Identity];
SNXCombPlot = Show[{SNExpXPlot, SNModelXPlot}, DisplayFunction -> Identity];
SNZCombPlot = Show[{SNExpZPlot, SNModelZPlot}, DisplayFunction -> Identity];

Show[GraphicsArray[{{NSXCombPlot, NSZCombPlot}, {NFXCombPlot, NFZCombPlot},
  {FNXCombPlot, FNZCombPlot}, {FSXCombPlot, FSZCombPlot},
  {SFXCombPlot, SFZCombPlot}, {SNXCombPlot, SNZCombPlot}}]]
;

CREATE COMPLETE FORCE VECTOR FOR ALL LOAD STEPS

NSLegendreData = Import["NSLegendreData.txt", "Table"];
NSLegendreGaussWeights = Transpose[NSLegendreData][[1,A11]];
NSLegendreGaussPoints = Transpose[NSLegendreData][[2,A11]];
NSEXPXForceAtGaussPoints = Transpose[NSLegendreData][[3,A11]];
NSEXPZForceAtGaussPoints = Transpose[NSLegendreData][[4,A11]];
NSArea = Flatten[Import["NSArea.txt", "Table"]];

NFLegendreData = Import["NFLegendreData.txt", "Table"];
NFLegendreGaussWeights = Transpose[NFLegendreData][[1,A11]];
NFLegendreGaussPoints = Transpose[NFLegendreData][[2,A11]];
NFEXPXForceAtGaussPoints = Transpose[NFLegendreData][[3,A11]];
NFEXPZForceAtGaussPoints = Transpose[NFLegendreData][[4,A11]];
NFArea = Flatten[Import["NFArea.txt", "Table"]];

SFLegendreData = Import["SFLegendreData.txt", "Table"];
SFLegendreGaussWeights = Transpose[SFLegendreData][[1,A11]];
SFLegendreGaussPoints = Transpose[SFLegendreData][[2,A11]];
SFEXPXForceAtGaussPoints = Transpose[SFLegendreData][[3,A11]];
SFEXPZForceAtGaussPoints = Transpose[SFLegendreData][[4,A11]];
SFArea = Flatten[Import["SFArea.txt", "Table"]];

SNLegendreData = Import["SNLegendreData.txt", "Table"];
SNLegendreGaussWeights = Transpose[SNLegendreData][[1,A11]];
SNLegendreGaussPoints = Transpose[SNLegendreData][[2,A11]];
SNEXPXForceAtGaussPoints = Transpose[SNLegendreData][[3,A11]];
SNEXPZForceAtGaussPoints = Transpose[SNLegendreData][[4,A11]];
SNArea = Flatten[Import["SNArea.txt", "Table"]];

FNLegendreData = Import["FNLegendreData.txt", "Table"];
FNLegendreGaussWeights = Transpose[FNLegendreData][[1,A11]];
FNLegendreGaussPoints = Transpose[FNLegendreData][[2,A11]];
FNEXPXForceAtGaussPoints = Transpose[FNLegendreData][[3,A11]];
FNEXPZForceAtGaussPoints = Transpose[FNLegendreData][[4,A11]];
FNArea = Flatten[Import["FNArea.txt", "Table"]];

FSLegendreData = Import["FSLegendreData.txt", "Table"];
FSLegendreGaussWeights = Transpose[FSLegendreData][[1,A11]];
FSLegendreGaussPoints = Transpose[FSLegendreData][[2,A11]];
FSEXPXForceAtGaussPoints = Transpose[FSLegendreData][[3,A11]];
FSEXPZForceAtGaussPoints = Transpose[FSLegendreData][[4,A11]];
FSArea = Flatten[Import["FSArea.txt", "Table"]];

INITIALIZE COMPLETE FORCE VECTOR

NSModelXForceAtGaussPoints =
  Flatten[Transpose[{tNSFunctX[NSLegendreGaussPoints/
    (2*NSMaxExperimentalDisplacement)}]]];
NSModelZForceAtGaussPoints =
  Flatten[Transpose[{tNSFunctZ[NSLegendreGaussPoints/
    (2*NSMaxExperimentalDisplacement)}]]];
NFMModelXForceAtGaussPoints =
  Flatten[Transpose[{tNFFunctX[NFLegendreGaussPoints/
    (2*NFMMaxExperimentalDisplacement)}]]];
NFMModelZForceAtGaussPoints =
  Flatten[Transpose[{tNFFunctZ[NFLegendreGaussPoints/
    (2*NFMMaxExperimentalDisplacement)}]]];
SFModelXForceAtGaussPoints =
  Flatten[Transpose[{tSFFunctX[SFLegendreGaussPoints/
    (2*SFMMaxExperimentalDisplacement)}]]];
SFModelZForceAtGaussPoints =
  Flatten[Transpose[{tSFFunctZ[SFLegendreGaussPoints/
    (2*SFMMaxExperimentalDisplacement)}]]];
SNModelXForceAtGaussPoints =
  Flatten[Transpose[{tSNFunctX[SNLegendreGaussPoints/
    (2*SNMaxExperimentalDisplacement)}]]];
SNModelZForceAtGaussPoints =
  Flatten[Transpose[{tSNFunctZ[SNLegendreGaussPoints/
    (2*SNMaxExperimentalDisplacement)}]]];
FNModelXForceAtGaussPoints =
  Flatten[Transpose[{tFNFunctX[FNLegendreGaussPoints/
    (2*FNMaxExperimentalDisplacement)}]]];

```



```

FNModelZForceAtGaussPoints =
  Flatten[Transpose[{tFNFuncZ[FNLegendreGaussPoints/
    (2*FNMaxExperimentalDisplacement)]]];
FSModelXForceAtGaussPoints =
  Flatten[Transpose[{tFSFuncX[FSLegendreGaussPoints/
    (2*FSMaxExperimentalDisplacement)]]];
FSModelZForceAtGaussPoints =
  Flatten[Transpose[{tFSFuncZ[FSLegendreGaussPoints/
    (2*FSMaxExperimentalDisplacement)]]];

NSXDiffForce = N[NSModelXForceAtGaussPoints] - NSEXPXForceAtGaussPoints;
NSZDiffForce = N[NSModelZForceAtGaussPoints] - NSEXPZForceAtGaussPoints;
NFXDiffForce = N[NFModelXForceAtGaussPoints] - NFEEXPXForceAtGaussPoints;
NFZDiffForce = N[NFModelZForceAtGaussPoints] - NFEEXPZForceAtGaussPoints;
FNXDiffForce = N[FNModelXForceAtGaussPoints] - FNEEXPXForceAtGaussPoints;
FNZDiffForce = N[FNModelZForceAtGaussPoints] - FNEEXPZForceAtGaussPoints;
FSXDiffForce = N[FSModelXForceAtGaussPoints] - FSEEXPXForceAtGaussPoints;
FSZDiffForce = N[FSModelZForceAtGaussPoints] - FSEEXPZForceAtGaussPoints;
SFXDiffForce = N[SFModelXForceAtGaussPoints] - SFEEXPXForceAtGaussPoints;
SFZDiffForce = N[SFModelZForceAtGaussPoints] - SFEEXPZForceAtGaussPoints;
SNXDiffForce = N[SNModelXForceAtGaussPoints] - SNEEXPXForceAtGaussPoints;
SNZDiffForce = N[SNModelZForceAtGaussPoints] - SNEEXPZForceAtGaussPoints;

```

COMPUTING PSEUDO ENERGY

```

NSXForceObjective = NSLegendreGaussWeights . NSXDiffForce2;
NSZForceObjective = NSLegendreGaussWeights . NSZDiffForce2;
NFXForceObjective = NFLegendreGaussWeights . NFXDiffForce2;
NFZForceObjective = NFLegendreGaussWeights . NFZDiffForce2;
FNXForceObjective = FNLegendreGaussWeights . FNXDiffForce2;
FNZForceObjective = FNLegendreGaussWeights . FNZDiffForce2;
FSXForceObjective = FSLegendreGaussWeights . FSXDiffForce2;
FSZForceObjective = FSLegendreGaussWeights . FSZDiffForce2;
SFXForceObjective = SFLegendreGaussWeights . SFXDiffForce2;
SFZForceObjective = SFLegendreGaussWeights . SFZDiffForce2;
SNXForceObjective = SNLegendreGaussWeights . SNXDiffForce2;
SNZForceObjective = SNLegendreGaussWeights . SNZDiffForce2;

```

OBJECTIVE FUNCTION

```

Ω = (1/2)*(NSXForceObjective + NSZForceObjective + NFXForceObjective +
  NFZForceObjective + FNXForceObjective + FNZForceObjective +
  FSXForceObjective + FSZForceObjective + SFXForceObjective +
  SFZForceObjective + SNXForceObjective + SNZForceObjective);

```

```

GradΩ1 = D[Ω, c1];
GradΩ2 = D[Ω, cmm];
GradΩ3 = D[Ω, cmm];
GradΩ4 = D[Ω, cms];
GradΩ5 = D[Ω, cmm];
GradΩ6 = D[Ω, cns];
GradΩ7 = D[Ω, css];

```

```

GradΩ = {GradΩ1, GradΩ2, GradΩ3, GradΩ4,
  GradΩ5, GradΩ6, GradΩ7};

```

```

HessianΩ1 = D[GradΩ, c1];
HessianΩ2 = D[GradΩ, cmm];
HessianΩ3 = D[GradΩ, cmm];
HessianΩ4 = D[GradΩ, cms];
HessianΩ5 = D[GradΩ, cmm];
HessianΩ6 = D[GradΩ, cns];
HessianΩ7 = D[GradΩ, css];

```

```

HessianΩ = N[Partition[Flatten[HessianΩ1, HessianΩ2, HessianΩ3,
  HessianΩ4, HessianΩ5, HessianΩ6, HessianΩ7], 7]];

```

DEFINE GRADIENT AND HESSIAN AS FUNCTIONS OF THE MATERIAL PARAMETERS

```

ΩFunct[{κ1_, κmm_, κmn_, κms_, κnn_, κns_, κss_}] :=
  Evaluate[Ω /. {c1 -> κ1, cmm -> κmm, cmm -> κmn, cms -> κms,
    cmm -> κnn, cns -> κns, css -> κss}];
GradΩFunct[{κ1_, κmm_, κmn_, κms_, κnn_, κns_, κss_}] :=
  Evaluate[GradΩ /. {c1 -> κ1, cmm -> κmm, cmm -> κmn, cms -> κms,
    cmm -> κnn, cns -> κns, css -> κss}];
HessianΩFunct[{κ1_, κmm_, κmn_, κms_, κnn_, κns_, κss_}] :=
  Evaluate[HessianΩ /. {c1 -> κ1, cmm -> κmm, cmm -> κmn, cms -> κms,
    cmm -> κnn, cns -> κns, css -> κss}];

```

INITIALIZATION OF MATERIAL PARAMETER VECTOR  $\theta$

```

 $\theta$ Prev = 2, 2, 2, 2, 2, 2, 2;
 $\Omega$ Now =  $\Omega$ Func[ $\theta$ Prev];
 $\Delta\Omega$  = 1;
 $\Delta\theta$  = 1;
i = 1;
 $\lambda$  = 1;

OPTIMISATION LOOP

While[ $\Delta\Omega$  >  $10^{-5}$  &&  $\Delta\theta$  >  $10^{-5}$ ,
   $\Omega$ Prev =  $\Omega$ Func[ $\theta$ Prev];
   $\Delta$  = -Inverse[Hessian $\Omega$ Func[ $\theta$ Prev] +  $\lambda$ *IdentityMatrix[7]] . Grad $\Omega$ Func[ $\theta$ Prev];
   $\theta$ Now = Flatten[ $\theta$ Prev +  $\Delta$ ];
   $\Omega$ Now =  $\Omega$ Func[ $\theta$ Now];
  If[ $\Omega$ Now <  $\Omega$ Prev,
     $\Delta\theta$  = ( $\theta$ Now -  $\theta$ Prev) . ( $\theta$ Now -  $\theta$ Prev);
     $\Delta\Omega$  = N[Abs[ $\Omega$ Now -  $\Omega$ Prev]];
     $\theta$ Prev =  $\theta$ Now;
    Print[ $\Omega$ Now];
    Print[ $\theta$ Now];
     $\lambda$  =  $\lambda/10$ ,
     $\lambda$  =  $10*\lambda$ 
  ];
  i = i + 1;
]

( Relative & ) Absolute Total Error— Total Error Over Total Area

 $\Omega$ Total =  $\Omega$ Now;
TotalEnergyContent = NSArea[[1]] + NSArea[[2]] + NFArea[[1]] + NFArea[[2]] +
  FNArea[[1]] + FNArea[[2]] + FSArea[[1]] + FSArea[[2]] +
  SFArea[[1]] + SFArea[[2]] + SNArea[[1]] + SNArea[[2]];
 $\Omega$ TotalRel =  $\Omega$ Now/TotalEnergyContent;

COVARIANCE MATRIX AND D - OPTIMALITY

Hessian $\Omega$ Func[ $\theta$ Prev]
Inverse[Hessian $\Omega$ Func[ $\theta$ Prev]]
DetH = Det[Hessian $\Omega$ Func[ $\theta$ Prev]]
CondH = MatrixConditionNumber[Inverse[Hessian $\Omega$ Func[ $\theta$ Prev]], 2]
MatrixConditionNumber[Hessian $\Omega$ Func[ $\theta$ Prev], 2]

M — OPTIMALITY

H = Hessian $\Omega$ Func[ $\theta$ Prev];
NormalisedH = Array[f, Dimensions[H]];
For[i = 1, i <= Length[H],
  For[j = 1, j <= Length[H],
    NormalisedH[[i,j]] = H[[i,j]]/Sqrt[H[[i,i]]*H[[j,j]]];
    j++;
  ];
  i++;
]
DetNormH = Det[NormalisedH]

PRINTOUT OPTIMIZED FORCE DISPLACEMENT CURVES

 $\theta$ InitGuess =  $\theta$ Prev;
 $\theta$ InitGuessNS = Flatten[Flatten[Take[ $\theta$ InitGuess, 1, 1]],
  Flatten[Take[ $\theta$ InitGuess, 5, 6]]];
 $\theta$ InitGuessNF = Flatten[Flatten[Take[ $\theta$ InitGuess, 1, 1]],
  Flatten[Take[ $\theta$ InitGuess, 3, 3]], Flatten[Take[ $\theta$ InitGuess, 5, 5]]];
 $\theta$ InitGuessFN = Take[ $\theta$ InitGuess, 1, 3];
 $\theta$ InitGuessFS = Flatten[Flatten[Take[ $\theta$ InitGuess, 1, 2]],
  Flatten[Take[ $\theta$ InitGuess, 4, 4]]];
 $\theta$ InitGuessSF = Flatten[Flatten[Take[ $\theta$ InitGuess, 1, 1]],
  Flatten[Take[ $\theta$ InitGuess, 4, 4]], Flatten[Take[ $\theta$ InitGuess, 7, 7]]];
 $\theta$ InitGuessSN = Flatten[Flatten[Take[ $\theta$ InitGuess, 1, 1]],
  Flatten[Take[ $\theta$ InitGuess, 6, 7]]];

NSModelXPlot = Plot[ModelOutcomeForceNS[ $\theta$ InitGuessNS,
  k/(2*NSMaxExperimentalDisplacement)][[3]],
  k, -NSMaxExperimentalDisplacement, NSMaxExperimentalDisplacement];
NSModelZPlot = Plot[ModelOutcomeForceNS[ $\theta$ InitGuessNS,
  k/(2*NSMaxExperimentalDisplacement)][[2]],
  k, -NSMaxExperimentalDisplacement, NSMaxExperimentalDisplacement];
NFMModelXPlot = Plot[ModelOutcomeForceNF[ $\theta$ InitGuessNF,
  k/(2*NFMMaxExperimentalDisplacement)][[1]],
  k, -NFMMaxExperimentalDisplacement, NFMMaxExperimentalDisplacement];
NFMModelZPlot = Plot[ModelOutcomeForceNF[ $\theta$ InitGuessNF,
  k/(2*NFMMaxExperimentalDisplacement)][[2]],
  k, -NFMMaxExperimentalDisplacement, NFMMaxExperimentalDisplacement];
FNMModelXPlot = Plot[ModelOutcomeForceFN[ $\theta$ InitGuessFN,
  k/(2*FNMMaxExperimentalDisplacement)][[2]],

```

```

k, -FNMaxExperimentalDisplacement, FNMaxExperimentalDisplacement];
FNModelZPlot = Plot[ModelOutcomeForceFN[θInitGuessFN,
k/(2*FNMaxExperimentalDisplacement)]][[1]],
k, -FNMaxExperimentalDisplacement, FNMaxExperimentalDisplacement];
FSModelXPlot = Plot[ModelOutcomeForceFS[θInitGuessFS,
k/(2*FSMaxExperimentalDisplacement)]][[3]],
k, -FSMaxExperimentalDisplacement, FSMaxExperimentalDisplacement];
FSModelZPlot = Plot[ModelOutcomeForceFS[θInitGuessFS,
k/(2*FSMaxExperimentalDisplacement)]][[1]],
k, -FSMaxExperimentalDisplacement, FSMaxExperimentalDisplacement];
SFModelXPlot = Plot[ModelOutcomeForceSF[θInitGuessSF,
k/(2*SFMaxExperimentalDisplacement)]][[4]],
k, -SFMaxExperimentalDisplacement, SFMaxExperimentalDisplacement];
SFModelZPlot = Plot[ModelOutcomeForceSF[θInitGuessSF,
k/(2*SFMaxExperimentalDisplacement)]][[3]],
k, -SFMaxExperimentalDisplacement, SFMaxExperimentalDisplacement];
SNModelXPlot = Plot[ModelOutcomeForceSN[θInitGuessSN,
k/(2*SNMaxExperimentalDisplacement)]][[2]],
k, -SNMaxExperimentalDisplacement, SNMaxExperimentalDisplacement];
SNModelZPlot = Plot[ModelOutcomeForceSN[θInitGuessSN,
k/(2*SNMaxExperimentalDisplacement)]][[3]],
k, -SNMaxExperimentalDisplacement, SNMaxExperimentalDisplacement];

NSXCombPlot = Show[{NSExpXPlot, NSModelXPlot}, DisplayFunction -> Identity];
NSZCombPlot = Show[{NSExpZPlot, NSModelZPlot}, DisplayFunction -> Identity];
NFXCombPlot = Show[{NFExpXPlot, NFModelXPlot}, DisplayFunction -> Identity];
NFZCombPlot = Show[{NFExpZPlot, NFModelZPlot}, DisplayFunction -> Identity];
FNXCombPlot = Show[{FNExpXPlot, FNModelXPlot}, DisplayFunction -> Identity];
FNZCombPlot = Show[{FNExpZPlot, FNModelZPlot}, DisplayFunction -> Identity];
FSXCombPlot = Show[{FSExpXPlot, FSModelXPlot}, DisplayFunction -> Identity];
FSZCombPlot = Show[{FSExpZPlot, FSModelZPlot}, DisplayFunction -> Identity];
SFXCombPlot = Show[{SFEExpXPlot, SFModelXPlot}, DisplayFunction -> Identity];
SFZCombPlot = Show[{SFEExpZPlot, SFModelZPlot}, DisplayFunction -> Identity];
SNXCombPlot = Show[{SNEExpXPlot, SNModelXPlot}, DisplayFunction -> Identity];
SNZCombPlot = Show[{SNEExpZPlot, SNModelZPlot}, DisplayFunction -> Identity];
FinalGraph = Show[GraphicsArray[Transpose[
{{NSXCombPlot, NSZCombPlot, NFXCombPlot, NFZCombPlot},
{FNXCombPlot, FNZCombPlot, FSXCombPlot, FSZCombPlot},
{SFXCombPlot, SFZCombPlot, SNXCombPlot, SNZCombPlot}}]]
]];

SetDirectory["E:\\Mathematica\\HomogeneousFitting\\GraphsForThesis"];
Export["CLSP17FinalGraphBW.eps", FinalGraph, "eps"];

SP17CLawAllData = Join[{ΩNow, ΩTotalRel, DetH, CondH, Re[DetNormH]}, Flatten[θPrev, 2]];

```

## **B.2 All Graphs for all Experiments, Homogeneous Model**

This section gives a list of all graphs obtained from the homogeneous model. They are listed in the order of experiments and within one experiment CL, SFL, PZL, TL, LECL. The dotted lines denote the experimental data and the solid lines denote the model results. This section is referred to in Sec.(6.3).

Graph of homogeneous model, experiment 1, CL

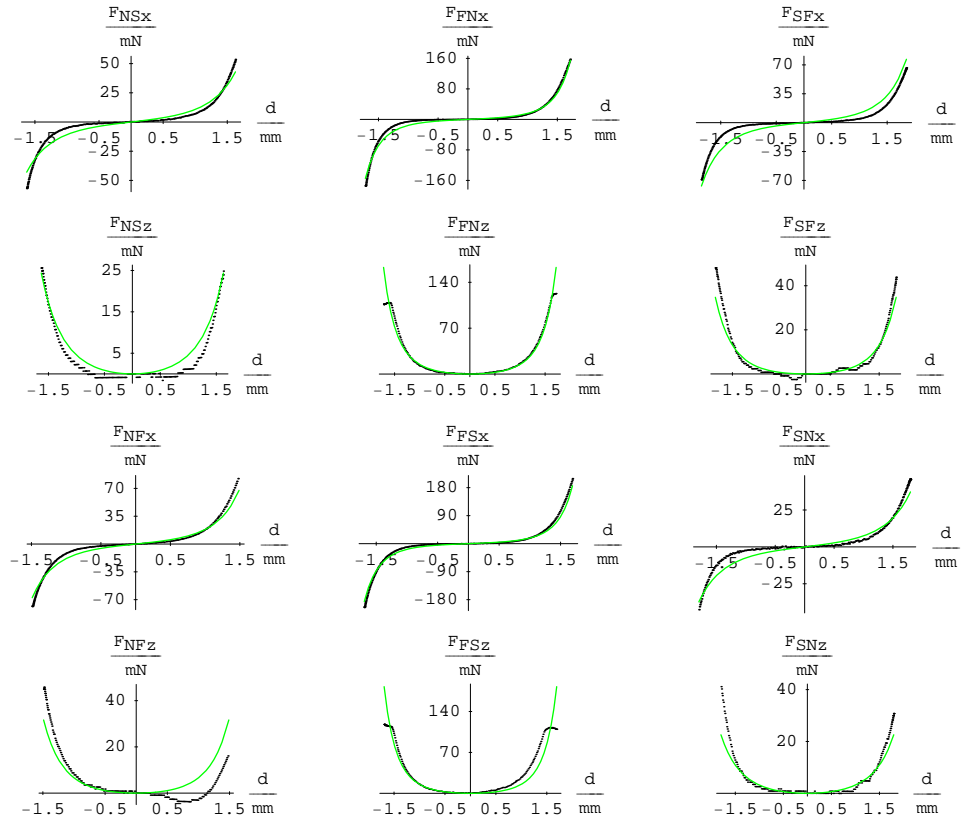


Figure B.1: This graph shows the result of the homogeneous model for experiment 1, CL.

Graph of homogeneous model, experiment 1, SFL

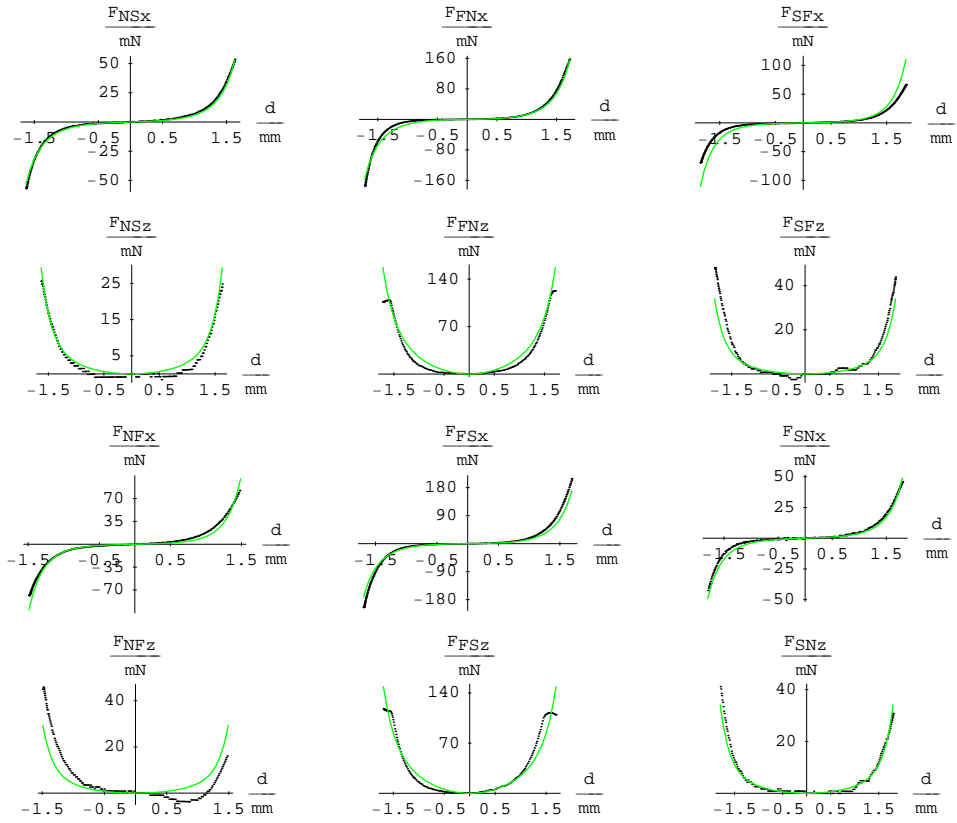


Figure B.2: This graph shows the result of the homogeneous model for experiment 1, SFL.

Graph of homogeneous model, experiment 1, PZL

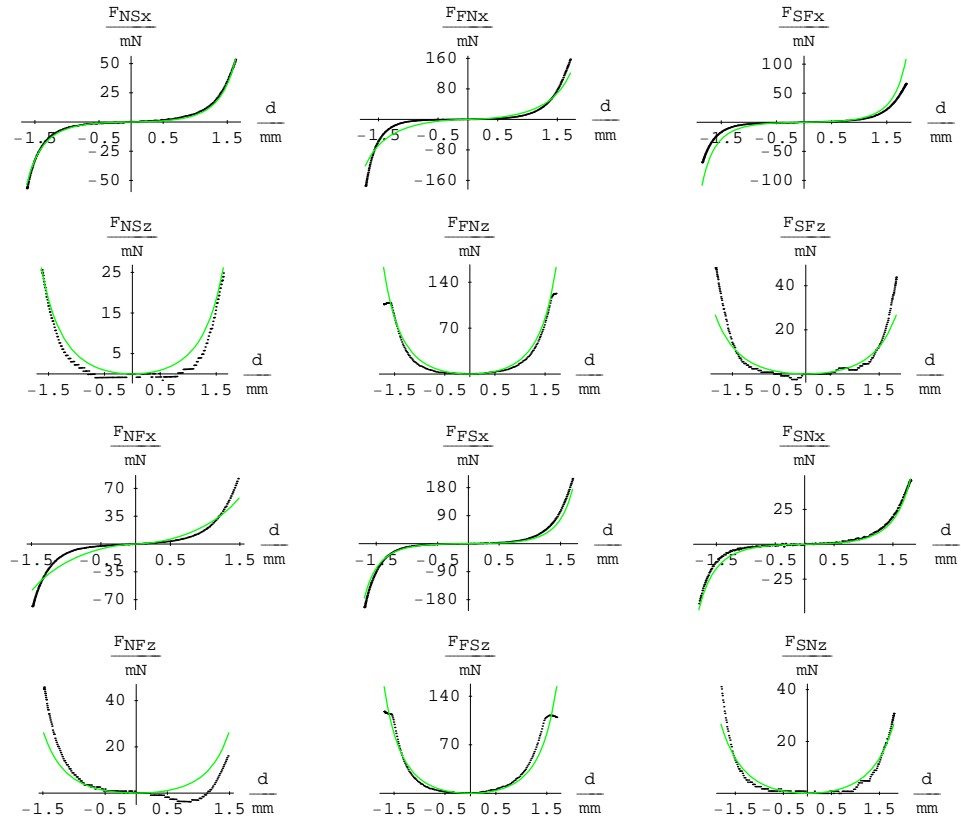


Figure B.3: This graph shows the result of the homogeneous model for experiment 1, PZL.

Graph of homogeneous model, experiment 1, TL

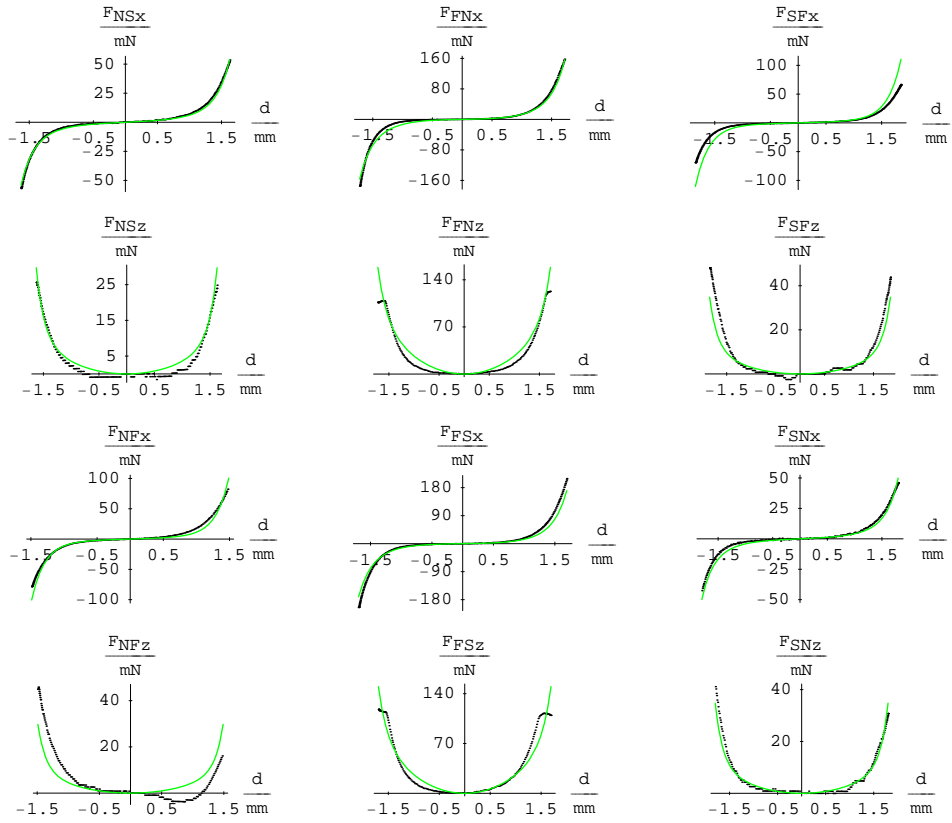


Figure B.4: This graph shows the result of the homogeneous model for experiment 1, TL.



Graph of homogeneous model, experiment 1, LECL

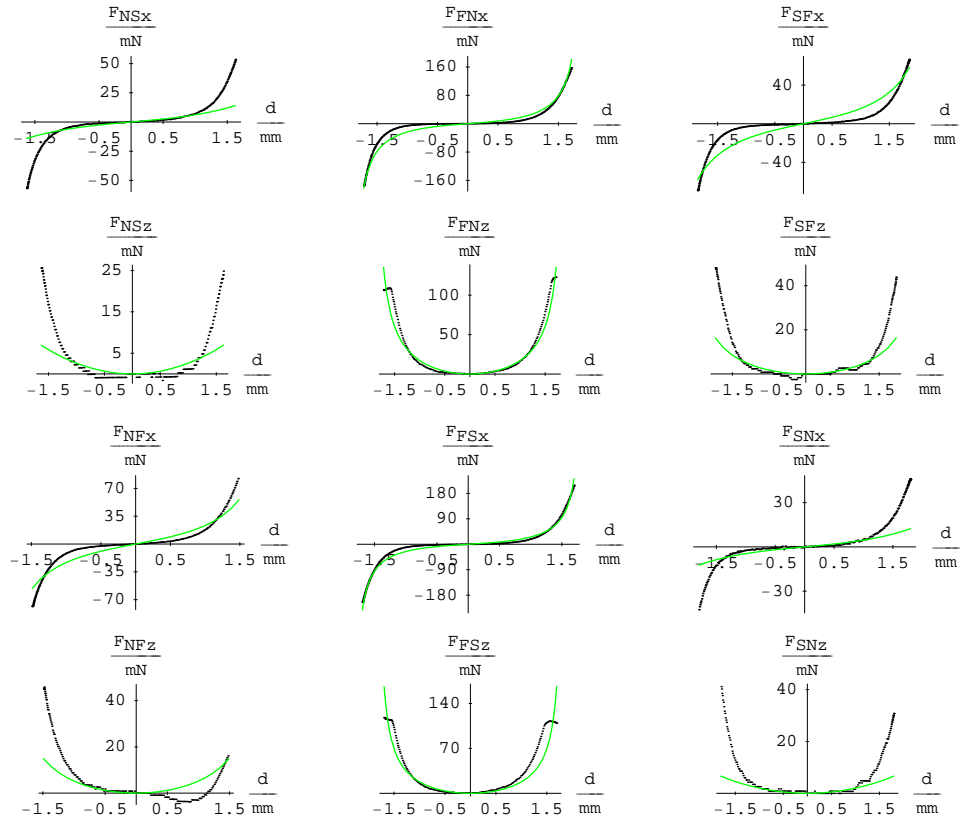


Figure B.5: This graph shows the result of the homogeneous model for experiment 1, LECL.

Graph of homogeneous model, experiment 2, CL

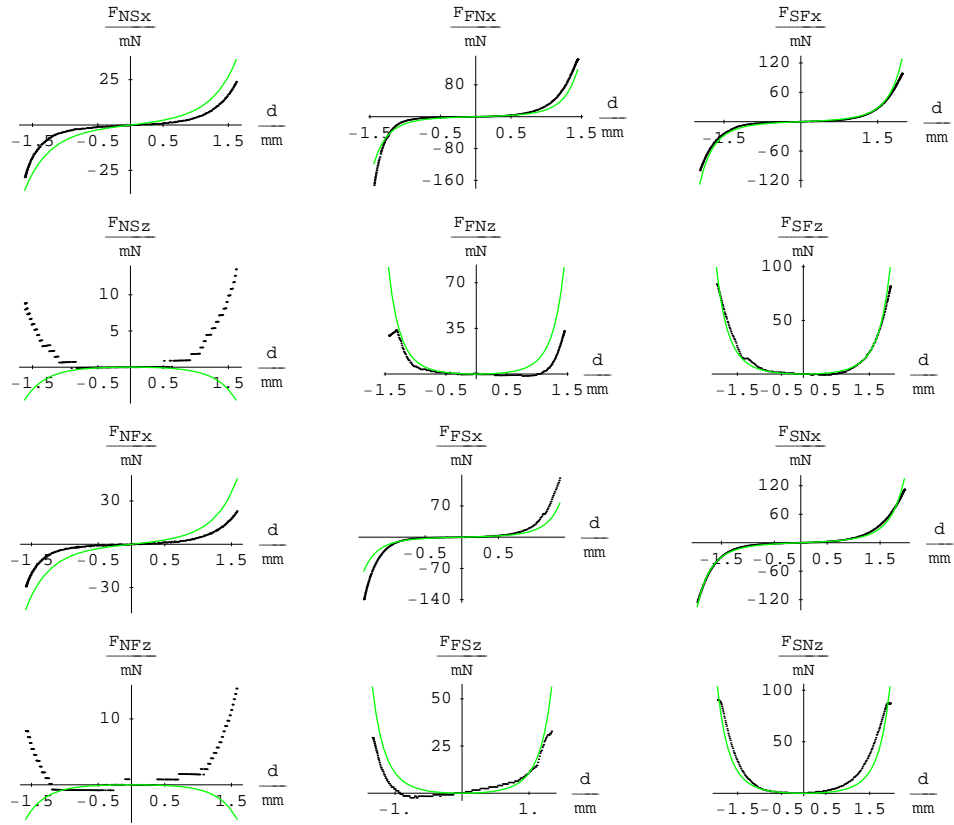


Figure B.6: This graph shows the result of the homogeneous model for experiment 2, CL.

## Graph of homogeneous model, experiment 2, SFL

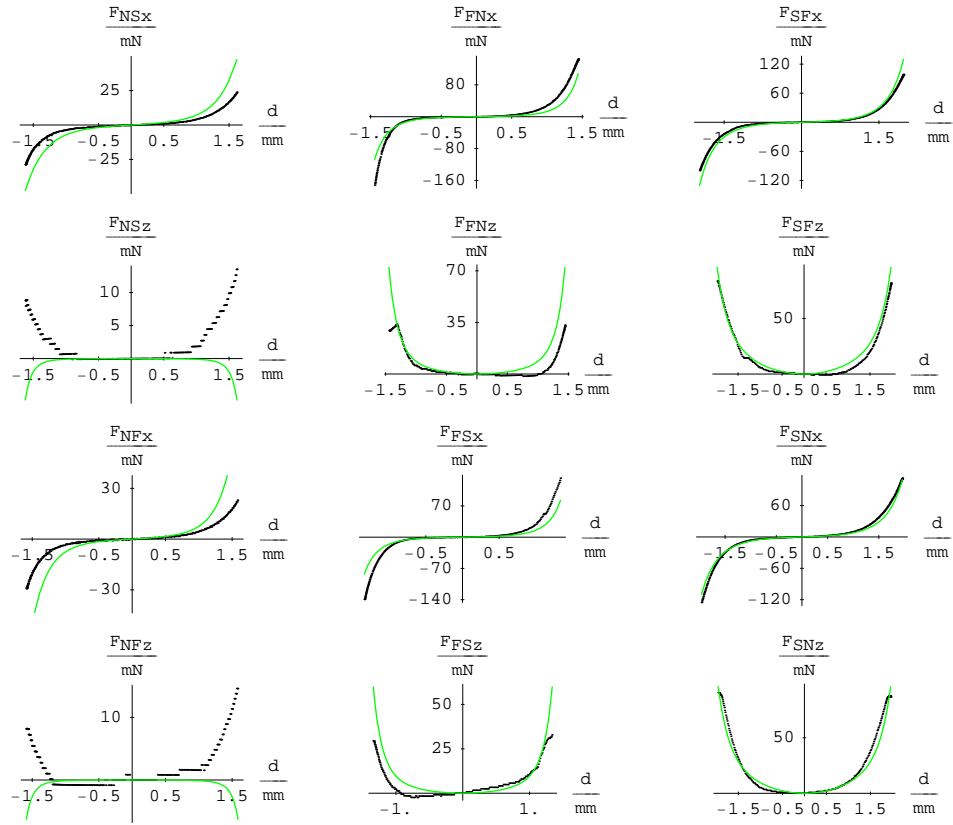


Figure B.7: This graph shows the result of the homogeneous model for experiment 2, SFL.

Graph of homogeneous model, experiment 2, PZL

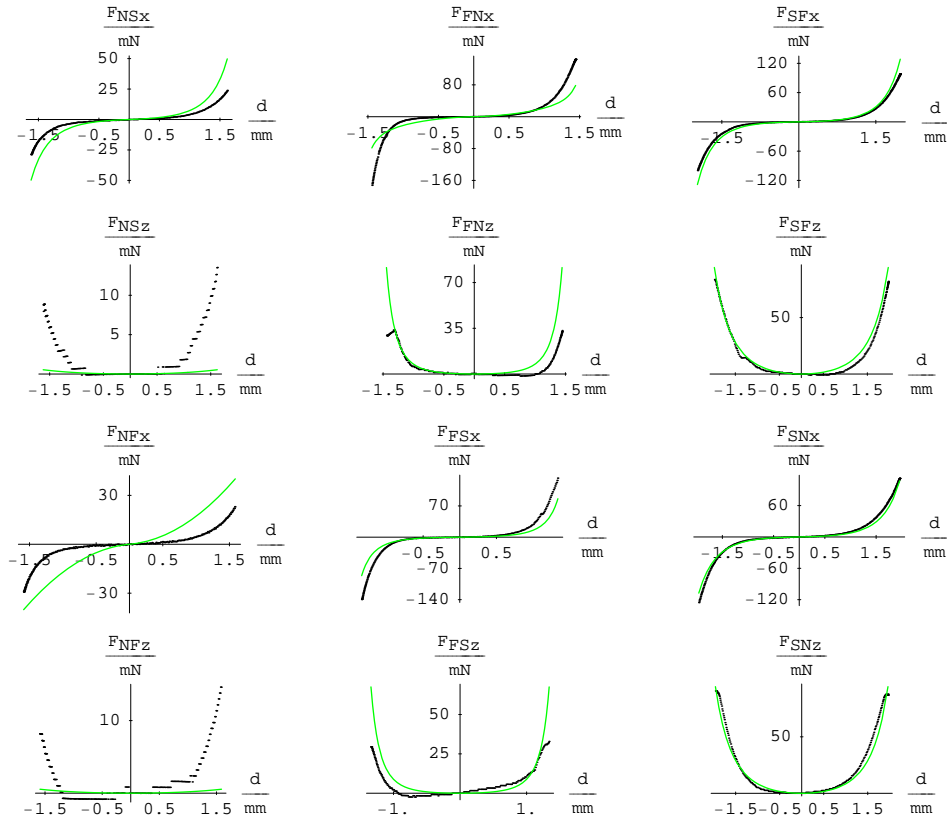


Figure B.8: This graph shows the result of the homogeneous model for experiment 2, PZL.

## Graph of homogeneous model, experiment 2, TL

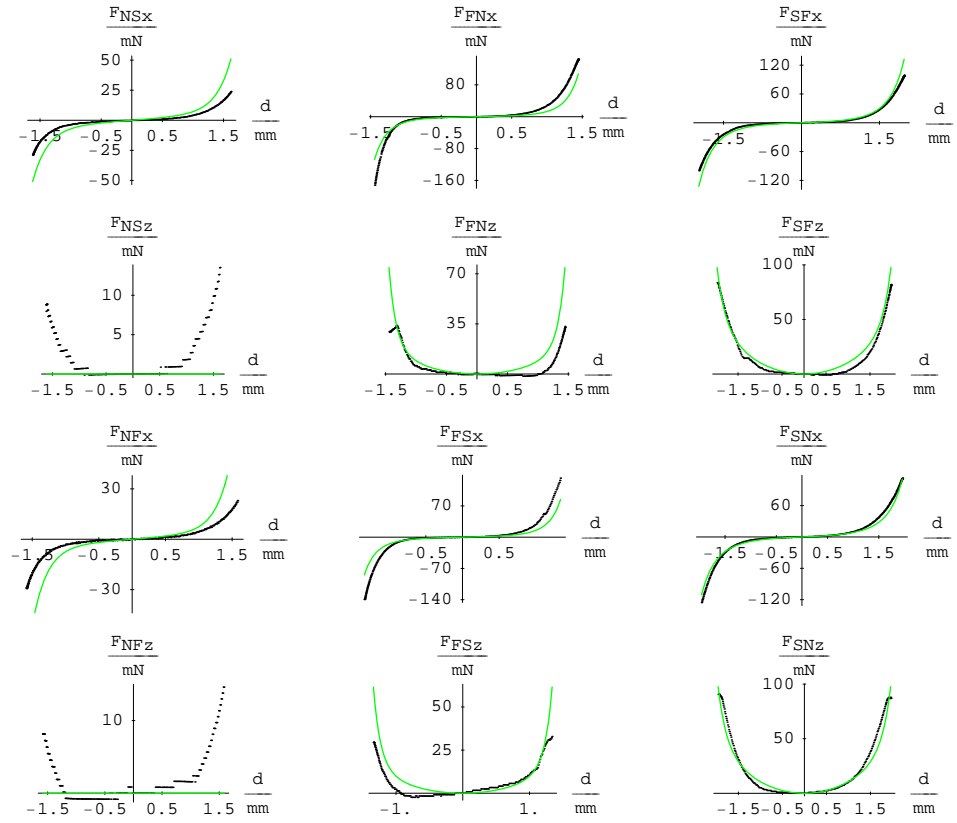


Figure B.9: This graph shows the result of the homogeneous model for experiment 2, TL.

## Graph of homogeneous model, experiment 2, LECL

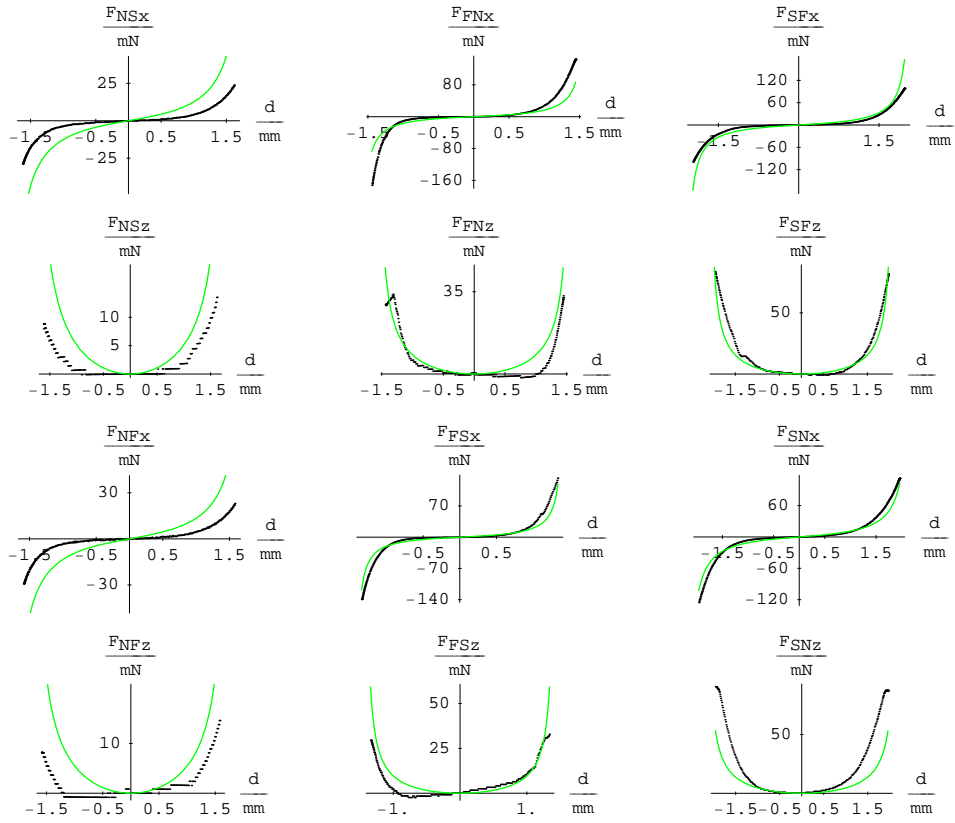


Figure B.10: This graph shows the result of the homogeneous model for experiment 2, LECL.

Graph of homogeneous model, experiment 3, CL

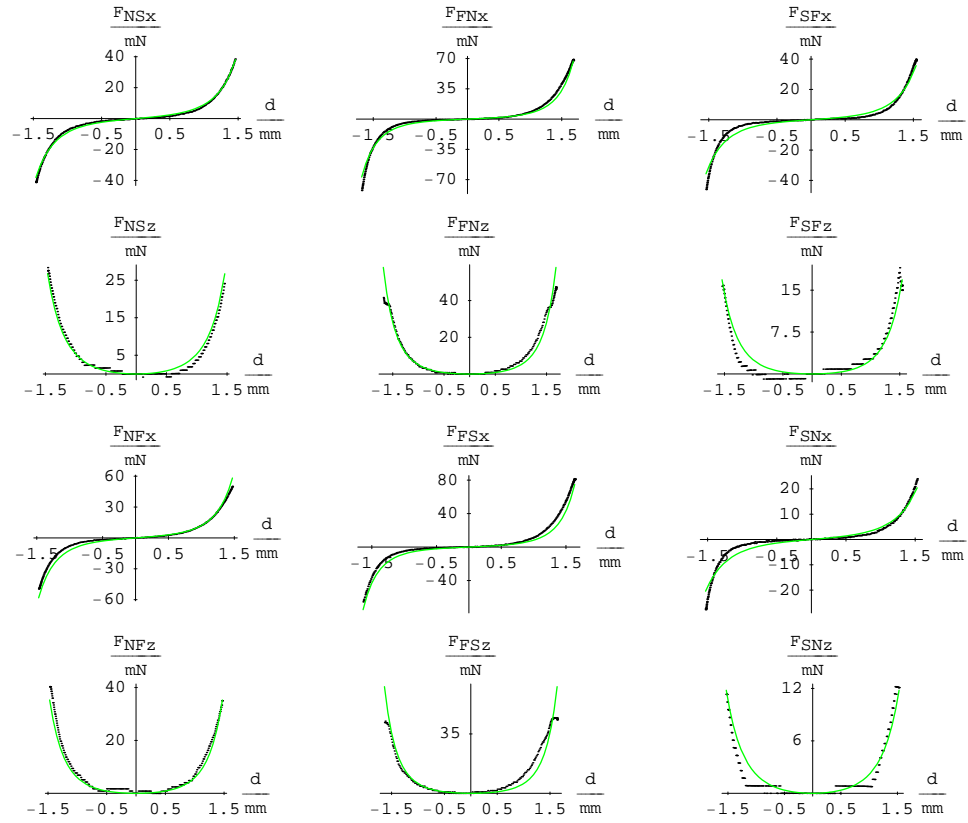


Figure B.11: This graph shows the result of the homogeneous model for experiment 3, CL.

Graph of homogeneous model, experiment 3, SFL

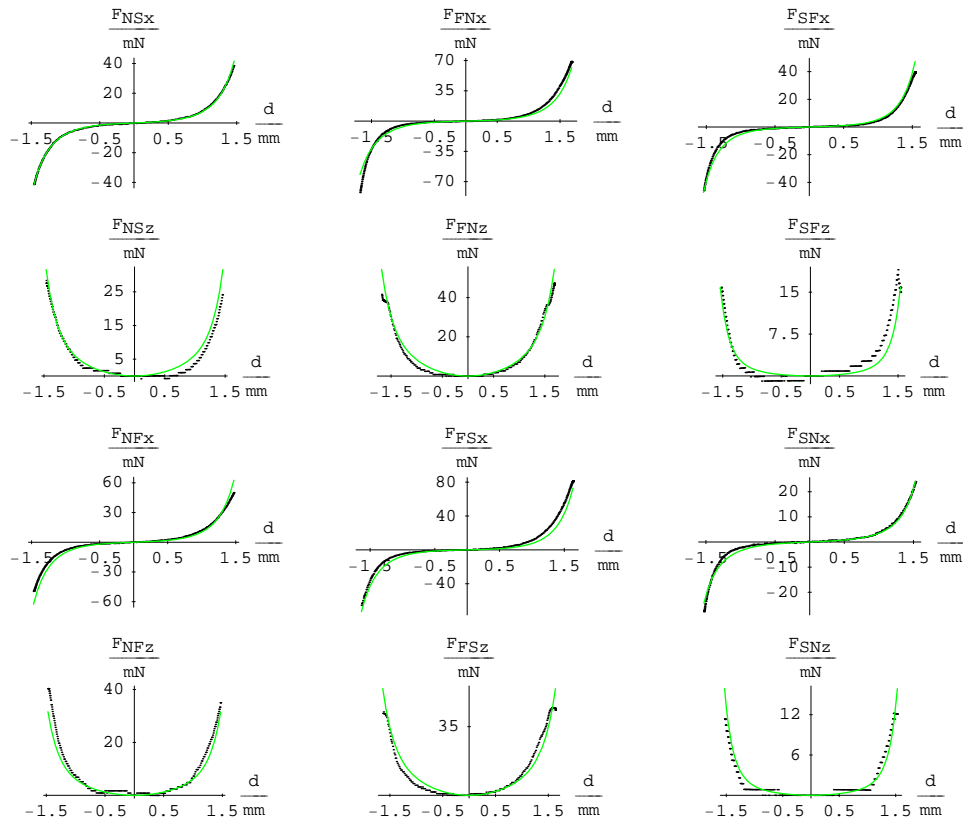


Figure B.12: This graph shows the result of the homogeneous model for experiment 3, SFL.



Graph of homogeneous model, experiment 3, PZL

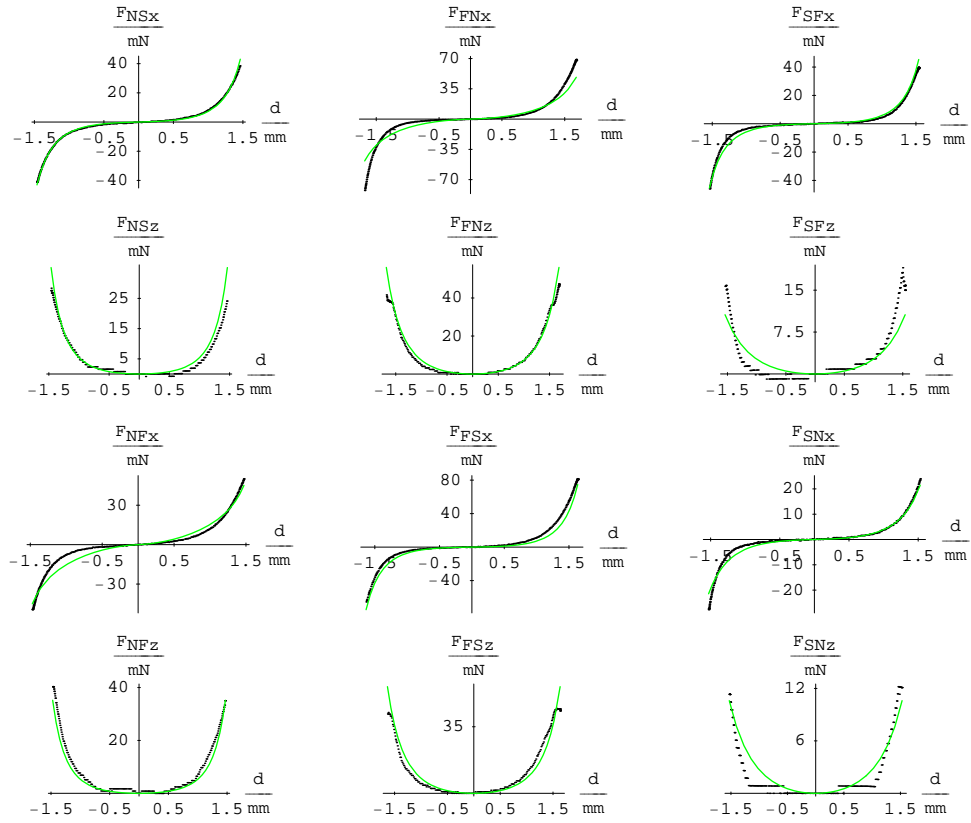


Figure B.13: This graph shows the result of the homogeneous model for experiment 3, PZL.

## Graph of homogeneous model, experiment 3, TL

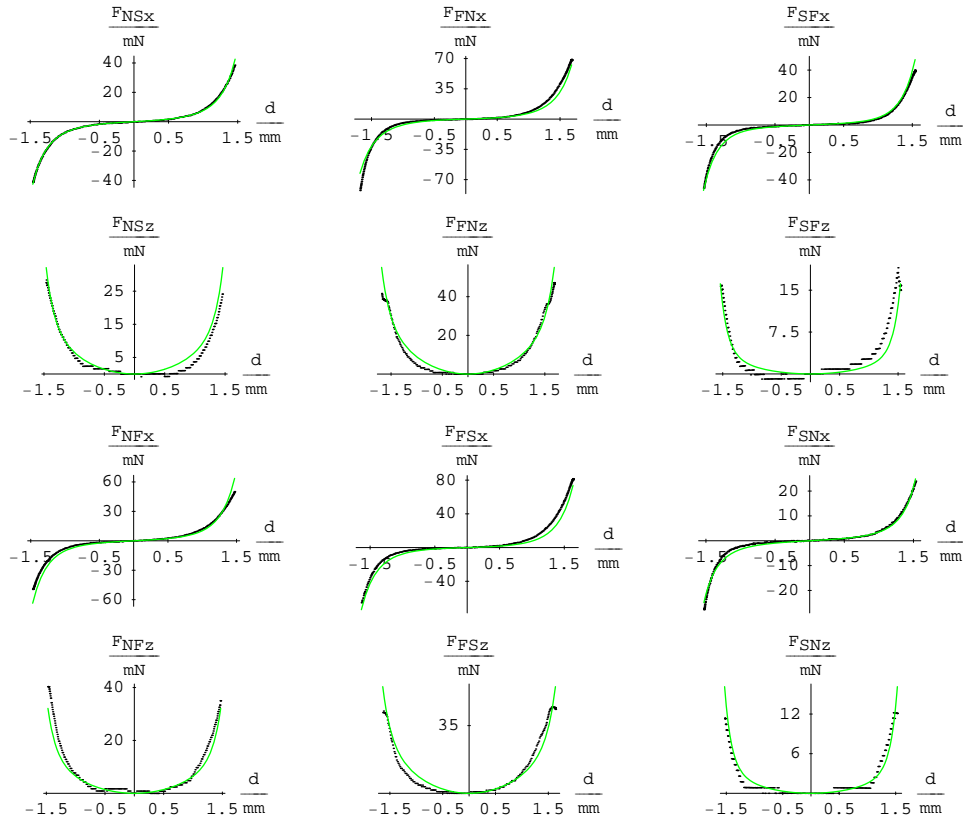


Figure B.14: This graph shows the result of the homogeneous model for experiment 3, TL.

Graph of homogeneous model, experiment 3, LECL

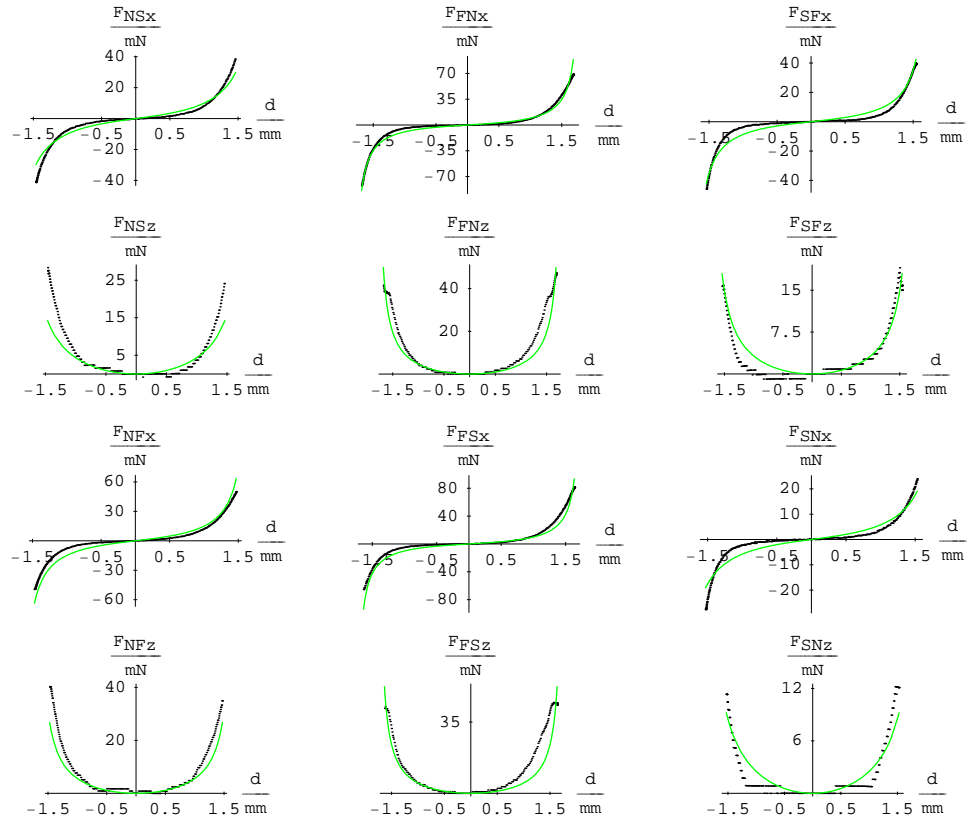


Figure B.15: This graph shows the result of the homogeneous model for experiment 3, LECL.

Graph of homogeneous model, experiment 4, CL

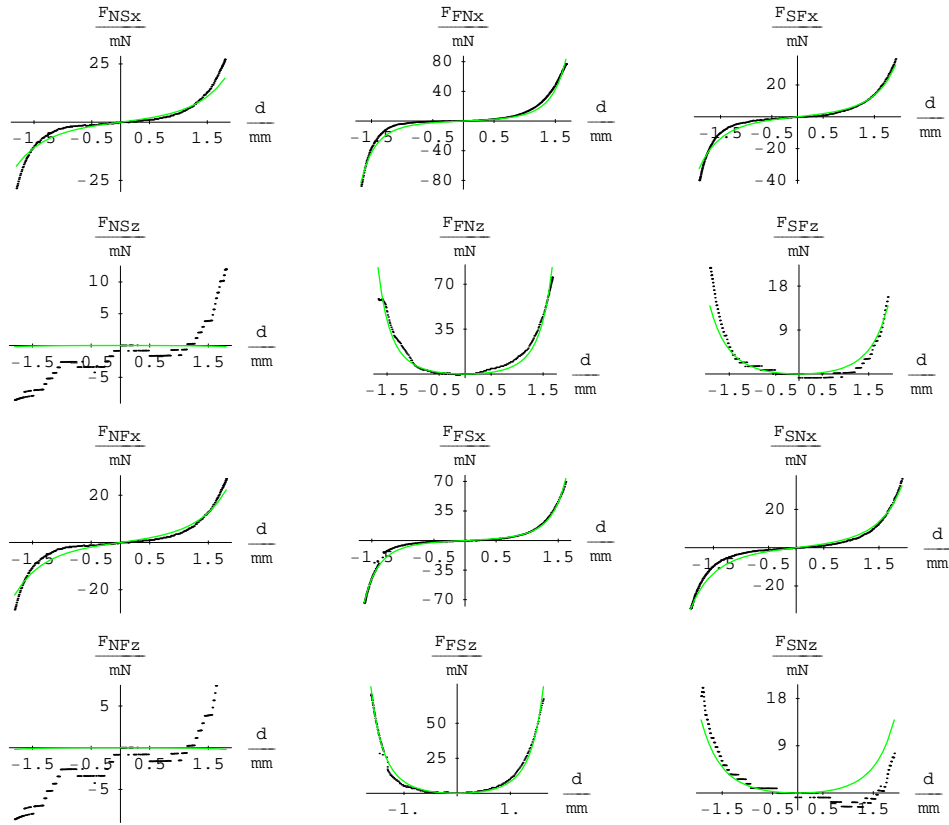


Figure B.16: This graph shows the result of the homogeneous model for experiment 4, CL.

Graph of homogeneous model, experiment 4, SFL

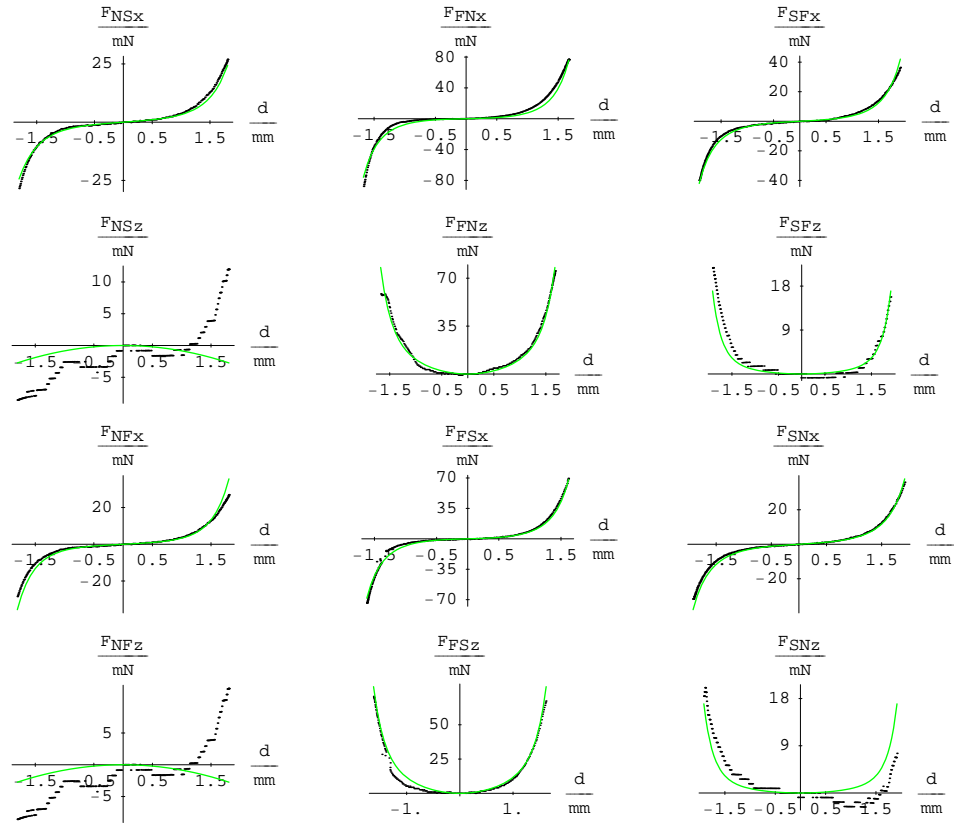


Figure B.17: This graph shows the result of the homogeneous model for experiment 4, SFL.

Graph of homogeneous model, experiment 4, PZL

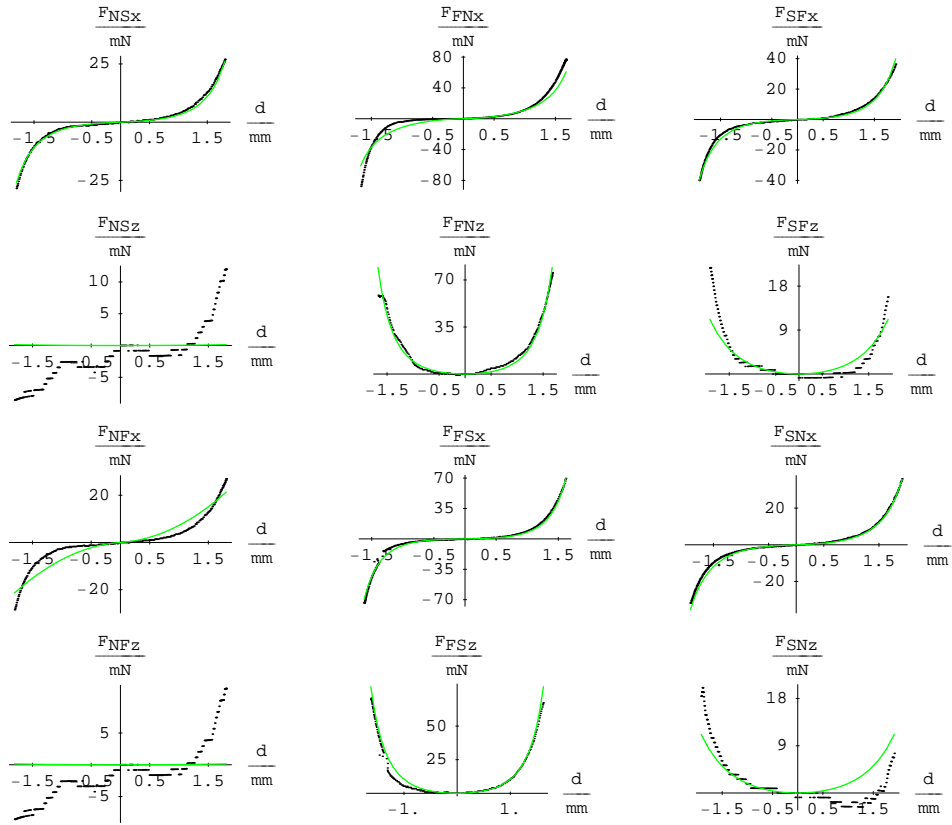


Figure B.18: This graph shows the result of the homogeneous model for experiment 4, PZL.

Graph of homogeneous model, experiment 4, TL

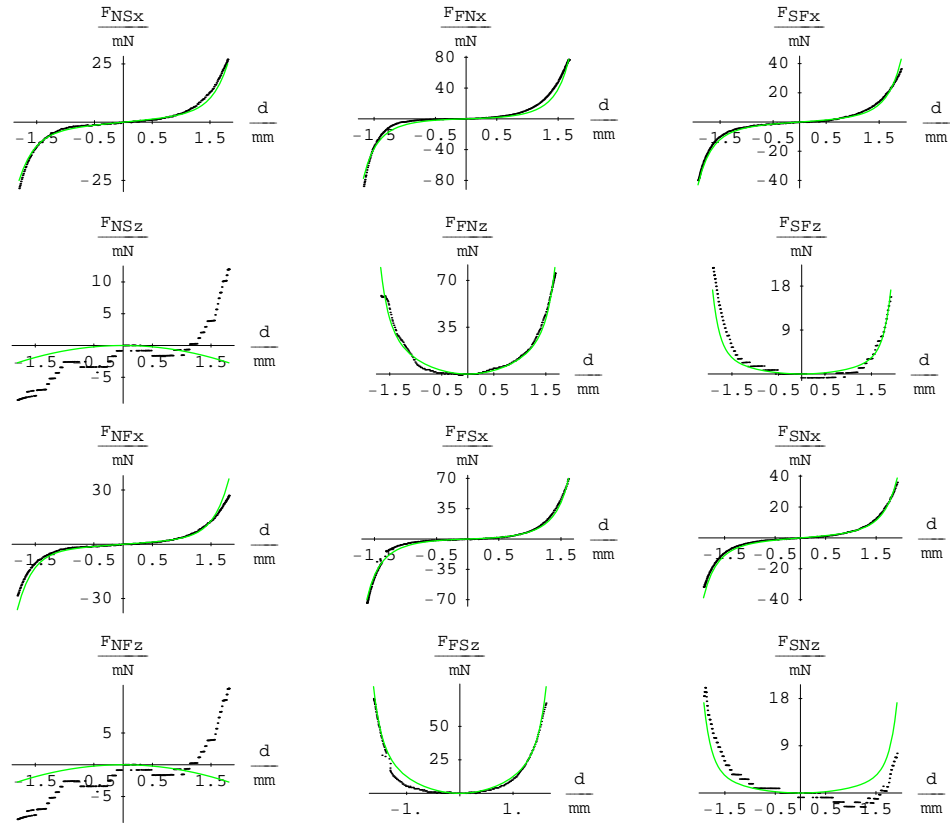


Figure B.19: This graph shows the result of the homogeneous model for experiment 4, TL.

Graph of homogeneous model, experiment 4, LECL

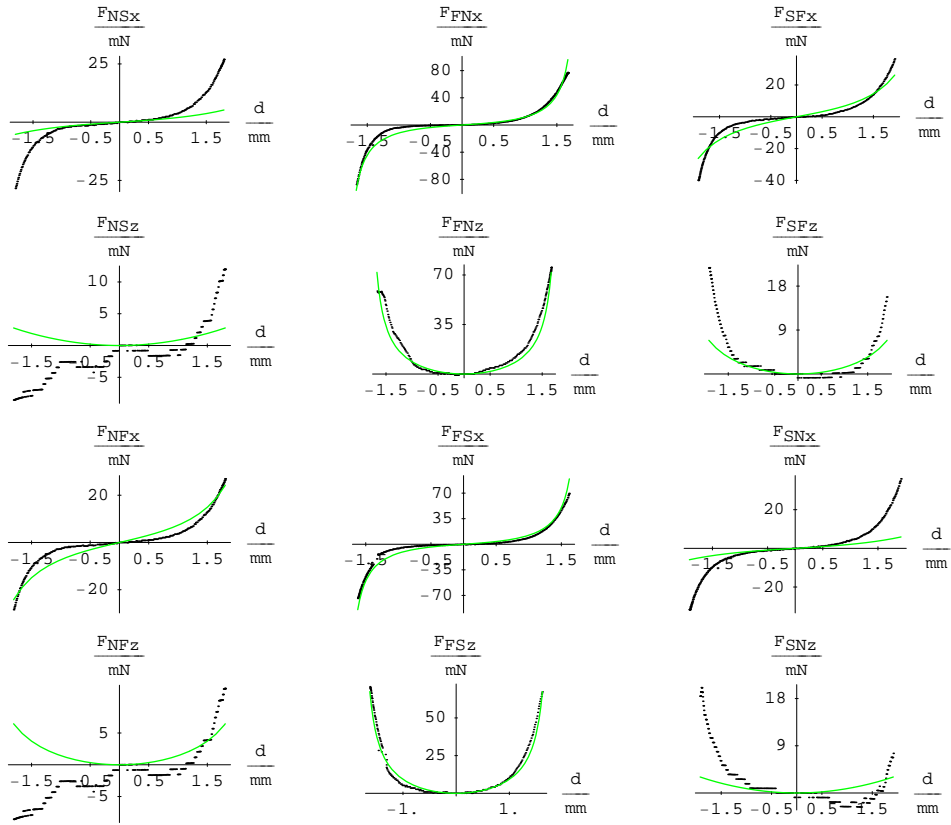


Figure B.20: This graph shows the result of the homogeneous model for experiment 4, LECL.



Graph of homogeneous model, experiment 5, CL

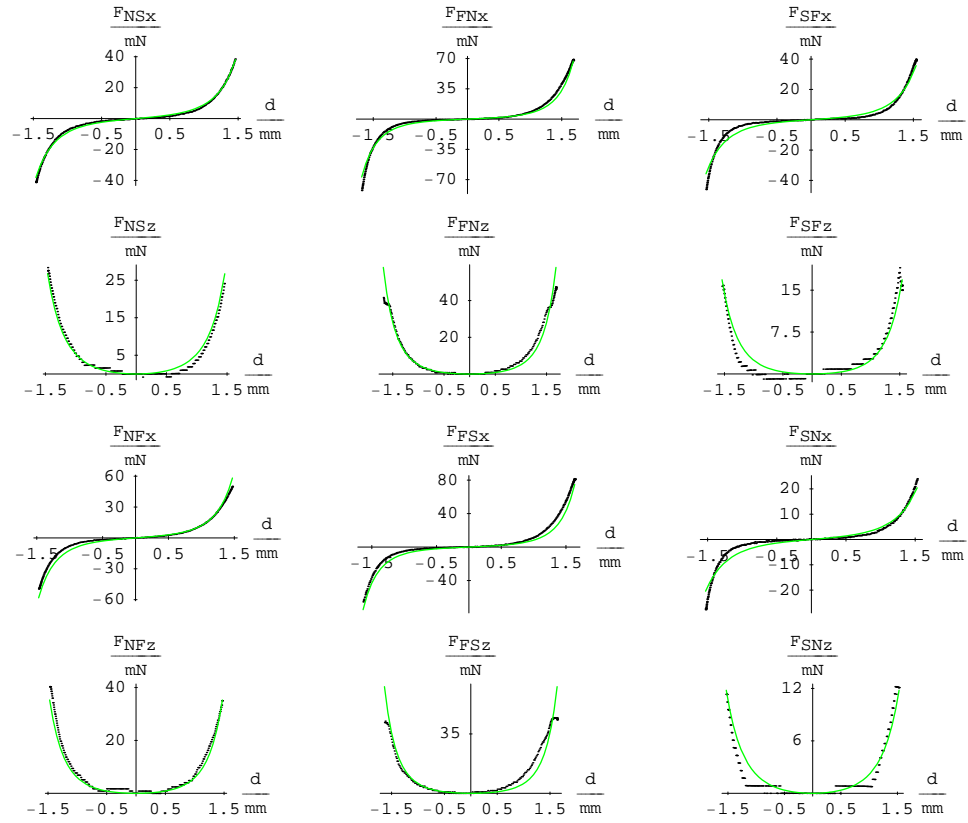


Figure B.21: This graph shows the result of the homogeneous model for experiment 5, CL.

Graph of homogeneous model, experiment 5, SFL

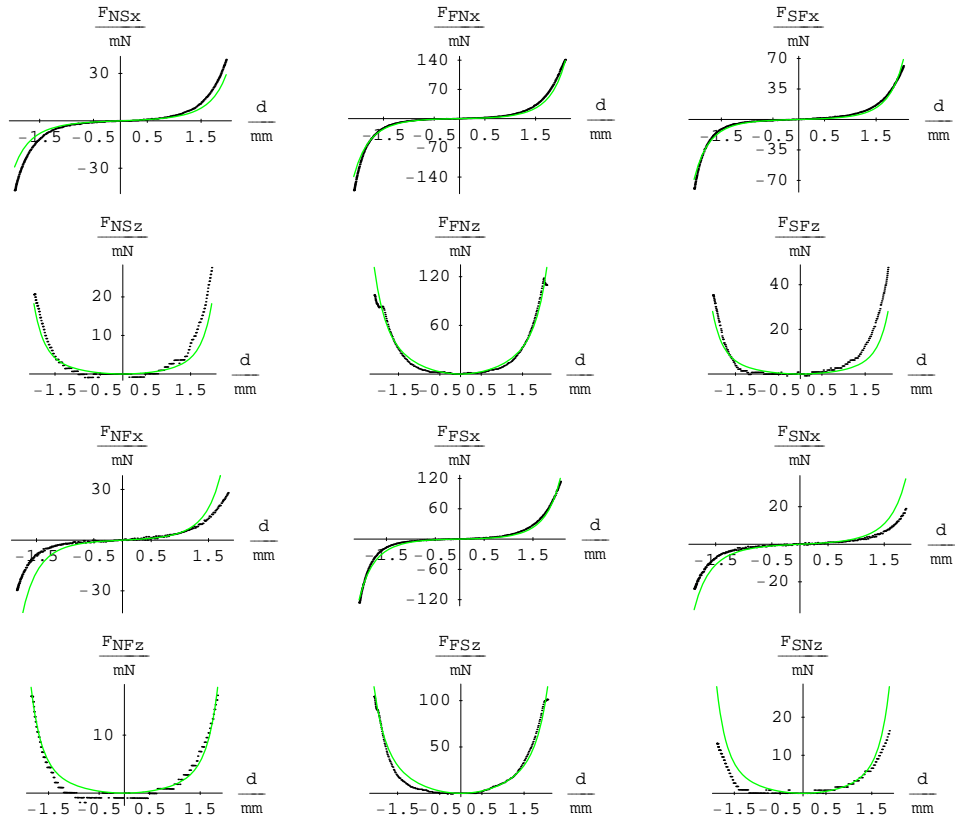


Figure B.22: This graph shows the result of the homogeneous model for experiment 5, SFL.

Graph of homogeneous model, experiment 5, PZL

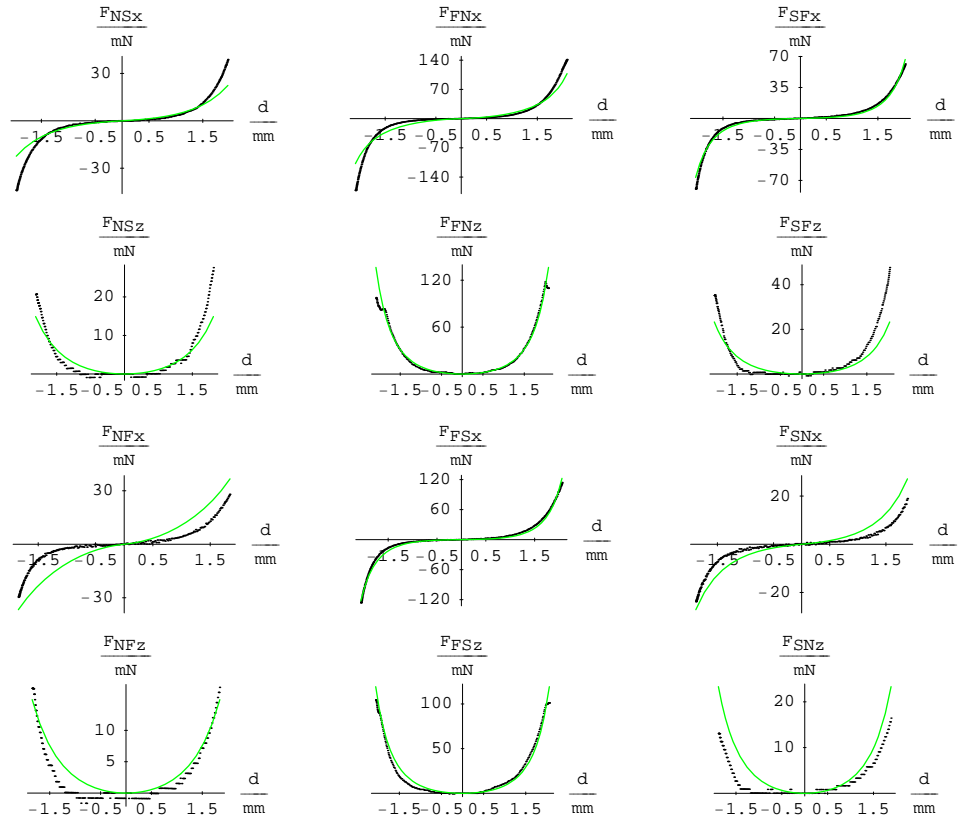


Figure B.23: This graph shows the result of the homogeneous model for experiment 5, PZL.

Graph of homogeneous model, experiment 5, TL

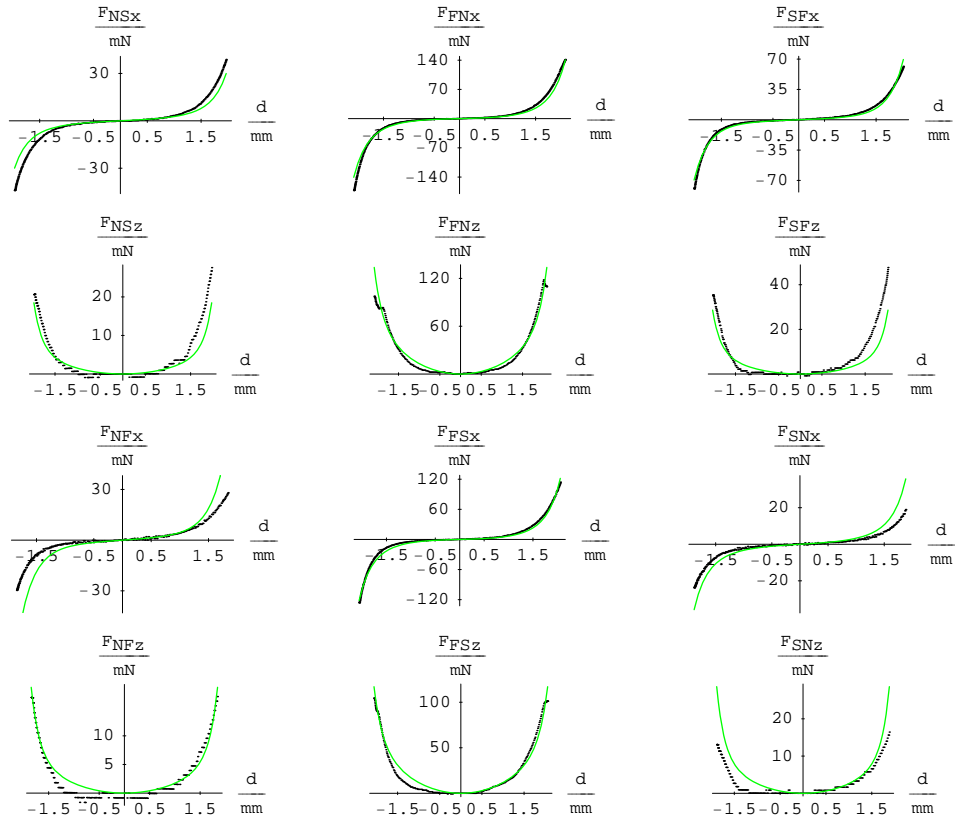


Figure B.24: This graph shows the result of the homogeneous model for experiment 5, TL.

Graph of homogeneous model, experiment 5, LECL

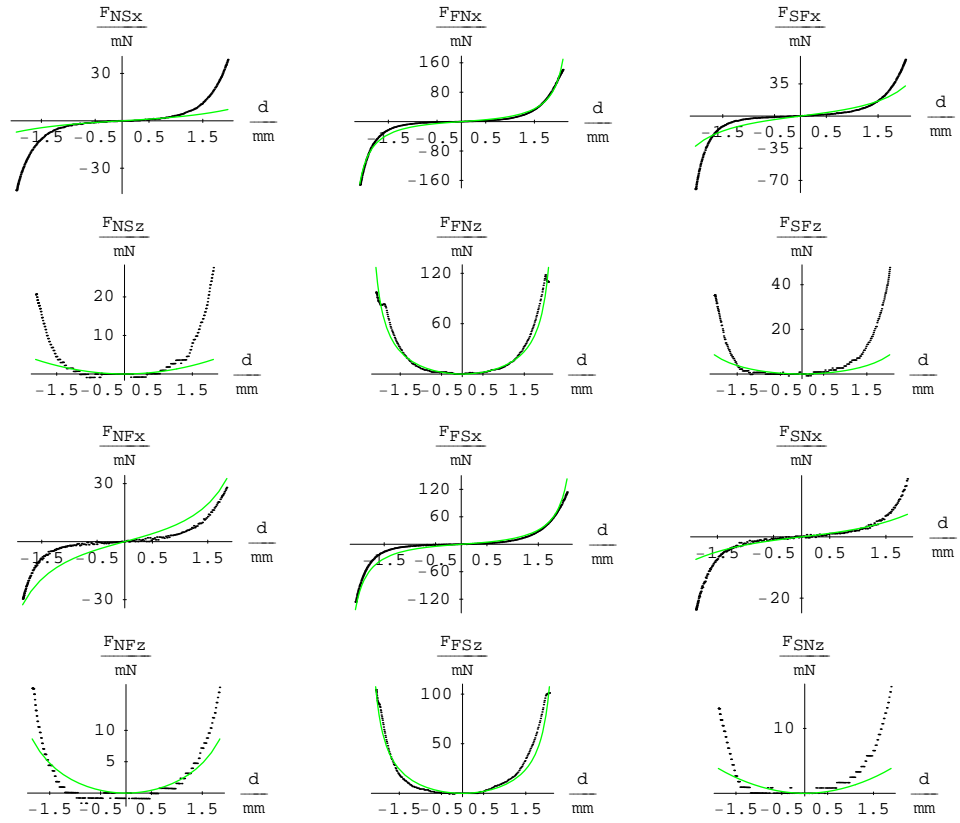


Figure B.25: This graph shows the result of the homogeneous model for experiment 5, LECL.

Graph of homogeneous model, experiment 6, CL

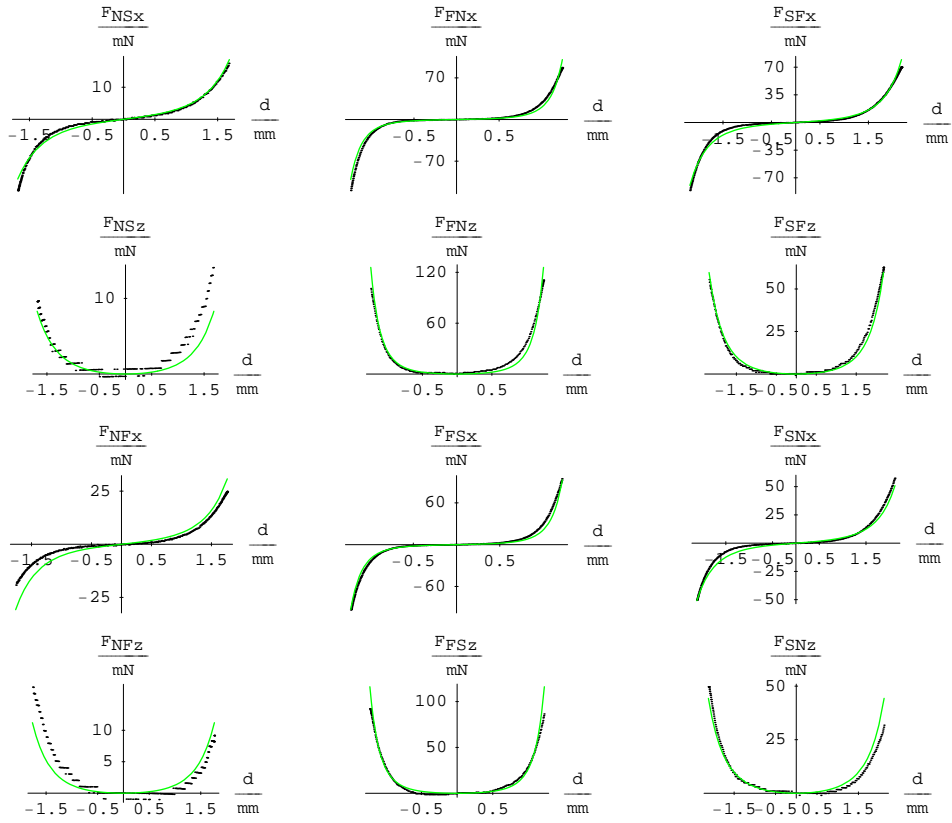


Figure B.26: This graph shows the result of the homogeneous model for experiment 6, CL.

Graph of homogeneous model, experiment 6, SFL

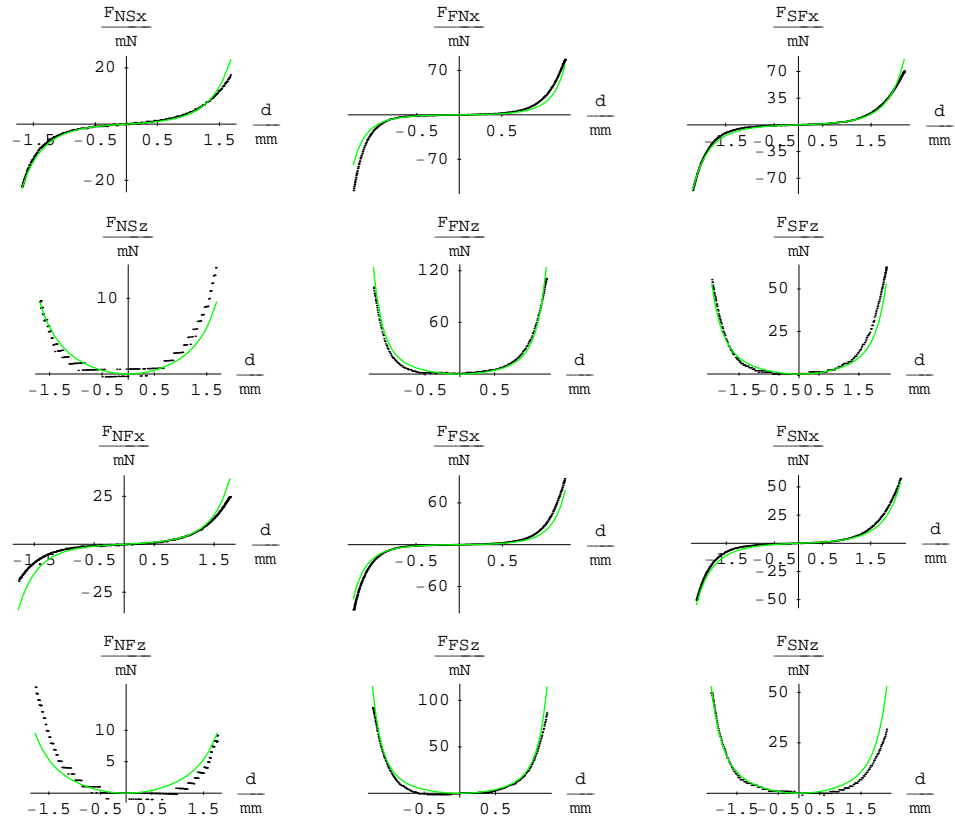


Figure B.27: This graph shows the result of the homogeneous model for experiment 6, SFL.

Graph of homogeneous model, experiment 6, PZL

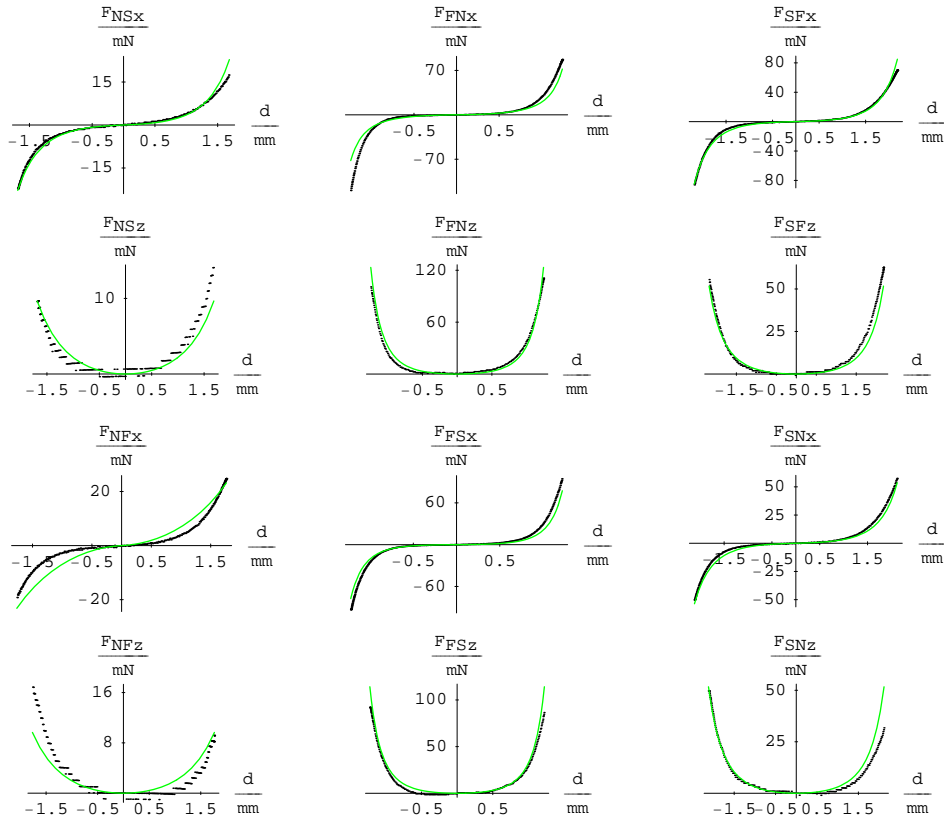


Figure B.28: This graph shows the result of the homogeneous model for experiment 6, PZL.



Graph of homogeneous model, experiment 6, TL

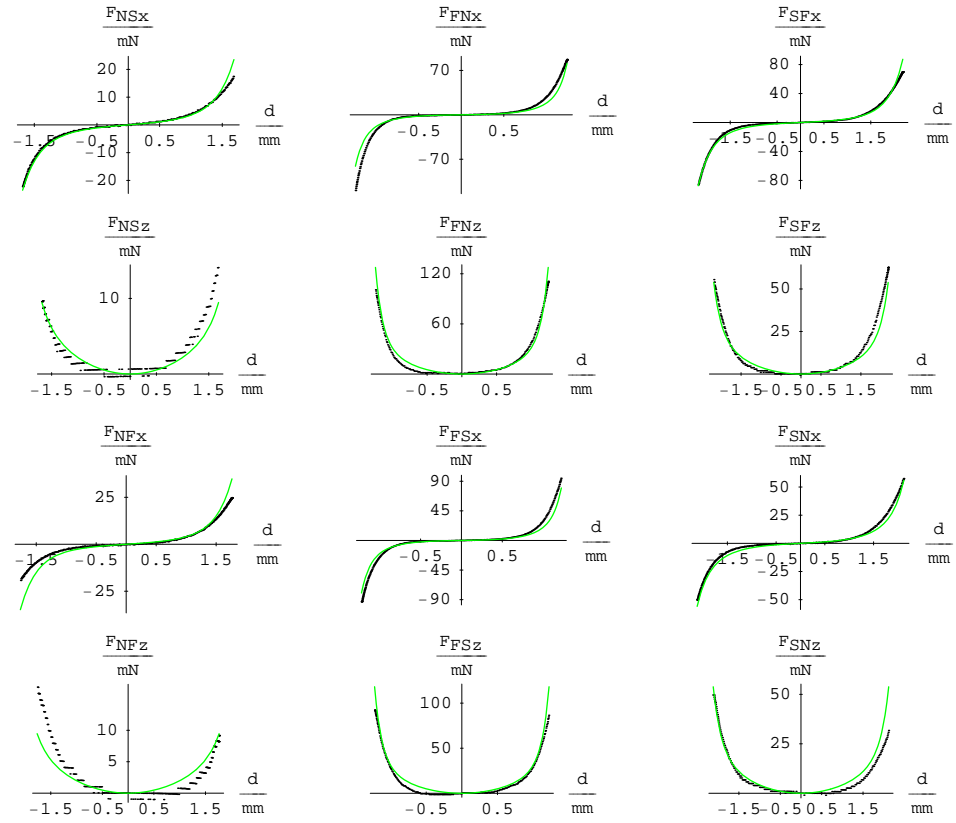


Figure B.29: This graph shows the result of the homogeneous model for experiment 6, TL.

Graph of homogeneous model, experiment 6, LECL

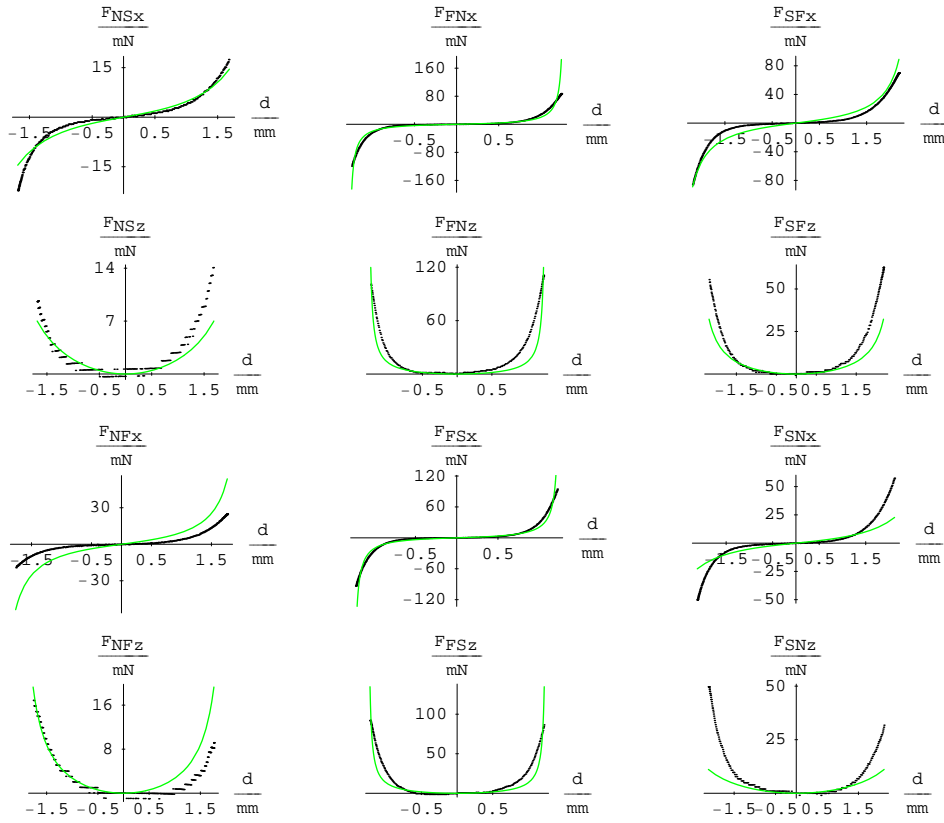


Figure B.30: This graph shows the result of the homogeneous model for experiment 6, LECL.



# Appendix C

## Additional Data for FE Model

This chapter gives additional data for the finite element model, i.e. Sec.(C.1) shows a sample file of the finite element model for experiment 3, i.e. a command file for the backend of the finite element package CMISS. Sec.(C.2) presents the tables of the convergence analysis of the finite element meshes (referred to in Sec.(7.1.3)) and Sec.(C.3) shows all graphs for all four laws and all experiments (referred to in Sec.(7.3)).

### C.1 Example File for FE Model, Exp. 3, CL

```
# Optimization_Costa.com

# Read data from file
(open datafile, "StepPercentage.ipdata" );
@Lines=<datafile>;
close(datafile);
@Gauss=();
foreach $Line (@Lines) {
    $Line=$Line+0;
    @Gauss=(@Gauss, "$Line");
}

$animal = "SP17"

@modes=("NS","NF","SN","SF","FS","FN") $ModelNum = 1;

if($RESOLVE ne "TRUE") {
    # Don't need to redo these commands when
    # resolving during optimisation

    fem define parameters;r;111cube;
    fem define coordinate;r;111cube;
    fem define base;r;111cube;
}

#loop over the shear modes $modenum = 0; foreach $mode ( @modes )
```

```

{

    $modenum = $modenum + 1;

    printf("=====\nMode %s;numbner%d\n",$mode,$modenum=====);

    # Read data from file before enter IF LOOP
    (open datafile, "${mode}_SQRTweight.ipdata");
    @Lines=<datafile>;
    close(datafile);
    @Weight=();
    foreach $Line (@Lines) {
        $Line=$Line+0;
        @Weight=(@Weight, "$Line");
    }

    print "\n Gauss:@Gauss \n Weight : @Weight"

    fem define node;r;555cube_${animal}_${mode};
    fem define fibre;r;555cube_${mode};

    if($RESOLVE ne "TRUE") {

        fem define element;r;555cube;
        fem define element;r;555cube fibre;

        # grouping elements at boundary
        fem group elements all external s3=0 as ZOFACE_ELEM;
        fem group elements all external s3=1 as ZIFACE_ELEM;

        # grouping nodes at boundary
        fem group nodes xi3=0 external element ZOFACE_ELEM as ZOFACE_NODE;
        fem group nodes xi3=1 external element ZIFACE_ELEM as ZIFACE_NODE;

        #grouping all elements
        fem group elem all_elements as ALL_ELEM

        fem define equations;r;shear_cube lock
        fem define materials;r;CellML

        # Solve in 1/2 (# of Gauss pts = 12) steps
        $number_steps=6;

        fem define initial;r;shear_${animal}_${mode};
        fem define solve;r;shear_cube

        #=====
        #=====Setup-material-law-throught-CellML-environment=====
        #=====
        if($FIRST ne "FALSE") {

            fem define grid;r;111cube gauss class 2

            fem update grid geometry
            fem group grid element ALL_ELEM as ALL_GRID_PT
            fem define equation;r;shear_CellML class 2

            fem define mater;d class 2

            fem define cell;r;Costa_seven_parameters class 2
            fem define material;r;Costa_seven_parameters cell class 2

            fem define initial;d class 2
            fem define solve;r;CellML class 2
            fem solve class 2 to 0;

            $FIRST = "FALSE";
        }

        #=====
        #=====CellML-Setup-Ends=====
        #=====

        # Load the experimental force components.
        # x and z directions are in indicies 1 and 3, respectively
        fem define data;r;${animal}_${mode};

        for($loadnum=1;$loadnum<=$number_steps;$loadnum++) {
            printf("=====\nStep %d\n",$loadnum);

            # solve for original (initial) material parameters
            fem solve increment $Gauss[$loadnum-1] iterate 40 error 0.00000001;

```

```

# Save intermediate solution
fem define initial;w;solution_${animal}_${mode}_step_${loadnum};
#fem define initial;r;solution_${animal}_${mode}_step_${loadnum}_Initial;

# Create a vector of the experimental reaction force for use by the optimiser
#
# We rearranged Dokos data, such that the x force of the first G/2 entries are positive
# and all z force entries are positive to account for both, model output and only
# solving for positive displacements to save computational time
#
# positive forces
fem update residual data point $loadnum index 1 residual%
    1+($loadnum-1)*2+($modenum-1)*4*$number_steps weight $Weight[$loadnum-1];
fem update residual data point $loadnum index 3 residual%
    2+($loadnum-1)*2+($modenum-1)*4*$number_steps weight $Weight[$loadnum-1];
# negative forces
fem update residual data point $loadnum+$number_steps index 1 residual%
    1+($loadnum-1)*2+($modenum-1)*4*$number_steps+$number_steps*2 weight $Weight[$loadnum-1];
fem update residual data point $loadnum+$number_steps index 3 residual%
    2+($loadnum-1)*2+($modenum-1)*4*$number_steps+$number_steps*2 weight $Weight[$loadnum-1];

} #for $loadnum
}

else { # i.e. if ($RESOLVE eq "TRUE")

# Need to update the material parameters to those being evaluated by the optimiser
fem update optimisation;

for($loadnum=1;$loadnum<=$number_steps;$loadnum++) {
printf("=====\nStep %d\n", $loadnum);

# read intermediate solution for current mode and load
fem define initial;r;solution_${animal}_${mode}_step_${loadnum};
fem define solve;r;shear_cube;

# solve for perturbed material parameters
fem solve increment 0.0 iterate 40 error 0.00000001;

# evaluate new (predicted-expt) reaction forces
# positive forces
fem evaluate reaction node ZiFACE_NODE direction 1 residual%
    1+($loadnum-1)*2+($modenum-1)*4*$number_steps weight $Weight[$loadnum-1];
fem evaluate reaction node ZiFACE_NODE direction 3 residual%
    2+($loadnum-1)*2+($modenum-1)*4*$number_steps weight $Weight[$loadnum-1];
# negative forces
fem evaluate reaction node ZiFACE_NODE direction 1 residual%
    1+($loadnum-1)*2+($modenum-1)*4*$number_steps+$number_steps*2 weight $Weight[$loadnum-1];
fem evaluate reaction node ZiFACE_NODE direction 3 residual%
    2+($loadnum-1)*2+($modenum-1)*4*$number_steps+$number_steps*2 weight $Weight[$loadnum-1];

fem define initial;w;solution_${animal}_${mode}_step_${loadnum};

} #for $loadnum
} #if $RESOLVE

} #foreach $mode

# Store the updated parameters into Optimized_Parameters fem
define optimise;w;Optimized_Parameters_555;

if($RESOLVE ne "TRUE") {
    $ITERATION = 1;
    $RESOLVE = "TRUE";
    # do the optimisation
    fem define optimise;r;new_shear_555_parameters;
    optimise;
    set output off;
}

```

## C.2 Convergence Analysis of the finite element meshes

Table (C.1) shows the numerical results of the convergence analysis for the CL. The analysis indicated that a 555cube was ideal for the study since the 666cube did only improve  $\Delta_{MP}^{m_\alpha \setminus m_\beta}$  by 0.89% and  $\Omega$  by 0.50%. The stress convergence also suggested this.

Furthermore the convergence analysis for the SFL, PZL and TL showed very similar results, which confirmed our choice of the 555cube. The notation used in the tables is defined in Sec.(4.4.6).

| CL  | $\Omega$ | $\Delta_{\Omega}^{\alpha \setminus \beta}$ | $\max(\Delta_{\gamma_i}^{\alpha \setminus \beta})$ | $\Delta_{MP}^{\alpha \setminus \beta}$ | $a$   | $\Delta_a^{\alpha \setminus \beta}$ | $b_{ff}$ | $\Delta_{b_{ff}}^{\alpha \setminus \beta}$ | $b_{fn}$ | $\Delta_{b_{fn}}^{\alpha \setminus \beta}$ | $b_{fs}$ | $\Delta_{b_{fs}}^{\alpha \setminus \beta}$ | $b_{nn}$ | $\Delta_{b_{nn}}^{\alpha \setminus \beta}$ | $b_{ns}$ | $\Delta_{b_{ns}}^{\alpha \setminus \beta}$ | $b_{ss}$ | $\Delta_{b_{ss}}^{\alpha \setminus \beta}$ |
|-----|----------|--|--|--|-------|-------------------------------------|----------|--|----------|--|----------|--|----------|--|----------|--|----------|--|
| 111 | 127.2    |  |  |  | 0.171 |                                     | 34.0     |  | 11.1     |  | 12.6     |  | 19.3     |  | 9.0      |  | 13.1     |  |
| 222 | 121.4    | 4.82%                                      | 25.7%  | 10.6%                                  | 0.189 | 9.3%                                | 36.7     | 7.3%                                       | 10.4     | 6.6%                                       | 12.1     | 3.9%                                       | 22.8     | 15.5%                                      | 8.5      | 5.7%                                       | 17.6     | 25.7%                                      |
| 333 | 121.3    | 0.06%                                      | 22.4%  | 12.4%                                  | 0.184 | 2.6%                                | 32.2     | 13.7%                                      | 11.6     | 10.1%                                      | 13.4     | 9.5%                                       | 19.3     | 18.3%                                      | 9.5      | 10.3%                                      | 14.4     | 22.4%                                      |
| 444 | 122.6    | 1.05%                                      | 5.0%   | 2.9%                                   | 0.185 | 0.38%                               | 31.2     | 3.5%                                       | 11.9     | 2.7%                                       | 13.7     | 2.6%                                       | 18.4     | 5.0%                                       | 9.7      | 2.5%                                       | 13.8     | 3.9%                                       |
| 555 | 123.9    | 1.07%                                      | 3.2%   | 1.9%                                   | 0.187 | 0.94%                               | 30.5     | 2.3%                                       | 12.1     | 1.7%                                       | 13.9     | 1.7%                                       | 17.8     | 3.2%                                       | 9.9      | 1.3%                                       | 13.6     | 2.1%                                       |
| 666 | 124.6    | 0.50%                                      | 1.4%   | 0.91%                                  | 0.187 | 0.51%                               | 30.2     | 0.97%                                      | 12.2     | 0.90%                                      | 14.1     | 0.94%                                      | 17.6     | 1.4%                                       | 9.9      | 0.74%                                      | 13.4     | 0.89%                                      |
| 777 | 124.8    | 0.21%                                      | 0.99%  | 0.67%                                  | 0.188 | 0.36%                               | 30.0     | 0.65%                                      | 12.3     | 0.68%                                      | 14.2     | 0.72%                                      | 17.4     | 0.99%                                      | 10.0     | 0.57%                                      | 13.3     | 0.70%                                      |
| 888 | 124.9    | 0.09%                                      | 0.58%  | 0.42%                                  | 0.189 | 0.20%                               | 29.9     | 0.35%                                      | 12.3     | 0.48%                                      | 14.3     | 0.50%                                      | 17.3     | 0.58%                                      | 10.0     | 0.43%                                      | 13.3     | 0.38%                                      |

Table C.1: Convergence analysis for CL.



| SFL | $\Omega$       | $\kappa_\Omega$ | $a_{ff}$ | $\Delta_a^{\alpha \setminus \beta}_{ff}$ | $a_{fn}$ | $\Delta_a^{\alpha \setminus \beta}_{fn}$ | $a_{fs}$ | $\Delta_a^{\alpha \setminus \beta}_{fs}$ | $a_{nn}$ | $\Delta_a^{\alpha \setminus \beta}_{nn}$ | $a_{ns}$ | $\Delta_a^{\alpha \setminus \beta}_{ns}$ | $a_{ss}$ | $\Delta_a^{\alpha \setminus \beta}_{ss}$ |
|-----|----------------|-----------------|----------|--|----------|--|----------|--|----------|--|----------|--|----------|--|
| 111 | 126            |                 | 0.279    |  | 0.0514   |  | 0.0380   |  | 0.0762   |  | 0.0454   |  | 0.0147   |  |
| 222 | 115            | 9.58%           | 0.287    | 2.8%                                     | 0.0218   | 136%                                     | 0.0199   | 90.6%                                    | 0.0819   | 7.0%                                     | 0.0211   | 115%                                     | 0.0316   | 53.5%                                    |
| 333 | 101            | 13.91%          | 0.264    | 8.6%                                     | 0.0214   | 2.0%                                     | 0.0211   | 5.8%                                     | 0.117    | 30.0%                                    | 0.0170   | 24.6%                                    | 0.0590   | 46.4%                                    |
| 444 | 96.2           | 5.22%           | 0.274    | 3.7%                                     | 0.0179   | 19.5%                                    | 0.0220   | 4.1%                                     | 0.168    | 30.4%                                    | 0.0144   | 17.8%                                    | 0.0507   | 16.3%                                    |
| 555 | 96.2           | 0.06%           | 0.280    | 1.8%                                     | 0.0172   | 4.1%                                     | 0.0221   | 0.38%                                    | 0.184    | 8.9%                                     | 0.0145   | 0.74%                                    | 0.0449   | 13.0%                                    |
| 666 | 97.4           | 1.15%           | 0.270    | 3.7%                                     | 0.0179   | 4.0%                                     | 0.0223   | 0.65%                                    | 0.175    | 5.4%                                     | 0.0171   | 15.0%                                    | 0.0414   | 8.4%                                     |
|     | $\kappa_{max}$ | $\kappa$        | $b_{ff}$ | $\Delta_b^{\alpha \setminus \beta}_{ff}$ | $b_{fn}$ | $\Delta_b^{\alpha \setminus \beta}_{fn}$ | $b_{fs}$ | $\Delta_b^{\alpha \setminus \beta}_{fs}$ | $b_{nn}$ | $\Delta_b^{\alpha \setminus \beta}_{nn}$ | $b_{ns}$ | $\Delta_b^{\alpha \setminus \beta}_{ns}$ | $b_{ss}$ | $\Delta_b^{\alpha \setminus \beta}_{ss}$ |
| 111 |                |                 | 56.7     |  | 19.6     |  | 24.2     |  | 70.8     |  | 17.1     |  | 122      |  |
| 222 | 136%           | 84.2%           | 57.9     | 2.1%                                     | 42.3     | 53.7%                                    | 49.6     | 51.2%                                    | 74.3     | 4.7%                                     | 36.6     | 53.2%                                    | 102      | 20.0%                                    |
| 333 | 78.6%          | 38.3%           | 55.2     | 5.0%                                     | 45.7     | 7.4%                                     | 53.4     | 7.1%                                     | 53.3     | 39.6%                                    | 42.1     | 13.1%                                    | 56.9     | 78.6%                                    |
| 444 | 34.2%          | 21.9%           | 52.1     | 5.9%                                     | 50.0     | 8.5%                                     | 54.0     | 1.2%                                     | 39.7     | 34.2%                                    | 45.6     | 7.6%                                     | 54.7     | 4.0%                                     |
| 555 | 13.0%          | 7.3%            | 50.3     | 3.6%                                     | 51.6     | 3.2%                                     | 55.0     | 1.8%                                     | 36.4     | 9.1%                                     | 46.1     | 1.1%                                     | 56.8     | 3.7%                                     |
| 666 | 15.0%          | 7.8%            | 51.4     | 2.2%                                     | 51.1     | 0.93%                                    | 55.1     | 0.17%                                    | 37.8     | 3.9%                                     | 43.9     | 5.0%                                     | 59.8     | 4.9%                                     |

Table C.2: Convergence analysis for SFL.

| PZL | $\Omega$   | $\kappa_{\Omega}$                      | $k_{ff}$ | $\Delta_{k_{ff}}^{\alpha \setminus \beta}$ | $k_{fn}$ | $\Delta_{k_{fn}}^{\alpha \setminus \beta}$ | $k_{fs}$ | $\Delta_{k_{fs}}^{\alpha \setminus \beta}$ | $k_{nn}$ | $\Delta_{k_{nn}}^{\alpha \setminus \beta}$ | $k_{ns}$ | $\Delta_{k_{ns}}^{\alpha \setminus \beta}$ | $k_{ss}$ | $\Delta_{k_{ss}}^{\alpha \setminus \beta}$ |
|-----|--|--|----------|--|----------|--|----------|--|----------|--|----------|--|----------|--|
| 111 | 547.6  | 1.93%                                  | 0.759    |  | 0.0606   |  | 0.0596   |  | 0.053    |  | 0.0644   |  | 0.0847   |  |
| 222 | 312.5  | 1.10%                                  | 0.774    | 1.9%                                       | 0.0204   | 198%                                       | 0.0271   | 120%                                       | 0.068    | 23.0%                                      | 0.0172   | 275%                                       | 0.0559   | 51.5%                                      |
| 333 | 286.1  | 1.01%                                  | 0.803    | 3.6%                                       | 0.0261   | 22.0%                                      | 0.0297   | 8.6%                                       | 0.306    | 77.7%                                      | 0.0105   | 64%  | 0.0418   | 33.9%                                      |
| 444 | 282.8  | 1.00%                                  | 0.822    | 2.3%                                       | 0.0280   | 6.7%                                       | 0.0304   | 2.2%                                       | 0.352    | 13.1%                                      | 0.0102   | 3.0%                                       | 0.0368   | 13.4%                                      |
| 555 | 283.3  | 1.00%                                  | 0.831    | 1.2%                                       | 0.0291   | 4.1%                                       | 0.0307   | 1.1%                                       | 0.298    | 18.3%                                      | 0.0111   | 8.0%                                       | 0.0365   | 0.84%                                      |
|     | $\max(\Delta_{\gamma_i}^{\alpha \setminus \beta})$ | $\Delta_{MP}^{\alpha \setminus \beta}$ | $a_{ff}$ | $\Delta_{a_{ff}}^{\alpha \setminus \beta}$ | $a_{fn}$ | $\Delta_{a_{fn}}^{\alpha \setminus \beta}$ | $a_{fs}$ | $\Delta_{a_{fs}}^{\alpha \setminus \beta}$ | $a_{nn}$ | $\Delta_{a_{nn}}^{\alpha \setminus \beta}$ | $a_{ns}$ | $\Delta_{a_{ns}}^{\alpha \setminus \beta}$ | $a_{ss}$ | $\Delta_{a_{ss}}^{\alpha \setminus \beta}$ |
| 111 |  |  | 0.354    |  | 0.370    |  | 0.370    |  | 0.276    |  | 0.431    |  | 0.282    |  |
| 222 | 275%   | 60.6%                                  | 0.358    | 0.94%                                      | 0.339    | 9.3%                                       | 0.365    | 1.5%                                       | 0.259    | 6.8%                                       | 0.369    | 16.8%                                      | 0.229    | 23.0%                                      |
| 333 | 77.7%  | 22.4%                                  | 0.372    | 3.9%                                       | 0.339    | 0.032%                                     | 0.360    | 1.3%                                       | 0.444    | 41.7%                                      | 0.331    | 11.5%                                      | 0.229    | 0.12%                                      |
| 444 | 13.4%  | 4.3%                                   | 0.377    | 1.3%                                       | 0.339    | 0.24%                                      | 0.359    | 0.32%                                      | 0.479    | 7.2%                                       | 0.326    | 1.42%                                      | 0.228    | 0.54%                                      |
| 555 | 18.3%  | 3.5%                                   | 0.381    | 1.0%                                       | 0.339    | 0.09%                                      | 0.357    | 0.54%                                      | 0.457    | 4.8%                                       | 0.327    | 0.31%                                      | 0.232    | 1.6%                                       |

Table C.3: Convergence analysis for PZL.

| TL  | $\Omega$       | $\kappa_{\Omega}$ | $a_{ff}$ | $\Delta_{a_{ff}}^{\alpha \setminus \beta}$ | $a_{fn}$ | $\Delta_{a_{fn}}^{\alpha \setminus \beta}$ | $a_{fs}$ | $\Delta_{a_{fs}}^{\alpha \setminus \beta}$ | $a_{nn}$ | $\Delta_{a_{nn}}^{\alpha \setminus \beta}$ | $a_{ns}$ | $\Delta_{a_{ns}}^{\alpha \setminus \beta}$ | $a_{ss}$ | $\Delta_{a_{ss}}^{\alpha \setminus \beta}$ |
|-----|----------------|-------------------|----------|--|----------|--|----------|--|----------|--|----------|--|----------|--|
| 111 | 132            |                   | 1.30     |  | 0.141    |  | 0.118    |  | 0.426    |  | 0.111    |  | 0.134    |  |
| 222 | 124            | 6.8%              | 1.38     | 5.5%                                       | 0.128    | 10.2%                                      | 0.124    | 5.0%                                       | 0.472    | 9.8%                                       | 0.108    | 2.83%                                      | 0.234    | 43.0%                                      |
| 333 | 108            | 14.1%             | 1.25     | 10.5%                                      | 0.130    | 2.0%                                       | 0.142    | 12.6%                                      | 0.553    | 14.6%                                      | 0.0930   | 16.49%                                     | 0.301    | 22.0%                                      |
| 444 | 103            | 5.7%              | 1.24     | 0.42%                                      | 0.115    | 12.9%                                      | 0.150    | 5.0%                                       | 0.681    | 18.8%                                      | 0.0790   | 17.70%                                     | 0.256    | 17.6%                                      |
| 555 | 103            | 0.00%             | 1.25     | 0.74%                                      | 0.112    | 3.0%                                       | 0.151    | 0.46%                                      | 0.713    | 4.5%                                       | 0.0784   | 0.78%                                      | 0.231    | 10.8%                                      |
| 666 | 103            | 0.64%             | 1.28     | 2.09%                                      | 0.110    | 2.1%                                       | 0.142    | 6.4%                                       | 0.715    | 0.33%                                      | 0.0864   | 9.22%                                      | 0.234    | 1.3%                                       |
|     | $\kappa_{max}$ | $\kappa$          | $b_{ff}$ | $\Delta_{b_{ff}}^{\alpha \setminus \beta}$ | $b_{fn}$ | $\Delta_{b_{fn}}^{\alpha \setminus \beta}$ | $b_{fs}$ | $\Delta_{b_{fs}}^{\alpha \setminus \beta}$ | $b_{nn}$ | $\Delta_{b_{nn}}^{\alpha \setminus \beta}$ | $b_{ns}$ | $\Delta_{b_{ns}}^{\alpha \setminus \beta}$ | $b_{ss}$ | $\Delta_{b_{ss}}^{\alpha \setminus \beta}$ |
| 111 |                |                   | 15.8     |  | 11.5     |  | 12.7     |  | 17.1     |  | 10.9     |  | 20.7     |  |
| 222 | 43.0%          | 7.7%              | 15.8     | 0.38%                                      | 11.9     | 3.2%                                       | 12.9     | 1.4%                                       | 17.5     | 2.3%                                       | 11.2     | 2.98%                                      | 19.6     | 5.7%                                       |
| 333 | 30.5%          | 11.8%             | 15.3     | 3.2%                                       | 12.4     | 3.7%                                       | 13.3     | 2.7%                                       | 14.9     | 16.9%                                      | 12.0     | 6.60%                                      | 15.0     | 30.5%                                      |
| 444 | 18.8%          | 8.6%              | 14.9     | 2.6%                                       | 12.9     | 4.2%                                       | 13.3     | 0.49%                                      | 12.8     | 16.3%                                      | 12.6     | 4.50%                                      | 14.6     | 2.8%                                       |
| 555 | 10.8%          | 2.7%              | 14.6     | 2.1%                                       | 13.1     | 1.7%                                       | 13.5     | 1.0%                                       | 12.3     | 4.5%                                       | 12.7     | 0.90%                                      | 14.8     | 1.7%                                       |
| 666 | 9.2%           | 2.5%              | 14.4     | 1.8%                                       | 13.3     | 0.95%                                      | 13.7     | 1.8%                                       | 12.2     | 0.92%                                      | 12.5     | 1.35%                                      | 14.7     | 1.2%                                       |

Table C.4: Convergence analysis for TL.

### **C.3 All Graphs for all Experiments, FE Model**

The dotted lines in the graphs denote the experimental data and the solid lines denote the model results.

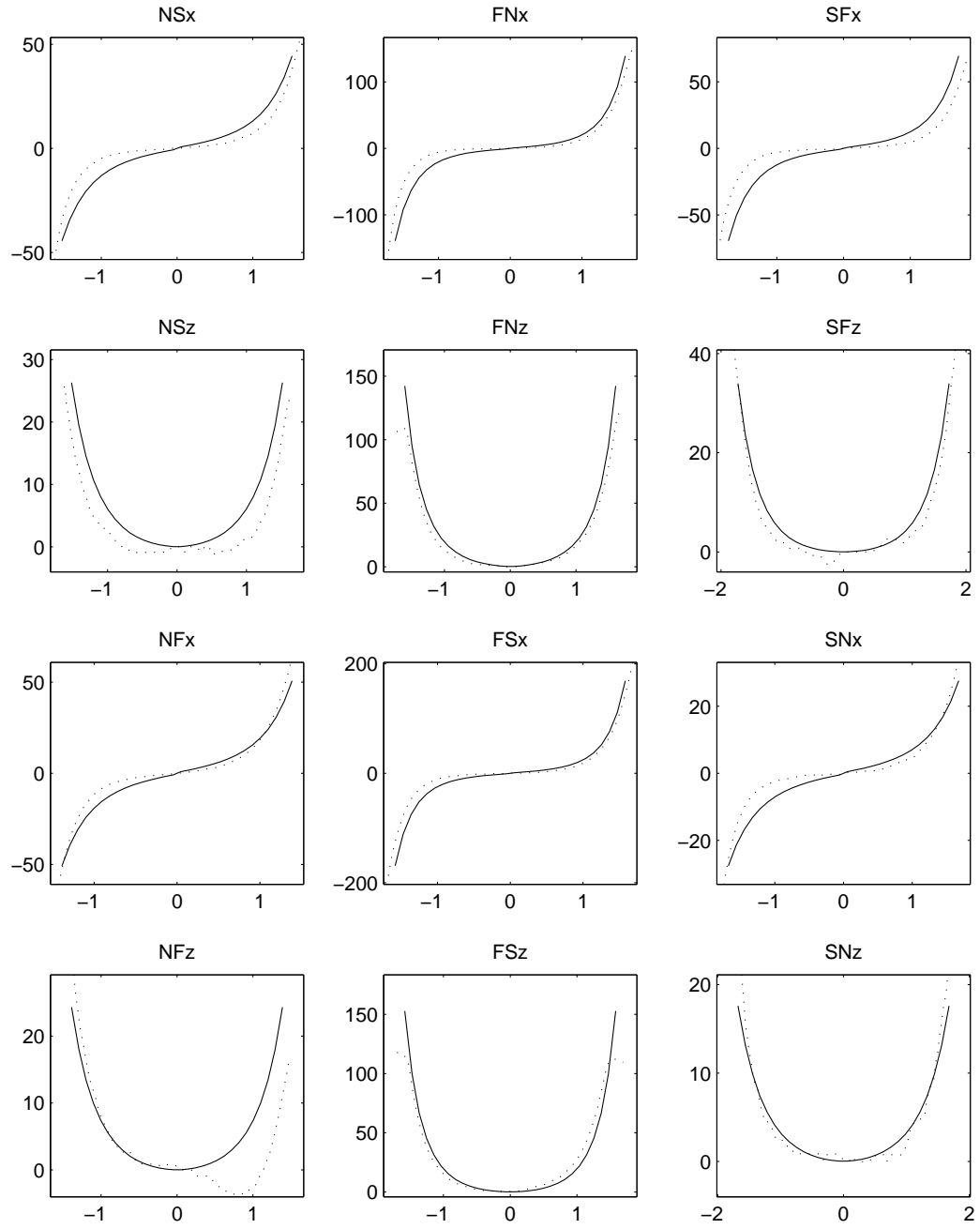
**Graph of FE model, experiment 1, CL**

Figure C.1: This graph shows the result of the FEM model for experiment 1, CL.

## Graph of FE model, experiment 1, SFL

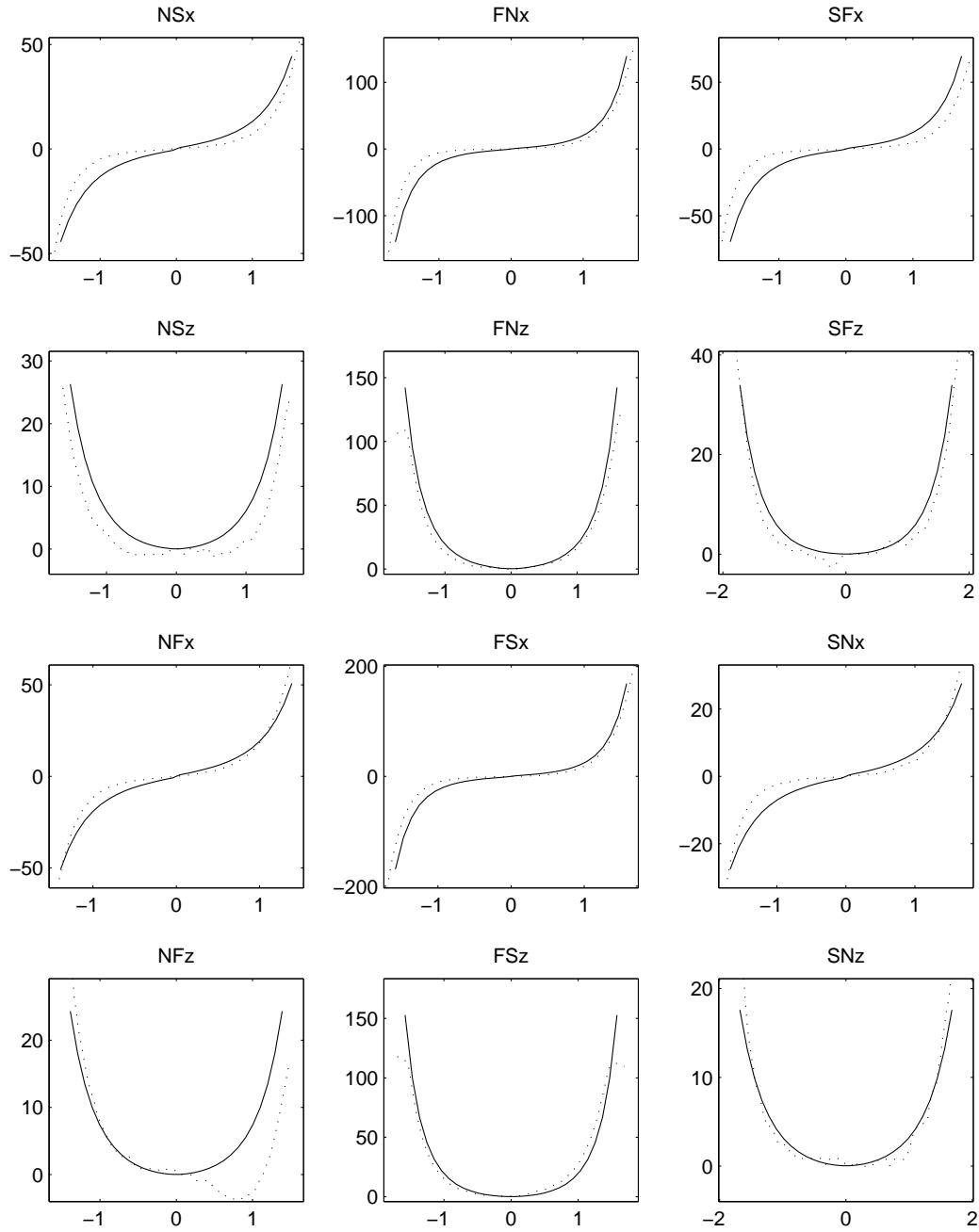


Figure C.2: This graph shows the result of the FEM model for experiment 1, SFL.

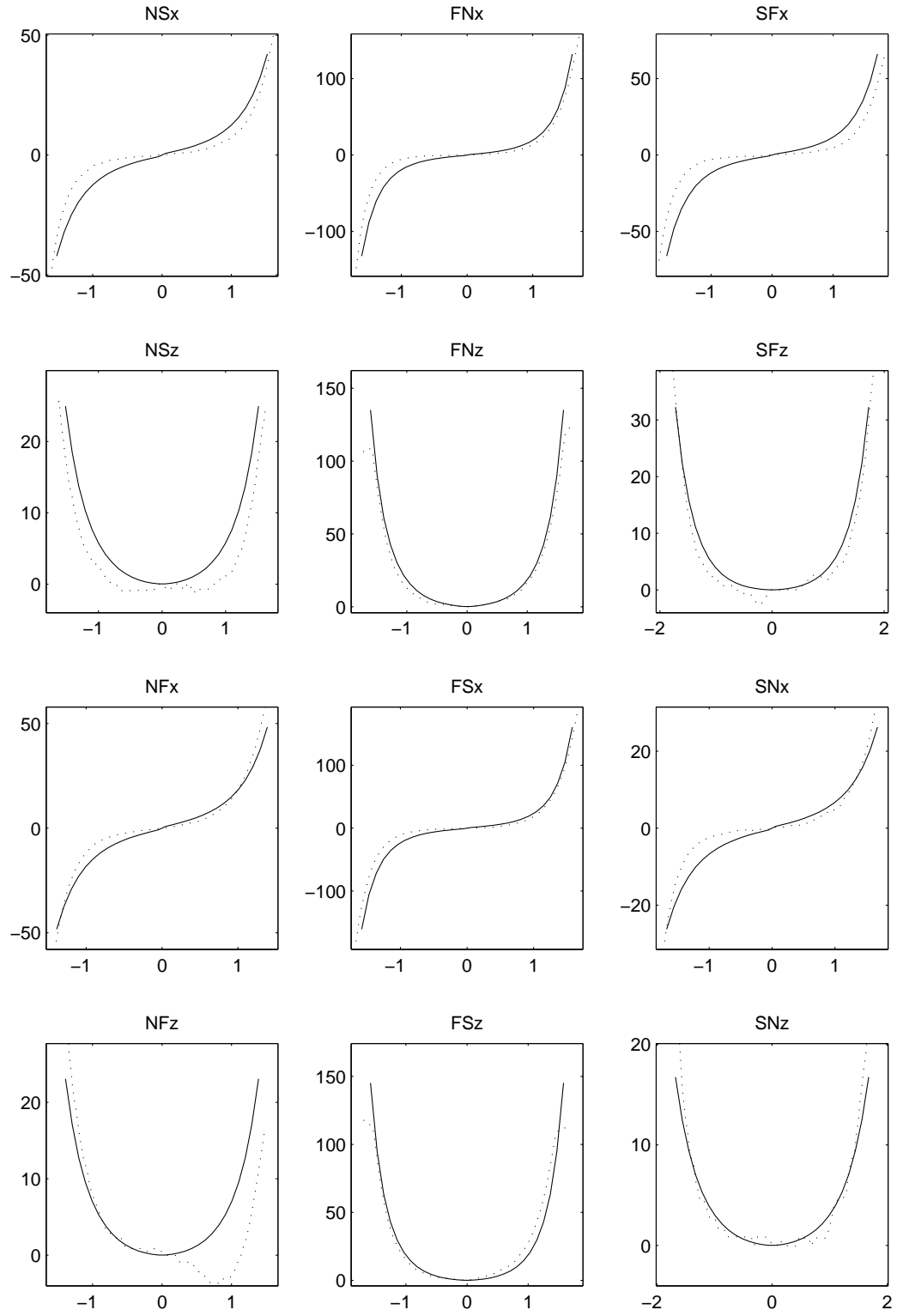
**Graph of FE model, experiment 1, PZL**

Figure C.3: This graph shows the result of the FEM model for experiment 1, PZL.

## Graph of FE model, experiment 1, TL

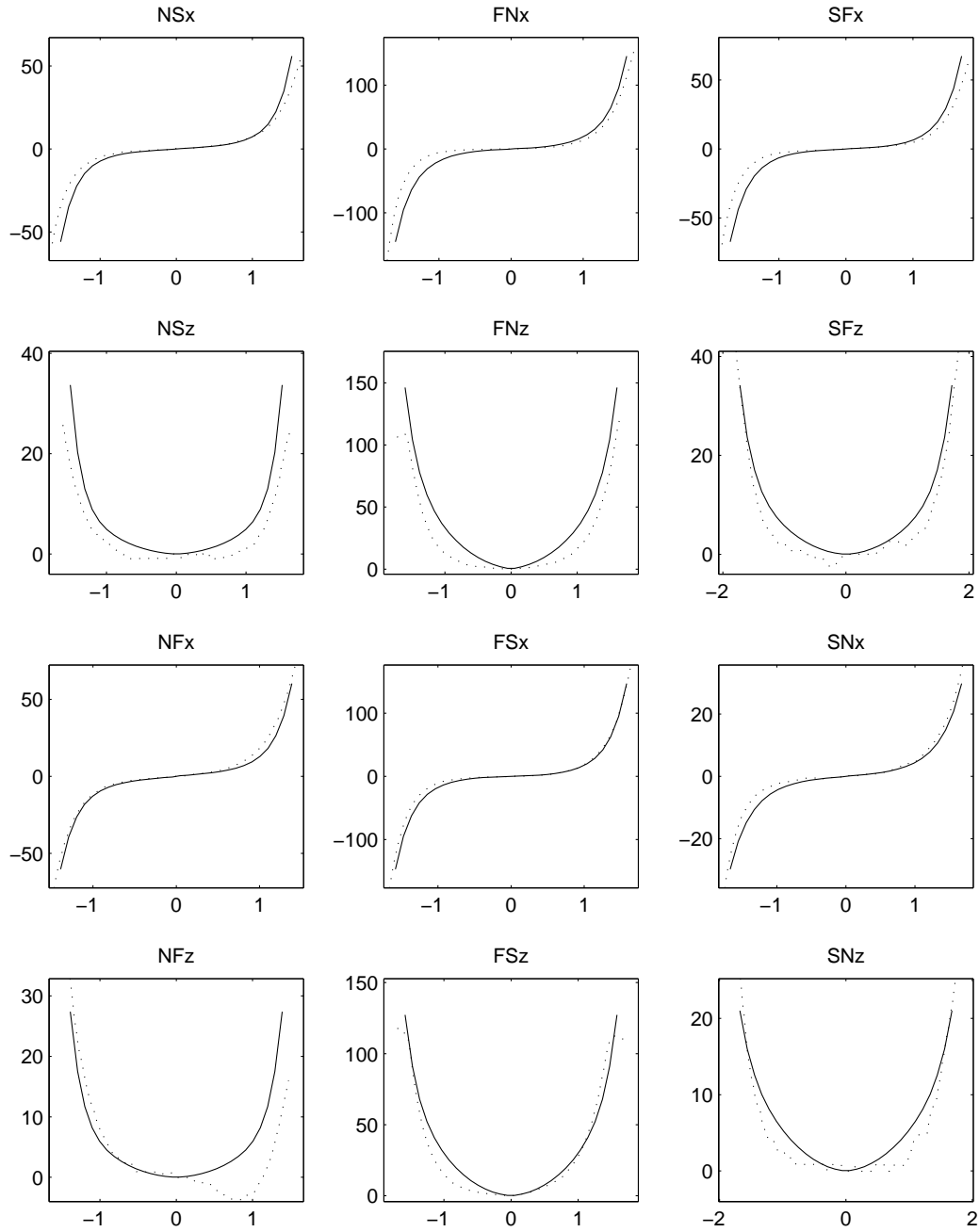


Figure C.4: This graph shows the result of the FEM model for experiment 1, TL.



**Graph of FE model, experiment 2, CL**

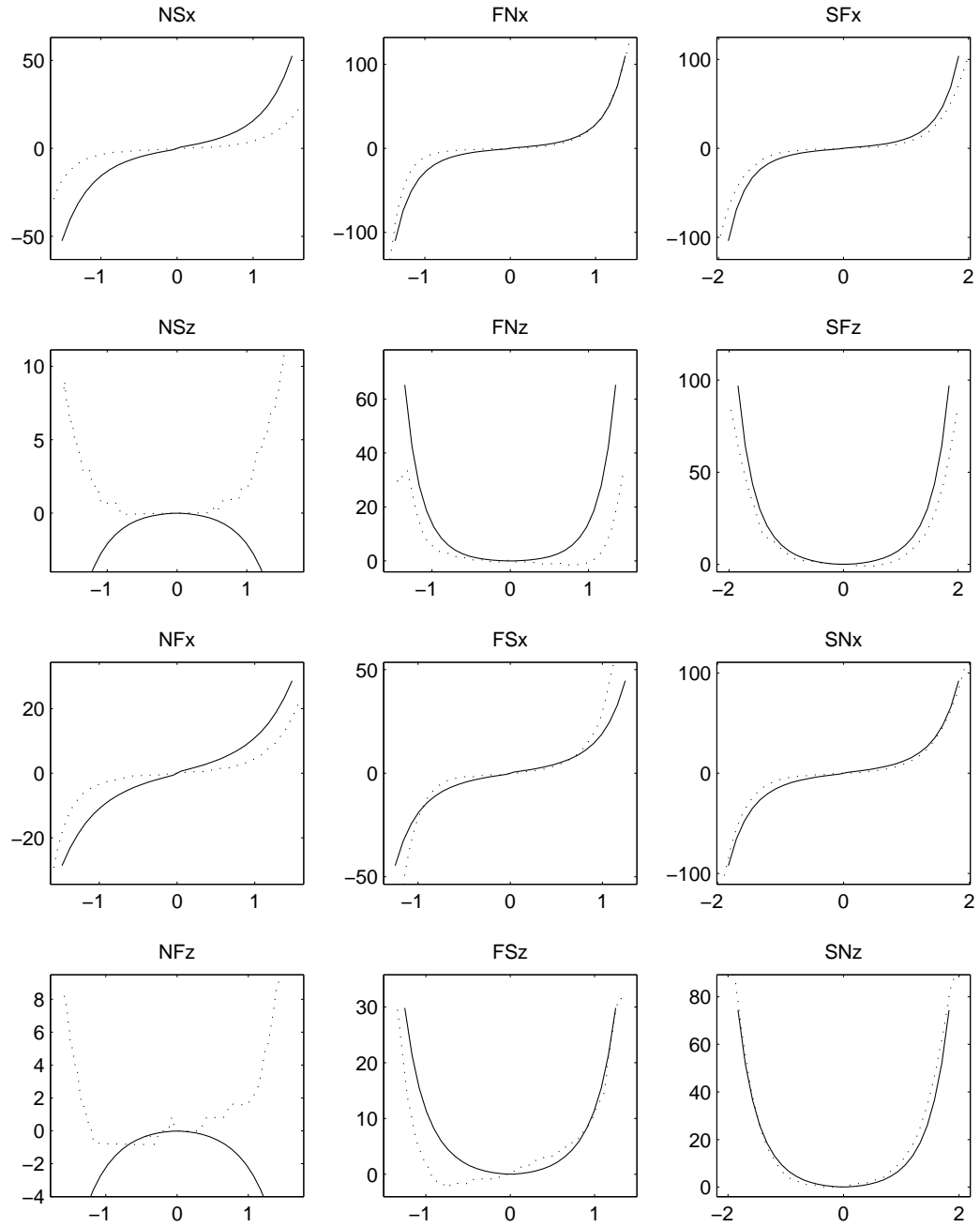


Figure C.5: This graph shows the result of the FEM model for experiment 2, CL.

## Graph of FE model, experiment 2, SFL

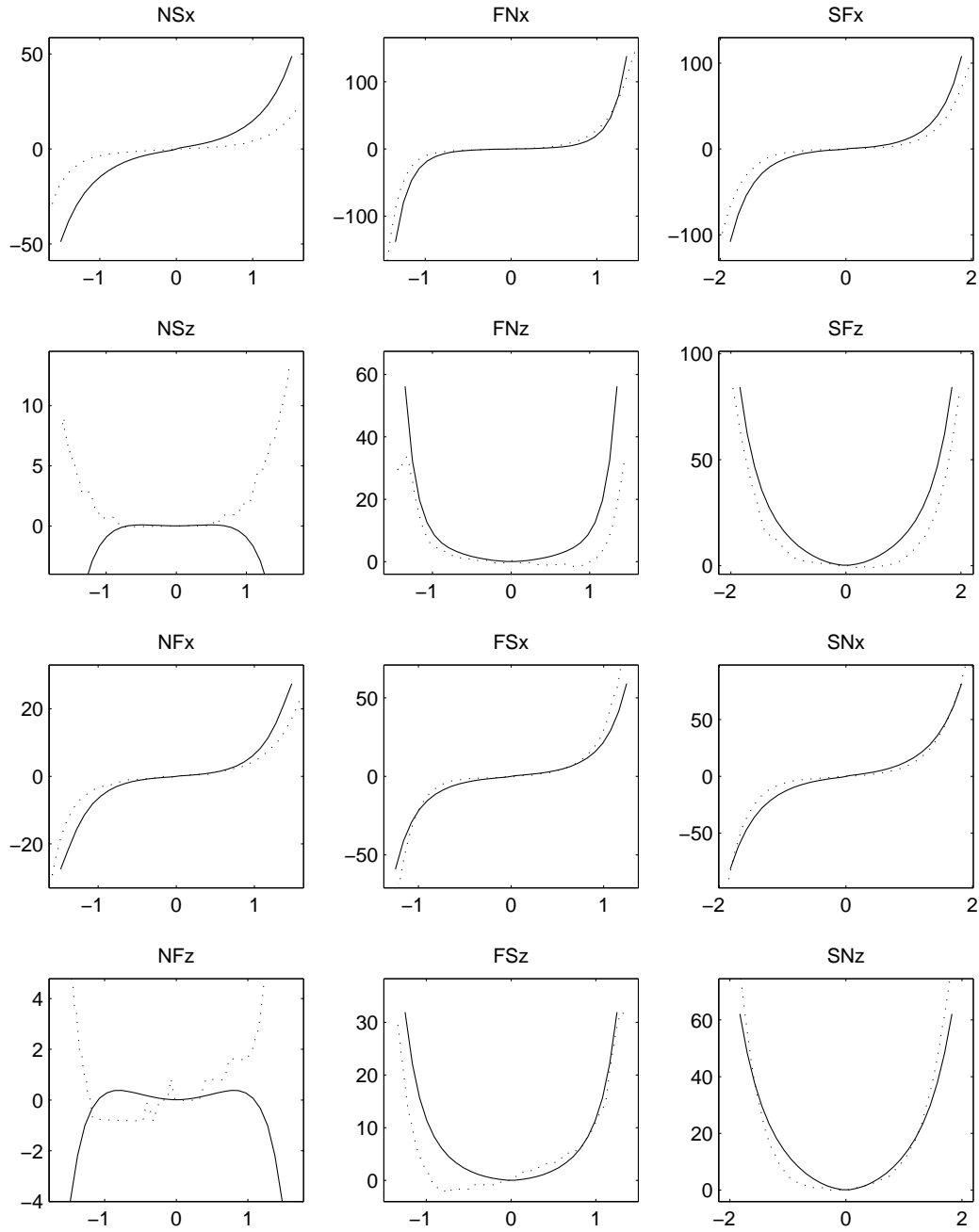


Figure C.6: This graph shows the result of the FEM model for experiment 2, SFL.

**Graph of FE model, experiment 2, PZL**

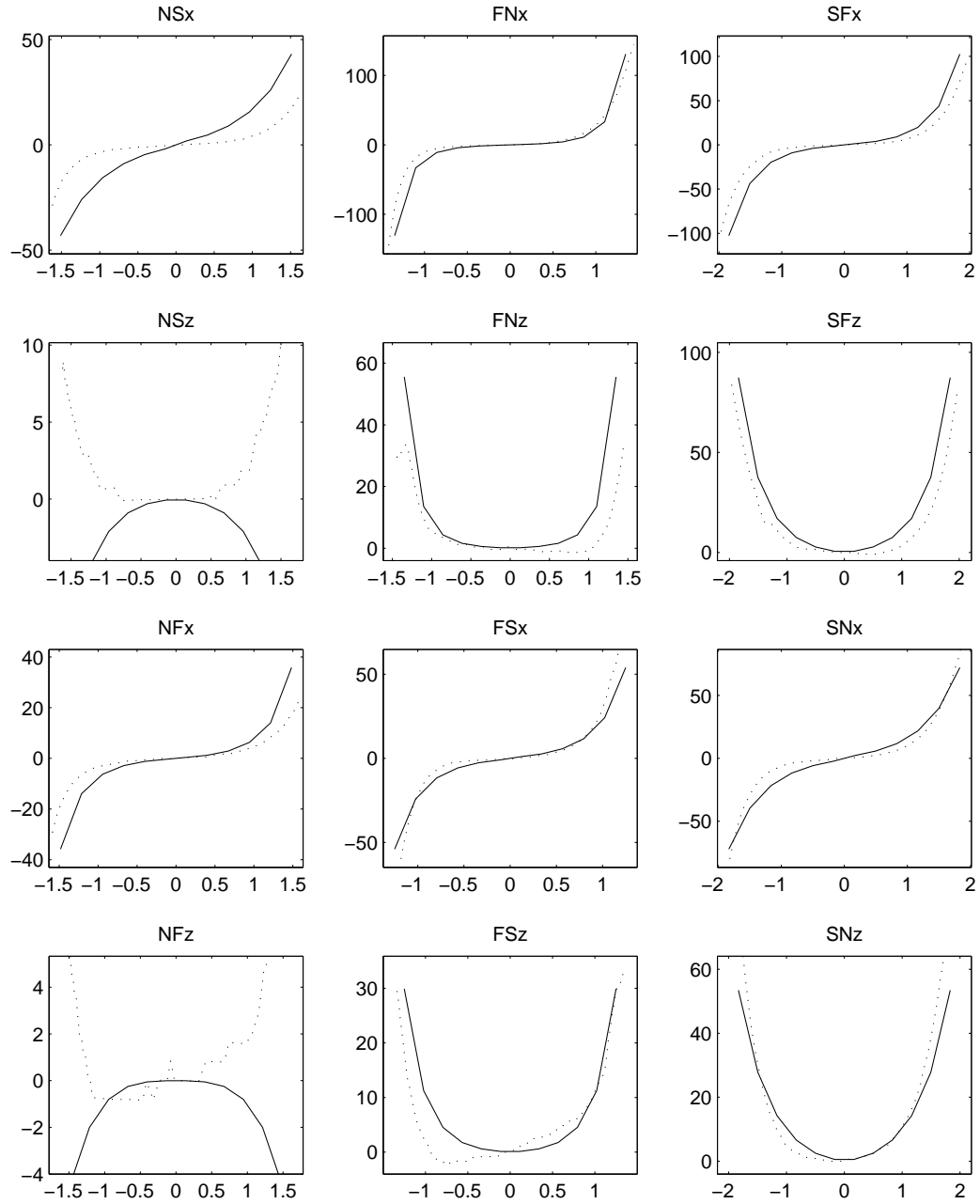


Figure C.7: This graph shows the result of the FEM model for experiment 2, PZL.

## Graph of FE model, experiment 2, TL

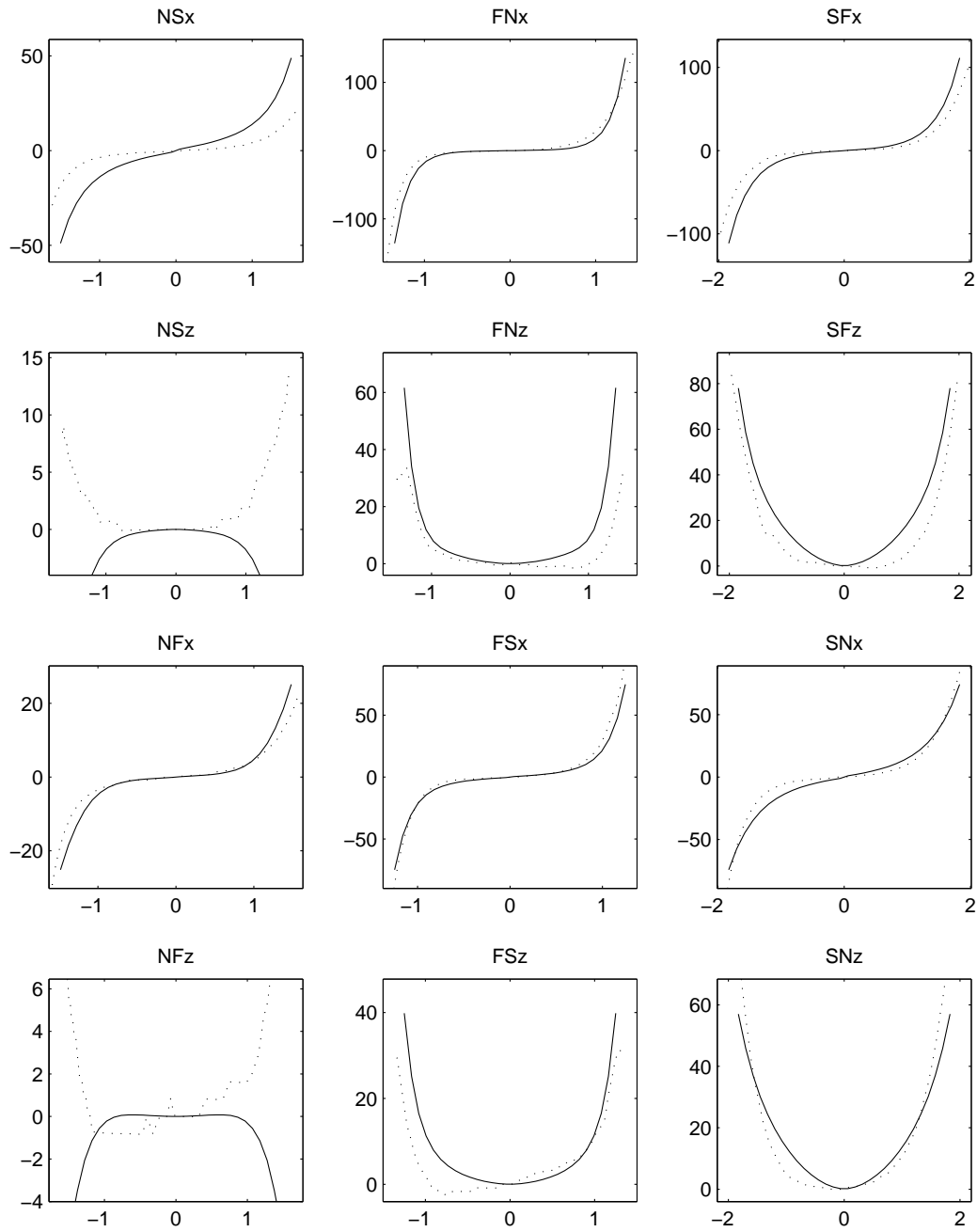


Figure C.8: This graph shows the result of the FEM model for experiment 2, TL.

**Graph of FE model, experiment 3, CL**

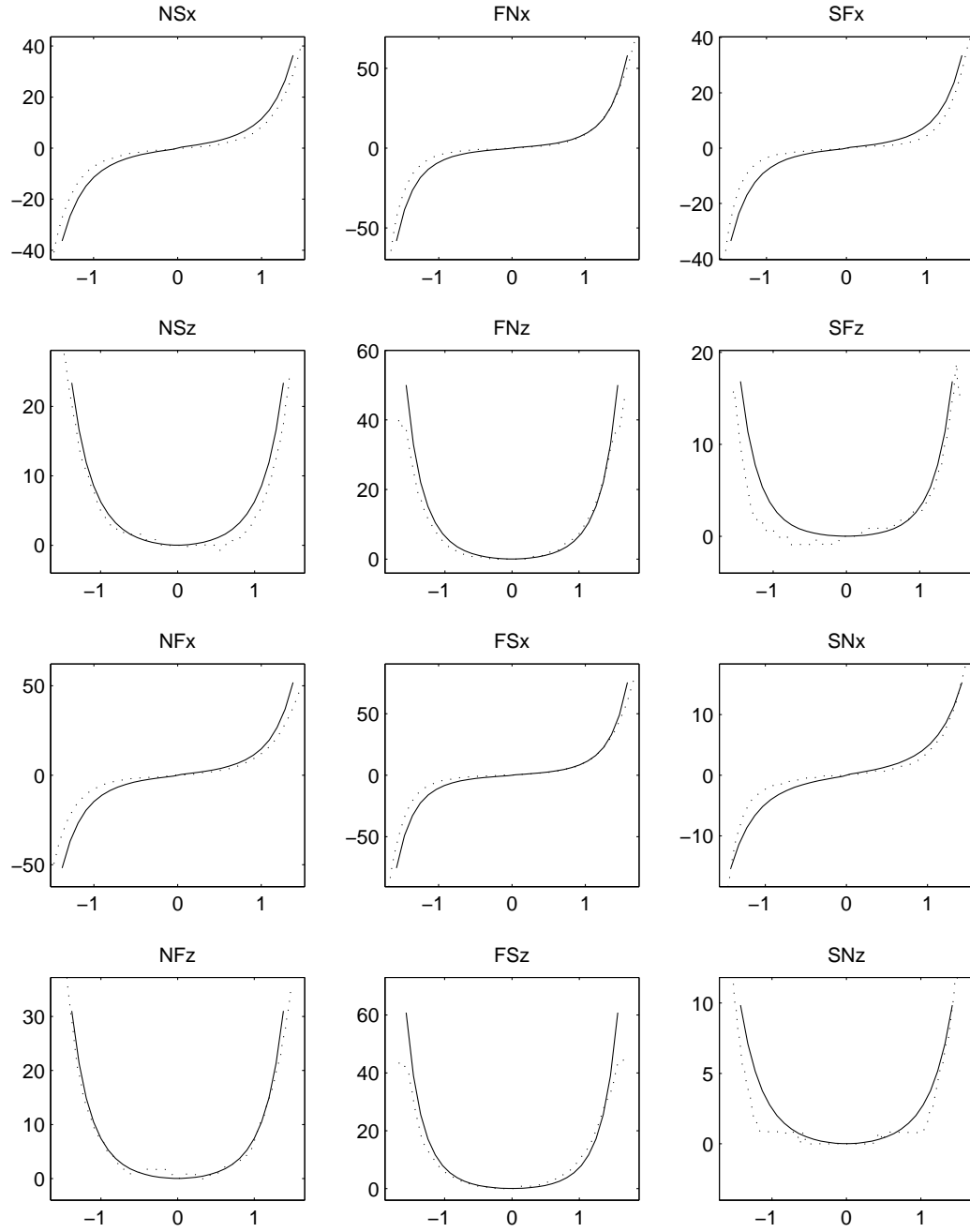


Figure C.9: This graph shows the result of the FEM model for experiment 3, CL.

Graph of FE model, experiment 3, SFL

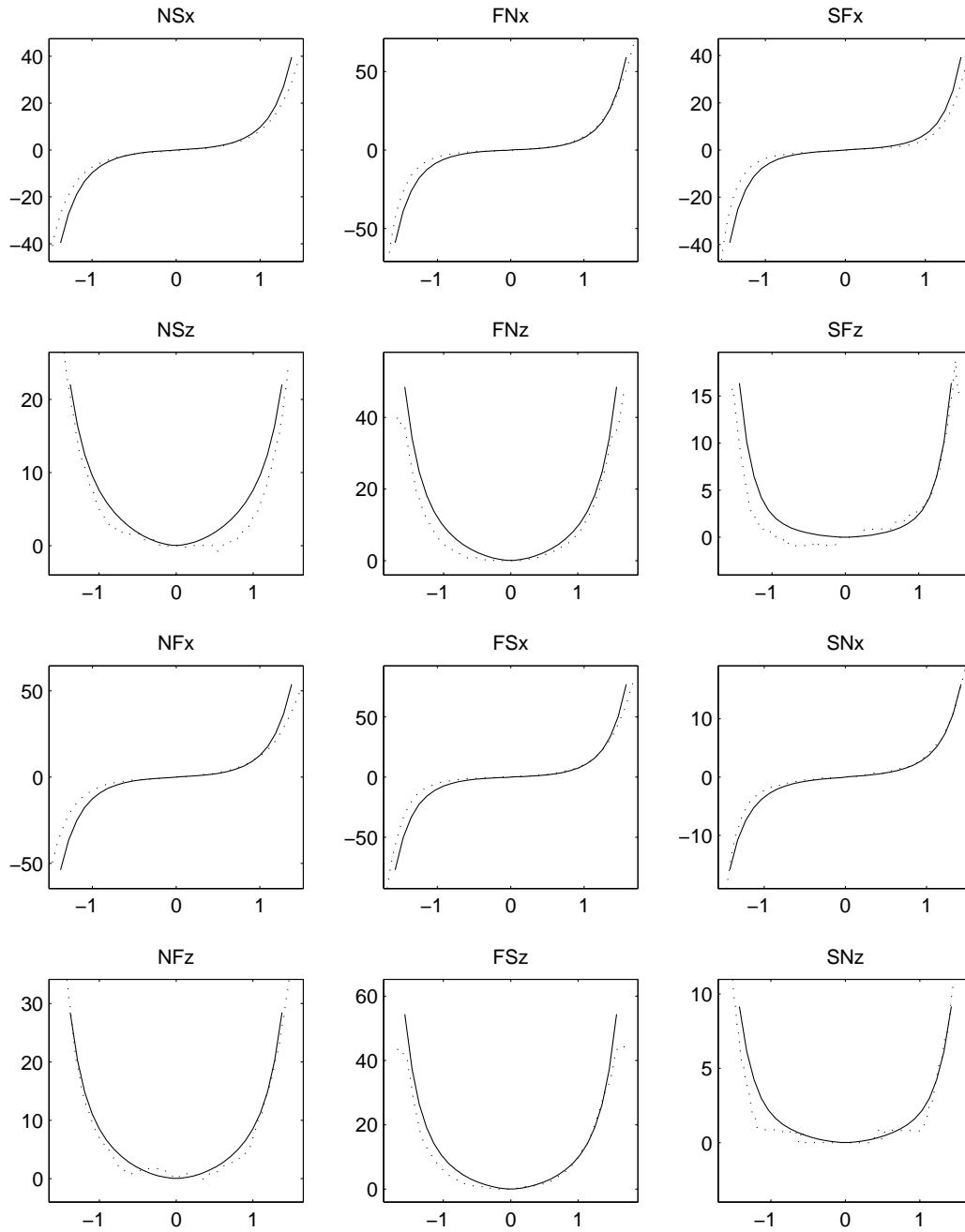


Figure C.10: This graph shows the result of the FEM model for experiment 3, SFL.

**Graph of FE model, experiment 3, PZL**

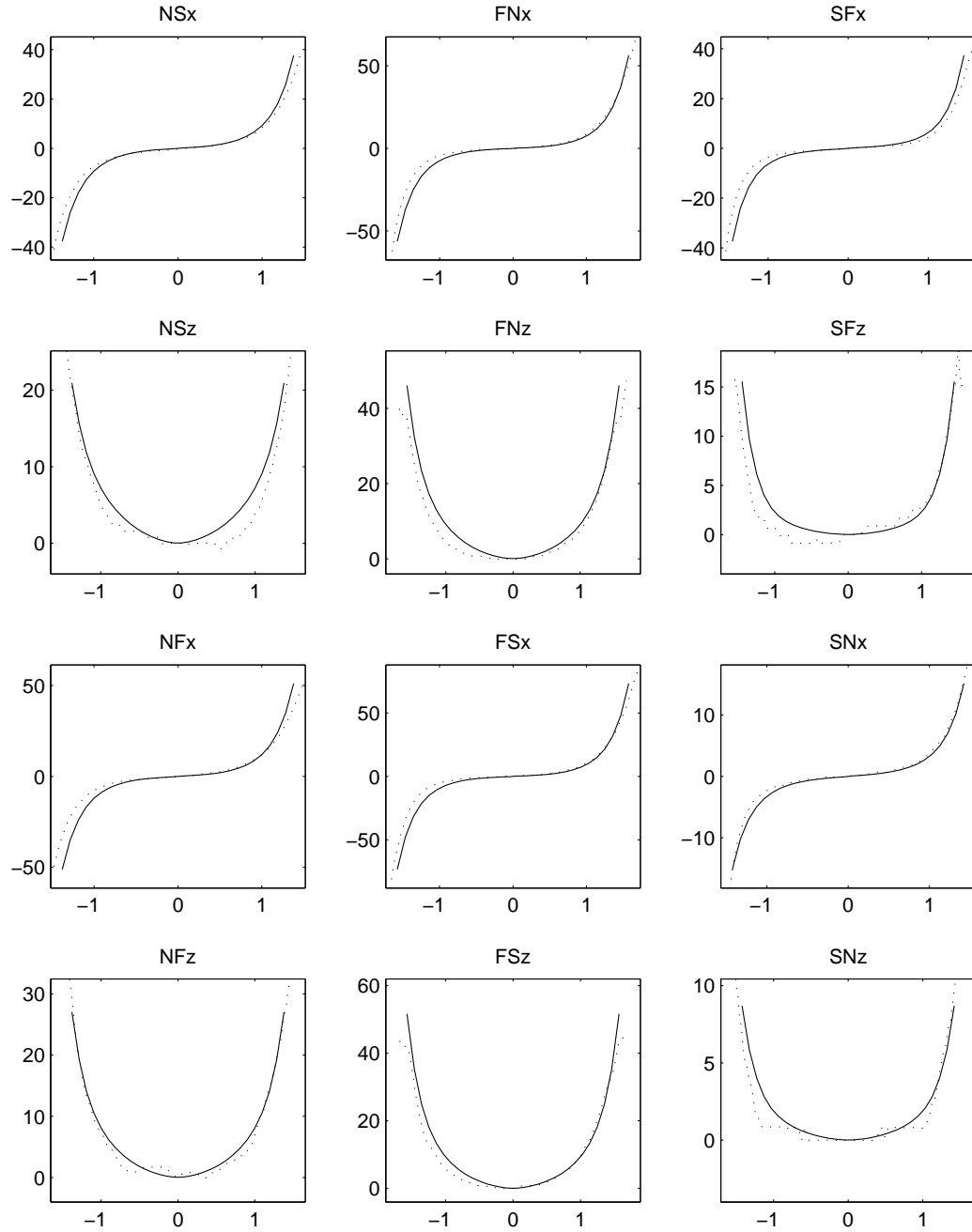


Figure C.11: This graph shows the result of the FEM model for experiment 3, PZL.

## Graph of FE model, experiment 3, TL

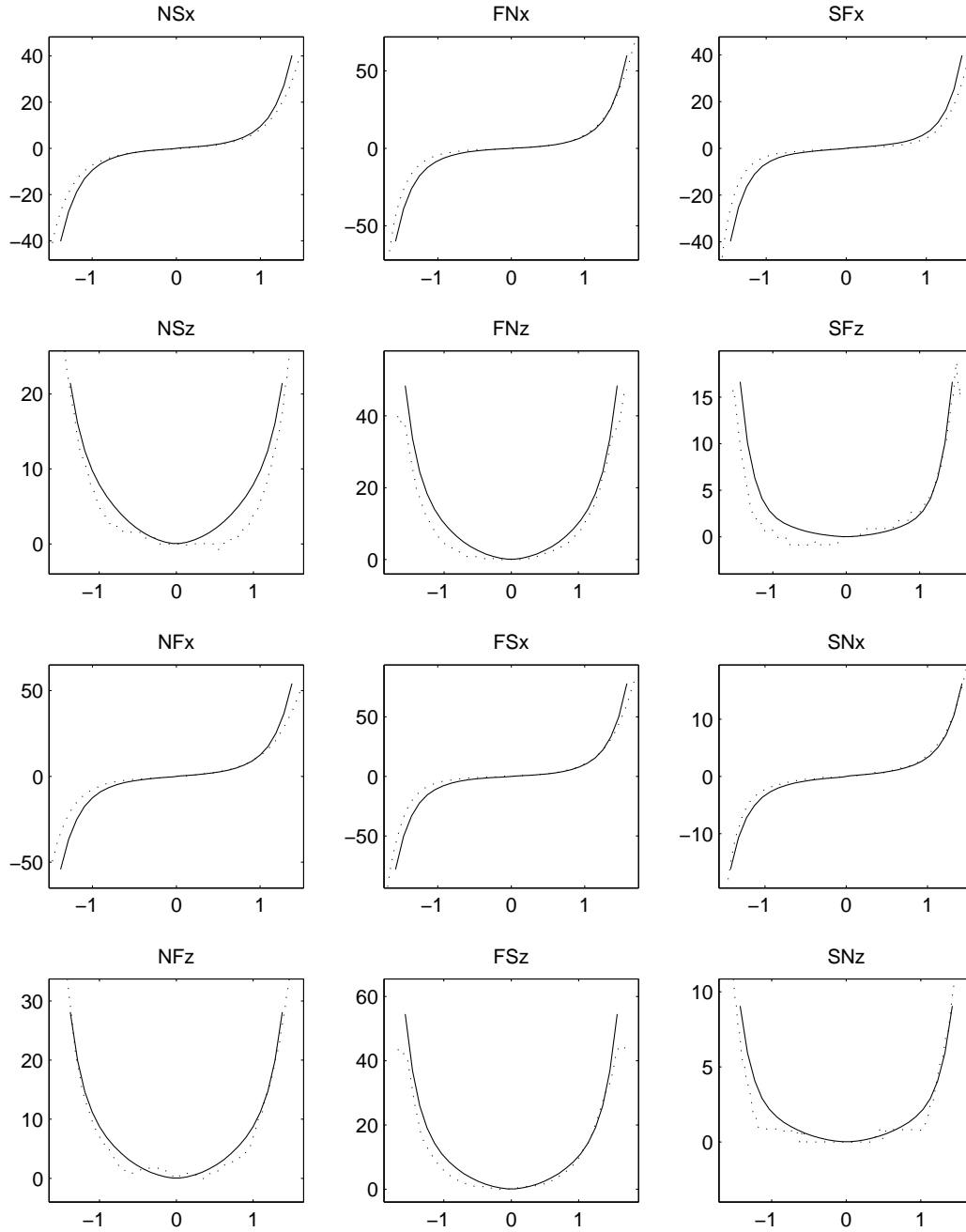


Figure C.12: This graph shows the result of the FEM model for experiment 3, TL.



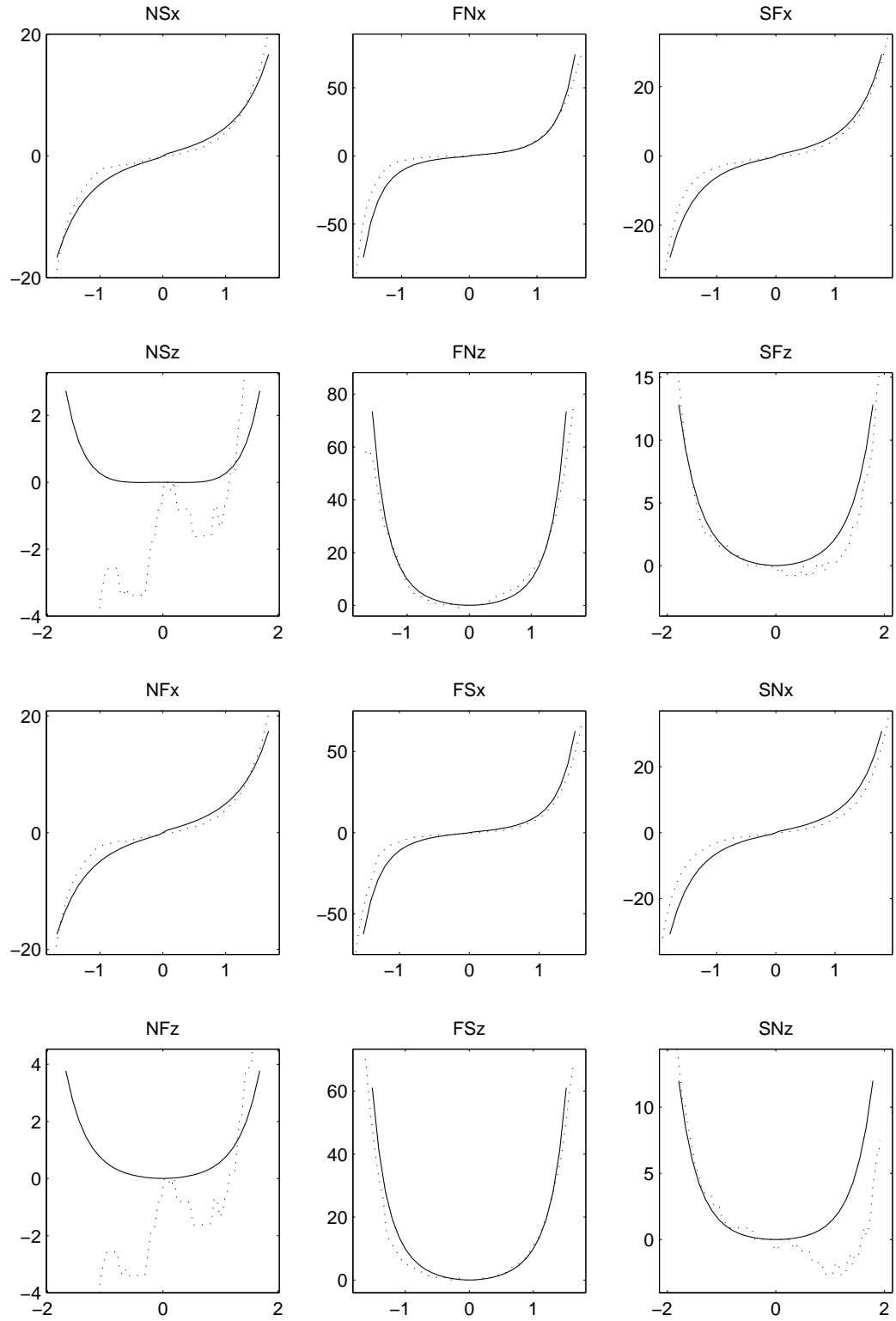
**Graph of FE model, experiment 4, CL**

Figure C.13: This graph shows the result of the FEM model for experiment 4, CL.

Graph of FE model, experiment 4, SFL

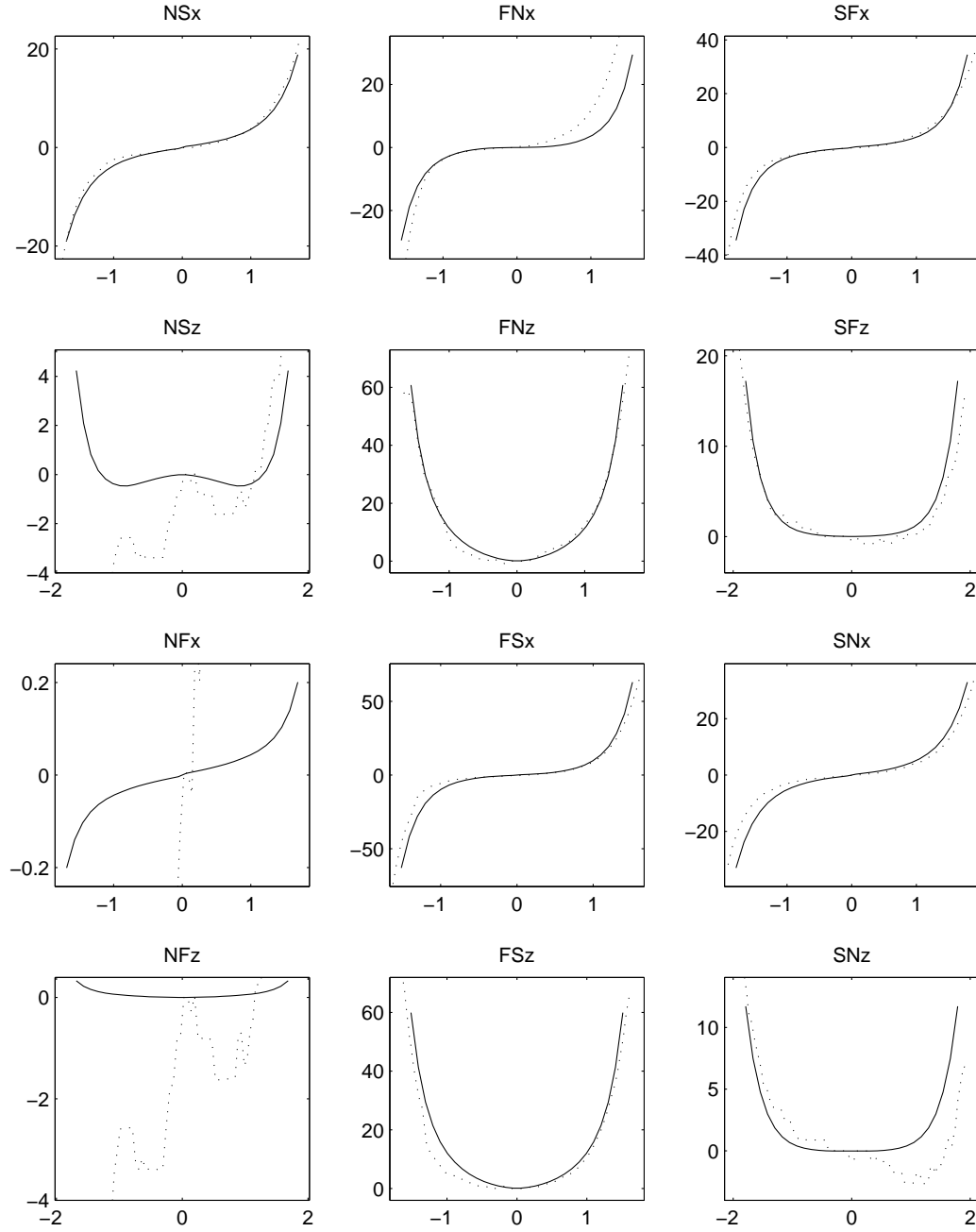


Figure C.14: This graph shows the result of the FEM model for experiment 4, SFL.

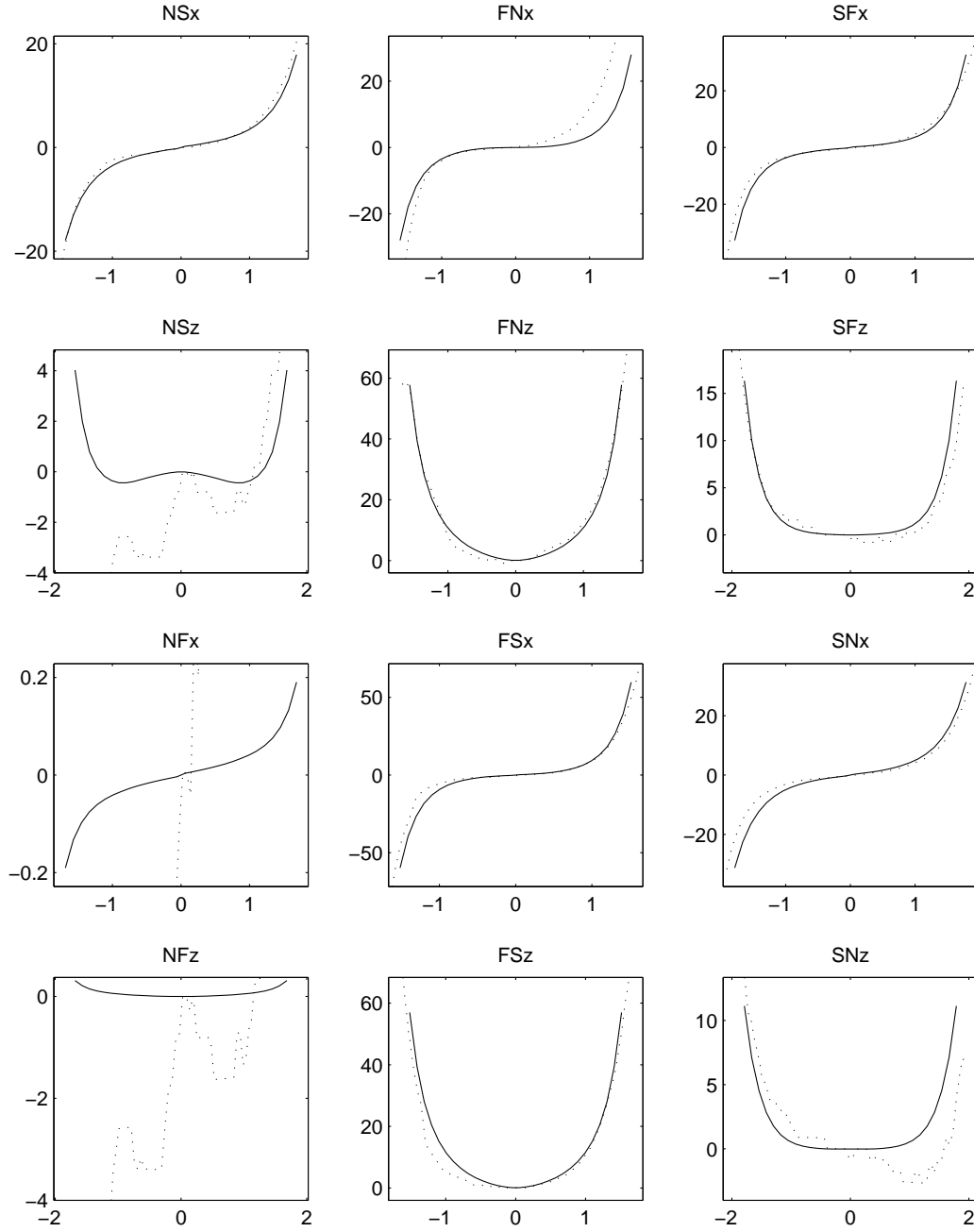
**Graph of FE model, experiment 4, PZL**

Figure C.15: This graph shows the result of the FEM model for experiment 4, PZL.

## Graph of FE model, experiment 4, TL

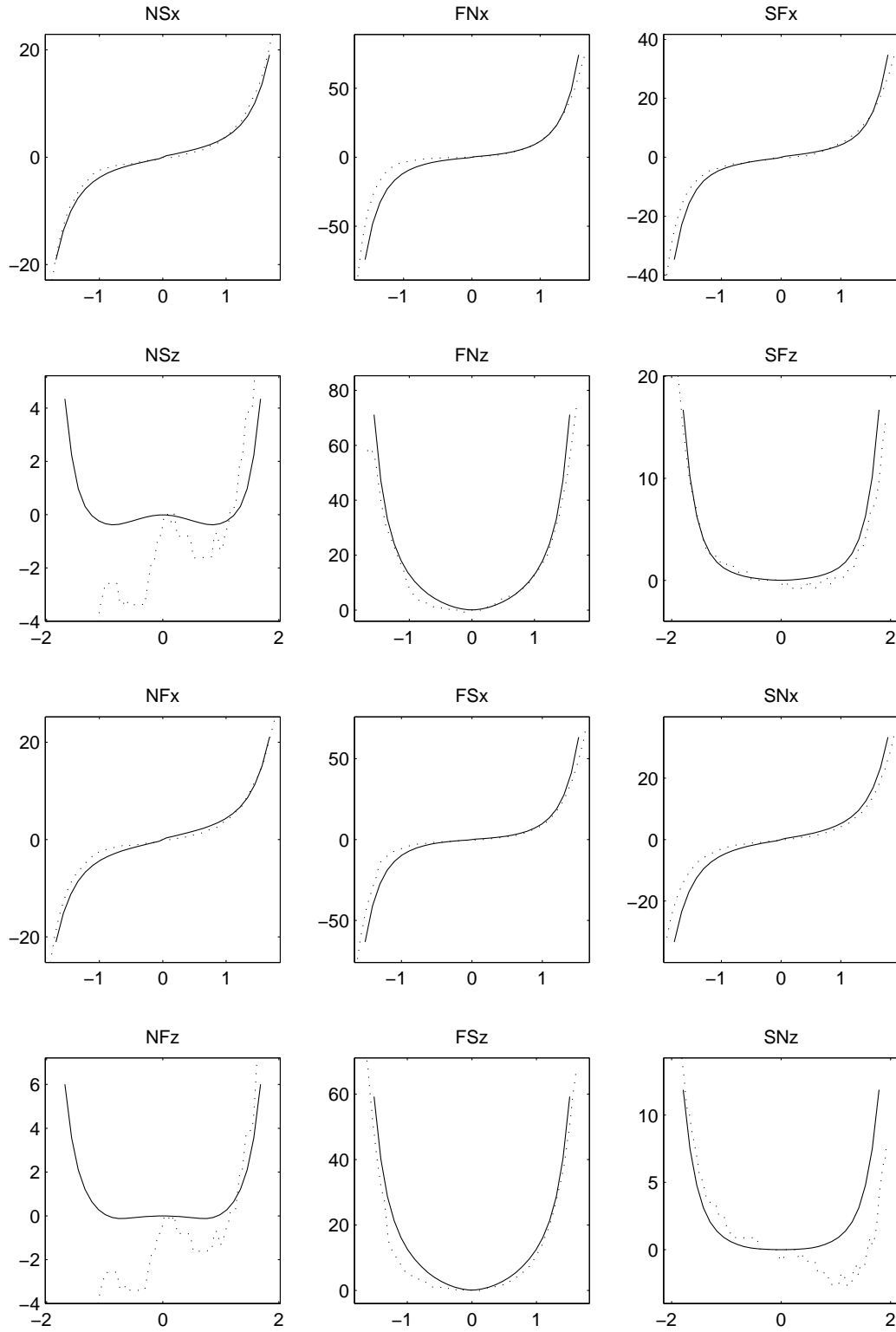


Figure C.16: This graph shows the result of the FEM model for experiment 4, TL.

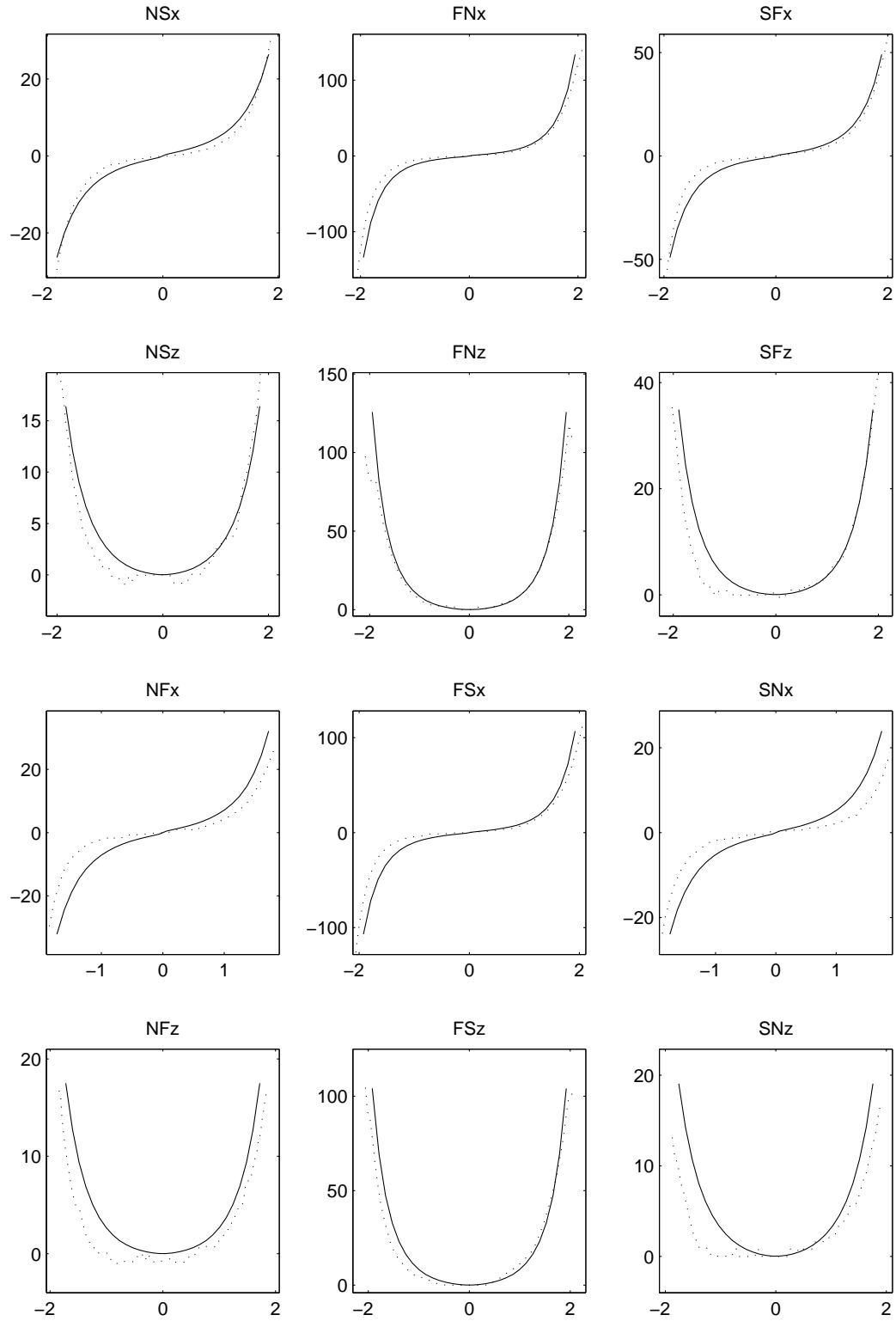
**Graph of FE model, experiment 5, CL**

Figure C.17: This graph shows the result of the FEM model for experiment 5, CL.

## Graph of FE model, experiment 5, SFL

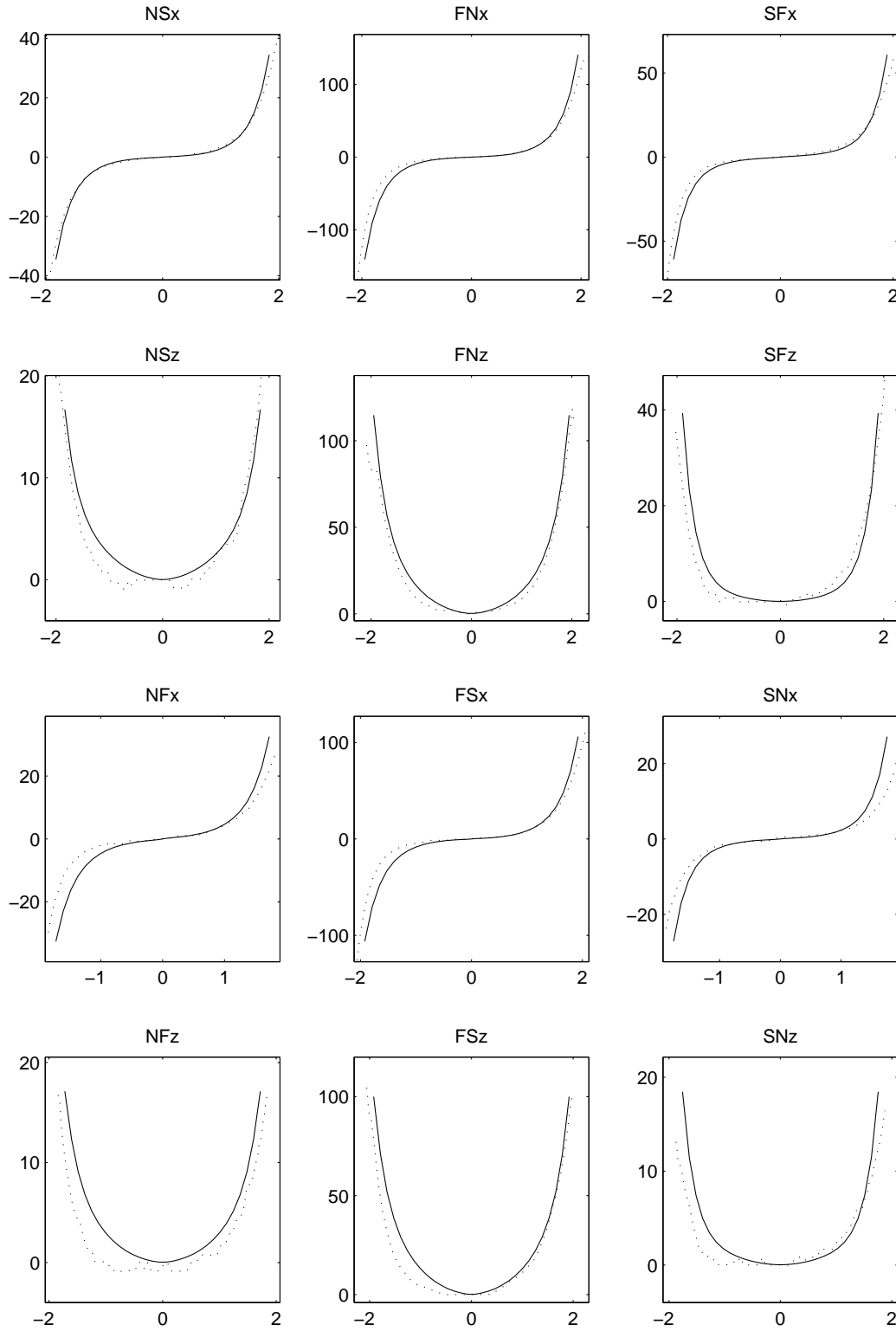


Figure C.18: This graph shows the result of the FEM model for experiment 5, SFL.

**Graph of FEM model, experiment 5, PZL**

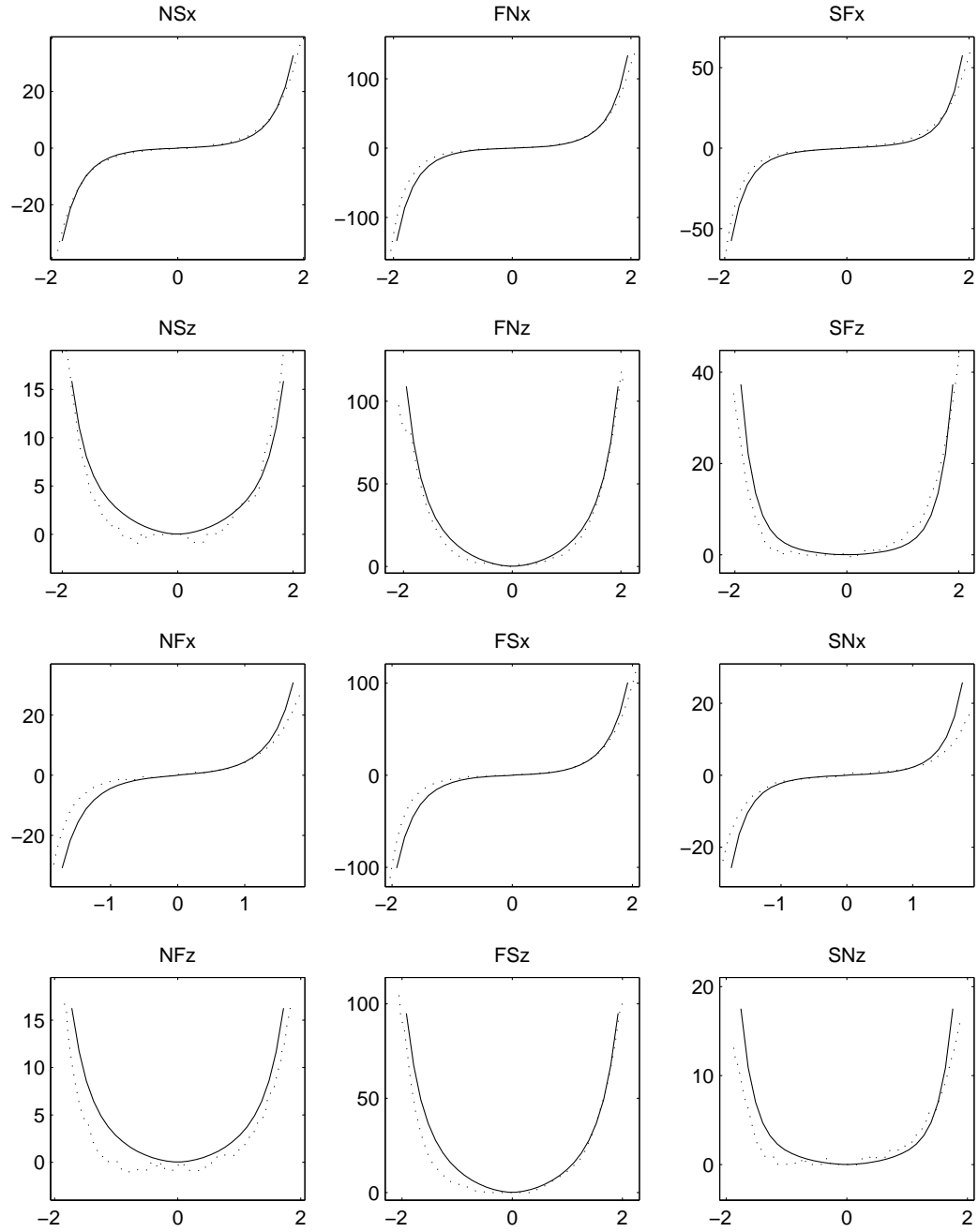


Figure C.19: This graph shows the result of the FEM model for experiment 5, PZL.

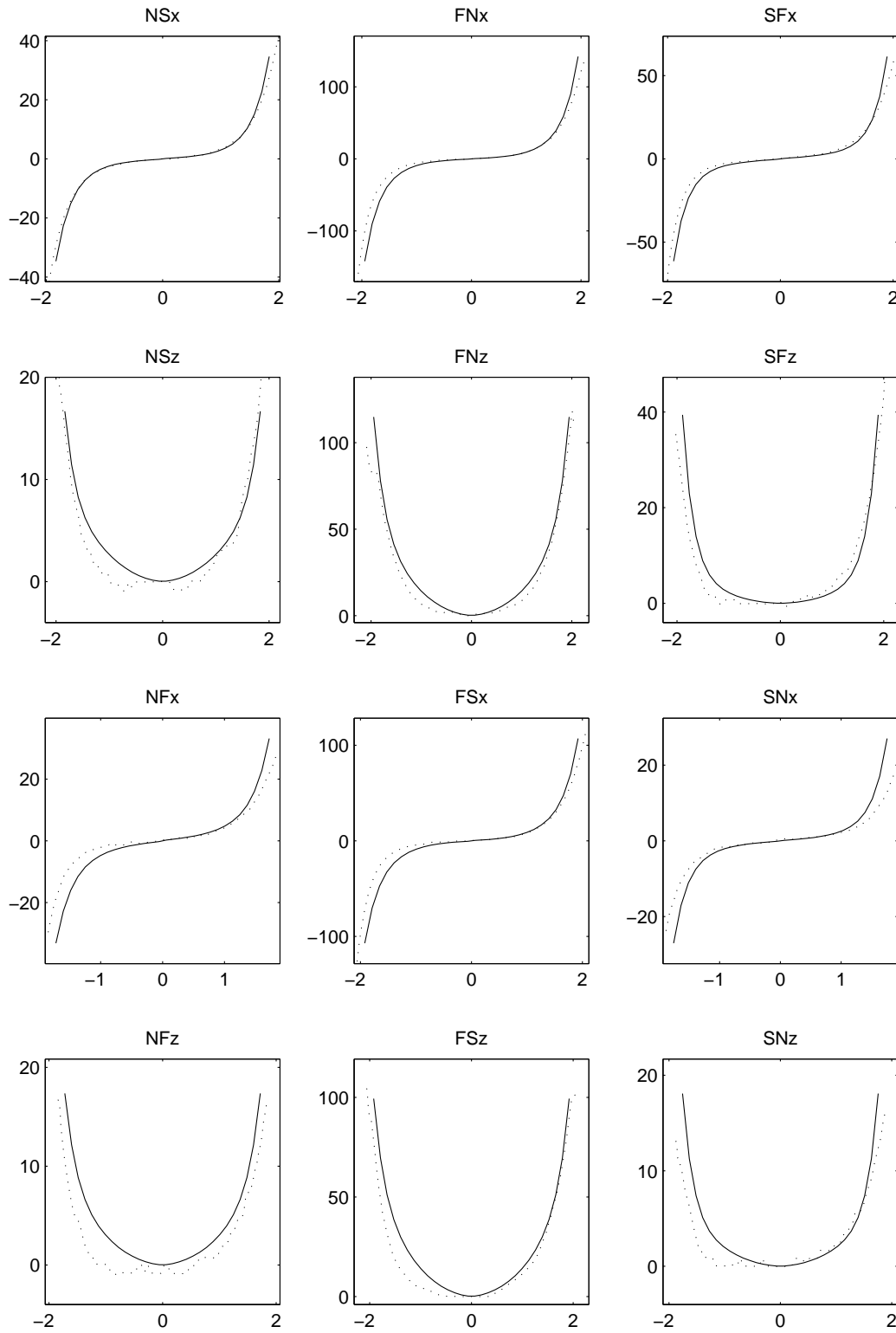
**Graph of FE model, experiment 5, TL**

Figure C.20: This graph shows the result of the FEM model for experiment 5, TL.



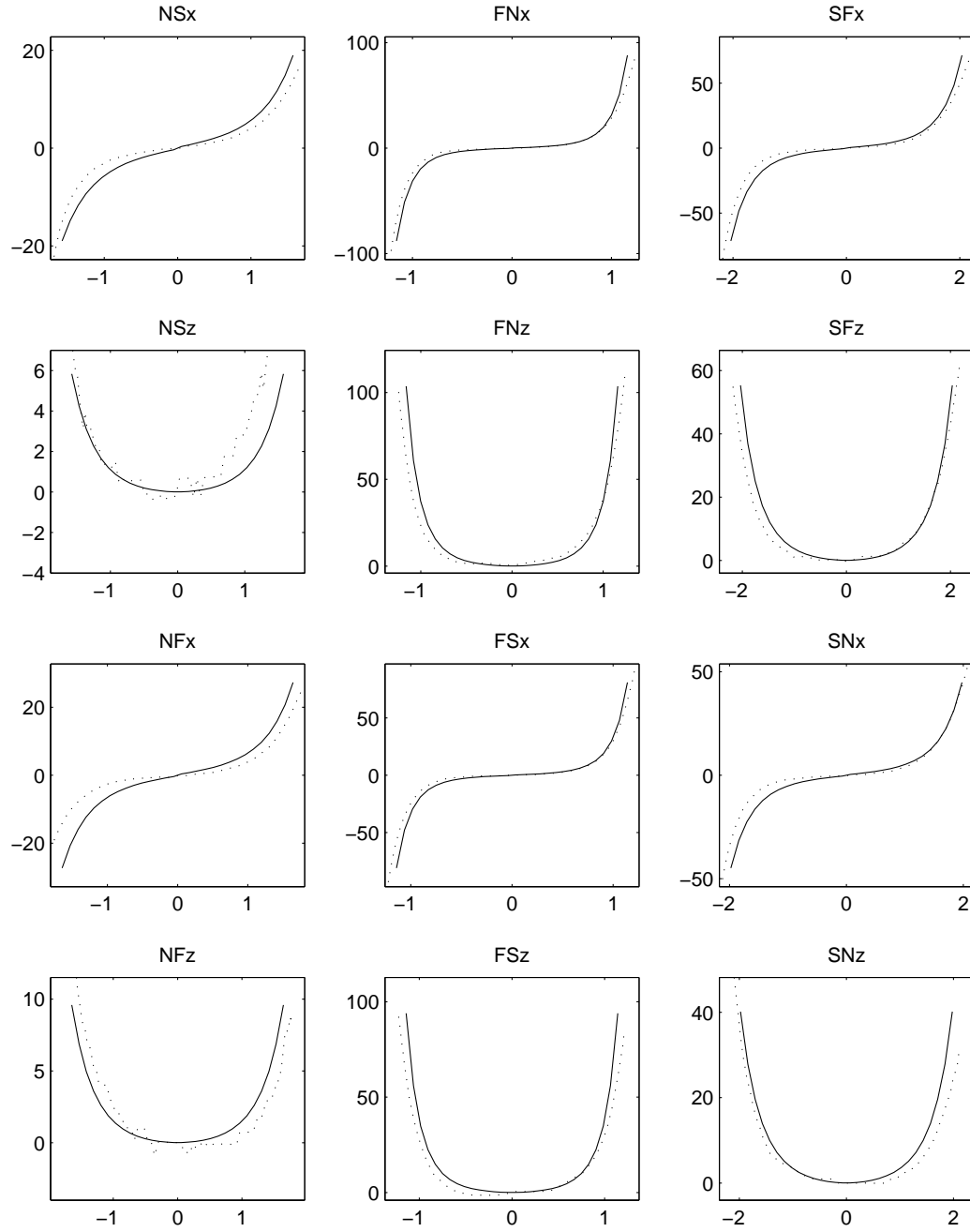
**Graph of FE model, experiment 6, CL**

Figure C.21: This graph shows the result of the FEM model for experiment 6, CL.

Graph of FE model, experiment 6, SFL

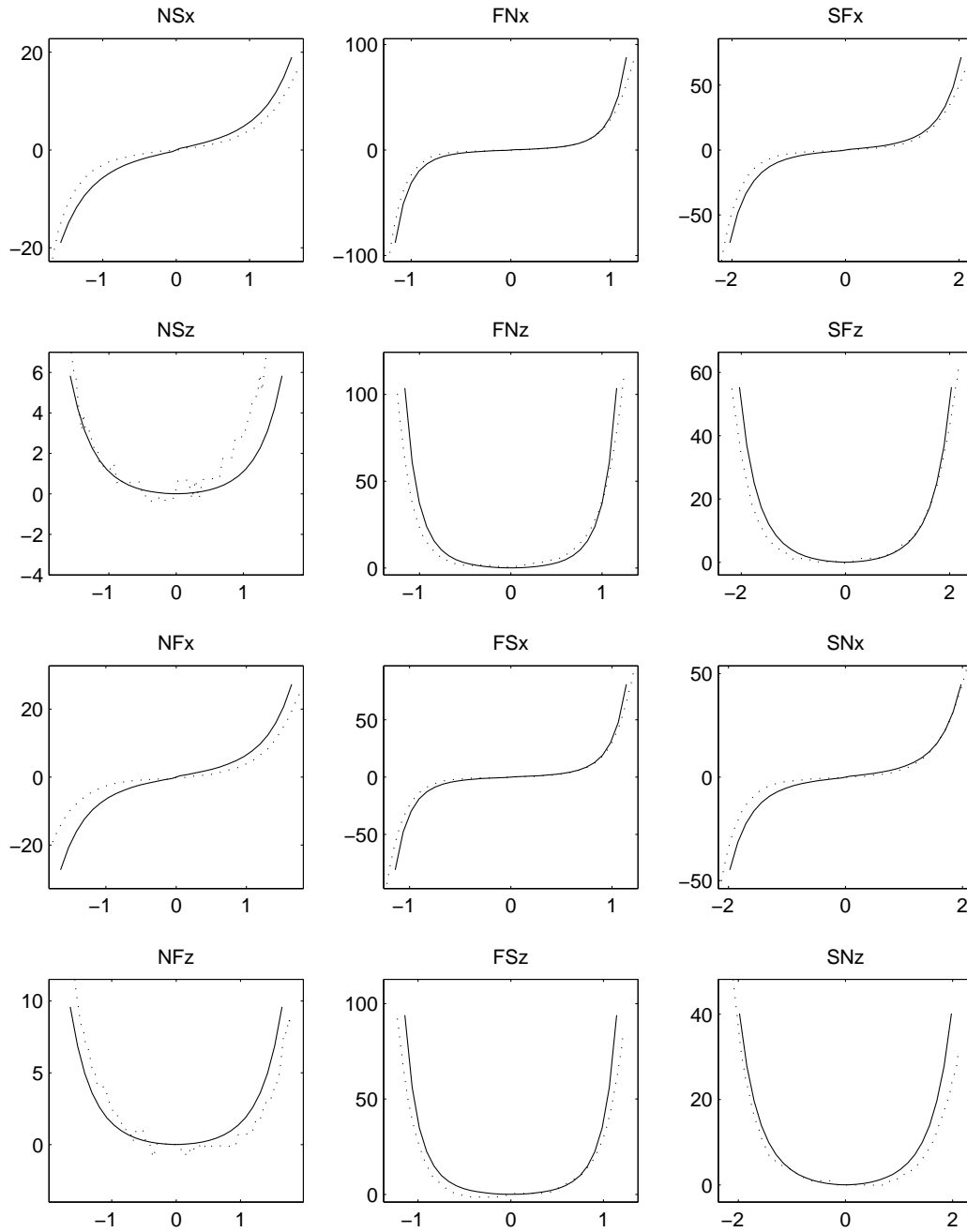


Figure C.22: This graph shows the result of the FEM model for experiment 6, SFL.

**Graph of FE model, experiment 6, PZL**

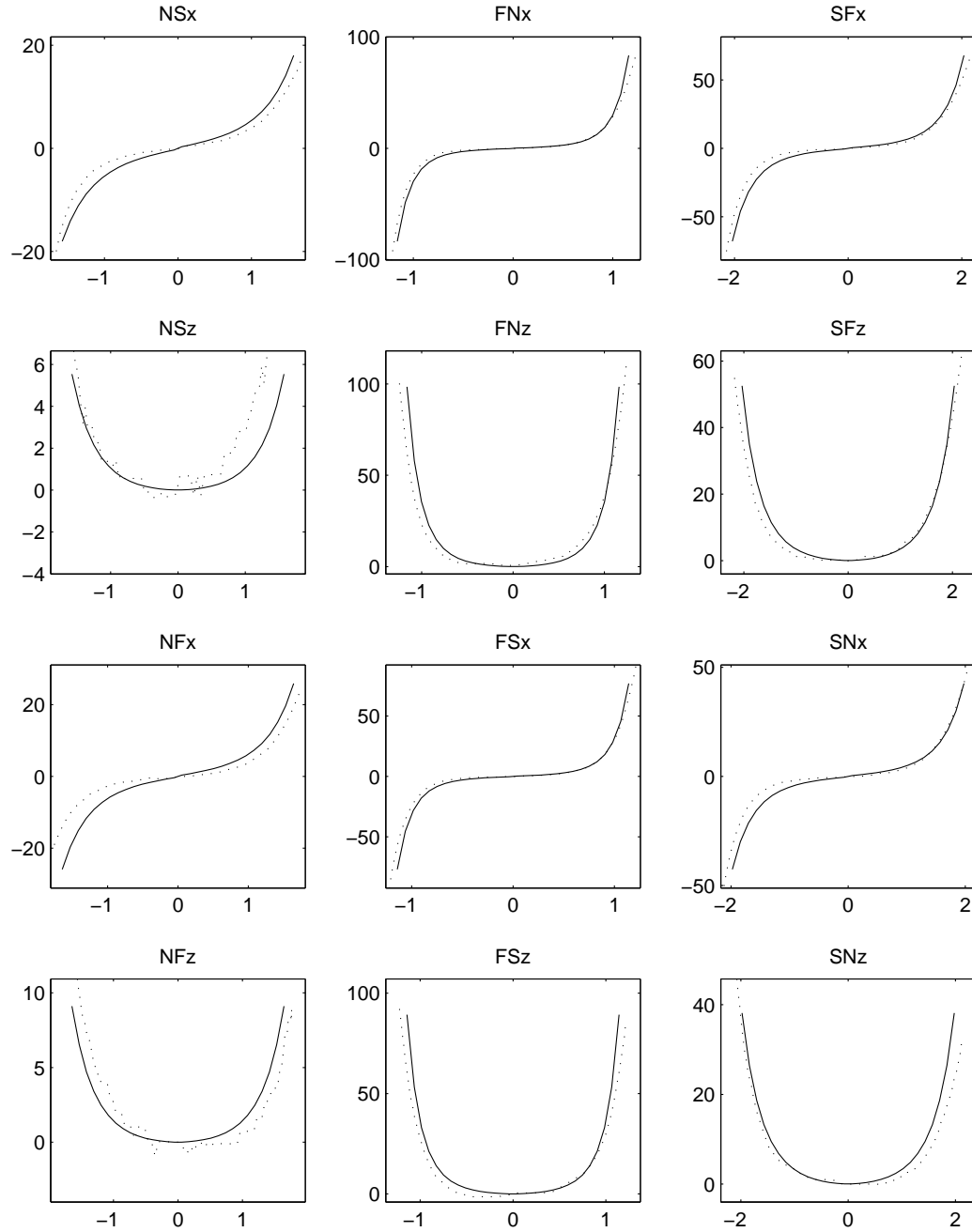


Figure C.23: This graph shows the result of the FEM model for experiment 6, PZL.

## Graph of FE model, experiment 6, TL

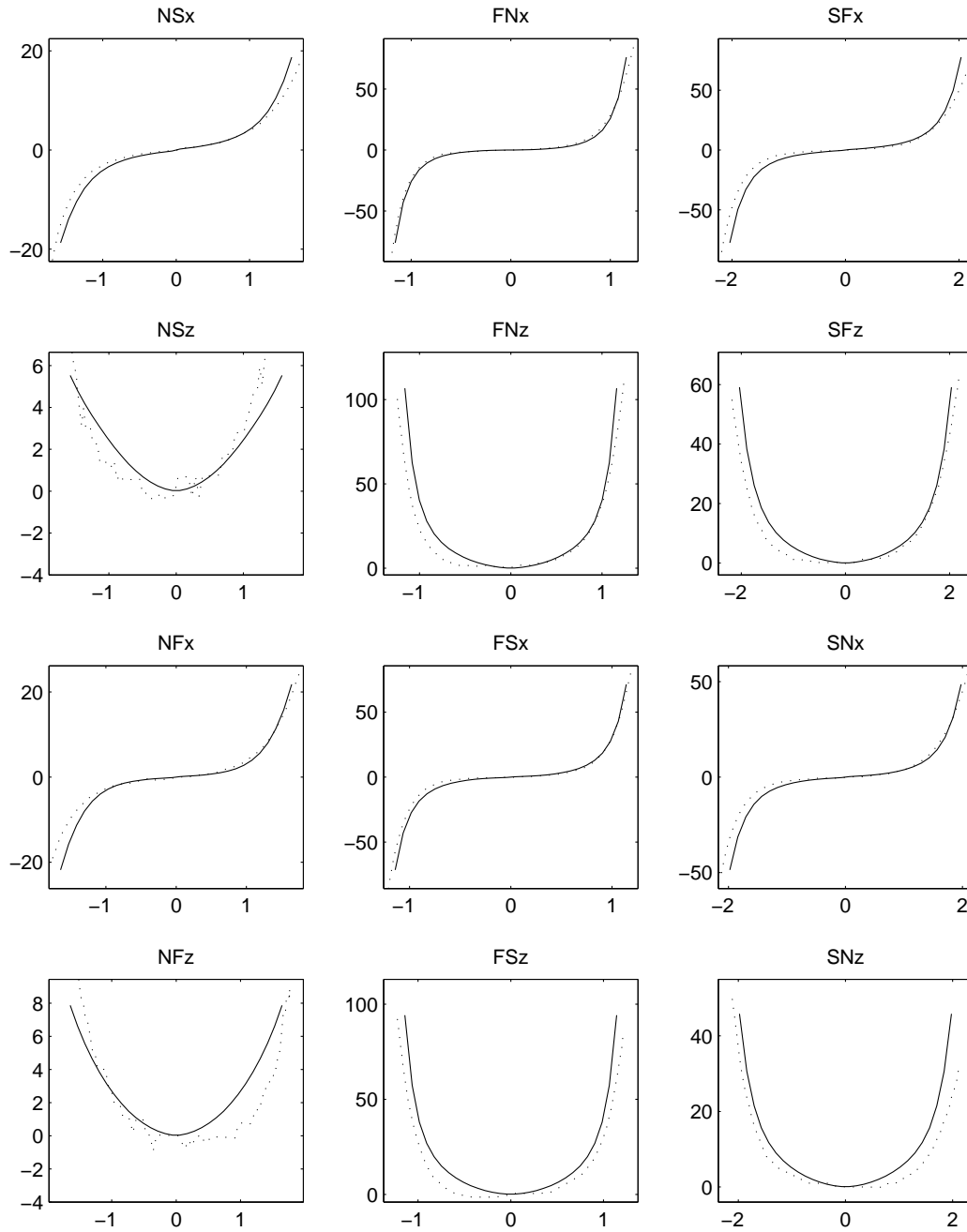


Figure C.24: This graph shows the result of the FEM model for experiment 6, TL.



# Bibliography

- [1] H. Akaike. Information theory as an extension of the maximum likelihood principle. *in B.N. Petrov and F. Csaki (eds.) Second International Symposium on Information Theory*, pages 267–281, 1973.
- [2] H. Akaike. A new look at the statistical model identification. *IEEE Transactions on Automatic Control AC*, 19:716–723, 1974.
- [3] H. Akaike. On entropy maximisation principle. *in P.R. Krishnaiah (ed.) Applications of Statistics, North-Holland, Amsterdam, The Netherlands*, 19:27–41, 1977.
- [4] J.A. Armour and W.C. Randall. Structural basis for cardiac function. *American Journal of Physiology*, 218(6):1517–1523, 1970.
- [5] T. Arts, K.D. Costa, J.W. Covell, and A.D. McCulloch. Relating myocardial laminar architecture to shear strain and muscle fiber orientation. *American Journal of Physiology*, 280:H2222–H2229, 2001.
- [6] R.J. Atkin and N. Fox. *An Introduction to the Theory of Elasticity*. Longman Inc., New York, 1980.
- [7] K. Atkinson. *An introduction to numerical analysis*. Wiley & Sons, Inc., New York, 2 edition, 1989.

- [8] K. Augenstein, E. McVeigh, and A.A. Young. Magnetic resonance imaging and ventricle mechanics. *Philosophical Transactions of the Royal Society of London. Series A, Mathematical and Physical Sciences*, 359(1783):1263–1275, 2001.
- [9] K. F. Augenstein. *FEM analysis of cardiac MRI data*. Phd thesis, University of Auckland, New Zealand, 2005.
- [10] Y. Bard. *Nonlinear Parameter Estimation*. Academic Press, New York and London, 1974.
- [11] K.J. Bathe. *Finite Element Procedures*. Prentice-Hall, Inc., New Jersey, 1982.
- [12] J.E. Bischoff, E.A. Arruda, and K. Grosh. A microstructurally based orthotropic hyperelastic constitutive law. *Journal of Biomechanical Engineering*, 69:570–579, 2002.
- [13] J. Bonet and R.D. Wood. *Nonlinear Continuum Mechanics for the Finite Element Analysis*. Cambridge University Press, 1997.
- [14] B.N. Boots. *Voronoi Polygons*. Geo Books, Norwich, UK, 1986.
- [15] R. Brighenti. Fibre distribution optimisation in fibre-reinforced composites by a genetic algorithm. *Composite Structures*, 71:1–15, 2005.
- [16] K.P. Burnham and D.R. Anderson. *Model selection and multi-model inference: a practical information-theoretic approach*. Springer, New York, 2 edition, 2002.
- [17] R. Busse and I. Fleming. Pulsatile stretch and shear stress: Physical stimuli determining the production of endothelium-derived relaxing factors. *Journal of Vascular Research*, 35:73–84, 1998.

- [18] D. Caillerie, A. Mourad, and A. Raoult. Cell-to-muscle homogenisation. application to a constitutive law for the myocardium. *ESAIM: Mathematical Modelling and Numerical Analysis*, 37(4):681–698, 2003.
- [19] R. S. Chadwick, A. Tedgui, J. B. Michel, J. Ohayon, and B. I. Levy. Phasic regional myocardial inflow and outflow: comparison of theory and experiments. *American Journal of Physiology – Heart and Circulatory Physiology*, 256(6):H1687–H1698, 1990.
- [20] H.S. Choi and R.P. Vito. Two-dimensional stress-strain relationship for canine pericardium. *Journal of Biomechanical Engineering*, 112(2):153–159, 1990.
- [21] T.J. Chung. *Applied Continuum Mechanics*. Cambridge University Press, Cambridge, 1996.
- [22] P.G. Ciarlet. *Mathematical Elasticity*, volume 1. North-Holland, 1988.
- [23] A. Cohen. A padé approximant to the inverse langevin function. *Rheologica Acta*, 30:270–273, 1991.
- [24] H. Cohen and C.-C. Wang. A note on hyperelasticity. *Archive of Rational Mechanics*, 85:213–236, 1984.
- [25] K.D. Costa, J.W. Holmes, and A.D. McCulloch. Modelling cardiac mechanical properties in three dimensions. *Philosophical Transactions of the Royal Society*, 359(1783):1233–1250, June 2001.
- [26] cran.r project.org.
- [27] J.C. Criscione. Rivlins representation formula is ill-conceived for the determination of response functions via biaxial testing. *Journal of Elasticity*, 70:129–147, 2003.



- [28] W.G. Dell and A.D. McCulloch. A novel numerical formulation for modelling tissue compressibility. *Advances in Bioengineering*, 39:391–392, 1998.
- [29] L.L. Demer and F.C.P. Yin. Passive biaxial mechanical properties of isolated canine myocardium. *Journal of Physiology*, 339:615–630, 1983.
- [30] S. Dokos, B.H. Smaill, A. Young, and I.J. LeGrice. Shear properties of passive ventricular myocardium. *American Journal of Physiology and Heart Circulation Physiology*, 283:H2650–H2659, 2002.
- [31] J. Fox. *Applied regression analysis, linear models, and related models*. Sage publications, Inc., Thousand Oaks, California 91320, 1997.
- [32] Y.C. Fung. *Foundations of Solid Mechanics*. Prentice–Hall, Inc., Englewood Cliffs, New Jersey, 1965.
- [33] Y.C. Fung. Biorheology of soft tissues. *Biorheology*, 10:139–155, 1973.
- [34] Y.C. Fung. *Biomechanics: Motion Flow, Stress and Growth*. Springer-Verlag, New York, 1990.
- [35] Y.C. Fung. *Biomechanics: Mechanical Properties of Living Tissues*. Springer, New York, 2 edition, 1993.
- [36] N. Ghoniem, E. Busso, N. Kioussis, and H. Huang. Multiscale modelling of nanomechanics and micromechanics: an overview. *Philosophical Magazine*, 83(31–34):3475–3528, 1. Nov –1. Dec 2003.
- [37] A.E. Green and J.E. Adkins. *Large Elastic Deformations*. Oxford Clarendon Press, Oxford, 1960.

- [38] A.E. Green and W. Zerna. *Theoretical Elasticity*. Oxford Clarendon Press, Oxford, 1954.
- [39] J.M. Guccione, A.D. McCulloch, and L.K. Waldmann. Passive material properties of intact ventricular myocardium determined from a cylindrical model. *Journal of Biomechanical Engineering*, 113:42–55, 1991.
- [40] M.E. Gurtin and S.J. Spector. On stability and uniqueness in finite elasticity. *Archive of Rational Mechanics*, 70:153–165, 1979.
- [41] S. Hartmann and P. Neff. Polyconvexity of generalized polynomial-type hyperelastic strain energy functions for near-incompressibility. *International Journal of Solids and Structures*, 40:2767–2791, 2003.
- [42] H. Hermann, H. Wendrock, and D. Stoyan. Cell-area distributions of planar voronoi mosaics. *Metallography*, 23(3):189–200, 1989.
- [43] J.W. Holmes. Determinants of left ventricular shape change during filling. *Journal of Biomechanical Engineering*, 126(1):98–103, 2004.
- [44] G.A. Holzapfel. *Nonlinear Solid Mechanics*. Wiley, Chichester, 2000.
- [45] G.A. Holzapfel and T.C. Gasser. A new constitutive framework for artiel wall mechanics and a comparative study for material models. *Journal of Elasticity*, 61:1–48, 2000.
- [46] A. Horowitz, Y. Lanir, F.C.P. Yin, M. Perl, I. Sheinman, and R.K. Strumpf. Structural three-dimensional constitutive law for the passive myocardium. *Journal of Biomechanical Engineering*, 110:200–206, 1988.

- [47] J. Humphrey, R. Strumpf, H. Halperin, and Frank Yin. *Toward a stress analysis in the heart in Theory of heart*, L. Glass, P.J. Hunter, A. McCulloch, eds, chapter 3, pages 59–75. Springer Verlag, New York, 1991.
- [48] J. D. Humphrey, R. K. Strumpf, and F. C. P. Yin. Determination of a constitutive relation for passive myocardium: I. a new functional form. *Journal of Biomechanical Engineering*, 112:333–339, 1990.
- [49] J.D. Humphrey. An evaluation of pseudoelastic descriptors used in arterial mechanics. *Journal of Biomechanical Engineering*, 121:259–262, 1999.
- [50] J.D. Humphrey. *Cardiovascular Solid Mechanics – Cells, Tissues, and Organs*. Springer, 2002.
- [51] J.D. Humphrey and K.R. Rajagopal. A constrained mixture model for growth and remodeling of soft tissues. *Mathematical Models and Methods in APplied Sciences*, 12(3):407–430, 2002.
- [52] J.D. Humphrey and K.R. Rajagopal. A constrained mixture model for arterial adaptations to a sustained step change in flow. *Biomechanics and Modelling in Mechanobiology*, 2:109–126, 2003.
- [53] P.J. Hunter. *Myocardial constitutive laws for continuum mechanics models of the heart*. In “*Molecular and subcellular cardiology: Effects of structure and function*”, Eds. S. Sideman and R. Beyar, volume 382, chapter Advances in Experimental Medicine and Biology, pages 303–318. Plenum Press, 1995.

- [54] P.J. Hunter, A.J. Pullan, and B.H. Smaill. Modelling total heart function. *Annual Review Biomedical Engineering*, 5:147–177, 2003. California.
- [55] S.C. Hunter. *Mechanics of Continuous Media*. Chichester: E. Horwood; New York: Halsted Press, New York, 1967.
- [56] M. Itskov and N. Aksel. A class of orthotropic and transversely isotropic hyperelastic constitutive models based on a polyconvex strain energy function. *International Journal of Solids and Structures*, 41:3833–3848, 2004.
- [57] K.-M. Jan. Distribution of myocardial stress and its influence on coronary blood flow. *Journal of Biomechanics*, 18(11):815–820, 1985.
- [58] J.S. Janicki and G.L. Brower. The role of myocardial collagen in ventricular remodeling and function. *Journal of Cardiac Failure*, 8(6):S319–S325, 2002.
- [59] J.S. Janicki and K.T. Weber. Ejection pressure and the diastolic left ventricular pressure-volume relation. *American Journal of Physiology*, 232(6):H545–H552, 1977.
- [60] W. Jaunzemis. *Continuum Mechanics*. The Macmillan Company, New York, 1967.
- [61] L. N. Katz. *Physiology of the Heart*. Raven Press, New York, 1977.
- [62] R.S. Kirton, A.J. Taberner, A.A. Young, P. Nielsen, and D.S. Loiselle. Strain-softening is not present during axial extensions of rat intact right-ventricular trabeculae, in the presence or absence of 2,3–

- butanedione monoxime. *American Journal of Physiology*, 286:H708–715, 2004.
- [63] Y. Lanir. Constitutive equations for fibrous connective tissue. *Journal of Biomechanics*, 16:1–12, 1982.
- [64] Y. Lanir, O. Lichtenstein, and O. Imanuel. Optimal design of biaxial tests for structural material characterization of flat tissues. *Journal of Biomechanical Engineering*, 118:41–47, 1996.
- [65] I.J. LeGrice. *A finite element model of myocardial structure: Implications for electrical activation in the heart*. Phd thesis, University of Auckland, New Zealand, 1992.
- [66] I.J. LeGrice, B.H. Smaill, L.Z. Chai, S.G. Edgar, J.B. Gavin, and P.J. Hunter. Laminar structure of the heart: ventricular myocyte arrangement and connective tissue architecture in the dog. *American Journal of Physiology, Heart Circulation Physiology* 38, 269:H571–H582, 1995.
- [67] I.J. LeGrice, Y. Takayama, and J.W. Covell. Transverse shear along myocardial cleavage planes provides a mechanism for normal systolic wall thickening. *Circulation Research*, 77:182–193, 1995.
- [68] J. Lemaitre and J.-L. Chaboche. *Mechanics of Solid Materials*. Cambridge University Press, The Bath Press, Avon, 1990.
- [69] K. Levenberg. A method for certain nonlinear problems in least squares. *Quart. Appl. Math.*, 2:164–168, 1944.
- [70] J.B. MacCallum. On the muscular architecture and growth of the ventricles of the heart. *John Hopkins Hospital Repertoire*, 9:307–335, 1900.

- [71] J. Weiss B. Maker and S. Govindjee. Finite–element impementation of incompressible, transversely isotropic hyperelasticity. *Computer Methods in Applied Mechanics and Engineering*, 135:107–128, 1996.
- [72] F.P. Mall. On the muscular architecture of the ventricles of the human heart. *American Journal of Anatomy*, 11(3):211–266, 1911.
- [73] L.E. Malvern. *Introduction to the Mechanics of a Continuous Medium*. Prentice–Hall, Inc., Englewood Cliffs, New Jersey, 1969.
- [74] K.V. Mardia and P.E. Jupp. *Directional Statistics*. John Wiley & Sons, Ltd., 2000.
- [75] J.E. Marsden and T.J.R. Hughes. *Mathematical Foundations of Elasticity*. Prentice–Hall, Inc., New Jersey, 1983.
- [76] G.E. Mase. *Theory and Problems of Continuum Mechanics*. Schaum’s Outline Series. Mc Graw–Hill, Inc., New York, 1980.
- [77] A.D. McCulloch. *Cardiac Biomechanics*, in J.D. Bronzino, ed., *The Biomedical Engineering Handbook*, chapter 31, pages 418–439. CRC Press, Inc., Florida, 1995.
- [78] M.R. McLean and J. Prothero. Coordinated three–dimensional reconstruction from serial sections at macroscopic and microscopic levels of resolution: The human heart. *The Anatomical Record*, 219, 1987.
- [79] S.W. Menard. *Applied Logistic Regression Analysis (Quantitative Applications in the Social Sciences)*. Sage Publications, Inc, 2 edition, October 2001.

- [80] A. Menzel and P. Steinmann. On the comparison of two strategies to formulate isotropic hyperelasticity. *Journal of Elasticity*, 62:171–201, 2001.
- [81] I. Mirsky. Assessment of passive elastic stiffness of cardiac muscle: Mathematical concepts, physiologic and clinical considerations, directions of future research. *Progress in cardiovascular diseases*, 18:277–308, 1976.
- [82] J. Moriarty. The law of laplace: Its limitations as a relation for diastolic pressure, volume or wall stress of the left ventricle. *Circulation Research*, 46:321–331, 1980.
- [83] M.J. Moulton, L.L. Creswell, R.L. Actis, K.W. Myers, M.W. Vannier, B.A. Szabo, and M.K. Pasque. An inverse approach to determining myocardial material properties. *Journal of Biomechanics*, 28(8):935–948, 1995.
- [84] M.P. Nash and P.J. Hunter. Computational mechanics of the heart. *Journal of Elasticity*, 61:113–141, 2000.
- [85] M.H. Nathanson and G.M. Saidel. Multiple-objective criteria for optimal experimental design: application to ferrokinetics. *American Journal of Physiology*, 17:R378–R386, 1985.
- [86] O. Nelles. *Nonlinear System Identification*. Springer Verlag, 2001.
- [87] P.M.F. Nielsen. *The anatomy of the heart: A finite element model*. Phd thesis, University of Auckland, New Zealand, 1987.

- [88] P.M.F. Nielsen, I.J. LeGrice, B.H. Smaill, and P.J. Hunter. Mathematical model of geometry and fibrous structure of the heart. *American Journal of Physiology*, 260(29):H1365–H1378, 1991.
- [89] V.P. Novak, F.C.P. Yin, and J.D. Humphrey. Regional mechanical properties of passive myocardium. *Journal of Biomechanics*, 27(4):403–412, 1994.
- [90] J.T. Oden. *Finite Elements of Nonlinear Continua — An Introduction*, volume 1. McGraw–Hill, 1972.
- [91] R.W. Ogden. *Non–Linear Elastic Deformations*. Dover, 1997.
- [92] A. Okabe, B. Boots, and K. Sugihara. *Spatial Tessellations — Concepts and Applications of Voronoi Diagrams*. John Wiley & Sons, New York, 1992.
- [93] M. Papadaki and S. Eskin. Effects of fluid shear stress on gene regulation of vascular cells. *Biotechnology Progress*, 13:209–221, 1997.
- [94] S.H. Peng and W.V. Chang. A compressible approach in finite element analysis of rubber–elastic materials. *Computers & Structures*, 62(3):573–593, 1997.
- [95] J.H. Poynting. On pressure perpendicular to the shear planes in finite pure shears, and on the lengthening of loaded wires when twisted. *Proceedings of the Royal Society of London*, A82:546–549, 1909.
- [96] W.H. Press, B.P. Flannery, S.A. Teukolsky, and W.T. Vetterling. *Numerical Recipes*. Cambridge University Press, 1989.
- [97] T.F. Robinson, L. Cohen-Gould, S.M. Factor, M. Eghbali, and O.O. Blumenfeld. Structure and function of connective tissue in cardiac



- muscle: Collagen types i and ii in endomysial struts and pericellular fibres. *Scanning Microscopy*, 2(2):1005–1015, 1988.
- [98] H. Sandler and H.T. Dodge. Left ventricular tension and stress in man. *Circulation Research*, 13(2):91–104, 1963.
- [99] G.B. Sands, D.A. Gerneke, D.A. Hooks, C.R. Green, B.H. Smaill, and I.J. LeGrice. Automated imaging of extended tissue volumes using confocal microscopy. *Microscopy Research and Technology*, 67:227–239, 2005.
- [100] G.B. Sands and M.L. Trew. Shock-induced transmembrane potential fields in a model of cardiac microstructure. *Journal of Cardiovascular Electrophysiology*, 16(9):1024, 2005.
- [101] S.J. Sarnoff, G.H. Welch Jr. E. Braunwald, R.B. Case, W.N. Stainsby, and R. Macruz. Haemodynamic determinants of oxygen consumption of the heart with special reference to the tension-time index. *American Journal of Physiology*, 192:148–156, 1958.
- [102] H. Schmid, M.P. Nash, C. Walker, G.B. Sands, A. Pope, I.J. LeGrice, A.A. Young, P. Nielsen, and P.J. Hunter. A framework for multi-scale modeling of the heart. *IFMBE Proceedings, Prague: IFMBE, ISSN 1727-1983. Eds: Jiri Hozman, Peter Kneppo (Proceedings of the 3rd European Medical & Biological Engineering Conference - EMBEC 05. Prague, Czech Republic, 20-25.11.2005), Id. 2535*, 11:4201–4205, 2005.
- [103] H. Schmid, M.P. Nash, A.A. Young, and P.J. Hunter. Myocardial material parameter estimation – a comparative study for simple shear. *Journal of Biomechanical Engineering*, 2006. accepted.

- [104] H. Schmid, M.P. Nash, A.A. Young, and P.J. Hunter. Myocardial material parameter estimation from simple shear tests – a non-homogeneous finite element study. *Journal of Biomechanical Engineering*, 2006. at review.
- [105] H. Schmid, M.P. Nash, A.A. Young, O. Röhrle, and P.J. Hunter. A computationally efficient optimization kernel for material parameter estimation procedures. *Journal of Biomechanical Engineering*, 2006. at review.
- [106] J.S. Sjöberg, Q. Zhang, L. Ljung, A. Benveniste, B. Deylon, P. Glorrenec, H. Hjalmarsson, and A. Juditsky. Nonlinear black-box modelling in system identification: A unified overview. *Automatica*, 31:1691–1724, 1995.
- [107] B. Smaill and P. Hunter. *Theory of Heart*, chapter 1, Structure and Function of the Diastolic Heart: Material Properties of Passive Myocardium, pages 1–29. Springer-Verlag, 1991.
- [108] N.P. Smith, D.P. Nickerson, E.J. Crampin, and P.J. Hunter. Multiscale computational modelling of the heart. *Acta Numerica*, pages 371–431, 2004.
- [109] I.S. Sokolnikoff. *Tensor Analysis: Theory and Application to Geometry and Mechanics of Continua*. John Wiley & Sons, Inc., New York, second edition, 1964.
- [110] A.J.M. Spencer. *Continuum Mechanics*. Longman Group Ltd., New York, 1980.

- [111] J.G. Stinstra, B. Hopenfield, and R.S. MacLeod. On the passive cardiac conductivity. *Annals of Biomedical Engineering*, 33(12):1743–51, Dec 2005.
- [112] G. Strang. *Linear Algebra and its Applications*. Academic Press, Inc., New York, 1976.
- [113] D.D. Jr. Streeter. *Gross Morphology and Fiber Geometry of the Heart*, in R.M. Berne and N. Sperelakis and S.R. Geiger, eds, *Handbook of Physiology (Section 2: The Cardiovascular System, Vol. 1: The Heart)*, chapter 4, pages 61–112. Williams and Wilkins Company, 1979.
- [114] D.D. Jr. Streeter, H.M. Spotnitz, D.P. Patel, J. Ross Jr., and E.H. Sonnenblick. Fiber orientation in the canine left ventricle during diastole and systole. *Circulation Research*, 24:339–347, 1969.
- [115] H. Suga, K. Sagawa, and A.A. Shoukas. Load independence of the instantaneous pressure-volume ratio of the canine left ventricle and effects of epinephrine and heart rate on the ratio. *Circulation Research*, 32:314–322, 1973.
- [116] M.L. Trew, I.J. LeGrice, B.H. Smaill, and A.J. Pullan. A finite volume method for modelling discontinuous electrical activation in cardiac tissue. *Annals of Biomedical Engineering*, 33(5):590–602, 2005.
- [117] C. Truesdell. *Continuum Mechanics I, The Mechanical Foundations of Elasticity and Fluid Dynamics*, volume 8 of *International Science Review Series*. Gordon and Breach Science Publishers, Inc., New York, 1966.
- [118] C. Truesdell and W. Noll. *The non-linear field theories of mechanics*. Springer Verlag, 1965.

- [119] C.R. Vogel. *Computational Methods for Inverse Problems*. SIAM, Philadelphia, 2002.
- [120] J.P. Wilber and J.R. Walton. The convexity properties of a class of constitutive models for biological soft tissues. *Mathematics and Mechanics of Solids*, 7:217–235, 2002.
- [121] A.Y.K. Wong and P.M. Rautaharju. Stress distribution within the left ventricular wall approximated as a thick ellipsoidal shell. *American Heart Journal*, 75(5):649–662, 1968.
- [122] R.H. Woods. A few applications of a physical theorem to membranes in the human body in a state of tension. *Journal of Anatomical Physiology*, 26:362–370, 1892.
- [123] [www.cellml.org](http://www.cellml.org).
- [124] [www.cmiss.org](http://www.cmiss.org).
- [125] [www.mathworks.com](http://www.mathworks.com).
- [126] [www.ni.com/labview/](http://www.ni.com/labview/).
- [127] F.C.P. Yin, P.H. Chew, and S.L. Zeger. An approach to quantification of biaxial tissue stress–strain data. *Journal of Biomechanics*, 19:27–37, 1986.
- [128] A.A. Young, I.J. LeGrice, M.A. Young, and B.H. Smaill. Extended confocal microscopy of myocardial laminae and collagen network. *Journal of Microscopy*, 192(2):139–150, 1998.
- [129] O.C. Zienkiewicz and R.L. Taylor. *The finite element method*, volume 3. Butterworth-Heinemann, Oxford, 5 edition, 2000.